# Engineering Bioaffinity Sensors toward Continuous Electrochemical Biosensing

Thesis by
Heather Lukas

In Partial Fulfillment of the Requirements for the
Degree of
Doctor of Philosophy


CALIFORNIA INSTITUTE OF TECHNOLOGY
Pasadena, California

2025
Defended August 16, 2024

Heather Lukas
ORCID: 0000-0002-8160-9066

# ACKNOWLEDGEMENTS

I dedicate this work to those who believed in me even when I did not believe in myself. Thank you for your guidance, support, and encouragement to keep pushing forward.

Firstly, I would like to express my deep gratitude and respect for my research advisor, Professor Wei Gao. When I first came to Caltech, Professor Gao and I connected over our passion for improving patient health and quality of life through medical technology innovation. While my research path twisted and turned, this was a core value that we always returned to. Thank you, Professor Gao, for your unwavering support in my scientific exploration and guidance toward the successful execution of this work. It has been an honor to be a member of the Gao Group.

I would also like to thank the members of my thesis committee, Professor Henry Lester, Professor Azita Emami, and Professor Mikhail Shapiro, for their time and support while at Caltech. Your feedback and insight has been invaluable to the completion of this research.

Additionally, I thank the Medical Engineering Department and more broadly the Engineering and Applied Science Division at Caltech for the amazing faculty and staff. Thank you to the Pyott Family and the Medical Engineering Department's financial support for enabling me to pursue these challenging problems with scientific freedom.

Many people were involved in the projects presented in this thesis. Thank you to the Gao Group for their interdisciplinary work and moral support that made this research possible. I am fortunate to have gained a breadth of knowledge and skills from the diverse expertise within our group. I would also like to thank my collaborators in the Lester Group for their contributions, shared use of their facilities, and stimulating discussions. The Lester Group ingrained in me a biochemist's mindset, making me a thoughtful engineer when it comes to experimental control design and troubleshooting.

During my time at Caltech, I have been fortunate to find support among several communities. Thank you to Womxn in EAS and the founding members that helped me build it up as an organization. Thank you to MedTech Innovator for reigniting my passion for entrepreneurship and supporting my professional development and growth. Thank you to Bar Method Pasadena for strengthening me physically and

mentally. And, thank you to my friends and roommates that have been there for me through it all.

Lastly, I would like to thank my family for their enduring support and role in shaping who I am today. Thank you to my parents for instilling in me the values of education and hard work. Thank you to my sister, Dr. Vanessa Lukas, for being an inspiration throughout my academic career. Thank you to my partner Jack Weeks for being a constant source of love and encouragement through the highs and lows of the PhD.

# ABSTRACT

The rise of wearable sensing through smartwatches and continuous glucose monitors has made health data more widely accessible. Advances in machine learning have also been pivotal in identifying personalized health insights from biometric data streams. However, continuous biochemical data has been limited in sensor design by the availability of oxidoreductases (e.g., glucose oxidase, lactate dehydrogenase) to a given target. The challenge in engineering diverse oxidoreductase enzymes has led to the exploration of other generalized approaches to continuous electrochemical biosensing. To meet this need, we have explored a variety of bioaffinity sensing schemes using broad bioreceptor classes including antibodies, nucleic acids, and periplasmic binding proteins. We present a case study in electrochemical sensor design utilizing high-affinity antibodies for the rapid diagnosis of COVID-19 disease states. We then investigate the potential of nucleic acid-based electrochemical sensors for continuous sensing with a focus on structure-switching nucleic acid aptamers. The utility of aptamer sensors is demonstrated in the development of a serotonin aptamer sensor embedded in an ingestible capsule for continuous biosensing in the gastrointestinal tract. Applying the principles of electrochemical aptamer-based sensing, we explored the development of an electrochemical protein-based sensor for nicotine, which exploits the hinge-like binding motion of periplasmic binding proteins while also capitalizing on decades of protein evolution and characterization research. With the goal of continuous, noninvasive biochemical sensing, we evaluate the design considerations and translatability of these sensors for wearable sweat analysis. These biosensing techniques may enable the future hardware necessary to expand accessible biomedical data for the next wave of personalized health monitoring.

# PUBLISHED CONTENT AND CONTRIBUTIONS

[1] Jihong Min, Hyunah Ahn, Heather Lukas, Xiaotian Ma, Rinni Bhansali, Sung-Hyuk Sunwoo, Canran Wang, Yadong Xu, Richard Yao, Gwangmook Kim, Zhaoping Li, Tzung K. Hsiai, Azita Emami, Hee-Tae Jung, and Wei Gao. "Continuous biochemical profiling of the gastrointestinal tract using a multiparametric ingestible capsule". *Nature Electronics* **submitted July 2024**,
W.G., and J.M. initiated the concept and designed the studies; W.G. supervised the work; J.M., and H.A. led the experiments and collected the overall data; H.L. led the design and validation of the serotonin aptamer sensor; R.B., and G.K. contributed to sensor characterization and validation; X.M., and S.S. contributed to the animal studies; Z.L., T.K.H., A.E., H.T.J. contributed the study design. All authors contributed the data analysis and provided the feedback on the manuscript.

[2] William Reis de Araujo, Heather Lukas, Marcelo D. T. Torres, Wei Gao, and Cesar de la Fuente-Nunez. "Low-Cost Biosensor Technologies for Rapid Detection of COVID-19 and Future Pandemics". *ACS Nano* **2024**, *18* (3), 1757–1777. DOI: 10.1021/acsnano.3c01629
All authors prepared the figures and the manuscript.

[3] Cui Ye, Heather Lukas, Minqiang Wang, Yerim Lee, and Wei Gao. "Nucleic acid-based wearable and implantable electrochemical sensors". *Chemical Society Reviews* **2024**, DOI: 10.1039/D4CS00001C
All authors prepared the figures and the manuscript.

[4] Jihong Min, Jiaobing Tu, Changhao Xu, Heather Lukas, Soyoung Shin, Yiran Yang, Samuel A. Solomon, Daniel Mukasa, and Wei Gao. "Skin-interfaced wearable sweat sensors for precision medicine". *Chemical Reviews* **2023**, *123* (8), 5049–5138. DOI: 10.1021/acs.chemrev.2c00823
All authors prepared the figures and the manuscript.

[5] Cui Ye, Minqiang Wang, Jihong Min, Roland Yingjie Tay, Heather Lukas, Juliane R. Sempionatto, Jiahong Li, Changhao Xu, and Wei Gao. "A wearable aptamer nanobiosensor for non-invasive female hormone monitoring". *Nature Nanotechnology* **2023**, 1–8. DOI: 10.1038/s41565-023-01513-0
W.G. and C.Y. initiated the concept and designed the overall studies. W.G. supervised the work. C.Y. and M.W. led the experiments and collected the overall data. J.M., R.Y.T., H.L., J.R.S. and C.X. contributed to sensor characterization and validation. J.L. contributed to the numerical simulation. All authors contributed the data analysis and provided feedback on the manuscript.

[6] Heather Lukas, Changhao Xu, You Yu, and Wei Gao. "Emerging telemedicine tools for remote COVID-19 diagnosis, monitoring, and management". *ACS*

*Nano* **2020**, *14* (12), 16180–16193. DOI: 10.1021/acsnano.0c08494
All authors prepared the figures and the manuscript.

[7] Rebeca M. Torrente-Rodríguez, Heather Lukas, Jiaobing Tu, Jihong Min, Yiran Yang, Changhao Xu, Harry B. Rossiter, and Wei Gao. "SARS-CoV-2 RapidPlex: A graphene-based multiplexed telemedicine platform for rapid and low-cost COVID-19 diagnosis and monitoring". *Matter* **2020**, *3* (6), 1981–1998. DOI: 10.1016/j.matt.2020.09.027
W.G., R.M.T.-R., and H.L. initiated the concept and designed the experiments; R.M.T.-R., H.L., and J.T. led the experiments and collected the overall data; Y.Y. performed electrode fabrication and characterization; J.M. performed the circuit design and platform test; C.X. contributed to sensor characterization; W.G., R.M.T.-R., and H.L. contributed the data analysis and co-wrote the paper. All authors provided the feedback on the manuscript.

# TABLE OF CONTENTS

# LIST OF ILLUSTRATIONS

# LIST OF TABLES

*Chapter 1*

# INTRODUCTION

Real-time health monitoring is key to medical diagnosis, intervention, and prevention. Biosensing through noninvasive wearable devices, such as smart watches, allows for continuous personalized health monitoring. Wearable physical sensors have been well-developed to noninvasively collect continuous vital sign data but provide minimal information to understand physiological changes. Therefore, increased quantity and diversity of high-quality biochemical data is needed to make better diagnostic predictions.

Electrochemical biosensors convert a molecular recognition event to a measurable electronic signal. The fundamental components of electrochemical sensor design include a biorecognition element, a signal transducer, a conductive interface, and processing electronics. Bioaffinity sensors utilize bioreceptors with a selective binding affinity for a target analyte. The intrinisic properties of the bioreceptor impact the operational performance of the sensor, including sensitivity, selectivity, stability, and regeneration. Key characteristics of the bioreceptor may also inform the signal transduction scheme.

Antibody-based biosensors are among the most common type of bioaffinity sensor. This is because they are high-affinity binding, allowing for ultrasensitive detection, and because they can be produced against diverse biomolecules. Antibodies have typically been used for the sensitive and selective detection of biomarkers through qualitative at-home tests, or quantitative lab-based enzyme-linked immunosorbent assay (ELISA) testing.

Considering COVID-19, we developed an ultrasensitive, multiplexed electrochemical sensor for the detection of COVID-19 antibodies, antigen, and C-reactive protein (CRP) to deliver rapid and quantitative results regarding a patient's infection status and severity (Chapter 2). The sensor was based on laser-engraved graphene electrodes with a sandwich ELISA scheme. HRP-conjugated detector antibodies labeled the bound target and facilitated a redox reaction that could be measured via chronoamperometry. Using high-affinity antibody-decorated electrodes, we were able to detect four biomarkers of interest simultaneously with high sensitivity and high selectivity in under 10 minutes of sample addition. While antibodies work well

as high-affinity biorecognition elements, irreversible binding and multistep labeling limits their applications to single-use assays.

In contrast to rapid diagnostics, continuous monitoring is important for a variety of health conditions and may be used for precision medicine and predictive diagnostics. Wearable continuous glucose monitors (CGM) have revolutionized diabetes management. Glucose oxidase is the constitutive enzyme of CGM sensors. As an oxidoreductase, glucose oxidase acts as regenerative bioreceptor and an electrochemical transducer. However, the challenge in engineering diverse oxidoreductase enzymes has limited the breadth of continuous biochemical sensors. To meet this need, we explore other generalized approaches to continuous electrochemical biosensing.

To achieve continuous sensing, we investigated two classes of high-affinity, folding biorecognition elements: (i) nucleic acid-based aptamers (Chapters 3 and 4) and (ii) periplasmic-binding proteins (PBP) (Chapter 5). While aptamers are a relatively new sensing element with unpredictable selection of reversible binding schemes, they present as a robust bioreceptor with simple redox moiety labeling for electrochemical signaling upon folding. The same signaling scheme may be applied to the well-characterized class of membrane receptors known as periplasmic-binding proteins. A broad database of PBPs exist, which can be further expanded through protein engineering techniques such as site-directed mutagenesis. By nature, PBPs elicit a large, reversible hinge-like binding motion. Employing these characteristics and applying electrochemical aptamer-based (EAB) sensing schemes, a new class of continuous electrochemical PBP (ePBP) sensors will be introduced.

Continuous electrochemical sensors may be implemented in both wearable and implantable form factors. To monitor localized gastrointestinal health and study the gut-brain axis, we developed an ingestible capsule incorporating an aptamer-based serotonin sensor (Chapter 4). The sensor continuously measures intestinal fluid serotonin levels as the capsule moves through the length of the gastrointestinal tract. We also consider the application of wearable sweat sensing (Chapter 6) and present a discussion of sweat physiology and induction to inform the feasibility of an ePBP-based nicotine sweat sensor.

In this work, we research the biorecognition bottleneck of continuous sensing. Combined with platform advancements including sweat induction, sweat collection, microfluidics, conductive nanomaterials, flexible electronics, and signal processing methods, we progress closer to the goal of broad spectrum continuous, noninvasive

biochemical sensing. Looking forward, we evaluate the translation and path to commercialization of these sensors for wearable sweat analysis (Chapter 6). Continuous wearable sensing technology may ultimately expand accessible biomedical data for the next wave of personalized health monitoring.

*Chapter 2*

# AFFINITY SENSORS FOR POINT-OF-CARE COVID-19 DIAGNOSIS

*Materials from this chapter appear in:*

Rebeca M. Torrente-Rodríguez et al. "SARS-CoV-2 RapidPlex: A graphene-based multiplexed telemedicine platform for rapid and low-cost COVID-19 diagnosis and monitoring". *Matter* **2020**, *3* (6), 1981–1998. DOI: 10.1016/j.matt.2020.09.027

Heather Lukas et al. "Emerging telemedicine tools for remote COVID-19 diagnosis, monitoring, and management". *ACS Nano* **2020**, *14* (12), 16180–16193. DOI: 10.1021/acsnano.0c08494

On March 11, 2020, the World Health Organization characterized the COVID-19 outbreak as a pandemic. Six months later, the global health crisis had continued with over 30 million confirmed cases of novel coronavirus globally, with over 22% of these being in the United States.[1] It is estimated that 14%–20% of patients will develop severe illness requiring hospitalization.[2] Initial efforts to mitigate the spread through state-mandated "stay-at-home" orders appeared effective; however, reopening of the United States economy resulted in renewed exponential spread of novel coronavirus, as predicted.[3] It is estimated that the United States gross domestic product will suffer losses upward of $45.3 billion during a flu-like pandemic without available vaccines[1].[5] Safe reopening of the economy, schools, and universities requires multiple approaches to mitigate the risks associated with COVID-19, including simple, affordable, and effective test-and-trace measures.

Containing the spread is difficult due to the challenges in identifying infectious individuals. Most COVID-19 community spread may occur in the absence of symptoms. Peak viremia may be at the end of the incubation period, allowing for a transmission-sufficient viral load 1-2 days prior to symptom onset.[3] Additionally,

[1] Retrospective macroeconomic studies estimate that the economic toll in the United States was a loss of $14 trillion by the end of 2023. Direct U.S. healthcare costs driven by hospitalizations were approximated around $200 billion over the first two years of the pandemic.[4]

due to the unknown duration and prevalence of asymptomatic cases, the true reproduction number may be underestimated.[6, 7] Reported incidence of asymptomatic patients ranges from 17.9% to 30.8%.[8, 9]

Increased access to COVID-19 testing has allowed increased monitoring of the community spread, but several diagnostic challenges remain. Currently, the standard testing method is viral nucleic acid real-time polymerase chain reaction (RT-PCR), which is a slow process and requires expensive equipment and trained technicians for nasopharyngeal swab sample collection and analysis.[10] In addition, the sheer volume of testing required is overwhelming the ability for healthcare systems to report RT-PCR results to patients, causing, in some states, delays of ∼7-10 days to inform positive[11] findings and enact isolation and monitoring protocols. Despite the recent advances on point-of-care (POC) rapid RT-PCR test,[12, 13, 14, 15, 16] nucleic acid tests are also known to produce false negatives, which may limit containment strategies and access to treatment.[17] An additional consideration for RT-PCR is that it only identifies active carriers of the virus. Identifying convalescent persons based on COVID-19 antibody presentation is equally important as it may provide health officials with crucial information regarding the potential impact of reopening measures. Serologic assays detect circulating antibodies specific to SARS-CoV-2 antigens, including the nucleocapsid protein and the outer spike protein.[10, 18, 19] However, it is not possible to differentiate between asymptomatic carriers and immune persons using antibody detection. Therefore, to effectively mitigate the risks of COVID-19 community spread, systems are required that determine simultaneously both the viral and serologic status of an individual. Moreover, recent studies show correlation between circulating inflammatory biomarker concentration and COVID-19 severity.[20] Increased C-reactive protein (CRP) concentration is found in patients diagnosed with COVID-19 pneumonia and is associated with increasing severity, suggesting a role in diagnosis and prognosis of COVID-19 patients.[21, 22]

There is a clear and urgent need for a highly sensitive, rapid, inexpensive, telemedicine COVID-19 test that can identify a patient's past and present infection status.[23] There has been progress toward POC COVID-19 testing, but all commercially available test kits provide only qualitative results. Quantitative analysis of COVID-19 biomarkers using a telemedicine device may provide predictive information of disease severity and provide seroconversion information regarding disease time course. Electrochemical biosensors, in this regard, are advantageous due to their rapid detec-

tion efficacy and ease of use for POC applications.[24, 25, 26, 27, 28] Simple, safe, and effective COVID-19 sample collection has proved challenging given current assay requirements. Saliva-compatible POC assays would be advantageous since saliva contains rich information and can be easily and noninvasively collected by patients themselves for telemedicine testing.[29]

| Viral Antigen | IgM | IgG | CRP | Expected Outcome |
|---|---|---|---|---|
| – | – | – | – | healthy |
| + | + \|\| – | – | – | infectious, presymptomatic |
| + | + \|\| + | | – | infectious, asymptomatic |
| + | + \|\| + | | + | infectious, symptomatic |
| – | + | + \|\| – | + \|\| – | recovered (recently) |
| – | – | + | – | recovered (long term) |
| – | – | – | + | inflammation/infection not due to COVID-19 |

+, higher than threshold; –, lower than threshold; ||, or.

Table 2.1: Key information on an individual's COVID-19 infection status provided by the SARS-CoV-2 RapidPlex.

In this chapter, we present a novel multiplexed, portable, wireless electrochemical platform for ultra-rapid detection of COVID-19: SARS-CoV-2 RapidPlex (Figure 2.1). This platform quantitatively detects biomarkers specific to COVID-19 in both blood and saliva including SARS-CoV-2 nucleocapsid protein (NP), specific immunoglobulins (Igs) against SARS-CoV-2 spike protein (S1) (S1-IgM and S1-IgG), and CRP, within physiologically relevant ranges. The platform uses capture antigens and antibodies immobilized on mass-producible, low-cost laser-engraved graphene (LEG)[30, 31] electrodes. This multiplexed platform tracks the infection progression by diagnosing the stage of the disease, allowing for the clear identification of individuals who are infectious, vulnerable, and/or immune (Table 2.1). The main features of SARS-CoV-2 RapidPlex are high sensitivity, low cost, ultra-fast detection, wireless remote and multiplexed sensing that provides information on three key aspects of COVID-19 disease: viral infection (NP),[32] immune response (IgG and IgM),[10] and disease severity (CRP).[20, 21, 22] We then provide a summary of additional telemedicine-based tools for COVID-19 diagnosis, symptom monitoring, prognosis, and risk prevention. We highlight rapid and remote diagnostics, wearables for symptom monitoring, and mobile platforms for tracking community spread. We also present novel electrochemical platforms developed for biomarker sensing for rapid diagnostics, risk assessment, and on-body monitoring at home.

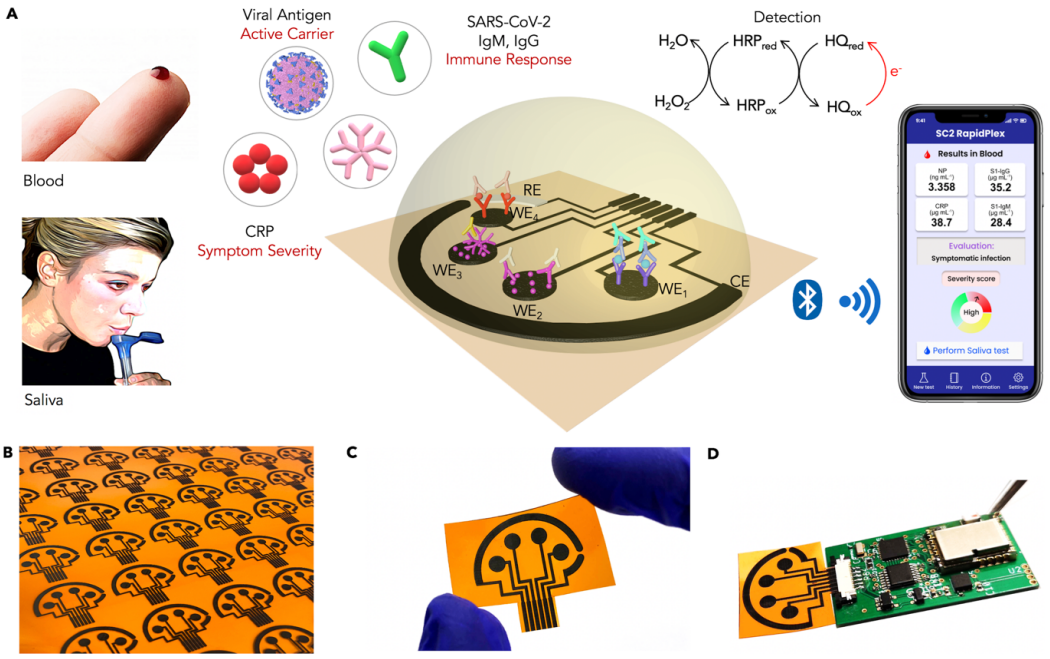


Figure 2.1: A wireless graphene-based telemedicine platform (SARS-CoV-2 RapidPlex) for rapid and multiplex electrochemical detection of SARS-CoV-2 in blood and saliva

(A) Schematic illustration of the SARS-CoV-2 RapidPlex multisensor telemedicine platform for detection of SARS-CoV-2 viral proteins, antibodies (IgG and IgM), and inflammatory biomarker – C-reactive protein (CRP). Data can be wirelessly transmitted to a mobile user interface. WE, working electrode; CE, counter electrode; RE, reference electrode. (B) Mass-producible laser-engraved graphene sensor arrays. (C) Photograph of a disposable and flexible graphene array. (D) Image of a SARS-CoV-2 RapidPlex system with a graphene sensor array connected to a printed circuit board for signal processing and wireless communication.

## 2.1 Design and Validation of the SARS-CoV-2 RapidPlex Platform

As illustrated in Figure 2.1A, SARS-CoV-2 RapidPlex is composed of four graphene working electrodes (WEs), a Ag/AgCl reference electrode (RE), and a graphene counter electrode (CE), all of them patterned on a polyimide (PI) substrate via $CO_2$ laser engraving, a fast, high-throughput, and cost-effective production method (Figure 2.1B,C). Our group has recently demonstrated the use of mesoporous graphene structure fabricated by laser engraving for high-performance and low-cost biosensing.[30, 31] The materials cost for the unmodified RapidPlex platform is within $0.05; additional chemical and reagent costs for the multiplexed sensor preparation are at the level of dollars depending on the order sizes. Detection of selected target proteins (NP and CRP) and specific immunoglobulins (S1-IgG and S1-IgM) is

achieved through sandwich- and indirect-based immunosensing strategies onto the LEG electrodes, respectively. The superior properties of graphene, in terms of high charge mobility and surface area together with the high sensitivity and selectivity of sensing strategies involving both capture and detector receptors, make our device (Figure 2.1D) a highly convenient tool for the rapid, accurate, and stage-specific detection of COVID-19 infection in blood as well as in noninvasive biofluid samples, such as saliva.

### 2.1.1 Materials and Methods

PBA (97%), PPA (97%), 1-ethyl-3-(3-dimethylamonipropyl)carbodiimide (EDC), N-hydroxysulfosuccinimide (sulfo-NHS), BSA, hydroquinone (HQ), 2-(N-morpholino)ethanesulfonic acid hydrate (MES), Tween 20, sodium thiosulfate, sodium bisulfite, and potassium ferrocyanide(II) were purchased from Sigma-Aldrich. Streptavidin-POD conjugate (streptavidin-HRP, 11089153001) was purchased from Roche. Sodium dihydrogen phosphate, potassium hydrogen phosphate, potassium chloride, hydrogen peroxide (30% [w/v]), sulfuric acid, and flat-bottom NUNC 96-well microplates were purchased from Fisher Scientific. Potassium ferricyanide(III) and silver nitrate, iron(III) chloride, and 0.1 M PBS (pH 7.4) were purchased from Acros Organics and Alfa Aesar, respectively. N,N-Dimethylformamide (DMF) and isopropyl alcohol (IPA) were purchased from Fisher Chemical and VWR Chemicals, respectively. Anti-CRP murine monoclonal antibody and human CRP standard were purchased from R&D Systems (DY1707). CRP polyclonal antibody labeled with horseradish peroxidase (HRP) (PA1-28329) and 3,3',5,5'-tetramethylbenzidine (TMB) colorimetric substrate was purchased from Invitrogen. Mouse NP monoclonal antibody (mAb) (40143-MM05), SARS-CoV-2 NP antigen (40588-V08B), SARS-CoV/SARS-CoV-2 nucleocapsid antibody, rabbit mAb (40143-R001), SARS-CoV NP antigen (HCoV-OC43; 40643-V07E), SARS-CoV-2 Spike S1-His recombinant protein (HPLC-verified) (40591-V08H), and SARS-CoV Spike S1 protein (S1 subunit, His-tag) (40150-V08B1) were purchased from Sino Biological. His-tagged SARS-CoV-2 Spike S1 protein (PNA002), His-tagged SARS-CoV-2 NP (PNA006), anti-Spike-RBD fully human mAb (IgG) (S1-IgG, AHA013), anti-NP mAb (IgG) (SARS-CoV-2 NPIgG, AHA009), SARS-CoV antibody-80R (IgG) (CHA001), and MERS-CoV antibody-2E6 (IgG) (CHA002) were purchased from Sanyou Bio. Rabbit anti-human IgG H&L (HRP) (ab6759), recombinant human BNP (ab87200), rabbit anti-human IgM mu chain (HRP) (ab97210), goat anti-rabbit IgG H&L (HRP)

(ab97051), and rabbit polyclonal anti-6×His-tag antibody (ab9108) were purchased from Abcam. Human Spike-SARS-CoV-2 IgM (S1-IgM, MBS2614311) were purchased from MyBiosource. MERS-CoV/SARS-CoV negative control (CI 2601-0101 Z) was purchased from Euroimmun. PI film (125 mm thick) was purchased from DuPont.

**Fabrication of Multiplex Array Electrode**

For four-channel graphene sensor fabrication, a PI film was attached onto a supporting substrate in a 50-W $CO_2$ laser cutter (Universal Laser System VLS3.50). Selected laser-cutting parameters were: power 8.0%, speed 15%, points per inch 1,000, in raster mode, and at focused height. Ag/AgCl REs were fabricated by electrodeposition in 40 μL of a mixture solution containing silver nitrate, sodium thiosulfate, and sodium bisulfite (final concentrations of 250 mM, 750 mM, and 500 mM, respectively) for 100 s at -0.2 mA, followed by drop-casting a 20-μL aliquot of $FeCl_3$ for 1 min.

**Functionalization of the SARS-CoV-2 RapidPlex and Electrochemical Readout**

A 10-μL aliquot of 5.0 mM PBA in DMF was drop-cast on the graphene surface and incubated for 2 h at room temperature in a humid chamber. After rinsing with DMF, IPA, and deionized (DI) water, and drying under air flow, electrodes were incubated with 10 μL of a mixture solution containing 0.4 M EDC and 0.1 M sulfo-NHS in 0.025 M MES (pH 6.5) for 35 min at room temperature under humid ambient conditions. Specific antibodies or coating protein were covalently attached onto activated surface by drop-casting 5.0 μL of the specific reagent (250 μg $mL^{-1}$ for S1-IgG, S1-IgM, and CRP, or 50× dilution for NP, in 0.01M PBS [pH 7.4]) and incubated for 3 h at room temperature, followed by a 90-min blocking step with 2.0% BSA prepared in 0.01 M PBS. Subsequently, 10 μL of the corresponding target analyte prepared in 0.01 M PBS containing 1.0% BSA was incubated for 1, 5, or 10 min at room temperature and, after one washing step with PBS, corresponding detector antibody (HRP-labeled or unlabeled) (250× dilution for NP, 2.0 μg $mL^{-1}$ for S1-IgG and S1-IgM, and 1.0 μg $mL^{-1}$ for CRP) in 0.01 M PBS containing 1.0% BSA was incubated for 5 min at room temperature. In the case of NP assay, after incubating detector antibody and performing the corresponding washing step with

PBS, 10 μL of 1.0 μg $mL^{-1}$ HRP-goat anti-rabbit IgG prepared in 0.01 M PBS containing 1.0% BSA was incubated for 5 min at room temperature. For each type of developed assay, amperometric readings were registered at -0.2 V (versus Ag/AgCl) in 0.05 M sodium phosphate buffer (pH 6.0) containing 2.0 mM HQ. The readout signal was obtained in the presence of 1.0 mM $H_2O_2$.

To characterize the morphology and material properties before and after surface modification with PBA, we obtained SEM images of graphene electrodes by focused ion beam SEM (FEI Nova 600 NanoLab).

**Electrochemical Characterization of the SARS-CoV-2 RapidPlex**

Amperometry, OCP-EIS, cyclic voltammetry, and DPV were carried out on a CHI820 electrochemical station. The electrochemical setup comprised laser-induced graphene electrodes as the WEs, a platinum wire as the CE, and a commercial Ag/AgCl electrode as the RE.

For each type of proposed assay, surface modification after each step was electrochemically characterized by DPV and OCP-EIS. Corresponding readings by means of each technique were carried out in 0.01 M PBS (pH 7.4) containing 2.0 mM $K_4Fe(CN)_6/K_3Fe(CN)_6$ (1:1) and under the following detailed conditions: potential range, -0.2 and 0.6 V; pulse width, 0.2 s; incremental potential, 4 mV; amplitude, 50 mV; frequency range, 0.1–$10^6$ Hz; amplitude, 5 mV. Graphene functionalization methods were evaluated for both CRP- and SARS-CoV-2-specific IgG assays, by comparing current responses obtained after developing each assay on both PBA and PPA-graphene, in the absence and in the presence of each of the corresponding target biomolecules (tested levels were 50 ng $mL^{-1}$ for CRP and 500 ng $mL^{-1}$ for SARS-CoV-2-specific IgG). Selectivity study was carried out by incubating corresponding interferential non-target molecules on the previously functionalized PBA-graphene. Concentration levels assayed for each interferent were the same as (or even higher than) the concentration of the target molecule in each case. Amperometric signals obtained for each interferent tested were compared with the current signals obtained in the absence and in the presence of the corresponding target analyte for each type of assay.

**Design and Fabrication of Electronic System for the SARS-CoV-2 RapidPlex**

The four-channel chronoamperometric measurements were performed by a custom PCB-based wireless potentiostat. An Arm Cortex-M4 microcontroller (STM32L432KC; STMicroelectronics), and a Bluetooth module (SPBT3.0DP2; STMicroelectronics) were used for potentiostat control and wireless communication. A single operational amplifier (AD8605; Analog Devices) was used as the control amplifier, and a quad operational amplifier (AD8608; Analog Devices) was used as a four-transimpedance amplifier to construct the potentiostat loop. A series voltage reference (ISL60002; Renesas Electronics) and the microcontroller unit's (MCU) built-in digital-to-analog converter were used to generate the voltage bias across the RE and WEs. Four MCU built-in analog-to-digital converter channels were used to concurrently acquire the measurements.

**Subjects and Procedures**

In compliance with the protocols approved by the Institutional Review Board (no. 19-089417-292-A2) at the California Institute of Technology (Caltech), the performance of SARS-CoV-2 RapidPlex was evaluated in human serum and saliva samples from healthy and confirmed COVID-19-infected patients. Serum samples from ten RT-PCR and IgG/IgM serology-confirmed COVID-19 patients (age range 24–77 years) and seven healthy subjects (age range 18–65 years) were purchased from BioIVT and Ray Biotech. The severity information of the BioIVT samples was provided by the phlebotomists during sample collection. Saliva samples from five RT-PCR and IgG/IgM serology test-confirmed COVID-19 patients (age range 28–46 years) were purchased from BioIVT. Three healthy saliva samples were used from pre-existing stocks collected from volunteers prior to the pandemic (recommended tips before saliva collection include avoiding foods with high sugar and caffeine content, not eating a major meal within 60 min of sample collection, and rinsing the mouth with water prior to sample collection). After receiving, serum and saliva samples were stored at -80°C until required for its analysis. For the analysis of NP, CRP, S1-IgG, and S1-IgM, no sample treatment was required for both serum and saliva samples; a simple dilution with 0.01 M PBS containing 1.0% BSA was performed prior to analysis.

**Determination of SARS-CoV-2-Related Selected Target Molecules in Serum and Saliva Samples**

NP antigen, CRP, and S1-IgG and S1-IgM isotypes were analyzed in commercial serum and saliva samples from RT-PCR COVID-19-confirmed positive patients ($n_{serum}$ = 10; $n_{saliva}$ = 5) and healthy subjects ($n_{serum}$ = 7; $n_{saliva}$ = 3). After 100× and 5× dilution of corresponding serum and saliva samples in PBS with 1.0% BSA, respectively, a 10-μL aliquot was incubated in each WE for 10 min at room temperature (25× dilution was used for 1-min incubation study in serum for Figure 5C). After a washing step with PBS buffer, corresponding detector reagents were incubated in each WE for 5 min and subsequent detection was performed. Comparison of sensor performance in buffer and diluted body fluids from healthy subjects spiked with increasing concentrations of target molecule was performed using CRP as a model molecule.

**Validation of Human Samples with the Gold-Standard ELISA**

ELISA tests for NP, S1-IgG, and CRP (selected as model targets) were performed in an accuSkan FC Filter-Based Microplate Photometer at a detection wavelength of 450 nm according to the manufacturer's instructions. In brief, plates were coated for 3 h, shaking at 37°C, with 4.0 μg $mL^{-1}$ of the corresponding capture receptor in each case and blocked with PBS containing 1.0% BSA for 2 h, shaking at 37°C, and standards (or properly diluted samples) were added to coated microtiter plate wells and incubated for 2 h, shaking at 37°C. Next, corresponding HRP-labeled detector antibody was incubated for 30 min at room temperature. Finally, 100 μL of TMB substrate was incubated for 15 min, and absorbance values were measured immediately after addition of 25 μL of 1 M $H_2SO_4$ in each well. Three washings with PBS containing 1.0% BSA were performed after each modification step.

### 2.1.2 Electrochemical Characterization of SARS-CoV-2 RapidPlex Platform

Functionalization and modification steps carried out on the LEG surfaces for the covalent attachment of each of the specific receptors required for the development of our SARS-CoV-2 RapidPlex platform is schematized in Figure 2.2A. 1-Pyrenebutyric acid (PBA) is used as the linker to anchor the required receptors to the graphene layer. Although attachment of functional groups directly on the $sp^2$ carbon atom surface is one of the common ways to functionalize graphene, these methods are associated

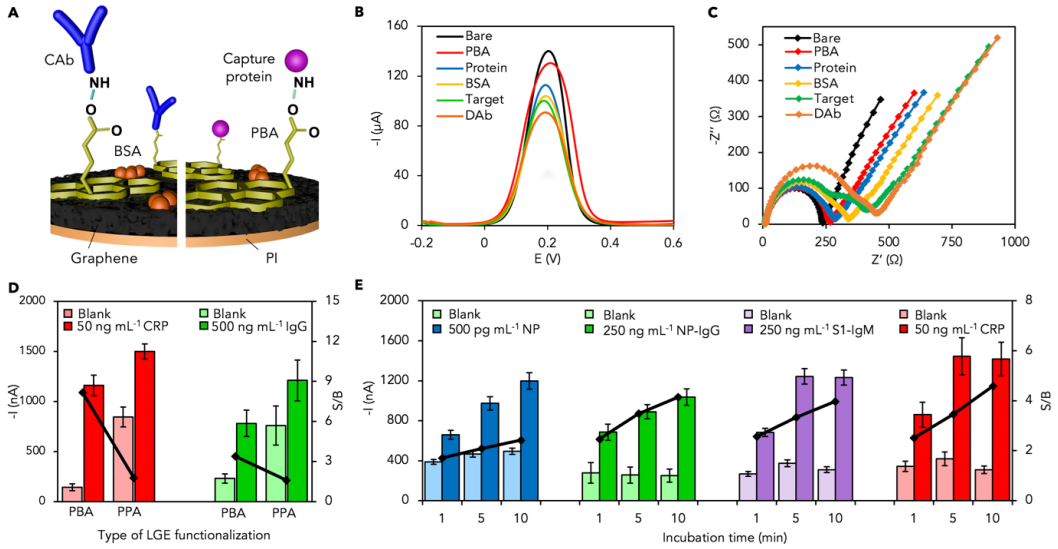


Figure 2.2: Characterization of electrochemical graphene biosensors comprising the SARS-CoV-2 RapidPlex platform

(A) Scheme detailing the methodology developed for the covalent attachment of the corresponding bioreceptor for the specific capture of the target analytes SARS-CoV-2 NP and CRP (left), and IgG and IgM isotypes against SARS-CoV-2 S1 protein (right). PBA, 1-Pyrenebutyric acid; BSA, bovine serum albumin; CAb, capture antibody; PI, polyimide. (B) and (C) Differential pulse voltammetry (DPV) and Nyquist plots of a graphene electrode in 0.01 M phosphate-buffered saline (PBS, pH 7.4) containing 2.0 mM of $K_4Fe(CN)_6/K_3Fe(CN)_6$ (1:1) after each modification step (S1-IgG assay as representative example): bare graphene (Bare), functionalization with PBA (PBA), immobilization of SARS-CoV-2 S1 protein (Protein), blocking with BSA (BSA), recognition of specific S1-IgG (Target), and incubation with enzyme-tagged anti-human IgG antibody (DAb). (D) Comparison of amperometric responses and overlaid signal-to-blank (S/B) ratio (black lines) for SARS-CoV-2 specific IgG and CRP detection using PBA and 1H-pyrrole-1-propionic acid (PPA) as linkers for the attachment of the corresponding capture bioreceptors. Data are presented as mean ± SD (n = 3). (E) Amperometric responses and overlaid S/B ratio (black lines) observed for 0.0 and 500 pg $mL^{-1}$ NP, 0.0 and 250 ng $mL^{-1}$ SARS-CoV-2 specific IgG and IgM, and 0.0 and 50 ng $mL^{-1}$ CRP, with 10, 5 and 1-minute incubation. Data are presented as mean ± SD (n = 3).

with the requirement of defects or edges in the sensor material, which could alter its specific physical properties.[33, 34] In contrast, introduction of functional groups on the sensing layer by means of pyrene derivatives is preferred here, as it does not disrupt the conjugation of the graphene sheets and improves its stability.[35, 36] PBA consisting of a pyrene group that contains $\pi$-electrons and a carboxylic group is used to functionalize graphene layers via $\pi$-stacking and hydrophobic interactions. The pyrene units of PBA strongly interact with graphene layers in the way that original structure and properties of the graphene are well maintained. The functional

moieties contained in each PBA molecule allow the preparation of the affinity-based biosensing platform through the covalent coupling between the carboxylic groups on PBA units and the $–NH_2$ groups of the respective capture receptors (specific antibodies or capture proteins). Blocking of unreacted sites with bovine serum albumin (BSA) impedes the nonspecific adsorption of other molecules involved in each assay configuration or circulating in the sample of interest.

Differential pulse voltammetry (DPV) and open-circuit potential-electrochemical impedance spectroscopy (OCP-EIS) techniques are employed to electrochemically characterize and prove the stepwise self-assembled processes in both assay configurations for the detection of selected target molecules. DPV readings reflect lower peak current intensity after each modification step related to S1-Ig assay due to the hindered diffusion of the redox label to the electrode surface derived from both the carboxyl groups and the attached proteins and biological macromolecules (Figure 2.2B). At the same time, resistance in the Nyquist plots from OCP-EIS is increased after each functionalization step (Figure 2.2C). The successful anchorage of PBA was also verified with scanning electron microscopy (SEM) (Figure A.1). Electrochemical characterization of the sandwich assay-based sensor modification using CRP as a model molecule and the aforementioned techniques are presented in Figure A.2.

To preserve the native structure and properties of the bound biomolecules, we chose PBA as a heterobifunctional linker, effectively preventing the direct interaction between large biomolecules and the graphene surface.[34] To verify this selection, we constructed CRP- and SARS-CoV-2-specific IgG assay configurations on graphene electrodes functionalized with PBA and another common linker, 1H-pyrrole-1-propionic acid (PPA).[31] Greater signal-to-blank (S/B) ratios were observed for both assays where PBA was used as a linker support (Figure 2.2D), mainly due to a significant decrease in the signals obtained in the absence of the corresponding target molecule when PBA was used instead of PPA. Together with an optimal blocking strategy, PBA can be used for the immobilization of specific biomolecular probes (e.g., antibodies, proteins) while avoiding nonspecific adsorptions in the context of immunoassays.[37]

The orientation of modified antigenic proteins on solid surfaces is strongly associated with their activity and reactivity. Specific anti-His antibodies can be used to orient the immobilization of antigenic receptors containing histidine residues, but this implies an additional step compared with their direct attachment on the sensing

layer, as schematized in Figure A.3A. Our results show no significant differences in assay performance for IgG detection on PBA-graphene electrodes covalently functionalized with the specific coating protein (direct immobilization) and with anti-His antibodies for the previous capture of the polyhistidine-tag specific coating protein (oriented immobilization) (Figure A.3B), proving that random protein orientation does not interfere with the epitope accessibility for effective recognition by specific target antibodies. This is in agreement with other reports confirming that His-tagged fusion antigens can be directly immobilized on different surfaces with protein orientations completely compatible with antibody recognition.[38, 39, 40, 41] To simplify and reduce the cost and time of the assay, we carried out direct immobilization of S1 protein for specific Ig detection.

Considering that rapid target binding is essential to the successful implementation of our proposed platform as a POC system, we investigated how target (or sample) incubation time affects the response of each biosensor comprising our SARS-CoV-2 RapidPlex platform. Figure 2.2E summarizes the amperometric signals obtained for each of the four sensing units at different incubation times (1, 5 and 10 min) in the absence (blank, B) and presence (S) of 500 pg $mL^{-1}$, 250 ng $mL^{-1}$, and 50 ng $mL^{-1}$ of NP, SARS-CoV-2-specific IgG and IgM isotypes, and CRP, respectively. It is important to note that although a 10-min incubation time was selected for most of the studies here in order to ensure the highest sensitivity for the determination of ultra-low levels of each target molecule, a significant difference between the absence and the presence of each of the corresponding targets is obtained with just 1-min incubation time. This provides one of the major advantages of our SARS-CoV-2 RapidPlex system as a rapid POC device for SARS-CoV-2 infection monitoring with the required sensitivity for both protein and Ig determination. ELISA,[18, 42, 43, 44, 45] nucleic acid amplification,[46, 47, 48, 49, 50] mass spectrometry,[51] or even combinations[52] have been reported very recently for determination of the proposed SARS-CoV-2-specific target molecules, among others. However, most of these methods show crucial pitfalls, mainly in terms of sample preparation, complexity, and expensive and bulky equipment requirements, making them still highly difficult to be implemented as POC systems. Our device provides an attractive alternative to standard assays for protein determination, such as ELISA, because of its multiplexing capabilities, remote functionality, and short sample-to-answer time.

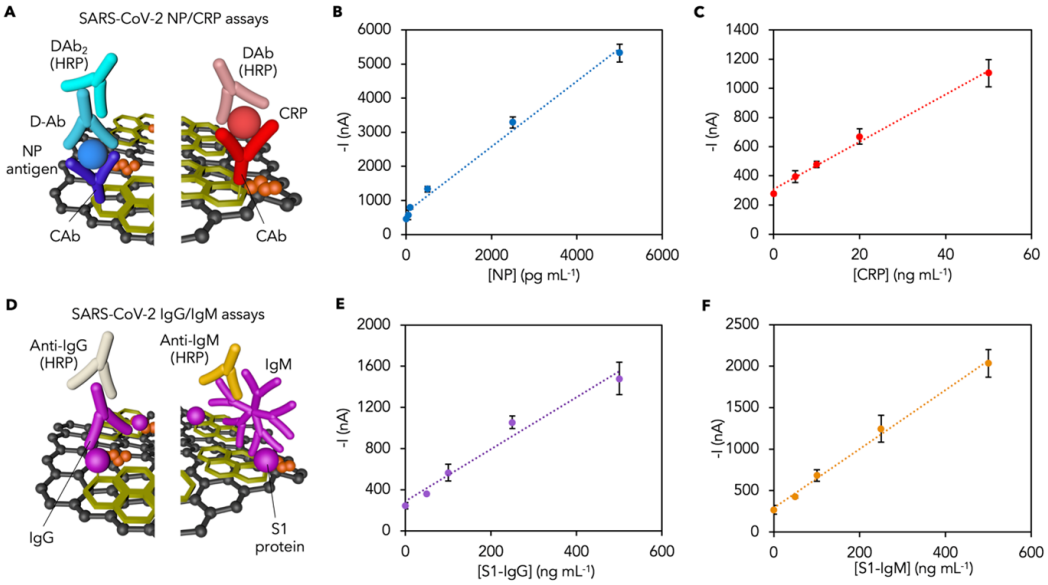


Figure 2.3: Evaluation of analytical sensor performance for the detection of physiological levels of target COVID-19 biomarkers

(A) Scheme of sensor preparation for detection of SARS-CoV-2 NP and CRP based on double-sandwich and sandwich assay configurations, respectively. CAb, capture antibody; DAb, detector antibody; DAb2, secondary detector antibody; HRP, horseradish peroxidase. (B) and (C) Calibration curves constructed for NP (B) and CRP (C) detection in phosphate-buffered saline (PBS, pH 7.4) supplemented with 1.0% BSA. Data are presented as mean ± SD (n = 3). (D) Scheme of sensor preparation for detection of S1-IgG and S1-IgM isotypes based on direct assay configurations. (E) and (F) Calibration curves constructed for S1-IgG (E) and S1-IgM (F) isotypes detection in phosphate-buffered saline (PBS, pH 7.4) supplemented with 1.0% BSA. Data are presented as mean ± SD (n = 3).

### 2.1.3 Evaluation of Analytical Performance of the SARS-CoV-2 RapidPlex

The performance of each biosensor contained in the SARS-CoV-2 RapidPlex was characterized in phosphate-buffered saline (PBS) solutions supplemented with 1.0% BSA by measuring the amperometric readout in the presence of increased concentrations of NP, S1-IgG, S1-IgM, and CRP (Figure 2.3). The selected strategies for NP viral antigen and CRP proteins are based on double-sandwich and sandwich configurations, respectively, as illustrated in Figure 2.3A. The sandwich-based immunoassays for antigen detection are, in general, highly sensitive due to the involvement of two different antibodies as capture and detector entities. According to the low levels that must be reached for NP and CRP in diluted serum and saliva (pg $mL^{-1}$ to ng $mL^{-1}$), we think these strategies are the most suitable to be implemented on our platform. Variation of cathodic currents with the concentration for NP and CRP in buffered solutions is presented in Figures 2.3B and 2.3C, respectively.

S1-IgG and S1-IgM were detected based on indirect immunoassays (Figure 2.3D), which are considered highly suitable for detection of circulating macromolecules in antisera and other biofluids. Figures 2.3E and 2.3F show the calibration curves for S1-specific Ig determination (S1-IgG and S1-IgM, respectively) in buffered solutions. Reproducibility was demonstrated through the relative standard deviation (RSD) values obtained with different biosensors prepared in the same manner on different days. RSD values of 6.3%, 8.4%, 6.0%, and 7.6% for 20 ng $mL^{-1}$ CRP, 250 ng $mL^{-1}$ S1-IgG, 250 ng $mL^{-1}$ S1-IgM, and 500 pg $mL^{-1}$ NP antigen (n = 5) demonstrate good reproducibility in both device preparation and signal transduction. In addition, the sensors showed stable responses over a 5-day storage period at 4°C (Figure A.4). We did not observe significant slope variations between data obtained in properly diluted human serum and in buffered solutions for the determination of each target analyte (for instance, the slope sensitivity value [16.28 nA mL $ng^{-1}$] obtained for CRP as model analyte in PBS-buffered solutions is nearly the same as that in diluted serum samples from a healthy volunteer [16.64 nA mL $ng^{-1}$]); therefore, accurate quantification of the proposed target analytes can be carried out by conducting a simple interpolation of the cathodic readings obtained for each sample tested in the corresponding calibration curve constructed in buffered solution.

Since diagnostic sensitivity and specificity of seroprevalence studies can be improved by using a mixture of antigenic proteins instead of a single protein,[53, 54] we modified graphene with a mixture of SARS-CoV-2 related antigens, NP and S1, to capture specific immunoglobulin isotypes against both antigens in the same WE. A calibration curve for (NP + S1)-IgG detection is shown in Figure A.5. Thus, this methodology can be tailored for detecting isotype-specific IgG (or IgM) or a combination of both Ig isotypes in the same sensing surface to better capture total Ig concentration and thus increase assay sensitivity across the patient population.

### 2.1.4 Investigation of the Selectivity and Multiplexed Performance of the SARS-CoV-2 RapidPlex

Human biofluids contain a complex and variable mixture of circulating molecules that could interfere with molecular sensing. In addition, negligible crosstalk between different working surfaces is an essential requirement for performing multiplexed detection readings accurately and meaningfully. Therefore, selectivity and crosstalk of the SARS-CoV-2 RapidPlex platform were evaluated. Amperometric readings obtained for each developed biosensor against non-target molecules are presented

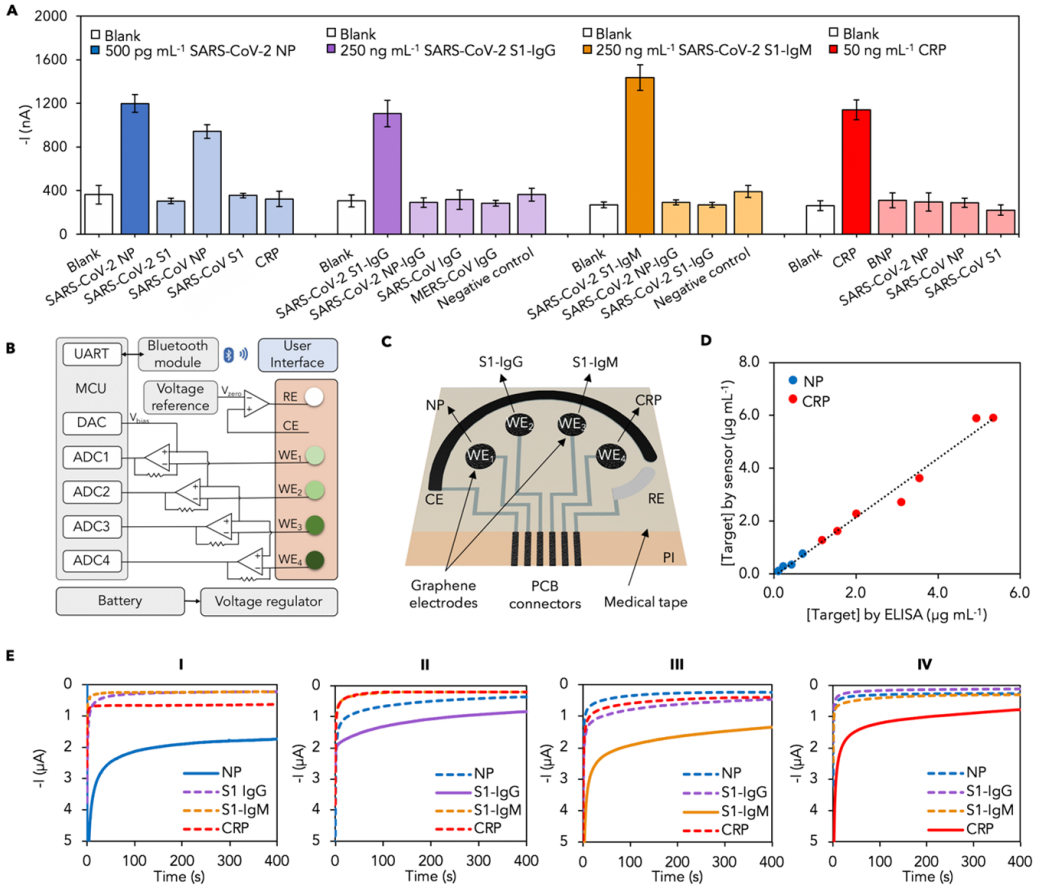


Figure 2.4: Investigation of the selectivity and multiplexed performance of the wireless SARS-CoV-2 RapidPlex platform

(A) Selective response of NP, S1-IgG and S1-IgM isotypes and CRP sensors against different non-target circulating analytes. Interferential molecules were tested at 500 pg mL$^{-1}$ (with an exception of 50 ng mL$^{-1}$ for CRP), 250 ng mL$^{-1}$ and 50 ng mL$^{-1}$ for NP, S1-IgG and S1-IgM, and CRP assays, respectively. Data are presented as mean ± SD (n = 3). (B) Validation of sample concentrations measured using the designed electrochemical sensor against sample concentrations measured using ELISA. (C) Block diagram of the SARS-CoV-2 RapidPlex platform. UART, universal asynchronous receiver/transmitter; MCU, microcontroller unit; DAC, digital-to-analog converter; ADC, analog-to-digital converter. (D) Schematic illustration of the graphene sensor array layout. (E) Experimental readings obtained with the functionalized SARS-CoV-2 RapidPlex platform after incubation of the four WEs with phosphate-buffered saline (PBS, pH 7.4) supplemented with 1.0% BSA containing 1.0 ng mL$^{-1}$ NP (I), 250 ng mL$^{-1}$ S1-IgG (II), 250 ng mL$^{-1}$ S1-IgM (III) and 50 ng mL$^{-1}$ CRP (IV).

in Figure 2.4A.We evaluated the specific binding for SARS-CoV-2 biomarkers in comparison with biomarkers of similar coronaviruses, including SARS-CoV and MERS-CoV. We observed no significant cross-reaction for NP, S1-IgG, S1-IgM, and CRP assays in the presence of each tested interferent, including SARS-CoV-

2 S1, SARS-CoV S1, and CRP (for NP assay), SARS-CoV-2 NP-IgG, SARS-CoV IgG, MERS-CoV IgG, S1-IgG, and negative controls containing mixtures of IgG and IgM against both MERS-CoV and SARS-CoV (for S1-IgG and S1-IgM assays), and B-type natriuretic peptide (BNP), NP, SARS-CoV NP, and SARS-CoV S1 (for CRP assay), respectively. However, SARS-CoV NP viral antigen interferent provided a cathodic current corresponding to ~80% of the raw current obtained for the detection of the specific NP antigen. Spike, envelope, and membrane SARS-CoV-2 proteins share 76%–95% sequence identity with those of SARS-CoV. This percentage homology is reduced to 30%–40% for MERS-CoV. Similarly, since SARS-CoV-2 NP is 90% identical to SARS-CoV NP,[18, 55, 56, 57] the interference observed from SARS-CoV NP antigen was expected. However, the lack of selectivity in this particular case is not a major concern due to the absence of new SARS-CoV cases detected recently; therefore, it can be inferred that this interference will not produce a barrier for selective SARS-CoV-2 NP determination in real samples. We further evaluated the amperometric-derived concentrations with absorbance-derived concentrations collected via ELISA. As presented in Figure 2.4B, the results from our functionalized electrochemical biosensor were linearly correlated (r = 0.955) with the results using the same reagents in a traditional ELISA protocol.

Once the performance and selectivity of each constructed biosensor was individually and exhaustively evaluated, we demonstrate the multiplexing capabilities of our four-working-electrode (4WEs) graphene array device designed with a Ag/AgCl RE and a graphene CE. The block diagram showing the functional units that constitute the integrated electronic system is illustrated in Figures 2.4C and 2.4D. Amperometric readings from the four channels are concurrently taken and data are wirelessly transmitted to a user device over Bluetooth. The electronic system, including the printed circuit board (PCB) and a lithium-ion polymer battery, is $20 \times 35 \times 7.3$ mm in dimension. The compact device can perform amperometric measurements continuously for over 5 h on a single charge.

With the objective of demonstrating the utility of our SARS-CoV-2 RapidPlex array for multiplexed and simultaneous quantification of selected target molecules, we evaluated the potential cross-reaction resulting from the diffusion of signal substances between adjacent immunosurfaces. To this end, each of the four conveniently functionalized working surfaces were incubated with buffered solutions containing significantly high concentration of each of the selected targets, followed by the

corresponding detector receptors in each case. The absence of crosstalk between the adjacent WEs is verified from the experimental readings in buffered solutions containing 1.0 ng $mL^{-1}$ NP antigen (I), 250 ng $mL^{-1}$ S1-specific IgG (II) and IgM (III), and 50 ng $mL^{-1}$ CRP (IV) (Figure 2.4E). As envisaged, significantly higher signal was obtained when each target was specifically captured and further labeled by its tracer antibody in the corresponding functionalized immunosurface. These results, in conjunction with those from Figure 2.4A, demonstrate the feasibility of the developed SARS-CoV-2 RapidPlex platform for fast, selective, and reliable determination of NP, S1-IgG, and S1-IgM isotypes, and CRP in one single experiment. It should be noted that since IgG and IgM have similar binding mechanisms to viral antigens and individual quantification of immunoglobulins requires no mixing of the specific detector labels, individual droplets were used on IgG and IgM sensing electrodes during modification and labeling.

### 2.1.5 Detection of SARS-CoV-2-Related Selected Targets in Human Biospecimens

To prove the utility of our device in a more complex and real scenario, we evaluated the multiplexed capabilities of SARS-CoV-2 RapidPlex in representative serum samples from COVID-19 RT-PCR-negative and -positive subjects. Sensor data from the serum samples of an RT-PCR-negative subject (Figure 2.5A) and an RT-PCR-positive patient (Figure 2.5B) show minimal crosstalk in a real and complex sample matrix, indicating the efficient functionality of SARS-CoV-2 RapidPlex to simultaneously differentiate the overexpressed presence of SARS-CoV-2-related target reporters in COVID-19-positive specimens. Moreover, the SARS-CoV-2 RapidPlex device is able to provide significant positive readings for all targets after incubating the COVID-19-positive serum sample for just 1 min (Figures 2.5C and A.6). The maintained high signal in positive patient samples demonstrates the great potential in future translation of the SARS-CoV-2 RapidPlex device as an ultra-fast POC remote diagnostic tool.

To further investigate NP, S1-IgG, S1-IgM, and CRP response to SARS-CoV-2 infection using our LEG-based biosensors, we measured each target molecule in serum and saliva samples from RT-PCR-confirmed COVID-19-positive and -negative subjects. Obtained results were plotted as the ratio between the amperometric readings for each sample tested (S) and the respective blank (B) in each case to compare target detection in different concentration ranges. Using the graphene sensors, a

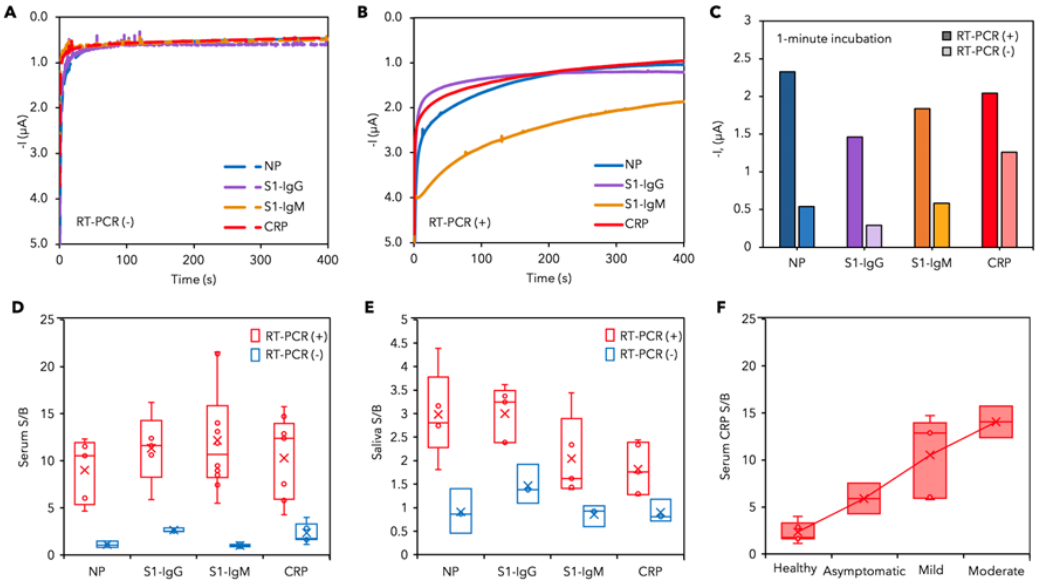


Figure 2.5: Application of SARS-CoV-2 RapidPlex in SARS-CoV-2 detection in blood and saliva samples from COVID-19 positive and negative subjects

(A and B) Experimental readings obtained with SARS-CoV-2 RapidPlex after 10 minutes incubation of the sensor array with serum samples from a representative COVID-19 RT-PCR negative (A) and positive patient (B). (C) The signal of each sensor obtained after 1-minute incubation with a serum sample from a COVID-19 positive patient (dark color) vs. the signal obtained after 10-minute incubation with a serum sample from a COVID-19 negative patient (light color). (D) A box-and-whisker plot of measured signal-to-blank ratios (S/B) for NP, S1-IgG, S1-IgM, and CRP in RT-PCR confirmed COVID-19 positive (n=5) and negative (n=6) serum samples. (E) A box-and-whisker of measured signal-to-blank ratios (S/B) for NP, S1-IgG, S1-IgM, and CRP in RT-PCR confirmed COVID-19 positive (n=5) and negative (n=3) saliva samples. (F) CRP levels in diluted serum samples plotted against given COVID-19 symptom severity, with "Healthy" referring to COVID-19 negative patient samples (n=7). Positive COVID-19 patients classified according to disease severity as asymptomatic (n=2), mild (n=5) and moderate (n=2).

total of 17 COVID-19 RT-PCR-tested serum samples (10 positive, 7 negative) were assayed, and a total of 8 COVID-19 RT-PCR-tested saliva samples (5 positive, 3 negative) were analyzed (Table A.1).

Results from Figures 2.5D and 2.5E corroborate that, as expected, compared with RT-PCR-negative subjects, RT-PCR-positive COVID-19 patients show significantly elevated levels of the selected targets in both serum and saliva samples, with median S/B ratios of 10.53, 11.62, 10.67, and 12.39 in serum and 2.81, 3.24, 1.62, and 1.76 in saliva, for NP, S1-IgG, S1-IgM, and CRP, respectively. We observed a concentration of NP in the range of 0.1-0.8 μg $mL^{-1}$ and 0.5-2.0 ng $mL^{-1}$ in COVID-19 patient serum and saliva, respectively; S1-IgG in the range of 20-40 μg $mL^{-1}$

and 0.2-0.5 μg $mL^{-1}$ in COVID-19 patient serum and saliva, respectively; S1-IgM in the range of 20-50 μg $mL^{-1}$ and 0.6-5.0 μg $mL^{-1}$ in COVID-19 patient serum and saliva, respectively; and CRP in the range of 10-20 μg $mL^{-1}$ and 0.1-0.5 μg $mL^{-1}$ in COVID-19 patient serum and saliva, respectively. The fact that all the positive samples show much higher signals compared with negative samples proves the real utility for the accurate evaluation of the COVID-19 biomarkers in biofluids using our LEG-based biosensors. In particular, the observed significant presence of COVID-19 biomarkers in saliva demonstrates the exceptional utility of this biofluid as a valuable source for noninvasively diagnosing and monitoring SARS-CoV-2 infection.

With the aim of confirming the relationship between the levels of inflammatory biomarkers involved in the cytokine storm directly associated with disease progression, severity, and outcome in COVID-19,[58, 59, 60, 61, 62, 63] we evaluated the variation of serum CRP levels in RT-PCR-negative subjects (n = 7) and RT-PCR-positive COVID-19 patients who were classified clinically according to disease severity as asymptomatic (n = 2), mild (n = 5), and moderate (n = 2). As shown in Figure 2.5F, we observed a positive association between CRP concentration and COVID-19 symptom severity grade, consistent with the recent literature reports.[21, 62] Future clinical testing using paired saliva and serum samples over the course of the infection is required to determine the relationship between saliva and serum concentrations and to validate the utility of our platform in identifying severity-specific COVID-19 (Table 2.1).

### 2.1.6 Conclusion

To address the increasing demands for effective diagnostic tools for simple COVID-19 detection with immediate sample-to-answer turnaround, we have developed and implemented the first multiplexed electrochemical graphene-based platform, SARS-CoV-2 RapidPlex, for sensitive, rapid, and selective simultaneous interrogation of NP viral antigen, S1-IgG and S1-IgM isotypes, and CRP in serum and saliva biofluids from healthy and RT-PCR-confirmed COVID-19-infected patients. The combination of the advantageous properties of graphene material with the high sensitivity and specificity of the immunosensing strategies makes our SARS-CoV-2 RapidPlex platform a promising diagnostic device for the accurate monitoring of COVID-19 infection in serum and noninvasively accessible body fluids free from complex sample pretreatment requirements. Due to the ease of use, saliva sample

compatibility, and rapid time to results, the SARS-CoV-2 RapidPlex platform has high potential for implementation at POC for patient triage, as well as for at-home use for telemedicine care and remote monitoring.

Monitoring of selected targets in one single and fast experiment (target capture can be as low as 1 min) provides substantial information, not only regarding early COVID-19 infection through viral antigen and IgM isotype detection but also about disease severity by means of CRP evaluation and potential acquired immunity through IgG isotype quantification. The rapid on-site evaluation of disease severity enabled by our SARS-CoV-2 RapidPlex introduces the unparalleled advantage of immediate COVID-19 triaging. In future clinical applications, this could not only alert attending physicians of cases requiring major and careful medical attention but also facilitate the efficient allocation of precious medical resources, such as ventilators and ICU beds, in the event of resurging outbreaks to optimize patient outcomes under an overloading of local healthcare systems.

Our proposed methodologies based on simple yet well-established surface functionalization techniques and sensing principles allow the ease of translation to the detection of other highly informative SARS-CoV-2-related reporters by simply changing the coating capture receptor. Further technological improvement could be achieved by introducing a fully automated sample-handling process through a microfluidic module for telemedicine deployment. Modification of our platform design may allow for rapid viral antigen and antibody panel testing such that COVID-19 infection could be clearly distinguished from nonspecific symptoms of seasonal respiratory infections such as influenza. Additionally, the wireless telemedicine diagnostic platform, when coupled with emerging wearable biosensors to continuously monitor vital signs and other chemical biomarkers, could provide comprehensive information on an individual's health status during the COVID-19 pandemic.[64, 65, 66, 67, 68]

Our platform pioneers multiplexed detection of stage-specific SARS-CoV-2-related biomarkers to provide a detailed and personalized snapshot of the COVID-19 infection. We firmly believe that our developed platform will be a high-utility testing method toward fighting this and future pandemics, helping to end one of the deepest global health, economic, and humanitarian crises in modern history.

## 2.2 Emerging Telemedicine Tools for Remote COVID-19 Diagnosis, Monitoring, and Management

The COVID-19 pandemic defined 2020, spreading globally to over 65 million cases in early December, with over 20% occurring in the United States (U.S.).[1] Initial efforts to mitigate the spread involved state-mandated "stay at home" orders and travel restrictions, which seemed to slow the spread temporarily but also severely impacted the global economy and disrupted daily life. However, upon reopening, even when daily cases were dramatically reduced as in France and Spain, countries saw a resurgence with higher incidence rates than the initial peak in April.[1] While simple measures of social distancing, face coverings, and increased access to testing have been implemented to seek a return to normal daily activities, there is a clear and present need for innovative tools to intercept the spread of COVID-19, increase the efficiency and quality of care, and alleviate pressures on the global healthcare system.

Telemedicine was well-positioned to address these needs through at-home COVID-19 screening, diagnosis, and monitoring. Telemedicine was instituted by many U.S. health systems to see patients at home and limit the possible spread of COVID-19, since many cases were observed to originate in hospital.[69, 70, 71] A major barrier to leveraging telemedicine for COVID-19 was the coordination of testing.[69] Testing strategies at the beginning of the pandemic were a resource intensive process, but they also could not keep up with the demand for testing with significant delays in results, which may have resulted in further delays in medical treatment. Once diagnosed, telemedicine treatment is the best strategy to prevent the inundation of hospitals with COVID-19 patients while also allowing patients to recover in the comfort of their own home. However, utilization of continuous monitoring tools at home is necessary for informed medical decisions such as when the patient should report to the hospital. By monitoring for biomarkers associated with COVID-19 prognosis using telemedicine sensors in home- and community-based settings, early medical intervention steps and more aggressive treatment plans may prevent patient degradation and death.

### 2.2.1 Telemedicine-Based COVID-19 Diagnostics

As communities seek a return to normalcy during the continued spread of COVID-19, greater emphasis has been placed on widespread access to testing, with the idea that those who become infected and exposed isolate, while others continue safe

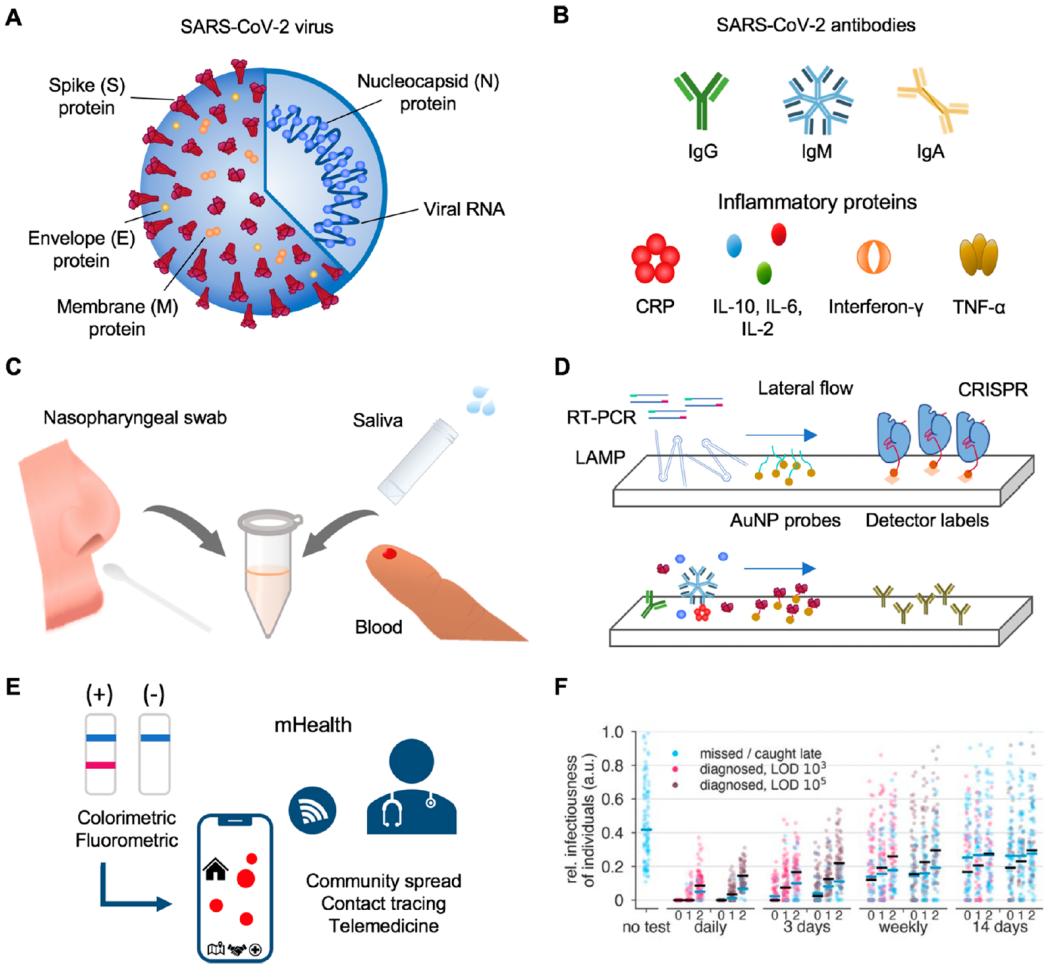


Figure 2.6: COVID-19 diagnosis through rapid and point-of-care biomarker detection

(A) SARS-CoV-2 viral products including antigens and RNA. (B) Antibodies and inflammatory proteins produced from the body's immune response to the SARS-CoV-2 virus. (C) Detection of COVID-19 biomarkers in nasopharyngeal swabs, saliva, and blood. (D) Lateral flow assays (LFAs) for the rapid detection of COVID-19 biomarkers. For RNA detection (top), amplified RNA through either real-time reverse transcriptase polymerase chain reaction or loop-mediated isothermal amplification is added and binds to AuNP conjugated complementary probes or CRISPR-based enzymes for colorimetric or fluorometric detection. For antibody and antigen detection (bottom), AuNP conjugated antibodies and antigens tag the associated target in solution and are then detected by the immobilized detector antibodies. (E) Results from LFAs can be captured by a portable user interface. The mHealth platforms may then facilitate case reporting, community spread mapping, contact tracing, and telemedicine treatment. (F) COVID-19 surveillance is most effective under daily testing with test sensitivity being secondary to test turnaround time in importance. Reproduced with permission from ref [72]. Copyright 2020 Larremore et al.

social practices. However, effectively implementing this public health strategy has proven difficult with significant backlogs in testing. The gold standard for diagnosing

COVID-19 has been real-time reverse transcriptase polymerase chain reaction (RT-PCR) for the detection of SARS-CoV-2 viral nucleic acid. RT-PCR is a slow process that takes on average 2-3 h to generate results.[10] It requires expensive equipment and trained technicians, such that tests may not be able to be performed on-site.[10] RT-PCR is also known to produce false negatives, which may limit containment strategies and access to treatment. One study reported a 70% positive rate for nasal swab samples from suspected COVID-19 patients.[73] While lung computed tomography (CT) scans have been suggested as a more accurate diagnostic tool for patients with COVID-19 symptoms, it is less practical to implement and may not be specific to COVID-19.[46]

Beyond the need for improving the accuracy of COVID-19 diagnostic tools, there is a need to make these tools compatible with point-of-care (POC) and at-home use. In public spaces, there is a need for COVID-19 screening tools. At the hospital, there is a need for patient severity information for effective triage and resource allocation. At home, there is a need for quarantined individuals to test for COVID-19 before reentering society, and in the case of a positive test, to monitor their symptoms via telemedicine to reduce the strain on hospital resources. Designing these diagnostic tools requires careful selection of target COVID-19 biomarkers, sample specimens, detection mechanisms, and mHealth integration.

**Biomarkers for COVID-19 Diagnosis**

SARS-CoV-2 is a genus $\beta$-coronavirus, like SARS-CoV and MERS-CoV, with a crown-like, enveloped, positive-strand ribonucleic acid (RNA) (Figure 2.6A). The single-stranded RNA is packaged into a helical structure defined by the nucleocapsid (N) protein.[74] The viral envelope is decorated with membrane (M) proteins, envelope (E) proteins, and spike (S) proteins. While M and E proteins play more structural roles, the protruding outer S protein is involved in binding to host cell angiotensin-converting enzyme 2 receptors to facilitate viral entry.[74] Each part of the SARS-CoV-2 virus can be detected for active infection diagnosis. Previous research on SARS-CoV found that viral antigen concentrations are in agreement with RT-PCR patterns.[75] One of the greatest challenges with viral particle detection is the molecular sensitivity. A variety of RNA amplification methods, including RT-PCR, loop-mediated isothermal amplification (LAMP), and recombinase polymerase amplification (RPA), have been developed to improve RNA detection. For antigen testing, ultrasensitive immunoassays are necessary. The N protein is the

most favorable for antigen detection since it is the most abundant viral protein,[18] yet it requires lysing of the virus and is similar to other coronaviruses, including being 90% identical in proteomic structure to that of SARS-CoV, potentially leading to reduced assay selectivity.[55, 57, 56]

One can also potentially diagnose COVID-19 based on the physiochemical response to infection (Figure 2.6B). Anti-SARS-CoV-2 antibodies provide information regarding the immune response. Antibodies appear later into the infection, as early as 4 days after symptom onset,[76] with immunoglobulin M (IgM) peaking around 12 days after symptom onset and seroconversion to immunoglobulin G (IgG) around 20 days after symptom onset.[18, 77, 78, 79] Because of variable antibody concentrations, simultaneous detection of IgM, IgG, and immunoglobulin A (IgA) antibodies may improve assay performance.[80] Although antibodies are not optimal for early diagnosis and detection, they may provide important temporal information on the infection course. Also, antibody testing may provide information regarding acquired immunity and community seroprevalence. In addition to the immune response, COVID-19 is known to cause a dysregulated inflammatory response, known as the "cytokine storm". Inflammatory cytokine levels may serve as important biomarkers for symptom severity and prognosis. Increased levels of C-reactive protein (CRP) have been found to correlate with lung lesions and disease severity.[81, 62, 58, 20, 22] Upregulation of interleukin (IL)-6 and IL-2 at late stages of infection is well correlated to fatality.[82] Other cytokines, chemokines, and growth factors, such as interferon-$\gamma$, tumor necrosis factor alpha (TNF-$\alpha$), and transforming growth factor-beta-induced protein K676Ac, have been found to be highly reliable, independent severity diagnostic biomarkers.[83, 84, 85] These symptomatic markers have been looked at as potential therapeutic targets in addition to diagnostic targets.[82, 85]

Biofluids containing these markers may contain active virus, therefore at-home sample collection is desirable. Nasopharyngeal swabs have been the standard collection technique for accessing viral samples of the respiratory infection. To reduce the possibility of false negatives, high efficiency swabs have been engineered using functionalized microneedles.[86] However, this sample collection method requires assistance by a healthcare professional, placing a strain on medical and personal protective equipment (PPE) resources. In addition to nasopharyngeal swabs, COVID-19 biomarkers have been detected in blood and saliva (Figure 2.6C).[87, 88, 89] Both blood and saliva provide alternative specimens for self-collection.

**Lateral Flow Assays for POC Detection**

Lateral flow assays (LFAs) have become a standard for commercial rapid, POC testing. LFAs are typically built on nitrocellulose membranes with a sample pad, a conjugate pad, and absorption pad and operate based on a wicking-directed flow of sample fluid over the binding and testing regions of the assay (Figure 2.6D). LFAs can be used for detection of amplified nucleic acids, antigens, and antibodies based on specific gold nanoparticle (AuNP) conjugated probes. Upon flow, they may bind to immobilized probes at the detection strip causing aggregation of AuNPs and a color change at the test line.[10, 90, 91] Nucleic acid LFAs may also use immobilized CRISPR-based enzymes, which cleave a reporter-quencher pair upon binding of the target nucleic acid sequence, producing a fluorometric signal at the test line.[92] A variety of LFAs are now commercially available, including the Abbot ID Now and the Cepheid Xpert Xpress for rapid molecular testing.[93]

Advances have been made based on the lateral flow design. A portable multiplexed microfluidic-based platform has been developed to provide rapid detection of IgG, IgM, and SARS-CoV-2 antigens simultaneously via fluorescent detection.[94] By testing for both antibodies and antigens, one can simultaneously identify infected and convalescent individuals. The Sikes group has designed and validated methods for developing lateral flow antigen assays using binding protein scaffolds based on the reduced charge Sso7d variant (rcSso7d) rather than capture antibodies. rcSso7d-based assays have similar limits of detection as antibody-based assays and even improve sensitivity when a larger sample volume is applied.[95] Their methodology allows for high-density adsorption to unmodified cellulose within 30 s.[96] Using binding protein scaffolds for paper-based immunoassays have many benefits including inexpensive and simple manufacturing methods. 3M collaborated with the Sikes group to develop a rapid, inexpensive lateral flow antigen test based on these methods.[97]

LFAs provide immediate POC results that may be easily interpreted through qualitative colorimetric or fluorometric readouts (Figure 2.6E). It is recommended that lateral flow assays use validated automated readings for reliable LFA deployment.[79] If readings are recorded electronically, the data can then be easily sent to an mHealth platform for community spread tracking, immediate contact tracing, and personal symptom monitoring and treatment via telemedicine. Viral transmission models demonstrate that frequency of testing and short sample-to-answer time should be prioritized in testing and surveillance (Figure 2.6F).[72] These factors prove to be

even more important than test sensitivity in controlling disease spread. These results demonstrate the importance that rapid POC tests like LFAs have in controlling the pandemic.

### Nanotechnology-Enabled Telemedicine Sensors for COVID-19 Diagnosis

Although LFAs have promise to be widely deployed as an inexpensive, rapid, at-home testing tool, they are limited to qualitative binary diagnostic results and have variable performance under independent reviews.[79, 19] Highly sensitive, quantitative testing methods may allow for earlier detection and more accurate screening for asymptomatic carriers as well as a more informative tool for monitoring disease progression at home through telemedicine care. Electrochemical sensors based on novel nanomaterials are well-positioned to provide rapid, highly sensitive testing that can be easily integrated into mHealth platforms.

An ultrasensitive field-effect transistor (FET)-based biosensor was recently developed for label-free detection of the SARS-CoV-2 S protein (Figure 2.7A).[25] The sensor was prepared using capture antibodies bound to graphene sheets of the FET using a 1-pyrenebutyric acid (PBA) Nhydroxysuccinimide ester linker. Using this electrochemical technique, the device could detect spike protein at the fg/mL level, with a limit of detection of 242 copies/mL in clinical nasopharyngeal sample specimens. The signal response was immediately observable upon antigen-binding with stable signals and quantitative detection achieved in under a minute.

Instead of developing a highly sensitive sensor, one can also amplify the signal to a detectable range. A POC aptamer-based sensor was developed in saliva that uses invertase to amplify the signal by converting sucrose to glucose (Figure 2.7B).[98] Upon antigen-aptamer binding, invertase-conjugated antisense strands are released from functionalized magnetic beads and separated. Using a commercial glucometer, the glucose concentration could be effectively calibrated to the antigen concentration. Given the commercial availability of glucometers and their connectivity to mHealth networks, this diagnostic platform cleverly utilizes existing technology for ready POC deployment.

Rapid, electrochemical sensing of cytokine biomarkers has been an ongoing field of research given the diagnostic use of monitoring the body's inflammatory response in several diseases. An aptamer-based graphene FET with a $HfO_2$ dielectric layer was demonstrated to detect IL-6 in saliva at the picomolar level.[101] For real-

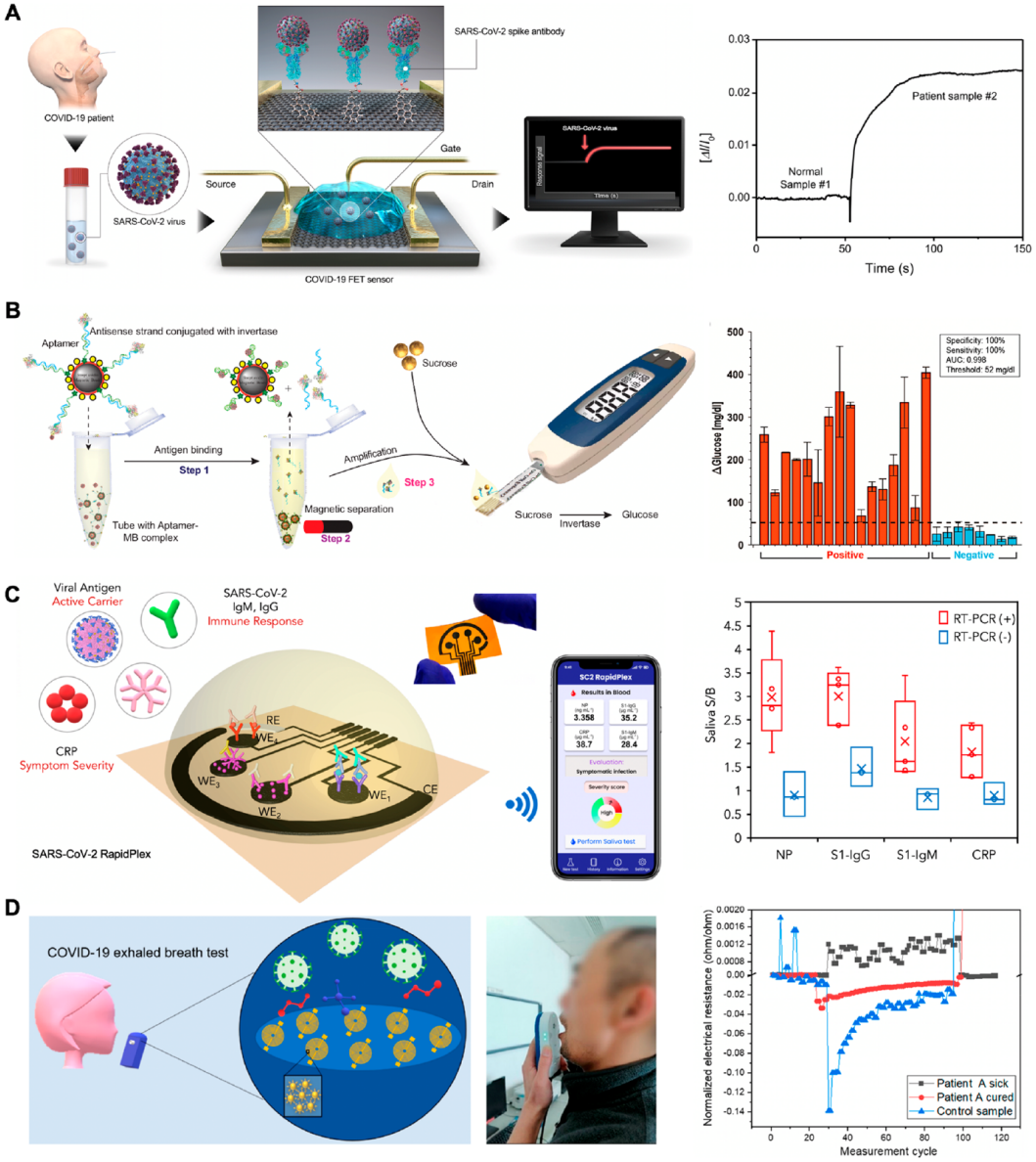


Figure 2.7: Nanoengineered electrochemical sensors for POC COVID-19 diagnosis

(A) Ultrasensitive and rapid detection of the SARS-CoV-2 antigen using a field-effect transistor-based biosensor. [25] (B) Point-of-care aptamer-based detection of SARS-CoV-2 antigen in saliva using invertase for signal amplification via a commercial glucometer. [98] (C) Rapid multiplexed detection of SARS-CoV-2 antigen, antibodies, and C-reactive protein using a laser-engraved graphene-based immunosensor with demonstrated use in saliva. [99] (D) A COVID-19 breath test that uses an array of nanomaterial-based hybrid sensors for exhaled breath analysis toward machine learning assisted COVID-19 diagnosis. [100]

time COVID-19 diagnosis based on viral-induced inflammation, an electrochemical sensor was reported to selectively detect the reactive oxygen species (ROS) levels in sputum samples.[102] During infection, mitochondrial ROS induce cytokine

dysregulation in the lungs. Using functionalized multiwalled carbon nanotubes, the sensor detects ROS levels in 30 s via cyclic voltammetry. The test achieved 97% sensitivity and was well-correlated to chest CT scan results. This electrochemical sensor has the potential to be adapted for an easy-to-use, reliable at-home test to diagnose COVID-19 and monitor lung health over the course of the infection.

A multiplexed electrochemical platform, SARS-CoV-2 RapidPlex, was developed for at-home diagnosis and monitoring via simultaneous detection of SARS-CoV-2 antigen, antibodies, and CRP.[89] In a single test, the platform provides quantitative information on viral infection, immune response, and disease severity. The platform is composed of an immunosensor array based on four 1-pyrenebutyric acid (PBA)-coated laser-engraved graphene working electrodes (Figure 2.7C). The design allows for ultrasensitive, selective, and simultaneous amperometric detection of SARS-CoV-2 N protein, anti-S1 IgG, anti-S1 IgM, and CRP. The data are wirelessly transmitted to a user interface via Bluetooth, allowing for remote reporting and monitoring. The platform was applied to both serum and saliva samples with substantial differences between COVID-19 positive and negative samples for all biomarkers (Figure 2.7C). Taking advantage of graphene's properties and using simple and well-established surface functionalization and immunosensing techniques, the SARS-CoV-2 RapidPlex platform provides a basis for quantitative panel testing of COVID-19 biomarkers.

Artificial intelligence (AI) has been incorporated into the diagnosis of COVID-19 based on standard laboratory testing, CT scans, and clinical presentation,[103] but it is also used to identify COVID-19 signatures in exhaled breath analysis through a hand-held breathalyzer system (Figure 2.7D).[100] A sensor array of AuNPs functionalized with organic ligands produces changes in the electric resistance due to shrinking and swelling of the nanomaterial film based on chemical reactions upon exposure of exhaled breath composed of respiratory gases, volatile organic compounds (VOCs), and water vapor. The testing procedure was observed to be highly specific for COVID-19 in comparison to other lung infections. Such immediate and simple testing procedures would allow for mass screening in public and POC settings.

The rapid development of diagnostic tools for SARS-CoV-2 has led to creative ways to exploit viral products and the immune response to provide key diagnostic information. However, few of these tools are ready for mass deployment, and some argue that the priorities of researchers are misaligned with the priorities of

clinicians.[104] In practice, robustness outweighs sensitivity. With more attention placed to clinical validation and reproducibility, these novel devices have great potential to address the challenges of current testing. Electrochemical sensors are prime for integration with mHealth platforms, allowing for immediate contact tracing and telemedicine access. Because of their rapid result turnaround, these tools may be used frequently before and ongoing during the infection to better monitor the disease progression.

### 2.2.2 Telemedicine Tools for Vital Sign Monitoring and Contact Tracing

Given the current challenges in implementing widespread testing, wearable sensors monitoring general vital signs may be used to continuously monitor for early warning signs and worsening of symptoms. Early symptoms of COVID-19 infections are nonspecific and typically present as fever, cough, shortness of breath, and fatigue.[110] Real-time and at-home monitoring of physiological signals using telemedicine devices may offer insight into the patient's health status to prompt medical treatment and prevent sudden degradation, thus reducing overall mortality rate (Figure 2.8A). Skin-interfaced wearable devices and mobile health (mHealth) monitors have been widely used for fitness tracking and daily life and, now, have the potential of translating toward collecting physiological signals during the pandemic to monitor and identify potential patients, and contain the COVID-19 outbreak (Figure 2.8B-E).[111, 112, 113, 64, 105, 106, 107, 108] These wearable devices can be deployed to healthy individuals who have the risk of potential exposure, asymptomatic persons, and people with mild symptoms, who are suggested to stay at home and self-quarantine without further medical care under current clinical guidances.[114] Additionally, monitoring physiological signals of patients continuously may offer a deeper understanding of the development of COVID-19 infections as well as the process of recovery or potential long-term sequelae.[66, 67] Population level mHealth monitoring will unveil the true incidence among communities, guide local reopening policies, and provide an early warning system to help reduce viral transmission and mortality rate. In this section, we summarize the clinical translation of physiological biomarkers that are strongly related with COVID-19 symptoms, introduce the wearable sensor platforms developed to track them, and then discuss the current progress of using these wearable vital sign monitors and the collected relevant data for COVID-19 monitoring and management.

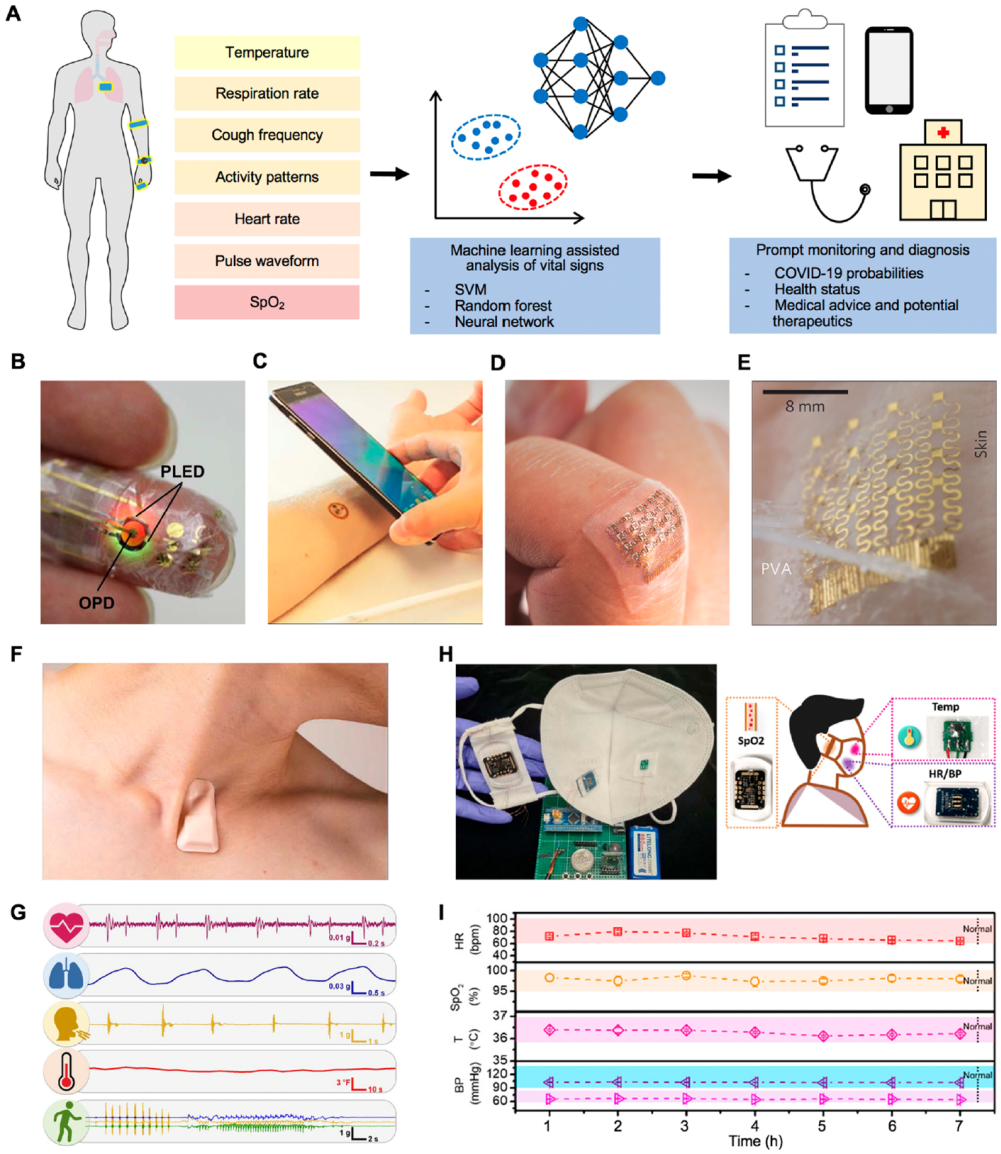


Figure 2.8: Skin-interfaced wearable sensors for continuous and noninvasive COVID-19 early detection and monitoring

(A) Wearable sensors for continuous monitoring of physiological biomarkers related to COVID-19 infections. Workflow of vital sign data analysis and COVID-19 predictive system. (B) A flexible pulse oximeter mounted on a subject's finger measuring oxygen saturation level. [105] (C) Wireless measurement of oxygenation with a smartphone. [106] (D) An epidermal ultrasonic device that monitors central blood pressure waveform. [107] (E) A skin TCR sensor array for temperature mapping. [108] (F) A soft skin-interfaced sensor platform designed for COVID-19 monitoring. [67] (G) Continuous multimodal monitoring of vital signs from a COVID-19 patient. [67] (H) A smart mask that monitors respiratory signs associated with COVID-19. [109] (I) Remote real-time monitoring of a person wearing the mask. [109]

**Wearable Sensors for Continuous Vital Sign Monitoring**

When a viral infection occurs, the immune system will defend against it by elevating body temperature. Temperature measurements are therefore indispensable and have been widely adopted in many countries. For example, a continuous body temperature monitoring program using the TempTraq system has been launched in University Hospitals in Ohio to monitor temperatures of caregivers who may be exposed to COVID-19.[115] The single use, disposable sensor patch can last up to 72 h and transmit real-time data wirelessly. When a fever is detected, the caregiver is immediately quarantined to ensure the safety of the general public. While identifying potential patients with fever may help control the spread to some degree, measuring temperature alone is neither sufficient nor accurate. Fever is also related with many other infections, such as the flu, and is not a hallmark symptom of COVID-19, as many patients are asymptomatic or do not experience a fever during infection.

Viral illness increases physiological stress leading to an increase in heart rate and blood pressure and change in pulse waveforms. One previous study reported predicting influenza-like illness by analyzing resting heart rate and sleeping duration based on commercial Fitbit and Huami devices.[116, 117] Recently, researchers at Stanford and Scripps have initiated app-based monitoring programs to detect and predict viral illnesses using Fitbit and Apple watch wearables, which extract heart rate and other health data.[118, 119] Studies have also shown that COVID-19 infections are associated with cardiovascular complications including myocarditis, heart failure, and venous thromboembolism.[120] Sudden cardiovascular death is highly related with COVID-19 infections and has become a major complication.[121] Thus, it is critical to monitor cardiac conditions such as heart rate variability (HRV) among COVID-19 patients using wearable electrocardiogram (ECG) sensors.

Respiration rate is of critical importance to monitor the lung functionality of COVID-19 patients. Normal respiration rates range from 12 to 20 rpm at rest, while infected lungs will cause increased respiration rates. Compared with body temperature measurements, monitoring respiration fluctuations may serve as a more specific biomarker for COVID-19 diagnosis, since most flu cases do not exhibit shortness of breath. It is worth noting that an elevated respiration rate usually requires oxygen therapy, and delayed treatment may cause the use of highly invasive procedures such as mechanical ventilation and intubation, which currently has a high mortality rate of 80%.[122] Measuring respiration rate using strain sensors can potentially monitor the coughing frequency as well, helping to assess in real-time and allow for timely

medical interventions before worsening symptoms arise.

Peripheral oxygen saturation ($SpO_2$) measures the oxygen carrying capability of hemoglobin. Normal blood oxygen saturation level is around 94% to 100%, while breathing problems may cause life threating hypoxemia. COVID-19 attacks the lungs differently from normal pneumonia and causes oxygen deprivation that is hard to detect initially during the incubation period. By the time noticeable shortness of breath is developed, the oxygen saturation levels of the patients have usually decreased to merely 50%.[122] This makes monitoring pulse oximetry a crucial early warning factor to prevent exacerbations. Pulse oximeters, wearable devices that are mounted on the fingers of the patients to continuously and noninvasively monitor oxygen saturation levels, have been proposed to monitor symptoms at home and prevent such silent hypoxia in COVID-19 patients.[122]

Activity patterns also have the potential of reflecting the individual's health status. With current stay-at-home guidelines, a significant decline in normal activity levels measured by step counts of Fitbit users have been shown.[123] Exercise has been proven to have health benefits for both healthy individuals and patients with various diseases.[124, 125] Regular physical exercise will improve cardiovascular functions,[126] increase the strength of respiratory muscles,[127] and maintain and enhance the immune system.[128, 129] Some pioneering research has been conducted to study activity patterns of COVID-19 patients using skin-interfaced wearable sensors (Figure 2.8F-I).[67, 109]

**Data Analysis and Pioneering Studies of mHealth for COVID-19 Monitoring**

Several COVID-19 monitoring mHealth apps have been developed to collect daily survey-based information, including whether people feel well and whether they develop COVID-19 symptoms, and to assess real-time community spread. For example, a web-based platform named CovidNearYou has been designed to visualize COVID-19 current and potential hotspots.[130] The platform has captured more than 1 million self-reports based on voluntary crowdsourced data. These apps can be used not only for the general public but also for screening health workers to implement effective containment strategies.[131] One challenge is that many infectious patients are not aware during the incubation period, which makes self-reporting a lagged measure in terms of prompt epidemiologic studies.

Given the highly diversified user health data, mHealth platforms such as smartphone

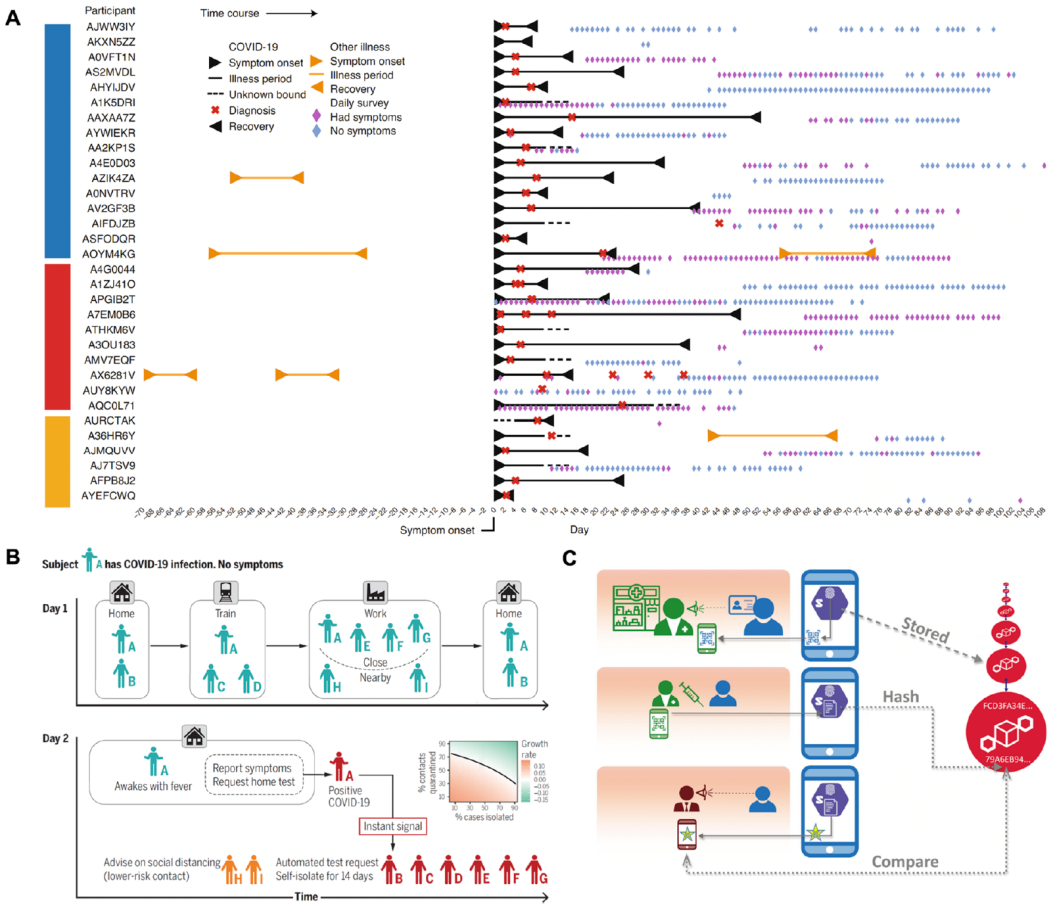


Figure 2.9: mHealth platforms for physiological data monitoring, analysis, and contact tracing

(A) Physiological monitoring of 31 COVID-19 positive patients using a smartwatch platform. [132] (B) Contact tracing and quarantine by monitoring the proximity between phones running the mHealth app. [133] (C) Schematic of testing, certification, and verification for data security using decentralized verifiable data registry. [134]

apps may be combined with wearable sensors to automatically analyze and manage the data as an elementary screening tool and reduce unnecessary hospital consultations.[135] Machine learning models along with predictive algorithms that can generalize among different populations can be built to understand inconspicuous health status and predict exacerbations.[103, 136] Some pioneering studies include early detection of COVID-19 using both commercial wearable products and customized wearable platforms. For example, researchers were able to distinguish cases based on changes in heart rate, steps, and sleep in 80% of COVID-19 infections by analyzing smartwatch data from 31 infected patients out of 5000 participants (Figure 2.9A).[132] These physiological alterations were detected before symptom onset in

over 85% of the positive cases, which could be used to predict asymptomatic and presymptomatic COVID-19 infections and better meet surges in medical demand.

Anonymous data containing geographic information can further enable contact tracing by monitoring the proximity between phones running the app (Figure 2.9B).[133] With approaches that ensure data security,[134] these population-wide platforms also identify potential regions at risk and new "hot spots" in the absence of widespread population testing (Figure 2.9C).[137] Some representative social-media platforms including WhatsApp, Facebook, and Twitter have also been used to broadcast instant information or updates to the public, which supplement public communication and health education.[138, 139, 140]

### 2.2.3 Telemedicine Metabolic Biosensors for COVID-19 Risk Assessments

Many studies have revealed that the risk of COVID-19 severity and death is extremely higher among individuals with chronic diseases and metabolic disorders such as obesity, diabetes, fatty liver disease, and alcoholism.[146, 147, 148, 149, 150, 151]

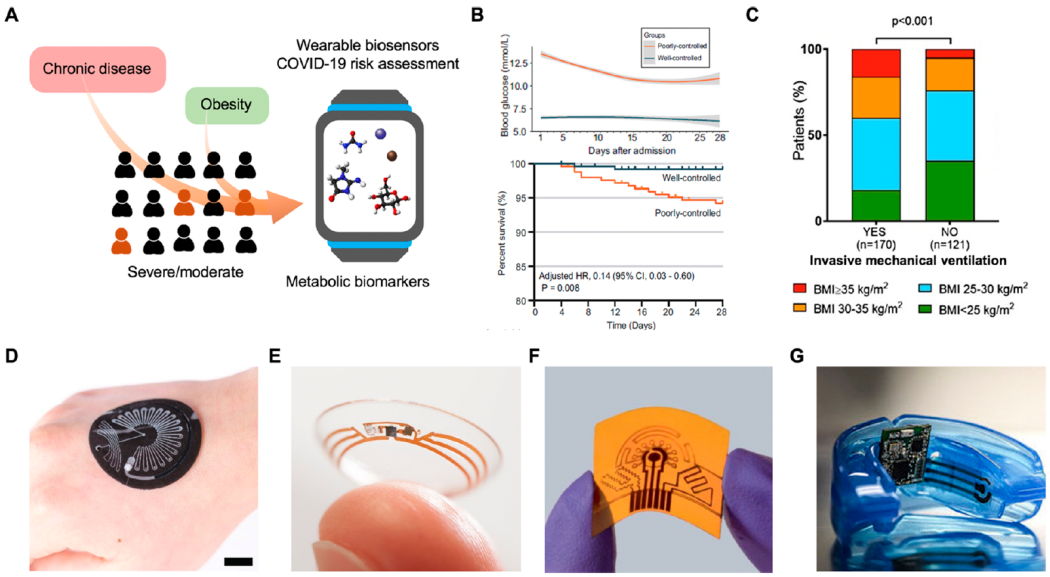


Figure 2.10: Wearable metabolic biosensors for COVID-19 risk assessment

(A) Schematic illustration for wearable chemical sensors for monitoring COVID-19 risk factors, severity, and prognosis. (B) Dynamics of blood glucose during the 28-day follow-up and survival rate curves of patients with poorly and well-controlled blood glucose. [141] (C) Association between obesity and COVID-19 severity. [142] (D and E) Photographs for wearable sensors for continuous and noninvasive glucose analysis in sweat (D) and tears (E). [143, 144] (F and G) Wearable chemical sensors for monitoring circulating metabolites and nutrients through in situ sweat (F) and saliva (G) analyses. [30, 145]

Understanding the risk of severe COVID-19 outcomes for these patient populations, it is important that individuals take preventative steps to lower their risk for severe COVID-19. Monitoring of metabolic biomarkers may better track patient progress under physician-guided lifestyle changes, such as diet and exercise. If infected, quantitative metabolic information may be used to screen for high-risk patients and better inform treatment decisions. Once patients exhibit clinical manifestations requiring inpatient interventions, they may have already progressed to a severe phase associated with other complications, such as heart failure, liver failure, or kidney failure. Therefore, this necessitates moving toward small and inexpensive telemedicine tools that may monitor general metabolic biomarkers continuously and alert clinicians in advance of patient degradation, allowing for early intervention in high-risk patients with severe prognoses (Figure 2.10A). In this section, we report metabolic biomarkers that are well-correlated with COVID-19 severity and outcome. We then discuss how these biomarkers may be monitored using wearable electrochemical sensors prior to infection for preventative measures and during infection to triage and monitor vital organ function.

**Metabolic Biomarkers and COVID-19 Severity**

Metabolic biomarkers have been proven as an effective tool to evaluate the etiology of diseases and assess the effects of pathologies.[152] A wealth of metabolic biomarkers have recently been detected from nonsevere and severe COVID-19 patient serum, such as urea, creatinine, uric acid, ions (potassium, sodium, iron, calcium, bicarbonate, chloride), glucose, and lactic acid.[153] Some of these metabolic biomarkers have attracted attention for their direct correlation with COVID-19 severity.[154, 155] As shown in Table 2.2, glomerular filtration biomarkers, urea and creatinine,

| metabolic biomarkers | reference range | range in mild cases | range in severe cases |
|---|---|---|---|
| creatinine | 60−120 $\mu$M | 40−60 $\mu$M | 50−160 $\mu$M |
| urea | 2.5−7.1 mM | 2−5 mM | 5−25 mM |
| potassium | 3.6−5.2 mM | 3.8−4.6 mM | 4.0−5.0 mM |
| iron | 60−170 $\mu$g/dL | 55−58 $\mu$g/L | median 25.5 $\mu$g/L |
| glucose | 4.4−6.1 mM | 4−20 mM | 6−25 mM |

Table 2.2: Exemplar small-molecule biomarkers in mild and severe patients with COVID-19.

increased by 5-fold in severe COVID-19 patients, indicating that severe infection may reduce kidney function or that patients with chronic kidney disease are at a higher risk for severe presentation of COVID-19. There was no significant difference for uric acid between COVID-19 patients and healthy reference values. Ions play an important role in blood to maintain osmotic balance, pH balance, and proper cellular function; therefore, variation in plasma ion concentrations may be indicative of metabolic disorders. The kidney regulates the levels of plasma ion concentrations including sodium, potassium, calcium, magnesium bicarbonate, and chloride. As described, COVID-19 may disrupt kidney function, changing ion concentrations in the process. Potassium showed higher concentrations of around 1 mM in severe cases.[156] Other ions like sodium, chloride, and bicarbonate showed no significant difference between the nonsevere and severe patients.[157] Iron, which is an essential element for nucleic acid replication, is an attractive biomarker for severe prognosis.[158] When the immune response is activated and the cytokine cascade starts, serum iron decreases and is converted to ferritin, leading to an observed decrease in concentration after infection when compared to normal reference values. In severe cases, serum iron concentration decreased significantly to 25.5 μg/dL due to lymphopenia, and ferritin increased correspondingly. The serum iron recovered after a median of 7-9 days of treatment in the intensive care unit. As a key biomarker for health, blood glucose increased after infection among COVID-19 patients and was well-correlated to disease severity.[146, 159] Well-controlled blood glucose concentrations significantly reduced complications, adverse outcomes, and death (Figure 2.10B).[141] Blood glucose provides novel insight into patients with severe COVID-19 and possible avenues aimed at improving their disease outcomes. Similar with glucose, lactic acid in serum increased after infection. In addition to diabetes mellitus and chronic kidney disease, obesity, another health condition in the metabolic syndrome cluster, has been linked to a high risk of severe COVID-19 illness and death.[160, 149] There is a clear relationship between increasing values of BMI and the proportion of patients with severe COVID-19 (Figure 2.10C).[142] These metabolic biomarkers paint an overall picture of the course and severity of COVID-19 infection. Identifying declined metabolic health may be of great importance in the early diagnosis and treatment, potentially reducing hospitalization for severe patients. However, it should be clarified that the reported results are limited by small sample sizes and monitoring of metabolic biomarkers during treatment, which may have had an unknown influence on the serology results. Additionally, these biomarkers are not as specific to COVID-19 as viral products.

**Wearable Chemical Sensors**

Wearable biosensors could play an important role for metabolic monitoring and infection risk assessment during the COVID-19 pandemic through real-time and continuous analysis of accessible body fluids like interstitial fluid, sweat, saliva, and tears (Figure 2.10D-G).[65, 161, 68] Through low-cost, commercially available wearable biosensors such as continuous glucose monitoring (CGM) devices to monitor blood glucose level in real-time, it is possible for clinicians to evaluate and treat patients more efficiently based on the observed increase in blood glucose after COVID-19 infection. Glycemic control through wearable CGM devices has been advocated for in-hospital use to monitor COVID-19 patients, especially those with diabetes, since hyperglycemia brought on by changes in medication and infrequent glucose monitoring during COVID-19 hospitalization is a poor prognostic indicator.[162, 163] More recently, wearable sensors with an enzymatic glucose sensor can noninvasively monitor external body fluids (sweat,[143, 164, 165] tears,[144] saliva[166]) and reflect the relative blood glucose levels (Figure 2.10D,E). The wearable biosensing technique can be applied to other biomarkers in sweat and saliva toward noninvasive personalized metabolic monitoring. For example, sweat electroactive metabolites and nutrients (e.g., uric acid, tyrosine) can be monitored by a laser-engraved microfluidic wearable sensor patch (Figure 2.10F),[30] and metabolites in saliva (e.g., uric acid and lactate) can also be monitored with a wireless mouthguard biosensor (Figure 2.10G).[145] Urea in sweat has been monitored using a urease-modified enzymatic ammonium-ion-selective electrode to track protein intake in the daily diet.[167] Besides the triage of severe cases, metabolic wearable biosensors could be used for lifestyle monitoring and diet personalization for preventative healthcare and lowering the risk of severe COVID-19 outcomes prior to infection.

These continuous chemical sensors may be combined with physical sensors described previously to create a multimodal platform for health monitoring. Through continuous data processing, machine learning, and mHealth incorporation of medical records, a multimodal health platform could provide key predictive information regarding COVID-19 risk and advanced warning of COVID-19 infection. It should also be noted that these telemedicine sensors could potentially allow noninvasive monitoring of stress and mental health monitoring which has become a crucial societal issue during the pandemic.[31, 168, 169] The future of personalized medicine will incorporate continuous and mHealth connected multimodal wearable platforms

in preventative treatment plans, early infection prognosis, and telemedicine monitoring.

### 2.2.4 Outlook

Based on recent global trends, it is clear that the battle against COVID-19 is not a passive one. While sheltering in place is the most effective method for stopping the spread of COVID-19, it is not compatible with the global economy and communal society we live in. Thus, in addition to face coverings and social distancing measures, how we approach COVID-19 screening, diagnosis, and treatment must be re-imagined. The ability to immediately isolate infected individuals and limit their contacts through telemedicine monitoring and prognosis is imperative to containing COVID-19.

COVID-19 testing has been one of the largest challenges during the pandemic. Widespread and frequent testing with rapid turnaround time is necessary since presymptomatic and asymptomatic carriers may contribute the most to spreading the disease. LFAs are being bet on as a cheap, mass-producible, simple, and rapid diagnostic tool. However, there are concerns that LFAs are not as accurate as the standard RT-PCR. Moving toward inexpensive telemedicine, electrochemical sensors may solve this problem with accurate and quantitative results, which may better inform physicians. Additionally, diagnostic platforms may be advanced to multiplexed designs to provide information regarding not only infection status but also the immune response, inflammatory markers, and metabolic markers to better understand the time course and severity of the infection. A key for telemedicine implementation though is that diagnostic tools must be self-administered using accessible samples including blood, saliva, or exhaled breath.

Once diagnosed, at-home isolation and monitoring of symptoms is necessary to prevent overwhelming healthcare systems. By pairing continuous wearables that monitor physiological markers and telemedicine platforms, physicians can track patient health statuses in real-time and determine when to change treatment courses. Through mHealth platforms, these data may be automatically analyzed for early warning signs of patient degradation. At-home monitoring of metabolic markers associated with prognosis may also allow for forward triage of COVID-19 patients. These tools may allow for earlier intervention in serious cases and efficient allocation of hospital resources to improve positive patient outcomes. Additionally, continued telemedicine monitoring of chronic metabolic disorders may allow for preventative

steps to be taken by changes in diet and lifestyle and treatments that would help to lower their risk of severe COVID-19 outcomes.

Considering the large infected population and high transmission rate, manual contact tracing and identification have become infeasible. Contact tracing and quarantine, case isolation and monitoring, hygiene, and decontamination will be the new normal until a vaccine is widely available.[133] With the widespread availability of commercial wearable devices and smartphone-based platforms, they can be used for continuous monitoring of individuals as well as autonomous tracing of disease activity. Machine learning and predictive algorithms of the user data will play a role in disease identification and assessment. At a population level, these algorithms combined with geographic app data may form more accurate models of the spread that may guide quarantine strategies and reopening policies.

In conclusion, with new advances in remote diagnostics and wearable sensors, telemedicine may be effectively leveraged for COVID-19. Through widespread, rapid screening and at-home testing, mHealth reporting, and integrated wearable technologies for symptom monitoring and prognosis, we may control future surges of COVID-19 infections and optimize patient outcomes.

## References


[1] *COVID-19 Map*. Johns Hopkins Coronavirus Resource Center. URL: https://coronavirus.jhu.edu/map.html (visited on 09/23/2020).

[2] Martin Zand and Jiong Wang. *Potential Mechanisms of Age Related Severity of COVID-19 Infection: Implications for Development of Vaccines, Convalescent Serum, and Antibody Therapies*. preprint. Open Science Framework, Mar. 18, 2020. DOI: 10.31219/osf.io/f3pze. URL: https://osf.io/f3pze (visited on 09/11/2020).

[3] Roy M Anderson et al. "How will country-based mitigation measures influence the course of the COVID-19 epidemic?" *The Lancet* **2020**, *395* (10228), 931–934. DOI: 10.1016/S0140-6736(20)30567-5

[4] Terrie Walmsley et al. "Macroeconomic consequences of the COVID-19 pandemic". *Economic Modelling* **2023**, *120*, 106147. DOI: 10.1016/j.econmod.2022.106147

[5] Fynnwin Prager, Dan Wei, and Adam Rose. "Total Economic Consequences of an Influenza Outbreak in the United States: Economic Consequences of Influenza". *Risk Analysis* **2017**, *37* (1), 4–19. DOI: 10.1111/risa.12625

[6] Sang Woo Park et al. *The time scale of asymptomatic transmission affects estimates of epidemic potential in the COVID-19 outbreak*. preprint. Infectious Diseases (except HIV/AIDS), Mar. 13, 2020. DOI: 10.1101/2020.03.09.20033514. URL: http://medrxiv.org/lookup/doi/10.1101/2020.03.09.20033514 (visited on 09/11/2020).

[7] Qun Li et al. "Early Transmission Dynamics in Wuhan, China, of Novel Coronavirus–Infected Pneumonia". *New England Journal of Medicine* **2020**, *382* (13), 1199–1207. DOI: 10.1056/NEJMoa2001316

[8] Kenji Mizumoto et al. "Estimating the asymptomatic proportion of coronavirus disease 2019 (COVID-19) cases on board the Diamond Princess cruise ship, Yokohama, Japan, 2020". *Eurosurveillance* **2020**, *25* (10), DOI: 10.2807/1560-7917.ES.2020.25.10.2000180

[9] Hiroshi Nishiura et al. "Estimation of the asymptomatic ratio of novel coronavirus infections (COVID-19)". *International Journal of Infectious Diseases* **2020**, *94*, 154–155. DOI: 10.1016/j.ijid.2020.03.020

[10] Zhengtu Li et al. "Development and clinical application of a rapid IgM-IgG combined antibody test for SARS-CoV-2 infection diagnosis". *Journal of Medical Virology* **2020**, *92* (9), 1518–1524. DOI: 10.1002/jmv.25727

[11] Sarah Mervosh and Manny Fernandez. "'It's Like Having No Testing': Coronavirus Test Results Are Still Delayed". *The New York Times* **2020**,

. [12] *ID NOW COVID-19 2.0*. URL: https://www.globalpointofcare.abbott/us/en/product-details/id-now-covid-19-us.html (visited on 07/20/2024).

[13] Jeanne E. van Dongen et al. "Point-of-care CRISPR/Cas nucleic acid detection: Recent advances, challenges and opportunities". *Biosensors and Bioelectronics* **2020**, *166*, 112445. DOI: 10.1016/j.bios.2020.112445

[14] Zhen Huang et al. "Ultra-sensitive and high-throughput CRISPR-p owered COVID-19 diagnosis". *Biosensors and Bioelectronics* **2020**, *164*, 112316. DOI: 10.1016/j.bios.2020.112316

[15] Lu Guo et al. "SARS-CoV-2 detection with CRISPR diagnostics". *Cell Discovery* **2020**, *6* (1), 1–4. DOI: 10.1038/s41421-020-0174-y

[16] Max J. Kellner et al. "SHERLOCK: nucleic acid detection with CRISPR nucleases". *Nature Protocols* **2019**, *14* (10), 2986–3012. DOI: 10.1038/s41596-019-0210-2

[17] Yang Yang et al. *Evaluating the accuracy of different respiratory specimens in the laboratory diagnosis and monitoring the viral shedding of 2019-nCoV infections*. preprint. Infectious Diseases (except HIV/AIDS), Feb. 12, 2020. DOI: 10.1101/2020.02.11.20021493. URL: http://medrxiv.org/lookup/doi/10.1101/2020.02.11.20021493 (visited on 09/11/2020).

[18] Nandini Sethuraman, Sundararaj Stanleyraj Jeremiah, and Akihide Ryo. "Interpreting Diagnostic Tests for SARS-CoV-2". *JAMA* **2020**, *323* (22), 2249. DOI: 10.1001/jama.2020.8259

[19] Mayara Lisboa Bastos et al. "Diagnostic accuracy of serological tests for covid-19: systematic review and meta-analysis". *BMJ* **2020**, m2516. DOI: 10.1136/bmj.m2516

[20] Jing Gong et al. *Correlation Analysis Between Disease Severity and Inflammation-related Parameters in Patients with COVID-19 Pneumonia*. preprint. Infectious Diseases (except HIV/AIDS), Feb. 27, 2020. DOI: 10.1101/2020.02.25.20025643. URL: http://medrxiv.org/lookup/doi/10.1101/2020.02.25.20025643 (visited on 09/11/2020).

[21] Chaomin Wu et al. "Risk Factors Associated With Acute Respiratory Distress Syndrome and Death in Patients With Coronavirus Disease 2019 Pneumonia in Wuhan, China". *JAMA Internal Medicine* **2020**, *180* (7), 934. DOI: 10.1001/jamainternmed.2020.0994

[22] Bo Zhou et al. *Utility of Ferritin, Procalcitonin, and C-reactive Protein in Severe Patients with 2019 Novel Coronavirus Disease*. preprint. In Review, Mar. 19, 2020. DOI: 10.21203/rs.3.rs-18079/v1. URL: https://www.researchsquare.com/article/rs-18079/v1 (visited on 09/11/2020).

[23] Eden Morales-Narváez and Can Dincer. "The impact of biosensing in a pandemic outbreak: COVID-19". *Biosensors and Bioelectronics* **2020**, *163*, 112274. DOI: 10.1016/j.bios.2020.112274

[24] Rekha Jalandra et al. "Strategies and perspectives to develop SARS-CoV-2 detection methods and diagnostics". *Biomedicine & Pharmacotherapy* **2020**, *129*, 110446. DOI: 10.1016/j.biopha.2020.110446

[25] Giwan Seo et al. "Rapid Detection of COVID-19 Causative Virus (SARS-CoV-2) in Human Nasopharyngeal Swab Specimens Using Field-Effect Transistor-Based Biosensor". *ACS Nano* **2020**, *14* (4), 5135–5142. DOI: 10.1021/acsnano.0c02823

[26] Pranjal Chandra. "Miniaturized label-free smartphone assisted electrochemical sensing approach for personalized COVID-19 diagnosis". *Sensors International* **2020**, *1*, 100019. DOI: 10.1016/j.sintl.2020.100019

[27] Subhasis Mahari et al. *eCovSens-Ultrasensitive Novel In-House Built Printed Circuit Board Based Electrochemical Device for Rapid Detection of nCovid-19 antigen, a spike protein domain 1 of SARS-CoV-2*. Pages: 2020.04.24.059204 Section: New Results. May 11, 2020. DOI: 10.1101/2020.04.24.059204. URL: https://www.biorxiv.org/content/10.1101/2020.04.24.059204v3 (visited on 07/20/2024).

[28] Suryasnata Tripathy and Shiv Govind Singh. "Label-Free Electrochemical Detection of DNA Hybridization: A Method for COVID-19 Diagnosis". *Transactions of the Indian National Academy of Engineering* **2020**, *5* (2), 205–209. DOI: 10.1007/s41403-020-00103-z

[29] E. Pasomsub et al. "Saliva sample as a non-invasive specimen for the diagnosis of coronavirus disease 2019: a cross-sectional study". *Clinical Microbiology and Infection* **2021**, *27* (2), 285.e1–285.e4. DOI: 10.1016/j.cmi.2020.05.001

[30] Yiran Yang et al. "A laser-engraved wearable sensor for sensitive detection of uric acid and tyrosine in sweat". *Nature Biotechnology* **2020**, *38* (2), 217–224. DOI: 10.1038/s41587-019-0321-x

[31] Rebeca M. Torrente-Rodríguez et al. "Investigation of Cortisol Dynamics in Human Sweat Using a Graphene-Based Wireless mHealth System". *Matter* **2020**, *2* (4), 921–937. DOI: 10.1016/j.matt.2020.01.021

[32] Bo Diao et al. *Diagnosis of Acute Respiratory Syndrome Coronavirus 2 Infection by Detection of Nucleocapsid Protein*. preprint. Epidemiology, Mar. 10, 2020. DOI: 10.1101/2020.03.07.20032524. URL: http://medrxiv.org/lookup/doi/10.1101/2020.03.07.20032524 (visited on 09/11/2020).

[33] Malkolm Hinnemo et al. "On Monolayer Formation of Pyrenebutyric Acid on Graphene". *Langmuir* **2017**, *33* (15), 3588–3593. DOI: 10.1021/acs.langmuir.6b04237

[34] Xuan Zhang et al. "Application of graphene–pyrenebutyric acid nanocomposite as probe oligonucleotide immobilization platform in a DNA biosensor". *Materials Science and Engineering: C* **2013**, *33* (7), 3851–3857. DOI: 10.1016/j.msec.2013.05.022

[35] Ellie Yi Lih Teo, Mashitah Mohd Yusoff, and Kwok Feng Chong. "1-Pyrenebutyric Acid Functionalized Reduced Graphene Oxide (1-Pb-Rgo) Energy Storage". In: *ICGSCE 2014*. Ed. by Md Amin Hashim. Singapore: Springer, 2015, pp. 185–193. ISBN: 978-981-287-505-1. DOI: 10.1007/978-981-287-505-1_22.

[36] Victor A. Karachevtsev et al. "Noncovalent Interaction of Single-Walled Carbon Nanotubes with 1-Pyrenebutanoic Acid Succinimide Ester and Glucoseoxidase". *The Journal of Physical Chemistry C* **2011**, *115* (43), 21072–21082. DOI: 10.1021/jp207916d

[37] Elisabete Fernandes et al. "Functionalization of single-layer graphene for immunoassays". *Applied Surface Science* **2019**, *480*, 709–716. DOI: 10.1016/j.apsusc.2019.03.004

[38] Emma M. Ericsson et al. "Site-Specific and Covalent Attachment of His-Tagged Proteins by Chelation Assisted Photoimmobilization: A Strategy for Microarraying of Protein Ligands". *Langmuir* **2013**, *29* (37), 11687–11694. DOI: 10.1021/la4011778

[39] Carlota Dobaño et al. "Highly Sensitive and Specific Multiplex Antibody Assays To Quantify Immunoglobulins M, A, and G against SARS-CoV-2 Antigens". *Journal of Clinical Microbiology* **2021**, *59* (2), 10.1128/jcm.01731–20. DOI: 10.1128/jcm.01731-20

[40] Chungen Qian et al. "Development and multicenter performance evaluation of fully automated SARS-CoV-2 IgM and IgG immunoassays". *Clinical Chemistry and Laboratory Medicine (CCLM)* **2020**, *58* (9), 1601–1607. DOI: 10.1515/cclm-2020-0548

[41] Huan Ma et al. *COVID-19 diagnosis and study of serum SARS-CoV-2 specific IgA, IgM and IgG by chemiluminescence immunoanalysis*. preprint. Infectious Diseases (except HIV/AIDS), Apr. 22, 2020. DOI: 10.1101/2020.04.17.20064907. URL: http://medrxiv.org/lookup/doi/10.1101/2020.04.17.20064907 (visited on 09/11/2020).

[42] Ling Ni et al. "Detection of SARS-CoV-2-Specific Humoral and Cellular Immunity in COVID-19 Convalescent Individuals". *Immunity* **2020**, *52* (6), 971–977.e3. DOI: 10.1016/j.immuni.2020.04.023

[43] Zhao Rongqing et al. "Early Detection of Severe Acute Respiratory Syndrome Coronavirus 2 Antibodies as a Serologic Marker of Infection in Patients With Coronavirus Disease 2019". *Clinical Infectious Diseases* **2020**, *71* (16), 2066–2072. DOI: 10.1093/cid/ciaa523

[44] Juanjuan Zhao et al. "Antibody Responses to SARS-CoV-2 in Patients With Novel Coronavirus Disease 2019". *Clinical Infectious Diseases* **2020**, *71* (16), 2027–2034. DOI: 10.1093/cid/ciaa344

[45] Thomas Nicol et al. "Assessment of SARS-CoV-2 serological tests for the diagnosis of COVID-19 through the evaluation of three immunoassays: Two automated immunoassays (Euroimmun and Abbott) and one rapid lateral flow immunoassay (NG Biotech)". *Journal of Clinical Virology* **2020**, *129*, 104511. DOI: 10.1016/j.jcv.2020.104511

[46] Tao Ai et al. "Correlation of Chest CT and RT-PCR Testing for Coronavirus Disease 2019 (COVID-19) in China: A Report of 1014 Cases". *Radiology* **2020**, *296* (2), E32–E40. DOI: 10.1148/radiol.2020200642

[47] Jasper Fuk-Woo Chan et al. "Improved Molecular Diagnosis of COVID-19 by the Novel, Highly Sensitive and Specific COVID-19-RdRp/Hel Real-Time Reverse Transcription-PCR Assay Validated In Vitro and with Clinical Specimens". *Journal of Clinical Microbiology* **2020**, *58* (5), 10.1128/jcm.00310–20. DOI: 10.1128/jcm.00310-20

[48] Cyril Chik-Yan Yip et al. “Development of a Novel, Genome Subtraction-Derived, SARS-CoV-2-Specific COVID-19-nsp2 Real-Time RT-PCR Assay and Its Evaluation Using Clinical Specimens”. *International Journal of Molecular Sciences* **2020**, *21* (7), 2574. DOI: 10.3390/ijms21072574

[49] Yinhua Zhang et al. *Rapid Molecular Detection of SARS-CoV-2 (COVID-19) Virus RNA Using Colorimetric LAMP*. Pages: 2020.02.26.20028373. Feb. 29, 2020. DOI: 10.1101/2020.02.26.20028373. URL: https://www.medrxiv.org/content/10.1101/2020.02.26.20028373v1 (visited on 07/20/2024).

[50] Fei Teng et al. “CDetection: CRISPR-Cas12b-based DNA detection with sub-attomolar sensitivity and single-base specificity”. *Genome Biology* **2019**, *20* (1), 132. DOI: 10.1186/s13059-019-1742-z

[51] Fabiane M. Nachtigall et al. “Detection of SARS-CoV-2 in nasal swabs using MALDI-MS”. *Nature Biotechnology* **2020**, *38* (10), 1168–1173. DOI: 10.1038/s41587-020-0644-7

[52] Pei Wang. “Combination of serological total antibody and RT-PCR test for detection of SARS-COV-2 infections”. *Journal of Virological Methods* **2020**, *283*, 113919. DOI: 10.1016/j.jviromet.2020.113919

[53] Ana Maria Ravena Severino Carvalho et al. “New antigens for the serological diagnosis of human visceral leishmaniasis identified by immunogenomic screening”. *PLOS ONE* **2018**, *13* (12), e0209599. DOI: 10.1371/journal.pone.0209599

[54] Safar Ali Alizadeh et al. “Evaluation of New ELISA based on rLsa63 – rLipL32 antigens for serodiagnosis of Human Leptospirosis”. *Iranian Journal of Microbiology* **2014**, *6* (3), 184–189

. [55] Wei Feng et al. “Molecular Diagnosis of COVID-19: Challenges and Research Needs”. *Analytical Chemistry* **2020**, *92* (15), 10196–10209. DOI: 10.1021/acs.analchem.0c02060

[56] Alba Grifoni et al. “A Sequence Homology and Bioinformatic Approach Can Predict Candidate Targets for Immune Responses to SARS-CoV-2”. *Cell Host & Microbe* **2020**, *27* (4), 671–680.e2. DOI: 10.1016/j.chom.2020.03.002

[57] Shantani Kannan et al. “Molecular Characterization and Amino Acid Homology of Nucleocapsid (N) Protein in SARS-CoV-1, SARS-CoV-2, MERS-CoV, and Bat Coronavirus”. *Journal of Pure and Applied Microbiology* **2020**, *14*, 757–763. DOI: 10.22207/JPAM.14.SPL1.13

[58] Fang Liu et al. “Prognostic value of interleukin-6, C-reactive protein, and procalcitonin in patients with COVID-19”. *Journal of Clinical Virology* **2020**, *127*, 104370. DOI: 10.1016/j.jcv.2020.104370

[59] Ian Huang et al. “C-reactive protein, procalcitonin, D-dimer, and ferritin in severe coronavirus disease-2019: a meta-analysis”. *Therapeutic Advances in Respiratory Disease* **2020**, *14*, 1753466620937175. DOI: 10.1177/1753466620937175

[60] Ying Sun et al. “Characteristics and prognostic factors of disease severity in patients with COVID-19: The Beijing experience”. *Journal of Autoimmunity* **2020**, *112*, 102473. DOI: 10.1016/j.jaut.2020.102473

[61] Weifeng Shang et al. “The value of clinical parameters in predicting the severity of COVID-19”. *Journal of Medical Virology* **2020**, *92* (10), 2188–2192. DOI: 10.1002/jmv.26031

[62] Chaochao Tan et al. “C-reactive protein correlates with computed tomographic findings and predicts severe COVID-19 early”. *Journal of Medical Virology* **2020**, *92* (7), 856–862. DOI: 10.1002/jmv.25871

[63] Wei Chen et al. “Plasma CRP level is positively associated with the severity of COVID-19”. *Annals of Clinical Microbiology and Antimicrobials* **2020**, *19* (1), 18. DOI: 10.1186/s12941-020-00362-2

[64] Changhao Xu, Yiran Yang, and Wei Gao. “Skin-Interfaced Sensors in Digital Medicine: from Materials to Applications”. *Matter* **2020**, *2* (6), 1414–1445. DOI: 10.1016/j.matt.2020.03.020

[65] Yiran Yang and Wei Gao. “Wearable and flexible electronics for continuous molecular monitoring”. *Chemical Society Reviews* **2019**, *48* (6), 1465–1491. DOI: 10.1039/C7CS00730B

[66] Catherine P. Adans-Dester et al. “Can mHealth Technology Help Mitigate the Effects of the COVID-19 Pandemic?” *IEEE Open Journal of Engineering in Medicine and Biology* **2020**, *1*, 243–248. DOI: 10.1109/OJEMB.2020.3015141

[67] Hyoyoung Jeong, John A. Rogers, and Shuai Xu. “Continuous on-body sensing for the COVID-19 pandemic: Gaps and opportunities”. *Science Advances* **2020**, *6* (36), eabd4794. DOI: 10.1126/sciadv.abd4794

[68] Jayoung Kim et al. “Wearable biosensors for healthcare monitoring”. *Nature Biotechnology* **2019**, *37* (4), 389–406. DOI: 10.1038/s41587-019-0045-y

[69] Judd E. Hollander and Brendan G. Carr. “Virtually Perfect? Telemedicine for Covid-19”. *New England Journal of Medicine* **2020**, *382* (18), 1679–1681. DOI: 10.1056/NEJMp2003539

[70] Dawei Wang et al. “Clinical Characteristics of 138 Hospitalized Patients With 2019 Novel Coronavirus–Infected Pneumonia in Wuhan, China”. *JAMA* **2020**, *323* (11), 1061. DOI: 10.1001/jama.2020.1585

[71] James R M Black et al. “COVID-19: the case for health-care worker screening to prevent hospital transmission”. *The Lancet* **2020**, *395* (10234), 1418–1420. DOI: 10.1016/S0140-6736(20)30917-X

[72] Daniel B. Larremore et al. “Test sensitivity is secondary to frequency and turnaround time for COVID-19 screening”. *Science Advances* **2020**, eabd5393. DOI: 10.1126/sciadv.abd5393

[73] Yang Yang et al. “Laboratory Diagnosis and Monitoring the Viral Shedding of SARS-CoV-2 Infection”. *The Innovation* **2020**, *1* (3), DOI: 10.1016/j.xinn.2020.100061

[74] Tianxing Ji et al. “Detection of COVID-19: A review of the current literature and future perspectives”. *Biosensors and Bioelectronics* **2020**, *166*, 112455. DOI: 10.1016/j.bios.2020.112455

[75] S. K. P. Lau et al. “Detection of Severe Acute Respiratory Syndrome (SARS) Coronavirus Nucleocapsid Protein in SARS Patients by Enzyme-Linked Immunosorbent Assay”. *Journal of Clinical Microbiology* **2004**, *42* (7), 2884–2889. DOI: 10.1128/JCM.42.7.2884-2889.2004

[76] Fei Xiang et al. “Antibody Detection and Dynamic Characteristics in Patients With Coronavirus Disease 2019”. *Clinical Infectious Diseases* **2020**, ciaa461. DOI: 10.1093/cid/ciaa461

[77] Andrea Padoan et al. “Analytical performances of a chemiluminescence immunoassay for SARS-CoV-2 IgM/IgG and antibody kinetics”. *Clinical Chemistry and Laboratory Medicine (CCLM)* **2020**, *58* (7), 1081–1088. DOI: 10.1515/cclm-2020-0443

[78] Kelvin Kai-Wang To et al. “Temporal profiles of viral load in posterior oropharyngeal saliva samples and serum antibody responses during infection by SARS-CoV-2: an observational cohort study”. *The Lancet Infectious Diseases* **2020**, *20* (5), 565–574. DOI: 10.1016/S1473-3099(20)30196-1

[79] Jeffrey D. Whitman et al. “Evaluation of SARS-CoV-2 serology assays reveals a range of test performance”. *Nature Biotechnology* **2020**, DOI: 10.1038/s41587-020-0659-0

[80] Huan Ma et al. “Serum IgA, IgM, and IgG responses in COVID-19”. *Cellular & Molecular Immunology* **2020**, *17* (7), 773–775. DOI: 10.1038/s41423-020-0474-z

[81] L. Wang. “C-reactive protein levels in the early stage of COVID-19”. *Médecine et Maladies Infectieuses* **2020**, *50* (4), 332–334. DOI: 10.1016/j.medmal.2020.03.007

[82] Zhi-Sheng Xu et al. “Temporal profiling of plasma cytokines, chemokines and growth factors from mild, severe and fatal COVID-19 patients”. *Signal Transduction and Targeted Therapy* **2020**, *5* (1), 100. DOI: 10.1038/s41392-020-0211-1

[83] Feiyun Cui and H. Susan Zhou. “Diagnostic methods and potential portable biosensors for coronavirus disease 2019”. *Biosensors and Bioelectronics* **2020**, *165*, 112349. DOI: 10.1016/j.bios.2020.112349

[84] Diane Marie Del Valle et al. “An inflammatory cytokine signature predicts COVID-19 severity and survival”. *Nature Medicine* **2020**, *26* (10), 1636–1643. DOI: 10.1038/s41591-020-1051-9

[85] Hee Ho Park et al. “Acetylated K676 TGFBIp as a severity diagnostic blood biomarker for SARS-CoV-2 pneumonia”. *Science Advances* **2020**, *6* (31), eabc1564. DOI: 10.1126/sciadv.abc1564

[86] Wei Chen et al. “Reducing false negatives in COVID-19 testing by using microneedle-based oropharyngeal swabs”. *Matter* **2020**, S2590238520305191. DOI: 10.1016/j.matt.2020.09.021

[87] Eloise Williams et al. “Saliva as a Noninvasive Specimen for Detection of SARS-CoV-2”. *Journal of Clinical Microbiology* **2020**, *58* (8), e00776–20, /jcm/58/8/JCM.00776–20.atom. DOI: 10.1128/JCM.00776-20

[88] Kelvin Kai-Wang To et al. “Consistent Detection of 2019 Novel Coronavirus in Saliva”. *Clinical Infectious Diseases* **2020**, *71* (15), 841–843. DOI: 10.1093/cid/ciaa149

[89] Rebeca M. Torrente-Rodríguez, Heather Lukas, Jiaobing Tu, Jihong Min, Yiran Yang, Changhao Xu, Harry B. Rossiter, and Wei Gao. “SARS-CoV-2 RapidPlex: A graphene-based multiplexed telemedicine platform for rapid and low-cost COVID-19 diagnosis and monitoring”. *Matter* **2020**, *3* (6), 1981–1998. DOI: 10.1016/j.matt.2020.09.027

[90] Xiong Zhu et al. “Multiplex reverse transcription loop-mediated isothermal amplification combined with nanoparticle-based lateral flow biosensor for the diagnosis of COVID-19”. *Biosensors and Bioelectronics* **2020**, *166*, 112437. DOI: 10.1016/j.bios.2020.112437

[91] Alexis C.R. Hoste et al. “Two serological approaches for detection of antibodies to SARS-CoV-2 in different scenarios: a screening tool and a point-of-care test”. *Diagnostic Microbiology and Infectious Disease* **2020**, *98* (4), 115167. DOI: 10.1016/j.diagmicrobio.2020.115167

[92] Meagan N. Esbin et al. “Overcoming the bottleneck to widespread testing: a rapid review of nucleic acid testing approaches for COVID-19 detection”. *RNA* **2020**, *26* (7), 771–783. DOI: 10.1261/rna.076232.120

[93] Marie C. Smithgall et al. "Comparison of Cepheid Xpert Xpress and Abbott ID Now to Roche cobas for the Rapid Detection of SARS-CoV-2". *Journal of Clinical Virology* **2020**, *128*, 104428. DOI: 10.1016/j.jcv.2020.104428

[94] Qiuyuan Lin et al. "Microfluidic Immunoassays for Sensitive and Simultaneous Detection of IgG/IgM/Antigen of SARS-CoV-2 within 15 min". *Analytical Chemistry* **2020**, *92* (14), 9454–9458. DOI: 10.1021/acs.analchem.0c01635

[95] Ki-Joo Sung et al. "Functional comparison of paper-based immunoassays based on antibodies and engineered binding proteins". *The Analyst* **2020**, *145* (7), 2515–2519. DOI: 10.1039/D0AN00299B

[96] Eric A. Miller et al. "Paper-based diagnostics in the antigen-depletion regime: High-density immobilization of rcSso7d-cellulose-binding domain fusion proteins for efficient target capture". *Biosensors and Bioelectronics* **2018**, *102*, 456–463. DOI: 10.1016/j.bios.2017.11.050

[97] *MIT team collaborates with 3M to develop rapid Covid-19 test*. MIT News | Massachusetts Institute of Technology. URL: https://news.mit.edu/2020/mit-collaborates-with-3m-develop-rapid-covid-19-test-0714 (visited on 09/11/2020).

[98] Naveen K. Singh et al. "Hitting the diagnostic sweet spot: Point-of-care SARS-CoV-2 salivary antigen testing with an off-the-shelf glucometer". *Biosensors and Bioelectronics* **2021**, *180*, 113111. DOI: 10.1016/j.bios.2021.113111

[99] Rebeca M. Torrente-Rodríguez et al. "SARS-CoV-2 RapidPlex: A Graphene-Based Multiplexed Telemedicine Platform for Rapid and Low-Cost COVID-19 Diagnosis and Monitoring". *Matter* **2020**, *3* (6), 1981–1998. DOI: 10.1016/j.matt.2020.09.027

[100] Benjie Shan et al. "Multiplexed Nanomaterial-Based Sensor Array for Detection of COVID-19 in Exhaled Breath". *ACS Nano* **2020**, acsnano.0c05657. DOI: 10.1021/acsnano.0c05657

[101] Zhuang Hao et al. "Graphene-based fully integrated portable nanosensing system for on-line detection of cytokine biomarkers in saliva". *Biosensors and Bioelectronics* **2019**, *134*, 16–23. DOI: 10.1016/j.bios.2019.03.053

[102] Zohreh Sadat Miripour et al. "Real-time diagnosis of reactive oxygen species (ROS) in fresh sputum by electrochemical tracing; correlation between COVID-19 and viral-induced ROS in lung/respiratory epithelium during this pandemic". *Biosensors and Bioelectronics* **2020**, *165*, 112435. DOI: 10.1016/j.bios.2020.112435

[103] Xueyan Mei et al. "Artificial intelligence–enabled rapid diagnosis of patients with COVID-19". *Nature Medicine* **2020**, *26* (8), 1224–1228. DOI: 10.1038/s41591-020-0931-3

[104] Thierry Leichlé, Liviu Nicu, and Thomas Alava. "MEMS biosensors and COVID-19 : missed opportunity". *ACS Sensors* **2020**, DOI: 10.1021/acssensors.0c01463

[105] Tomoyuki Yokota et al. "Ultraflexible organic photonic skin". *Science Advances* **2016**, *2* (4), e1501856. DOI: 10.1126/sciadv.1501856

[106] Jeonghyun Kim et al. "Battery-free, stretchable optoelectronic systems for wireless optical characterization of the skin". *Science Advances* **2016**, *2* (8), e1600418. DOI: 10.1126/sciadv.1600418

[107] Chonghe Wang et al. "Monitoring of the central blood pressure waveform via a conformal ultrasonic device". *Nature Biomedical Engineering* **2018**, *2* (9), 687–695. DOI: 10.1038/s41551-018-0287-x

[108] R. Chad Webb et al. "Ultrathin conformal devices for precise and continuous thermal characterization of human skin". *Nature Materials* **2013**, *12* (10), 938–944. DOI: 10.1038/nmat3755

[109] Liang Pan et al. "Lab-on-Mask for Remote Respiratory Monitoring". *ACS Materials Letters* **2020**, *2* (9), 1178–1181. DOI: 10.1021/acsmaterialslett.0c00299

[110] Wei-jie Guan et al. "Clinical Characteristics of Coronavirus Disease 2019 in China". *New England Journal of Medicine* **2020**, *382* (18), 1708–1720. DOI: 10.1056/NEJMoa2002032

[111] Tyler R. Ray et al. "Bio-Integrated Wearable Systems: A Comprehensive Review". *Chemical Reviews* **2019**, *119* (8), 5461–5533. DOI: 10.1021/acs.chemrev.8b00573

[112] Ming Wang et al. "Artificial Skin Perception". *Advanced Materials* **2021**, *33* (19), 2003014. DOI: 10.1002/adma.202003014

[113] Mallory L. Hammock et al. "25th Anniversary Article: The Evolution of Electronic Skin (E-Skin): A Brief History, Design Considerations, and Recent Progress". *Advanced Materials* **2013**, *25* (42), 5997–6038. DOI: 10.1002/adma.201302240

[114] CDC. *Coronavirus Disease 2019 (COVID-19)*. Centers for Disease Control and Prevention. Feb. 11, 2020. URL: https://www.cdc.gov/coronavirus/2019-ncov/hcp/clinical-guidance-management-patients.html (visited on 09/23/2020).

[115] *News | Best Baby Digital Thermometer | TempTraq | TempTraq*. URL: https://www.temptraq.com/News/University-Hospitals-expands-use-of-TempTraq%C2%AE-syst (visited on 09/15/2020).

[116] Jennifer M Radin et al. "Harnessing wearable device data to improve state-level real-time surveillance of influenza-like illness in the USA: a population-based study". *The Lancet Digital Health* **2020**, *2* (2), e85–e93. DOI: 10.1016/S2589-7500(19)30222-5

[117] Guokang Zhu et al. “Learning from Large-Scale Wearable Device Data for Predicting Epidemics Trend of COVID-19”. *Discrete Dynamics in Nature and Society* **2020**, *2020*, 1–8. DOI: 10.1155/2020/6152041

[118] *Scripps, Stanford working with Fitbit to assess wearables’ COVID-19 tracking abilities*. Healthcare IT News. Apr. 17, 2020. URL: https://www.healthcareitnews.com/news/scripps-stanford-working-fibit-assess-wearables-covid-19-tracking-abilities (visited on 09/15/2020).

[119] *Apple Watch, Fitbit data can spot if you are sick days before symptoms show up | ZDNet*. URL: https://www.zdnet.com/article/apple-watch-fitbit-data-can-find-covid-19-infections-days-before-symptoms-show-up/ (visited on 09/15/2020).

[120] Elissa Driggin et al. “Cardiovascular Considerations for Patients, Health Care Workers, and Health Systems During the COVID-19 Pandemic”. *Journal of the American College of Cardiology* **2020**, *75* (18), 2352–2371. DOI: 10.1016/j.jacc.2020.03.031

[121] Samira Shirazi et al. “Sudden cardiac death in COVID-19 patients, a report of three cases”. *Future Cardiology* **2020**, fca–2020–0082. DOI: 10.2217/fca-2020-0082

[122] Jason Teo. “Early Detection of Silent Hypoxia in Covid-19 Pneumonia Using Smartphone Pulse Oximetry”. *Journal of Medical Systems* **2020**, *44* (8), 134. DOI: 10.1007/s10916-020-01587-6

[123] *The Impact Of Coronavirus On Global Activity - Fitbit Blog*. URL: https://blog.fitbit.com/covid-19-global-activity/ (visited on 09/15/2020).

[124] Xin Luan et al. “Exercise as a prescription for patients with various diseases”. *Journal of Sport and Health Science* **2019**, *8* (5), 422–441. DOI: 10.1016/j.jshs.2019.04.002

[125] Peijie Chen et al. “Coronavirus disease (COVID-19): The need to maintain regular physical activity while taking precautions”. *Journal of Sport and Health Science* **2020**, *9* (2), 103–104. DOI: 10.1016/j.jshs.2020.02.001

[126] Kelsey Pinckard, Kedryn K. Baskin, and Kristin I. Stanford. “Effects of Exercise to Improve Cardiovascular Health”. *Frontiers in Cardiovascular Medicine* **2019**, *6*, 69. DOI: 10.3389/fcvm.2019.00069

[127] Donald C McKenzie. “Respiratory physiology: adaptations to high-level exercise”. *British Journal of Sports Medicine* **2012**, *46* (6), 381–384. DOI: 10.1136/bjsports-2011-090824

[128] Gilson P. Dorneles et al. "New Insights about Regulatory T Cells Distribution and Function with Exercise: The Role of Immunometabolism". *Current Pharmaceutical Design* **2020**, *26* (9), 979–990. DOI: 10.2174/1381612826666200305125210

[129] Johan Jakobsson et al. "Physical Activity During the Coronavirus (COVID-19) Pandemic: Prevention of a Decline in Metabolic and Immunological Functions". *Frontiers in Sports and Active Living* **2020**, *2*, 57. DOI: 10.3389/fspor.2020.00057

[130] *Outbreaks Near Me*. Outbreaks Near Me. URL: https://outbreaksnearme.org (visited on 07/21/2024).

[131] Haipeng Zhang et al. *A Web-based, Mobile Responsive Application to Screen Healthcare Workers for COVID Symptoms: Descriptive Study*. preprint. Health Informatics, Apr. 22, 2020. DOI: 10.1101/2020.04.17.20069211. URL: http://medrxiv.org/lookup/doi/10.1101/2020.04.17.20069211 (visited on 09/15/2020).

[132] Tejaswini Mishra et al. "Pre-symptomatic detection of COVID-19 from smartwatch data". *Nature Biomedical Engineering* **2020**, *4* (12), 1208–1220. DOI: 10.1038/s41551-020-00640-6

[133] Luca Ferretti et al. "Quantifying SARS-CoV-2 transmission suggests epidemic control with digital contact tracing". *Science* **2020**, *368* (6491), eabb6936. DOI: 10.1126/science.abb6936

[134] Marc Eisenstadt et al. "COVID-19 Antibody Test/Vaccination Certification: There's an App for That". *IEEE Open Journal of Engineering in Medicine and Biology* **2020**, *1*, 148–155. DOI: 10.1109/OJEMB.2020.2999214

[135] Daniel Shu Wei Ting et al. "Digital technology and COVID-19". *Nature Medicine* **2020**, *26* (4), 459–461. DOI: 10.1038/s41591-020-0824-5

[136] Shayan Hassantabar et al. "CovidDeep: SARS-CoV-2/COVID-19 Test Based on Wearable Medical Sensors and Efficient Neural Networks". *arXiv:2007.10497 [cs]* **2020**,

. [137] Alaa A. R. Alsaeedy and Edwin K. P. Chong. "Detecting Regions At Risk for Spreading COVID-19 Using Existing Cellular Wireless Network Functionalities". *IEEE Open Journal of Engineering in Medicine and Biology* **2020**, *1*, 187–189. DOI: 10.1109/OJEMB.2020.3002447

[138] *WhatsApp Coronavirus Information Hub*. WhatsApp.com. URL: https://www.whatsapp.com/coronavirus/?lang=fb (visited on 09/15/2020).

[139] *COVID-19 Map*. Johns Hopkins Coronavirus Resource Center. URL: https://coronavirus.jhu.edu/map.html (visited on 09/11/2020).

[140] *The COVID Tracking Project (@COVID19Tracking) / Twitter*. Twitter. URL: https://twitter.com/COVID19Tracking (visited on 09/15/2020).

[141] Lihua Zhu et al. “Association of Blood Glucose Control and Outcomes in Patients with COVID-19 and Pre-existing Type 2 Diabetes”. *Cell Metabolism* **2020**, *31* (6), 1068–1077.e3. DOI: 10.1016/j.cmet.2020.04.021

[142] Cyrielle Caussy et al. “Obesity is Associated with Severe Forms of COVID-19”. *Obesity* **2020**, *28* (7), 1175–1175. DOI: 10.1002/oby.22842

[143] Jonathan T. Reeder et al. “Resettable skin interfaced microfluidic sweat collection devices with chemesthetic hydration feedback”. *Nature Communications* **2019**, *10* (1), 5513. DOI: 10.1038/s41467-019-13431-8

[144] Google. *Smart Contact Lens*. URL: https://sites.google.com/site/smartcontactlens/ (visited on 09/23/2020).

[145] Jayoung Kim et al. “Wearable salivary uric acid mouthguard biosensor with integrated wireless electronics”. *Biosensors and Bioelectronics* **2015**, *74*, 1061–1068. DOI: 10.1016/j.bios.2015.07.039

[146] G. Targher et al. “Patients with diabetes are at higher risk for severe illness from COVID-19”. *Diabetes & Metabolism* **2020**, *46* (4), 335–337. DOI: 10.1016/j.diabet.2020.05.001

[147] Shuke Nie et al. *Metabolic disturbances and inflammatory dysfunction predict severity of coronavirus disease 2019 (COVID-19): a retrospective study*. Pages: 2020.03.24.20042283. Mar. 26, 2020. DOI: 10.1101/2020.03.24.20042283. URL: https://www.medrxiv.org/content/10.1101/2020.03.24.20042283v1 (visited on 07/21/2024).

[148] Feng Gao et al. “Obesity Is a Risk Factor for Greater COVID-19 Severity”. *Diabetes Care* **2020**, *43* (7), e72–e74. DOI: 10.2337/dc20-0682

[149] Naveed Sattar, Iain B. McInnes, and John J.V. McMurray. “Obesity Is a Risk Factor for Severe COVID-19 Infection: Multiple Potential Mechanisms”. *Circulation* **2020**, *142* (1), 4–6. DOI: 10.1161/CIRCULATIONAHA.120.047659

[150] Piero Portincasa et al. “COVID-19 and non-alcoholic fatty liver disease: Two intersecting pandemics”. *European Journal of Clinical Investigation* **2020**, *50* (10), e13338. DOI: 10.1111/eci.13338

[151] Stefan R. Bornstein et al. “Practical recommendations for the management of diabetes in patients with COVID-19”. *The Lancet Diabetes & Endocrinology* **2020**, *8* (6), 546–550. DOI: 10.1016/S2213-8587(20)30152-2

[152] Janelle S. Ayres. “A metabolic handbook for the COVID-19 pandemic”. *Nature Metabolism* **2020**, *2* (7), 572–585. DOI: 10.1038/s42255-020-0237-2

[153] Nikhil Bhalla et al. “Opportunities and Challenges for Biosensors and Nanoscale Analytical Tools for Pandemics: COVID-19”. *ACS Nano* **2020**, *14* (7), 7783–7807. DOI: 10.1021/acsnano.0c04421

[154] Fesih Ok et al. "Predictive values of blood urea nitrogen/creatinine ratio and other routine blood parameters on disease severity and survival of COVID-19 patients". *Journal of Medical Virology* **2021**, *93* (2), 786–793. DOI: 10.1002/jmv.26300

[155] Jianlin Xiang et al. *Potential biochemical markers to identify severe cases among COVID-19 patients*. preprint. Epidemiology, Mar. 23, 2020. DOI: 10.1101/2020.03.19.20034447. URL: http://medrxiv.org/lookup/doi/10.1101/2020.03.19.20034447 (visited on 09/24/2020).

[156] Chaolin Huang et al. "Clinical features of patients infected with 2019 novel coronavirus in Wuhan, China". *The Lancet* **2020**, *395* (10223), 497–506. DOI: 10.1016/S0140-6736(20)30183-5

[157] Changzheng Wang et al. "Preliminary study to identify severe from moderate cases of COVID-19 using combined hematology parameters". *Annals of Translational Medicine* **2020**, *8* (9), 593–593. DOI: 10.21037/atm-20-3391

[158] Giuliano Bolondi et al. "Iron metabolism and lymphocyte characterisation during Covid-19 infection in ICU patients: an observational cohort study". *World Journal of Emergency Surgery* **2020**, *15* (1), 41. DOI: 10.1186/s13017-020-00323-2

[159] Bo Shen et al. "Proteomic and Metabolomic Characterization of COVID-19 Patient Sera". *Cell* **2020**, *182* (1), 59–72.e15. DOI: 10.1016/j.cell.2020.05.032

[160] Feng Gao et al. "Metabolic associated fatty liver disease increases coronavirus disease 2019 disease severity in nondiabetic patients". *Journal of Gastroenterology and Hepatology* **2020**, jgh.15112. DOI: 10.1111/jgh.15112

[161] Jungil Choi et al. "Skin-interfaced systems for sweat collection and analytics". *Science Advances* **2018**, *4* (2), eaar3921. DOI: 10.1126/sciadv.aar3921

[162] Nicole Ehrhardt and Irl B. Hirsch. "The Impact of COVID-19 on CGM Use in the Hospital". *Diabetes Care* **2020**, dci200046. DOI: 10.2337/dci20-0046

[163] David C. Klonoff and Guillermo E. Umpierrez. "Letter to the Editor: COVID-19 in patients with diabetes: Risk factors that increase morbidity". *Metabolism* **2020**, *108*, 154224. DOI: 10.1016/j.metabol.2020.154224

[164] Wei Gao et al. "Fully integrated wearable sensor arrays for multiplexed in situ perspiration analysis". *Nature* **2016**, *529* (7587), 509–514. DOI: 10.1038/nature16521

[165] Hyunjae Lee et al. "A graphene-based electrochemical device with thermoresponsive microneedles for diabetes monitoring and therapy". *Nature Nanotechnology* **2016**, *11* (6), 566–572. DOI: 10.1038/nnano.2016.38

[166] Takahiro Arakawa et al. “Mouthguard biosensor with telemetry system for monitoring of saliva glucose: A novel *cavitas* sensor”. *Biosensors and Bioelectronics* **2016**, *84*, 106–111. DOI: 10.1016/j.bios.2015.12.014

[167] You Yu et al. “Biofuel-powered soft electronic skin with multiplexed and wireless sensing for human-machine interfaces”. *Science Robotics* **2020**, *5* (41), eaaz7946. DOI: 10.1126/scirobotics.aaz7946

[168] Betty Pfefferbaum and Carol S. North. “Mental Health and the Covid-19 Pandemic”. *New England Journal of Medicine* **2020**, *383* (6), 510–512. DOI: 10.1056/NEJMp2008017

[169] Xiaoyun Zhou et al. “The Role of Telehealth in Reducing the Mental Health Burden from COVID-19”. *Telemedicine and e-Health* **2020**, *26* (4), 377–379. DOI: 10.1089/tmj.2020.0068

*Chapter 3*

# NUCLEIC ACID-BASED WEARABLE AND IMPLANTABLE ELECTROCHEMICAL SENSORS

*Materials from this chapter appear in:*
Cui Ye et al. "Nucleic acid-based wearable and implantable electrochemical sensors". *Chemical Society Reviews* **2024**, DOI: 10.1039/D4CS00001C

Biomarker information collected through blood sample analysis offers critical insights into health management. However, this traditional approach is intermittent, requiring frequent clinic appointments and invasive blood draws. The emerging fields of implantable and wearable biosensing technologies present a dynamic shift toward continuous, remote monitoring of health analytes. These innovations promise a new era of precision medicine by allowing the collection of longitudinal health data with biochemical sensors capable of measuring diverse biomolecular targets with high sensitivity and robust stability (Figure 3.1).[1, 2, 3, 4, 5, 6, 7, 8, 9]

Implantable sensors may provide real-time insights into circulatory biomarkers in the blood and interstitial fluid (ISF), as well as localized indicators of tissue health and organ function. For instance, a biosensor placed in the brain can effectively monitor neurochemical signals associated with mood, cognition, and brain health.[10] Innovations in biofluid sampling and collection have enabled wearable noninvasive analysis of health biomarkers through alternative biofluids such as ISF, sweat, saliva, breath condensate, and tears.[11] With different secretory mechanisms and biomolecular partitioning, each of these fluids offers a unique lens on the body's internal state. Wearable microneedle arrays can be used to monitor circulatory biomarkers in ISF, while sweat may be collected from the skin surface and monitored for a wide range of small molecules such as amino acids, metabolites, hormones, ethanol, and therapeutic and abused drugs.[3, 11, 12]

The development of wearable and implantable biochemical sensors is considerably more challenging than creating activity trackers or traditional lab-based sensors. The complexity arises from the need for these devices to not only enable continuous

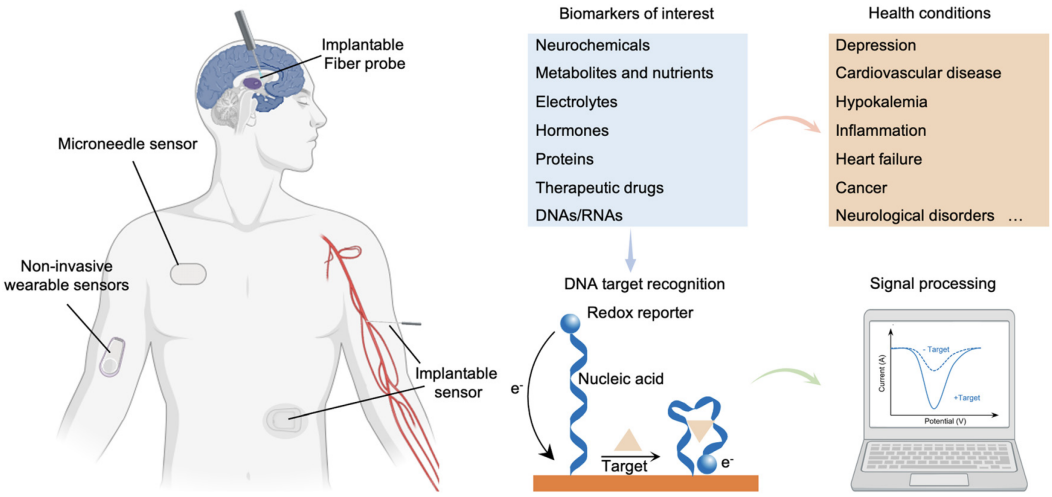


Figure 3.1: Overview of nucleic acid-based implantable/wearable electrochemical sensors

on-body biochemical sensing but also ensure a reliable and precise analyte measurement in the complex biofluid matrix. This requires highly specific biorecognition elements with fast binding kinetics, highly efficient signal transduction, and in situ regeneration capabilities for repeated measurements.[13, 14]

Conventional protein-based sensors relying on antibodies and enzymes are challenging to synthetically engineer for novel and diverse molecular targets. While burgeoning biotherapeutic research has enhanced synthetic antibody discovery and optimized high-affinity target binding, a lack of label-free electrochemical signal transduction and sensor regeneration has limited their use in continuous on-body sensing applications. Naturally occurring redox enzymes, such as glucose oxidase, address these continuous sensing challenges, yet they have limited generalizability due to the difficulty of simultaneously engineering for selective binding of new targets and high catalytic activity.[15] Proteins thus present a gap in biosensing that easily modifiable and amplifiable nucleic acids can bridge.

With the advent of systematic evolution of ligands by exponential enrichment (SELEX), nucleic acid sequences have been designed to bind with high affinity to molecular targets beyond the antisense strand. Employing nucleic acids as biorecognition elements holds great significance in implantable and wearable sensor design as they possess robust binding capabilities, ensuring selective detection of specific molecules. The high affinity of nucleic acids also translates to minimal background noise, further enhancing the reliability of the measurements. Moreover, their ease of synthesis and ability to be regenerated make them both effective and economical

choices for sensor design.[14, 16, 17]

This chapter discusses how nucleic acid-based sensors have expanded continuous electrochemical biosensing capabilities, especially in small molecule detection. Various nucleic acid design schemes are presented for biorecognition and electrochemical signal transduction, including strand displacement and aptamer structure switching, as well as redox probe manipulation and transistor-based sensing, respectively. The role of nucleic acid sensors in continuous sensing is contextualized through key examples in wearable and implantable sensing platforms. Lastly, design criteria for the ideal continuous nucleic acid sensor are summarized with an outlook toward the next generation of wearable and implantable nucleic acid sensors.

## 3.1 Nucleic Acid-Based Sensing Strategies

Nucleic acid hybridization is one of the most specific biorecognition events in nature. Predictable base pairing and hydrogen bond interactions make nucleic acids easy to engineer as nucleic acid bioreceptors and malleable to non-nucleic acid target biorecognition. High-throughput nucleic acid amplification enables efficient, low-cost bioreceptor discovery. Well-studied, unique properties of deoxyribonucleic acid (DNA) allow for nucleic acid-specific sensor designs that might exploit DNA hybridization, thermal denaturing, and DNA's negatively charged phosphate backbone to name a few. For these reasons, nucleic acid-based sensors have emerged as versatile and significant tools for biochemical sensing.

In this section, we delve into the variety of nucleic acid biorecognition elements and discuss the signal transduction mechanisms employed in implantable and wearable sensor applications (Figure 3.2). Our analysis encompasses the key categories of nucleic acid recognition elements, namely single-stranded nucleic acid probes and aptamers, which serve as both direct binding and strand-displacement sensing agents. Additionally, hybrid mechanisms that combine properties of nucleic acid strands with the biorecognition capability of proteins and antibodies are gaining prominence in the realm of innovative sensing approaches. Nucleic acid structure switches leveraging binding-induced conformational changes are dually explored as selective biorecognition elements and effective transducers. We then discuss signal transduction methods with a primary focus on redox probe-based electrochemical sensing and transistor-based sensing.

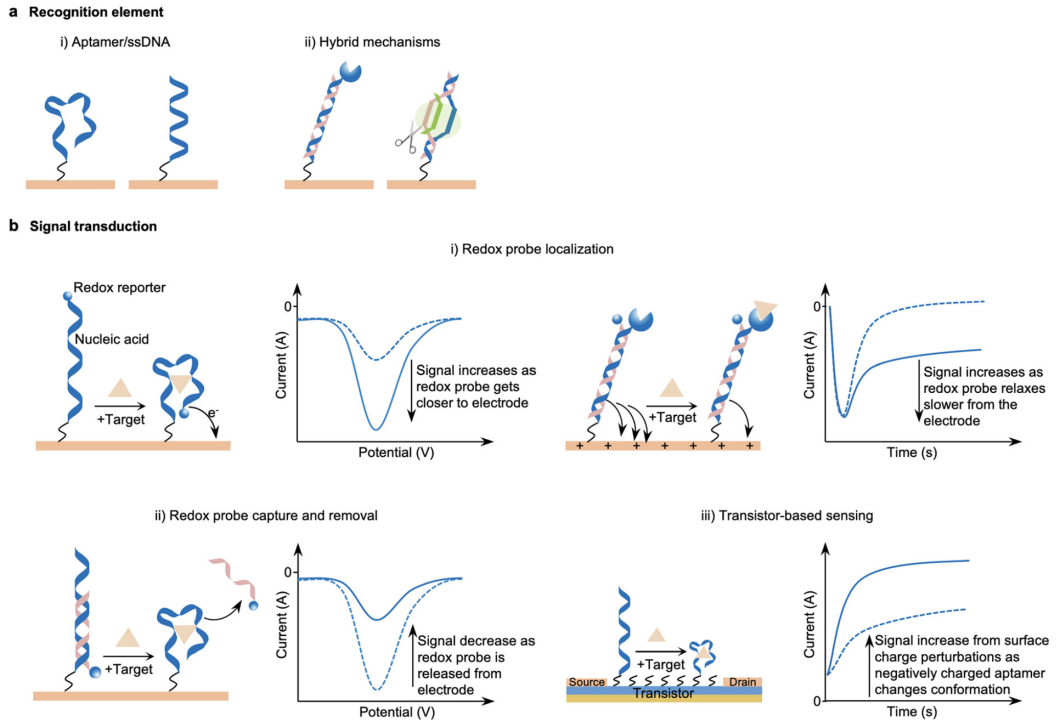


Figure 3.2: Nucleic acid-based implantable/wearable sensing strategies

(A) Classes of available nucleic acid-based recognition elements. (B) Signal transduction strategies, including redox probe localization, redox probe capture and removal, and transistor-based sensing.

### 3.1.1 Biorecognition

Nucleic acid sensing of genetic markers, cell-free DNA, and pathogenic DNA relies on direct binding of complementary DNA (cDNA) probes. Assuming sufficient target DNA is present for interaction (possibly requiring amplification), spontaneous and selective hybridization will occur. Nucleic acid biorecognition was improved upon with the introduction of self-hybridizing hairpin molecular beacons that transduce the precise recognition of complementary targets to a detectable signal.[18] The molecular beacon sensing scheme has served as a springboard for modern nucleic acid-based sensor designs. With the advancement of reproducible, high-throughput nucleic acid synthesis, nucleic acid binding capabilities have expanded to non-nucleic acid targets. We describe the key nucleic acid-based biorecognition elements that have been realized for wearable and implantable biochemical sensing. Our discussion focuses on aptamers and hybrid mechanisms, such as clustered regularly interspaced short palindromic repeats (CRISPR)-Cas systems and protein-coupled molecular pendulums.

**Aptamers**

The capability of nucleic acids to bind small ligands motivated the in vitro selection of single-stranded ribonucleic acid (RNA) and DNA oligonucleotides that bind to specific ligands.[19] This new class of nucleic acid binding species, termed aptamers, could bind a wide variety of molecular targets for therapeutic and diagnostic applications. Aptamers noncovalently interact with ions, small molecules, peptides, proteins, and hormones.[20] Like molecular beacons, aptamers undergo binding-induced conformational changes based on their self-hybridized hairpin structures.[21] The structure-switching behavior allows aptamers to also transduce the biorecognition event to an optical or electrochemical signal.

An in vitro method known as SELEX is widely used for aptamer discovery and selection of structure-switching aptamers.[21, 22, 23] In this method, a library of randomized RNA or DNA recognition sequences undergoes a variety of successive selection rounds to tune the selectivity and affinity of the aptamer to the target. The binding kinetics and signaling response is evaluated for the final selected sequences. This iterative process is highly customizable with alternative library designs and innovative selection rounds having the potential to produce a variety of structure-switching aptamers.[21]

Aptamer structure plays a significant role in the signal transduction and sensor design scheme. Aptamers are 20-100 nucleotides in length yet can form a variety of structures including duplexes, hairpins, and G-quadruplexes that are either stabilized or destabilized through noncovalent target interactions.[20, 24] Structure-switching classes of aptamers include stem-loop aptamers, split aptamers, strand-displacement aptamers, and triple-helix aptamers.[21, 25] Stem-loop aptamers are based on the molecular beacon designs with a hairpin structure stabilized by a self-hybridized stem region of optimal length.[21] Split aptamer designs cleave a target-binding sequence at non-binding loop regions to create fragments that only associate in the presence of the target. This design may help to preserve structural elements key to target binding, but it also presents the challenge of coordinating the target-specific assembly of multiple components. Strand-displacement aptamers involve a complementary cDNA strand that is initially hybridized to the aptamer. Upon binding of the target molecule to the aptamer, the cDNA strand is displaced, signaling the presence of the target. The triple-helix molecular switch involves a hairpin aptamer that is stabilized by an oligonucleotide sandwiched between the stem strands.[25] Similar to strand-displacement aptamers, the target-binding of the outer hairpin

results in dissociation from the sandwiched strand, which then participates in signal transduction. In any case, the aptamer design process requires thermodynamic optimization between the bound and unbound states that is adjusted for by the introduction of destabilizing mutations.[17, 21] Aptamers thus face a recurring challenge of bioreceptor design: the trade-off between affinity and dissociation, key factors in determining a biosensor's sensitivity and regeneration capability for repeated use.

### Hybrid Mechanisms

Programmable CRISPR-Cas gene editing techniques have demonstrated highly selective recognition of target nucleic acid sequences that may be adapted for biosensing. The hybrid system relies on guide RNA (gRNA) hybridization to a target sequence to activate Cas enzyme cleavage of the target DNA.[26] CRISPR-Cas DNA sensing surpasses the detection accuracy of hybridization-based electrochemical DNA sensors enabling point-mutation analysis. Electrochemical CRISPR (E-CRISPR) sensing is performed using an electrode functionalized with a redox-labeled cDNA strand which captures the target single stranded DNA (ssDNA). CRISPR-Cas9 and CRISPR-Cas12a systems are typically used to recognize the target sequence and cleave the cDNA strand releasing the redox probe from the electrode surface and producing a measurable change in the redox current.[26] E-CRISPR signal transduction has also been performed using a functionalized graphene field effect transistor.[27] E-CRISPR sensing enables ultrasensitive label-free detection of unamplified target genes and pathogenic DNA.[27, 28, 29] Combined aptamer-CRISPR systems allow for molecular detection beyond nucleic acids.[28] Due to their modular design and high accuracy, CRISPR-Cas sensors demonstrate great promise for wearable health monitoring.[30, 31]

DNA can also be coupled with traditional bioreceptors, such as antibodies, to form a hybrid molecular switch. Antibody-based assays for small molecule sensing are often competitive assays with multi-step labeling. Linked DNA scaffolds can be used to attach a molecular competitor within the vicinity of the antibody enabling continuous concentration-dependent competitive binding and fluorescent beacon signaling. Antibody-switches have been used to continuously sense cortisol and the cardiac glycoside digoxin in human blood.[32, 33] In a molecular pendulum design scheme, a DNA linker anchors the bioreceptor to the electrode surface and provides a means for signal transduction with a redox probe-labeled cDNA. This hybrid mechanism allows for high-affinity target binding at picomolar levels and

label-free signal transduction by exploiting the electrostatic properties of DNA. Molecular pendulum designs have been demonstrated using antibodies for a variety of targets including troponin I, B-type natriuretic peptide (BNP), interleukin-6, immunoglobulin E, and SARS-CoV-2 spike protein.[34, 35] Molecular pendulum designs utilizing aptamer recognition elements have also been demonstrated for BNP and N-terminal pro BNP (NT-proBNP).[36] With a modular biorecognition element, hybrid molecular switches expand the sensing capabilities of nucleic acid-based sensors to targets beyond nucleic acids and small molecules.

### 3.1.2 Signal Transduction

Nucleic acid sensing has traditionally relied on optical signal transduction methods. A fluorophore interacts with a quencher based on nucleic acid molecular interactions to produce a concentration-dependent fluorescent signal via fluorescence resonance energy transfer (FRET). Due to the simple signal transduction, molecular beacon fluorescence may be modulated in a variety of ways, including strand displacement, CRISPR-Cas cleavage, and aptamer structural switches. FRET quenching has played a significant role in aptamer beacon discovery, enabling the screening and selection of aptamer sequences with significant conformational changes upon molecular binding.[21, 22, 37] However, for wearable and implantable applications, optical systems face challenges in miniaturization and form factor in comparison to electrical systems. Fortunately, these optical techniques are easily translated to electrochemical methods by using redox moieties like methylene blue (MB) and ferrocene (Fc).[38] Additionally, nucleic acid-functionalized transistors act as both electrochemical transducers and amplifiers, further enhancing molecular detection capabilities. Here, we provide an overview of how nucleic acid-based biorecognition mechanisms are employed for transducing biomolecular binding events into measurable electrical signals.

#### Redox Probe Localization

For electrochemical signal transduction, the nucleic acid detection probe is often labeled with a redox moiety like MB to observe target-dependent changes in electron transfer. The electron transfer of a redox reporter can be manipulated by changing the distance of the reporter to the working electrode surface. Electrochemical aptamer-based (EAB) sensors utilize a redox moiety-labeled aptamer attached to the electrode surface to measure the target binding-induced conformational change.

The change in position of the redox probe can be interrogated using a variety of electrochemical techniques, including square wave voltammetry (SWV), cyclic voltammetry (CV), chronoamperometry (CA), intermittent pulse amperometry (IPA), and electrochemical impedance spectroscopy (EIS).[17, 39]

Amperometric techniques directly measure the current decay rate from the surface-tethered redox probes. In the folded state, the redox reporter moves closer to the surface and experiences a stronger electric field for accelerated electron transfer measured by a faster current decay rate. The time constant of the measured current is easily optimized for by overlaying chronoamperometric traces.[39] CA and IPA allow for rapid time-resolved measurements limited only by data acquisition rates.[40] A tobramycin EAB sensor response was demonstrated as fast as 2 ms using IPA interrogation.[39]

SWV is the most common method for EAB sensor interrogation. SWV potential scans result in a peak current at the reporter's redox potential. This technique is favored for its measurement sensitivity by limiting the nonfaradaic current contribution. A key SWV parameter for EAB measurement is the SWV frequency, which relates to the optimized time constant used in amperometric methods.[41] At high frequencies, fast electron transfer of probes close to the electrode surface is captured. At low frequencies, slow electron transfer of probes far from the electrode surface is captured. Depending on the SWV measurement frequency and binding dynamics of the aptamer probe, the current will vary logarithmically with target concentration in either a signal-off or signal-on manner. The SWV amplitude also requires optimization since reduction and oxidation rates of the redox reporter vary differentially between the bound and unbound states.[41]

The intrinsic electron transfer of the chosen redox moiety as an additional sensor design factor plays a significant role in maximizing the EAB signal response. Anthraquinone and Fc redox reporters exhibit slow and fast electron transfer, respectively, relative to MB, limiting these responses to either the signal-on or signal-off regime.[41] In contrast, MB-coupled aptamers often have a signal-off, nonresponsive, and signal-on SWV frequency, enabling normalization calculations to account for signal drift and batch variation.[42, 43]

For molecular pendulum signal transduction, the redox-labeled pendulum arm is manipulated using electrostatic attraction. When a positive potential is applied to the electrode, the negatively charged DNA linker bends toward the electrode surface. As the angle between the electrode and the pendulum arm decreases, the redox

probe at the terminus of the cDNA strand moves closer to the electrode surface and down the electric field gradient. By choosing a redox reporter that is oxidized at a positive potential, such as Fc, electron transfer by the redox reporter can be measured as current. While the DNA linker arm experiences an electrostatic force toward the electrode surface, the terminal biorecognition element contributes significantly to an opposing hydrodynamic drag force. Binding of the target analyte to the molecular pendulum only increases the drag and subsequent transit time toward the electrode surface. The transit time is then correlated to the current decay such that current measurements at a chosen time constant from a chronoamperometric trace are correlated with the target concentration. This technique maintains strong performance across different biofluids, such as blood, saliva, sweat, tears, and urine, despite changes in viscosity impacting the molecular pendulum transit time.[34] Rather, the signal transduction is significantly influenced by the size of the target. A prime example of this is in the molecular pendulum's ability to distinguish between free spike protein and a SARS-CoV-2 viral particle using the same anti-spike antibody molecular pendulum.[35] The molecular pendulum is thus a promising nucleic acid-based approach for ultrasensitive, label-free sensing of peptides and proteins.

**Redox Probe Capture and Removal**

Standard structure switching EAB sensors are limited in sensitivity by high background current and low transduction efficiency. The disadvantage of redox probe localization is that the signal response is low due to a non-zero background signal from redox probes maintained within proximity to the electrode surface. In contrast, redox probe capture and removal allows for clearly defined bound and unbound signal states, enhancing the signal response and dynamic range. This method is employed primarily by strand displacement switches and E-CRISPR. For strand displacement switches, the redox-labeled nucleic acid strand is not tethered to the electrode surface but is instead displaced during target-binding. As described previously, E-CRISPR sensors remove the redox probe by target-mediated Cas cleavage.

A strand-displacement aptamer sensor for estradiol achieved picomolar detection in sweat.[44] Target binding to an aptamer tethered at a biorecognition interface released the MB-conjugated cDNA, which was then captured by a tethered ssDNA at a parallel sensing electrode. This provides an indirect measure of the number of bound aptamer receptors. Since the aptamer is not the electrochemical probe, strand

displacement is a promising signal transduction method for aptamer sequences with strong target binding affinity that may not elicit a large conformational change.

### Transistor-Based Sensing

Biomolecular interactions may be amplified using transistor-based approaches for efficient signal transduction. The nonlinear signal response of transistors enables high sensitivity and a large dynamic range for target detection. In the case of field-effect transistor (FET) sensors, nucleic acid bioreceptors tethered to thin-film semiconductor channels alter the transconductance upon target binding, resulting in significant changes in the measured source-drain current. Aptamer-based FET designs have been demonstrated for a variety of charged, neutral, and zwitterionic target biomarkers.[45, 46, 47] The structure-switching aptamer redistributes surface charges as the negatively charged aptamer reorients closer to or away from the FET, thus changing the effective gate potential and source-drain current. Starting with a high transconductance is important to achieve a highly sensitive FET. Choosing a semiconductor with high electron mobility, such as indium oxide or graphene, enhances the intrinsic signal response. Additionally, interdigitating the source and drain electrodes increases the channel width, which increases the transconductance and the biorecognition area.[45] Although FETs have promising detection capabilities, fabrication challenges often lead to batch variation. Calibration methods may be used to help account for device-to-device variation.[46]

The Debye-length limitation requires that FET recognition events occur within the Debye length. A molecular electromechanical system (MolEMS) approach improved aptamer-FET sensing by using a rigid tetrahedral double-stranded DNA (dsDNA) base with a flexible ssDNA cantilever ending in an aptamer bioreceptor.[48] The aptamer in this setup has the flexibility to capture analytes beyond the Debye length, with an extension length of about 12 nm. Upon applying a negative gate potential, the cantilever was actuated toward the FET surface for FET detection within the Debye length. This technique demonstrated selective detection of proteins, small molecules, ions, and nucleic acids at sub-attomolar concentrations. Moreover, the tetrahedral base serves as an antifouling layer suppressing nonspecific adsorption to the FET channel.

In contrast to FETs, organic electrochemical transistors (OECTs) are easily patterned using a conducting polymer channel interfacing with the gate electrode by a

liquid electrolyte. Ease of fabrication allows OECTs to take on a variety of form factors to directly interface with biofluids for wearable and implantable sensing.[49, 50, 51] In this method, the binding of the target to the biorecognition element alters the gate current, which ultimately controls ion penetration into the volume of the polymer channel, typically made of poly(3,4ethylenedioxythiophene) doped with poly(styrene sulfonate) (PEDOT:PSS). Changes in the ion-modulated channel conductance are then measured as the source-drain current. OECTs have been demonstrated to amplify the electron transfer kinetics of redox-labeled aptamers attached to the gate electrode.[52, 53] Aptamer-based OECT transduction was optimized further by applying a pulsed square wave gate voltage sweep to better capture transient currents of the redox reporter.[51] Using gate and working electrodes of the same size, the OECT SWV signal amplifies the standard aptamer 3-electrode SWV signal by almost 200-fold. Also, relative OECT amplification increases as the channel size decreases, such that the signal is maintained in smaller devices. Pulsed aptamer-based OECT thus enables the miniaturization of EAB sensing.

To summarize, the modular design of nucleic acid-based sensors presents diverse biochemical sensing opportunities. The regeneration capabilities of some aptamers demonstrates their potential as continuous sensing bioreceptors.[17] Label-free signal transduction using redox probes or transistors allows for automatic detection and repeated interrogation. Additionally, nucleic acid-based signal transduction mechanisms employ few components, alluding to low-cost and facile fabrication for mass manufacturing. These characteristics make nucleic acid-based sensors highly translatable to wearable and implantable applications for continuous health monitoring.

## 3.2 Nucleic Acid-Based Wearable Sensors

Wearable biosensors have emerged as a progressive tool in the health and medical fields, offering the ability to continuously monitor physiological states in real-time through minimally invasive or noninvasive methods.[2, 12, 54, 55] These devices analyze biochemical markers present in alternative biofluids such as sweat, tears, saliva, and ISF, providing valuable health insights without the discomfort or complexity associated with traditional blood tests.[56] The adaptation of nucleic acid-based biosensor systems for use in wearable technologies presents innovative opportunities as well as unique design challenges.

Key considerations in the development of these wearable nucleic acid-based biosen-

sors include the stability of the nucleic acid components in diverse biofluids, the need for robust and reliable signal transduction mechanisms that function effectively in the wearable format, and the integration of data processing and communication technologies for real-time analysis and feedback.[12] Additionally, it is crucial that biomarkers present at lower concentrations in alternative biofluids are met with highly sensitive biosensors.[57] Wearable biosensors must be designed with user comfort and convenience in mind, ensuring that they are lightweight, flexible, and capable of performing continuous monitoring without interfering with daily activities. Addressing these challenges requires innovative materials science, bioengineering, and electronic design strategies to create wearable nucleic acid-based biosensors that are not only effective but also practical for everyday use. As we navigate these challenges, the potential for wearable biosensors to transform health monitoring and personalized medicine becomes increasingly tangible, promising a future where detailed physiological insights are seamlessly integrated into daily life.

### 3.2.1 Wearable Microneedle Sensors in ISF

Unlike subcutaneous implants, wearable microneedle patches offer a minimally invasive, painless method for the collection of ISF from the skin for post-sampling analysis or in situ real-time biosensing (Figure 3.3A).[58, 59] This innovative approach facilitates disease diagnosis and the monitoring of long-term drug pharmacokinetics through wearable devices.

The first use of microneedle EAB sensors for continuous molecular measurements was demonstrated in flow systems in vitro using single and multiplexed microneedle array configurations (Figure 3.3B).[60] Recent EAB microneedle implementations have fallen short in vivo sensing performance despite using complex and expensive microneedle fabrication methods. A robust gold nanoparticle (AuNP) coated microneedle coupled with an EAB biosensing patch (μNEAB-patch) was introduced for minimally invasive, continuous, and real-time monitoring of drug pharmacokinetics in ISF (Figure 3.3C).[61] Widely available clinical-grade needles optimized for dermal application are readily transformed with a single Au deposition step and aptamer coating to cost-effectively produce a high-quality working electrode for transdermal sensing. This simultaneously leverages the needle's sharpness for skin penetration and its conductivity for signal transduction. This approach enables the detection of a broad range of ISF analytes, particularly focusing on antibiotics with narrow therapeutic windows, demonstrating its potential for clinical applications in

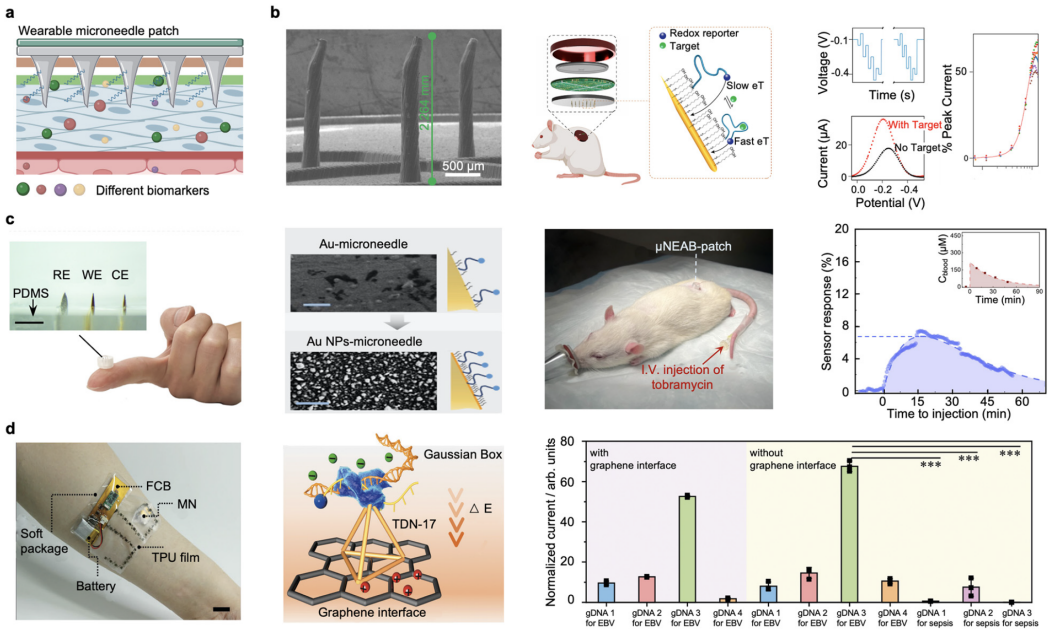


Figure 3.3: Nucleic acid-based wearable microneedle sensor in interstitial fluid

(A) Principle of wearable microneedle sensor. (B) Microneedle aptamer-based sensors for continuous, real-time therapeutic drug monitoring. [60] (C) Wearable microneedle-based electrochemical aptamer biosensing of various drugs with narrow therapeutic windows. [61] (D) Tetrahedral nanostructure-based *Natronobacterium gregoryi* Argonaute (NgAgo) for long-term stable monitoring of ultratrace unamplified nucleic acids. [62]

drug exposure monitoring through in vivo animal studies.[63, 64]

Apart from the small molecule analysis from ISF, a wearable device utilizing *Natronobacterium gregoryi* Argonaute (NgAgo) coupled with tetrahedral DNA nanostructures was demonstrated for the sensitive and long-term monitoring of unamplified nucleic acids in vivo, targeting applications like sepsis detection through a microneedle biosensor integrated with a flexible circuit and a stretchable epidermis patch (Figure 3.3D).[30, 62] Specifically, the in vivo experiments, exploring the NgAgo/guide DNA recognition mechanism and signal processing, demonstrate the device's capability for real-time monitoring of cell-free DNA and RNA with femtomolar sensitivity over 14 days, offering a new approach for on-body nucleic acid detection and personal health management.

Microneedle-based wearable sensors represent a pivotal innovation in the field of minimally invasive biosensing, enabling the real-time monitoring of ISF biomarkers for disease diagnosis and drug monitoring.[63] Despite their significant advantages over subcutaneous implants, including painless application and the ability to conduct post-sampling analysis or in situ biosensing, these devices face several operational

challenges that can impact their performance and reliability. One such challenge is the poor signal-to-noise ratio (SNR) encountered in some EAB microneedle sensors, which can obscure the detection of target analytes and reduce the accuracy of the measurements. Additionally, the degradation of the sensing layer during in vivo operation presents a critical hurdle, affecting the sensor's longevity and functionality. These issues are compounded by the complexity and cost of the fabrication processes required to construct these advanced biosensing platforms, posing barriers to widespread adoption and clinical integration.

Recent advancements in microneedle technology indeed offer solutions to some of these challenges by enhancing the stability and conductivity of the microneedles, thus facilitating stronger aptamer immobilization for accurate biomarker detection in vivo. However, ensuring consistent and reliable skin penetration without causing tissue damage, alongside maintaining the sensor's integrity and performance over extended periods, remains a significant concern. Moreover, expanding the range of detectable analytes, particularly for complex biomarkers like unamplified nucleic acids, introduces additional complexities in sensor design and signal processing. Nonetheless, advancing microneedle-based wearable sensors toward clinical application necessitates overcoming these operational challenges through continued innovation in materials science, sensor technology, and fabrication techniques, ensuring that these promising devices can fulfill their potential in personalized healthcare and disease management.

### 3.2.2 Wearable Sensors for Noninvasive Molecular Analysis

Since extracting diagnostically useful ISF at sufficient volumes is challenging, noninvasive wearable devices provide an alternative pathway to clinical diagnostics (Figure 3.4A).[12, 67] In contrast to minimally invasive wearable microneedle-based devices, noninvasive wearable chemical sensors using alternative body fluids, such as sweat, saliva, and tears, can provide real-time analysis that is difficult to achieve in typical laboratory blood analysis.[1, 11, 12, 68, 69] Due to their diverse biomarker compatibility and a modular design scheme, the nucleic acid-based wearable devices can be designed to perform multiplexed measurements of biochemical markers in real-time that would be transformative for diagnostics. These low-cost devices enable remote, at-home health monitoring with high-resolution and time-resolved electrochemical recordings informing physiological and psychological dynamics.

Accessible secretory fluids such as sweat, saliva, and tears are highly filtered from

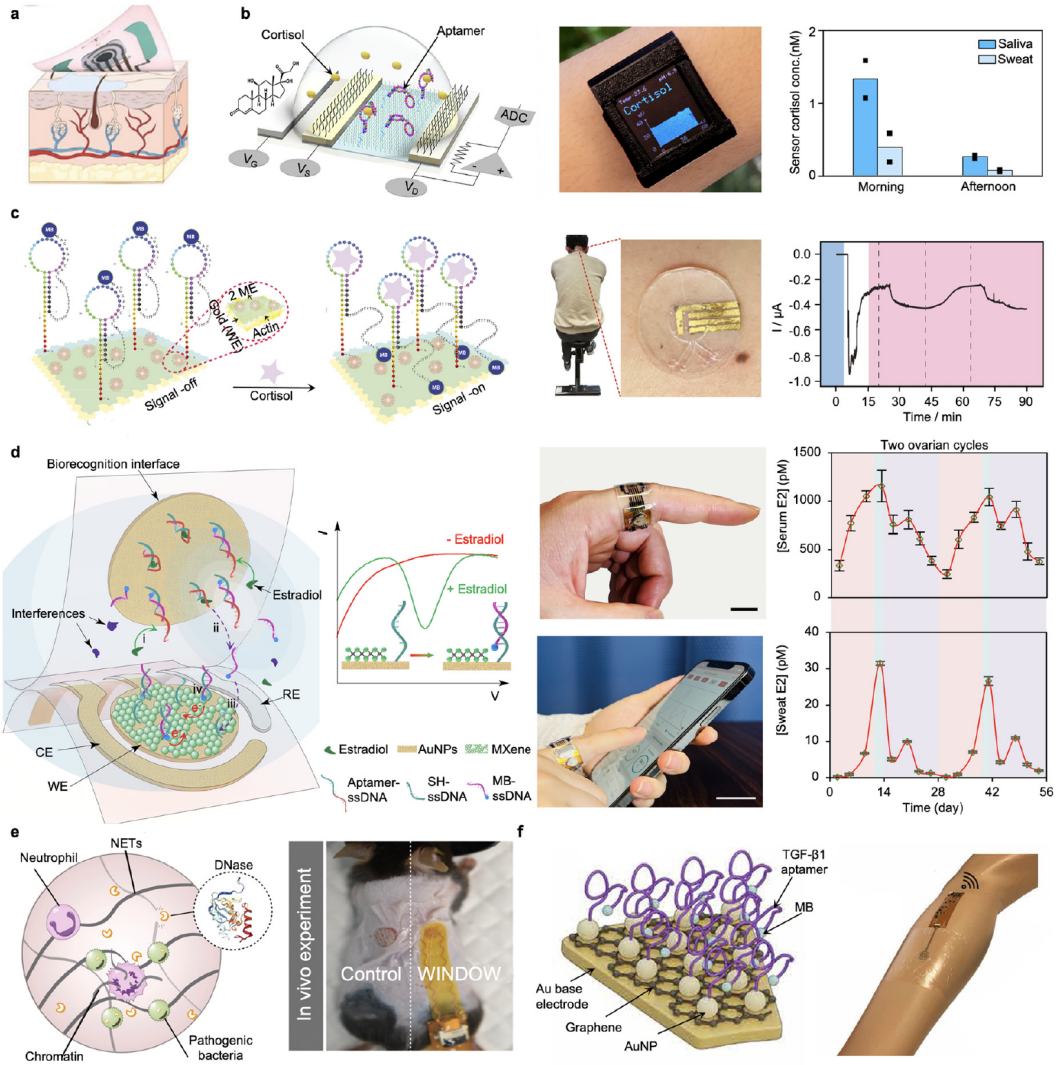


Figure 3.4: Nucleic acid-based wearable sensors for noninvasive molecular analysis

(A) Principle of noninvasive wearable sensor. (B) Wearable aptamer-field-effect transistor sensor for noninvasive cortisol monitoring. [46] (C) A noninvasive pseudoknot-assisted aptamer wearable stress patch for real-time cortisol measurement. [**singh_noninvasive_2023**] (D) Wearable aptamer nanobiosensor for noninvasive female hormone monitoring. [44] (E) A bacteria-responsive DNA hydrogel-based battery-free wearable sensor for wound infection monitoring. [65] (F) A multiplexed aptamer sensor array for in situ wound monitoring of inflammatory mediators and microbial proliferation. [66]

their blood and ISF origins, leading to substantially lower biomarker concentrations than in blood. toward this end, a flexible biosensor array utilizing a cortisol aptamer integrated with thin-film $In_2O_3$ FETs was reported for picomolar level cortisol detection (Figure 3.4B).[46] The study tracked salivary cortisol levels in stress test participants and correlated these with diurnal sweat samples, leading to the development of an aptamer-FET smartwatch for continuous, real-time monitor-

ing of cortisol. To meet the high demand for wearables mounted on the skin or integrated into clothing, the ultra-lightweight conductive nanofibers were electrospun to fabricate a liquid-ion gated FET on polyester for wearable cortisol aptamer sensing.[70]

Higher sensitivity and dynamic range may also be obtained by reducing the background current and improving the SNR of the sensor. EAB sensors typically rely on a conformation switch resulting in high background current due to the unclear position of the signal molecule in its unbound state. To improve upon this, a pseudoknot-assisted structure switching aptamer was implemented in a flexible electronic and soft microfluidic wearable platform for pH-calibrated, continuous, noninvasive cortisol monitoring in sweat (Figure 3.4C).[**singh_noninvasive_2023**] The pseudoknot tethers the redox reporter to the loop region of the unbound aptamer receptor, locking it in a distanced position from the electrode to minimize the background current. To address ultralow detection limits, unique redox probe capture and removal methods can be employed. A skin-interfaced wearable aptamer sensing platform was constructed using a target-induced strand displacement method, enabling noninvasive, in situ monitoring of female hormone levels in sweat (Figure 3.4D).[44] The sensing scheme is amplification-free and reagentless, and yet achieves a picomolar detection limit using a signal-on approach coupled with a AuNP-MXene modified working electrode. This comprehensive system can realize sweat analysis at rest autonomously via iontophoresis induction and microfluidic sample collection. Additionally, to support sweat matrix variability, the sensing platform conducts real-time calibration utilizing a multivariable analysis of pH, ionic strength, and temperature. The platform then wirelessly sends measured and processed sweat hormone data to a mobile device application for review. Such skin-conforming microfluidic nucleic acid-based sensors have great potential to help individuals monitor their health noninvasively at-home.

Wound infections represent a considerable clinical challenge, necessitating timely detection for effective intervention. Wireless wearable sensing technology enables direct wound interfacing for advanced, home-based detection and management of medical conditions.[71, 72, 73] A bacteria-responsive DNA hydrogel was used to fabricate the battery-free wearable sensor for wound infection monitoring on the basis of pathogenic nuclease activity (Figure 3.4E).[65] The sensor patch identifies clinical levels of *Staphylococcus aureus* before any visible signs of infection become apparent. Monitoring additional parameters in the wound bed can yield informed,

proactive treatment for improved wound management. However, existing sensing technologies can only track a limited number of wound parameters. A flexible and multiplexed biosensing platform was developed by integrating an aptameric sensor array for measuring inflammatory mediators and physicochemical parameters (Figure 3.4F).[66] This technology was demonstrated to enable in situ multiplexed wound monitoring in a mouse model and patients with venous leg ulcers. Its immense potential lies in personalizing wound management, thereby enhancing the healing outcomes of chronic wounds.

The advent of wearable biosensors for noninvasive monitoring of biomarkers in alternative biofluids, such as sweat, saliva, tears, and wound exudate, is a leap in diagnostics with transformative implications for personalized, at-home health monitoring. These needle-free devices offer a less intrusive alternative to traditional blood tests and ISF microneedles and enable the continuous tracking of physiological and psychological states in real-time. However, the operational challenges associated with working in alternative secretory fluids are significant and multifaceted, particularly when it comes to maintaining accuracy and reliability. Strain, temperature, pH, biofouling, and immune reactions under long-term use are critical factors that can affect sensor performance.[1, 2, 3, 4, 5, 6, 7, 16, 31, 59, 74] For example, the mechanical strain from daily movements can alter sensor readings, while temperature variations can affect the biochemical reactions that sensors rely on for biomarker detection. The pH of biofluids can also vary between individuals and over time, potentially impacting biosensor function. In the case of wearable technology for chronic wound management, significant challenges remain in their practical application. A smart dressing should maintain a moist environment to protect against secondary infections and promote tissue regeneration, while also absorbing and removing exudate from the wound.

Addressing these challenges requires innovative sensor design and materials science approaches to improve the resilience and adaptability of wearable biosensors. For instance, employing flexible, skin-like conductive materials that can conform to the wearer's movements and resist biofouling, alongside integrating microfluidic systems for sweat analysis that are calibrated for pH and temperature, can enhance sensor accuracy. For chronic non-healing wounds, a highly breathable, wearable smart dressing would shield the wound bed from bacterial infiltration and monitor for infection risk for early intervention. Furthermore, the development of signal-on detection mechanisms minimizing background current and boosting sensitivity

showcases the importance of engineering solutions to biochemical challenges in wearable sensor design. As research and development in wearable biosensors advance, overcoming the operational challenges will enable these technologies to fully realize their potential, ushering in a new era of healthcare monitoring and personalized medicine.

## 3.3 Nucleic Acid-Based Implantable Sensors

Implantable medical devices are pivotal in modern healthcare, providing essential diagnostic, therapeutic, and regenerative functions across various clinical applications such as drug delivery, vital signs monitoring, and tissue repair.[75, 76, 77] Among these, nucleic acid-based implantable sensors stand out for their ability to offer real-time, reagent-free sensing of biomarkers through affinity-based molecular detection. These devices are designed with biocompatible housings, detection systems employing electrochemical or optical methods, and advanced communication interfaces for seamless data transmission.[78, 79] Material selection plays a critical role in the development of implantable sensors, particularly when leveraging affinity probes such as nucleic acid-based recognition elements for the selective detection of neurochemical markers and circulating biomarkers.[80, 81] The choice of materials is guided by the need for biocompatibility, ensuring that the sensors not only integrate seamlessly into the body's physiological environment without eliciting significant inflammatory responses but also maintain their functional integrity over time. Biocompatible materials, including polymers, metals, silicon, and their composites, are engineered to mimic the mechanical properties of native tissues and be biochemically inert to prevent an immune response and fouling, all toward facilitating accurate and stable sensing capabilities.[82] This engineering approach enables the deployment of implantable sensors that can monitor a variety of molecular targets directly within the cerebrospinal fluid (CSF) or through intravenous and subcutaneous routes for the analysis of biomarkers in blood and ISF.[11, 79] By integrating nucleic acid-based recognition elements, these sensors offer the selectivity needed for the detection of specific neurotransmitters and circulating biomarkers, enhancing our ability to diagnose and monitor neurological conditions and systemic diseases.

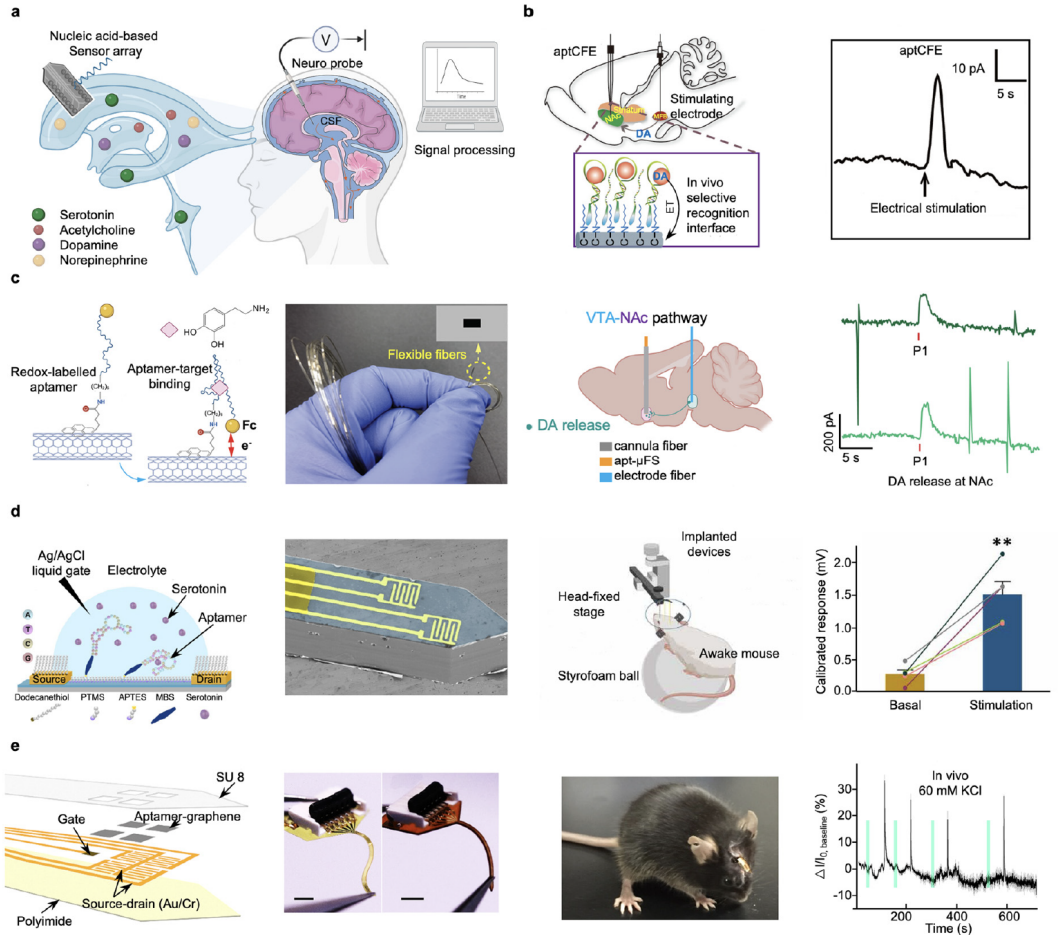


Figure 3.5: Nucleic acid-based implantable neurochemical sensing

(A) Principle of implantable neurochemical sensing. (B) Aptamer cholesterol amphiphiles on the alkyl chain-functionalized carbon fiber microelectrodes for probing neurochemical dynamics. [83] (C) Aptamer-coupled microelectrode fiber sensor for in vivo dopamine detection. [84] (D) Flexible and implantable neuroprobes with aptamer-field-effect transistor biosensors for neurotransmitter monitoring. [85] (E) Soft implantable aptamer-graphene microtransistor probe for real-time monitoring of neurochemical release. [86]

### 3.3.1 Implantable Neurochemical Sensing

Nucleic acid-based implantable neurochemical sensors represent a critical approach in neurological monitoring and nervous system signaling. Utilizing the unique properties of nucleic acids, particularly aptamers, these sensors offer a highly selective and sensitive method for detecting and quantifying neurochemicals in real-time (Figure 3.5A).[87] The levels of neurochemicals in the extracellular fluid are crucial for studying brain functions. However, monitoring these levels is challenging due to the chemical and physiological complexity of the central nervous system (CNS).[10] A variety of synthetic aptamers have been designed to bind neurotransmitters and

other neurologically relevant molecules, making them ideal for continuous sensing applications.[88] This provides an invaluable tool for the continuous monitoring of neurochemical biomarkers, essential for understanding normal neural function, diagnosing neurological disorders, and evaluating the efficacy of treatments. For instance, monitoring fluctuations in neurotransmitters such as dopamine and serotonin provides insights into various psychiatric and neurodegenerative conditions, including depression, schizophrenia, Parkinson's, and Alzheimer's disease.[89]

The conventional use of rigid materials in implantable electrodes can induce adverse tissue responses that compromise sensor functionality. Traditional implantable electrodes, such as early neuroprobes, are made from rigid materials like silicon or metal, which significantly differ in stiffness compared to biological tissues.[88] For instance, silicon's stiffness is around 200 GPa, which is in stark contrast with the brain tissue's softness, measured at roughly 10 kPa.[90] This vast discrepancy in Young's modulus triggers immune reactions and the formation of glial scars, greatly impacting the biosensor performance. The immune reactions can cause signal degradation due to biofouling, while scar tissue formation can reduce the precision and sensitivity of the device over time by obstructing the interaction between the sensor surface and the surrounding tissue.[**zou_antifouling_2021**] However, recent advances in soft and flexible electronics offer promising solutions to these challenges, suggesting a way forward for improving implantable sensor performance.

A strategy for interfacing aptamers with carbon fiber microelectrodes (CFEs) was developed to create highly selective systems for dopamine (DA) sensing in vivo (Figure 3.5B).[83] An interfacial functionalization strategy was applied to assemble aptamer cholesterol amphiphiles (aptCAs) onto alkyl chain-functionalized CFE surfaces through noncovalent interactions, enabling aptamer immobilization on the CFE surface and neurotransmitter recognition with high sensitivity. The integration of high-affinity aptamers into these platforms marks a significant advancement by addressing the issue of nonspecific binding that hampers clinical translation. A flexible and multifunctional polymer-based fiber microelectrode was modified with Fc-tagged aptamers for highly selective DA detection, where the redox reaction of Fc serves as an indicator and signal output based on the target binding-induced aptamer conformation change (Figure 3.5C).[84] The study demonstrated the potential of fiber-based toolsets for multimodal exploration of brain pathophysiology, showing how these sensors can provide valuable insights into the neurochemical basis of neurological conditions.

Implantable aptamer-functionalized $In_2O_3$ FET neuroprobes were fabricated by high-throughput microelectromechanical system (MEMS) technologies (Figure 3.5D).[85] Thiol-terminated aptamers designed for specific target recognition are attached to semiconductor surfaces of FETs, where conformational changes upon target capture lead to surface charge redistribution. This change can be detected by the voltage-gated semiconductor, thus aptamer-FET neuroprobes enable femtomolar serotonin measurement in brain tissue with minimal biofouling. Despite the necessity for flexible devices for neurotransmitter monitoring, the Young's moduli of many flexible substrates (such as PET) remain significantly higher than that of brain tissue. A viable approach is to make these materials thinner, since the bending stiffness is proportional to the cube of thickness following a rectangular beam geometry. Polyimide devices with thicknesses <10 μm have been shown to have optimal bending stiffness and conformal contact with tissue. The neuroprobe, incorporating an aptamer FET, was employed to develop a flexible and implantable sensor for monitoring DA, one of the small neurotransmitter molecules (Figure 3.5E).[86] Aptamer configuration switching occurred via the recognition between aptamer and target DA, resulting in the augment of source-drain current due to p-doping effect on the graphene channel. Compared with $In_2O_3$-based FET neuroprobes, a graphene-based microtransistor is a three-terminal electronic device because graphene can act as a channel material between the source and drain terminals. As graphene offers much higher charge mobility compared with $In_2O_3$, graphene-based FET neuroprobes are capable of good sensing performance. Graphene also has good biocompatibility and chemical inertness ideal for in vivo applications. An implantable sensing platform was established for real-time serotonin monitoring using a aptamer-graphene microtransistor probe that can capture DA release in vivo selectively and sensitively.[81, 91]

Overall, nucleic acid-based implantable sensors for neurochemical detection mark a significant advancement in neuroscience, offering a path to real-time monitoring of critical neurotransmitters like dopamine and serotonin. Despite their high selectivity and sensitivity enabled by aptamer technology, these sensors face operational challenges such as the mismatch in mechanical properties between traditional rigid sensor materials and soft brain tissue, which can trigger immune responses and scar tissue formation, impairing sensor functionality over time. Recent developments in flexible and soft electronics are addressing these challenges, with innovations such as carbon fiber microelectrodes and polymer-based fibers that are more compatible with brain tissue. However, ensuring stable nucleic acid immobilization on these flexible substrates remains a hurdle. Addressing these operational challenges

will help drive the clinical translation of nucleic acid-based implantable sensors interfacing with the brain and other organs throughout the body.

### 3.3.2 Implantable Sensing of Circulating Biomarkers

Circulating biomarkers in the blood and ISF are of paramount importance for personalized healthcare. These biomarkers including drugs, metabolites, hormones, and proteins offer a window into the body's physiological and pathological states.[92, 93, 94, 95] Their detection and quantification can provide critical insights into an individual's health status, enabling early diagnosis of diseases, monitoring of disease progression, and evaluation of treatment responses (Figure 3.6A). Circulating biomarkers in the blood can indicate a wide range of conditions, from cardiovascular diseases and cancer to inflammatory and neurodegenerative disorders. In addition to circulating biomarkers that filter from blood into ISF, localized ISF biomarkers can reveal surrounding tissue health and metabolic processes. The ability to accurately monitor these biomarkers presents vast possibilities for preventive medicine, tailored treatment plans, and real-time tracking of health outcomes, making it a cornerstone of personalized medicine.[14, 96, 97]

Real-time therapeutic drug monitoring is pivotal for personalized dosing, tailoring treatment to the unique metabolic profiles of individual patients. Regrettably, there is only a limited number of targets that can be continuously measured in real-time, i.e., oxygen, lactose, glucose. Addressing this limitation, the microfluidic electrochemical detector for in vivo continuous monitoring (MEDIC) was introduced.[98] This device's modularity allows for the reagentless monitoring of a diverse array of molecules by simply swapping out aptamers, thus broadening the applications for continuous drug monitoring. Intravenous EAB sensors were evaluated for the continuous, real-time monitoring of multiple circulating drugs, including aminoglycoside antibiotics and the chemotherapeutic doxorubicin, in a rat model (Figure 3.6B).[99] The EAB sensor scheme was further employed for vancomycin, a drug with a narrow therapeutic window challenged by individual metabolic variations, where they successfully demonstrated feedback-controlled drug delivery.[100] In parallel, to focus on the tumor microenvironment, a microelectrode sensor array was utilized to directly measure drug levels within tumor sites in rodents.[101] Additionally, to address the fouling related signal drift, biocompatible agarose gel was utilized as a protective layer to fabricate the gel-protective implantable EAB sensor for in vivo real-time drug analysis.[102] This innovative approach offers critical in-

sights into drug distribution challenges within tumors, such as irregular blood flow and cellular density, potentially influencing the efficacy of cancer treatments.

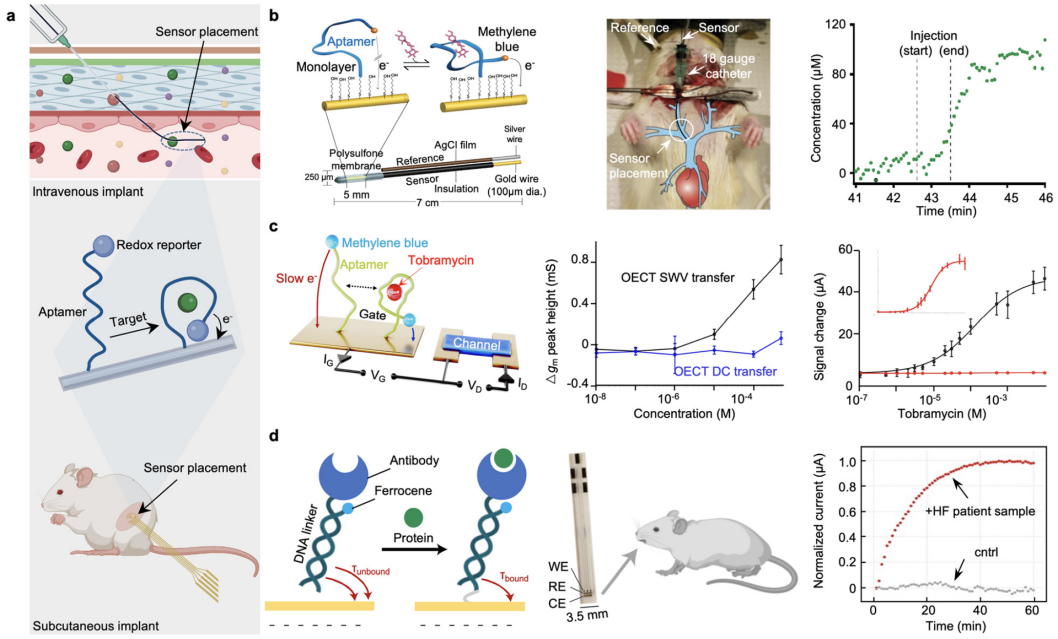


Figure 3.6: Nucleic acid-based implantable sensing of circulating biomarkers

(A) Principle of implantable sensing of circulating biomarkers. (B) Electrochemical aptamer-based sensors for real-time measurement of therapeutic drugs in the bloodstream. [99] (C) Square wave gate potential profiles support high-gain aptamer-based organic electrochemical transistor sensing. [51] (D) Reagentless biomolecular analysis using a molecular pendulum. [34, 36]

As discussed previously, nucleic acid-based transistor designs provide simultaneous signal transduction and amplification, a notable advancement over conventional electrode-based sensors. An aptamer-based OECT applied a square wave potential across its aptamer-decorated gate electrode to achieve a level of current modulation in the transistor channel surpassing that of traditional transistor interrogation (Figure 3.6C).[51] The OECT design demonstrated signal amplification in whole blood and, upon miniaturization, enabled potential future application in implantable sensors. The authors postulate that signal amplification by OECT may also extend the operation life of the sensor since signal degradation of nucleic acid-based sensors remains a challenge for the field. Beyond circulatory measurements, miniaturized OECT arrays may be the future of biochemical sensing for high-resolution spatial measurements at the brain and muscle tissue interface.

Building on these technological strides, the quest for creating sensors capable of identifying molecular analytes in biological fluids without external reagents have

opened new frontiers in personalized health monitoring. However, the diversity of molecular targets detectable by such reagentless sensors has been limited until now. Addressing this, a reagentless sensing technique was introduced that leverages the movement of a molecular structure, reminiscent of an inverted pendulum, whose motion is influenced by an electric field in response to the binding of an analyte (Figure 3.6D).[34, 36] This technique assesses the sensor's movement by analyzing the electron transfer rates to an indicator molecule, utilizing time-sensitive electrochemical analysis to monitor the sensor's unique motion. This allows for the continuous, real-time detection of a wide range of analytes, demonstrating compatibility with various biological fluids such as blood, saliva, urine, tears, and sweat, thereby enabling data collection directly within living organisms. Blood has been a primary biofluid for sampling in the lab and at-home and is the standard biofluid for biosensor in vitro validation and testing. Synthetic nucleic acid-based bioreceptors can be tuned to be highly selective for their target, and membrane coatings and surface chemistry can also be used to prevent nonspecific binding and adsorption. Measurements in filtered biofluids such as ISF and sweat avoid some of these challenges, but typically at the cost of lower target concentrations.

As nucleic acid-based sensors are implanted intravenously for continuous operation, the challenges of operation under continuous and variable blood flow are presented. Implantable sensors for circulating biomarker quantification must contend with the dynamic nature of blood and ISF, which can be influenced by hydration levels, blood pressure, and other systemic factors. Additionally, the integration of these sensors into the cardiovascular or lymphatic systems introduces risks associated with blood clotting and embolism. Therefore, the materials and the sensor's surface properties must be meticulously designed, like robust anchoring mechanisms that do not compromise the integrity or functionality of surrounding tissues to avoid triggering any adverse vascular responses. Moreover, to protect sensors from fouling, various methods are utilized to effectively prevent signal degradation in biological environments. These advancements enable promising prospects for long-term in vivo monitoring applications.

Overall, the development of implantable sensors requires addressing a complex array of challenges. These include ensuring accurate biomarker detection across a wide range of concentrations, maintaining sensor stability and calibration in a dynamic systemic environment, mitigating risks associated with sensor site implantation, and designing robust sensors without inducing an adverse foreign body reaction. Despite

recent advancements in nucleic acid-based sensors, the quest for implantable probes that can provide continuous, real-time data on a wide array of circulating biomarkers with minimal operational challenges remains ongoing, underscoring the need for continued research and development in this critical area of personalized medicine.

### 3.4 Design Considerations Toward Continuous in situ Biomarker Analysis

The primary objective driving the development of wearable and implantable sensors is to enable the continuous monitoring of biomarkers within body fluids. Successful and robust measurement of molecular biomarkers is challenging for several reasons, including the intricacies of multi-step bioaffinity assays, sensor regeneration, sensor stability, gradual biofouling of sensor surfaces, efficient transport of samples over the sensor, and calibration issues specific to on-body sensing. In this section, we will

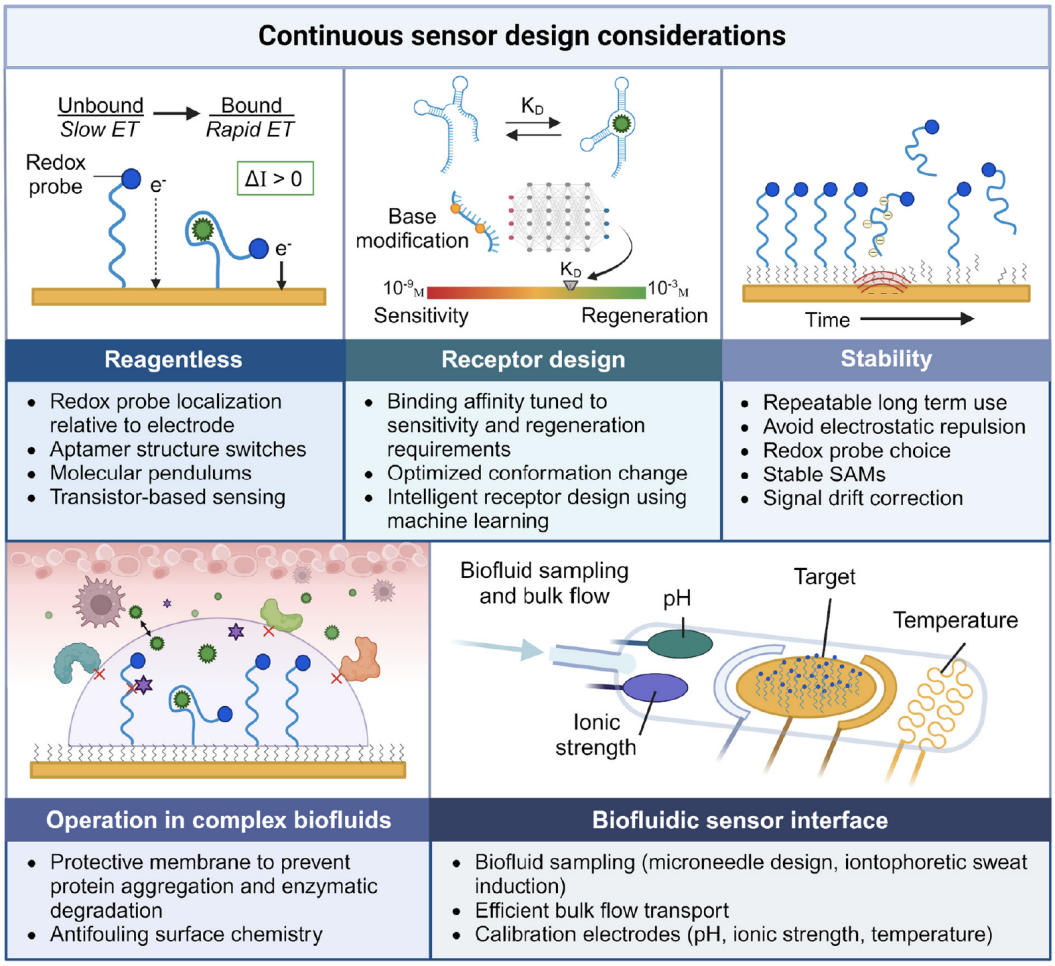


Figure 3.7: Design considerations toward continuous, in situ, and real-time molecular analysis

introduce the challenges associated with various systems and biofluids and discuss potential solutions and guidelines for the design of next-generation nucleic acid-based wearable and implantable biosensors (Figure 3.7). We will provide insights into future research directions and the promising prospects within this dynamic research field toward seamless, continuous monitoring of biomarkers in situ.

### 3.4.1 Reagentless Real-Time Sensing of Ultralow-Level Biomarkers

Given that strategies designed for externally added reporter molecules may not be compatible with on-body based biomolecular sensing, we focus on reagentless sensing approaches aimed at sequential real-time monitoring of ultralow-level biomarkers. Ideal reagentless sensing seamlessly integrates the biorecognition event with signal transduction. Redox reporter-labeled aptamers undergo a binding-induced conformational change that alters the detected electron transfer rate. Redox reporter-labeled molecular pendulums exhibit changes in the detected electron transfer rate due to the drag force elicited by target binding. Selective molecular binding at the surface of the transistor gate redistributes surface charges amplified to a measurable source-drain current. These modular design schemes provide a basis for reagentless nucleic acid-based sensing.

Conventional nucleic acid-based sensor designs involving a redox reporter have relied on dual-frequency SWV measurements, which have been found to limit the time resolution of the sensor to approximately 6 to 22 s.[103] To accelerate electrochemical interrogation and further approach real-time sensing, fast Fourier transform electrochemical impedance spectroscopy (FFT-EIS) was used.[103] FFT-EIS simultaneously captures the impedance at multiple frequencies in under 2 s to evaluate the electron transfer rate without the need for individual sensor calibration and drift correction. This finding emphasizes the need for ongoing exploration of analytical electrochemistry techniques in the biosensor space.

Transient circulating metabolites and trace biomarkers require ultrasensitive detection by implantable sensors. Additionally, noninvasive wearable sensing in peripheral biofluids often requires biomarker detection at low concentrations relative to blood.[11, 12] Nucleic acid-based sensors have demonstrated excellent sensitivity in a variety of biofluids. Beyond the nucleic acid binding scheme, high efficiency electron transfer is key to the performance of the sensor. Nanostructured materials with high electroactive surface areas and charge carrier mobility improve the electrochemical sensor's SNR.[104] The presence of nanopores reduces the impact

of charge screening, thus reducing Debye length limitations and enhancing signal gain.[105] Nanostructured gold electrodes for high-performance nucleic acid-based sensors have been fabricated using a variety of methods, including inkjet printing of AuNPs, deposition of Au nanowire-polymer nanocomposites, electrodeposition of 3D Au nanostructures, electrochemical roughening, and selective etching of cosputtered Au alloys to form nanoporous Au.[36, 44, 105, 106, 107] Graphene among other semiconductor nanomaterials has also been exploited for its exceptional conductivity, flexibility, and biocompatibility, with many implementations in nucleic acid-based transistors.[27, 30, 48, 86, 108, 109] MXene composites may further enhance electrode performance through the incorporation of transition metals and electrode modification with reactive functional groups.[44]

Signal amplification methods may also be used to detect ultralow-level biomarkers in real-time. Transistor-based sensors allow for ultrasensitive detection due to the signal amplification of the biorecognition event.[14] Enzymatic signal amplification has also recently been explored through the use of DNA aptamer-enzyme complexes.[110] Ultimately, sensitivity is limited to the affinity of the biorecognition element. This presents a key challenge in reagentless real-time biosensing of balancing high-affinity ligand binding with bioreceptor autoregeneration.

### 3.4.2 Bioreceptor Design Toward Continuous Monitoring

Nucleic acid receptor sequences are often selected using SELEX, which favors the selection of high-affinity receptors for optimal sensitivity and selectivity. However, for continuous sensing, reversible binding is necessary to capture fluctuating target concentrations. An apparent trade-off exists between receptor sensitivity and regeneration. Here, we deliberate on nucleic acid receptor sequence design according to dissociation kinetics.

Biochemical strategies to tune the nucleic acid dynamic range include sequence mutations, structural changes, and allosteric inhibition.[111, 112] Taking a high-affinity aptamer, the aptamer's bound state can be destabilized by making nucleotide substitutions, shortening the length of the terminal stem, and using a circular permutation of the sequence.[111] Intramolecular strand-displacement switch design was presented as a strategy to decouple aptamer thermodynamics and kinetics in an effort to tune the temporal resolution of the aptamer without reducing the effective binding affinity.[112] In this method, the native aptamer sequence is extended to a stem-loop structure with a poly-T linker and complementary displacement strand

with fluorophore-quencher interactions informing target binding during stem-loop unfolding. Loop length, displacement strand length, and base-mismatch mutations were then used to tune the aptamer binding kinetics. Engineering aptamer dissociation kinetics via mutagenesis is difficult since the three-dimensional structure of aptamers is often unknown. Additionally, mutagenesis may result in changes in the specificity of the bioreceptor. To obviate changing the aptamer sequence, allosteric inhibition was explored to alter binding dynamics.[111] Oligonucleotide inhibitor strands bind to portions of the aptamer to stabilize the nonbinding configuration. This competitive binding between the oligonucleotide inhibitor and the target is easily optimized by tuning the concentration and complementary sequence length.

Machine learning has enabled in silico aptamer discovery. A machine learning-guided particle display methodology was developed to generate libraries of high-affinity aptamers against a chosen target and furthermore truncate aptamer sequences while maintaining the affinity.[113] This methodology led to more and higher quality aptamer candidates. Another approach to aptamer discovery emphasized overall secondary structure by using a sequential multidimensional analysis algorithm for aptamer discovery from high-throughput SELEX pool sequencing data.[114] The algorithm evaluated motif and substructure patterns, aptamer family abundance, and secondary structure stability. Integrating algorithmic tuning of aptamer features into parallelized SELEX workflow can rapidly accelerate aptamer generation and selection to a matter of days.[115] Future multi-parameter machine learning models may allow for the simultaneous optimization of aptamer characteristics such as affinity, specificity, dissociation kinetics, structure, and stability, beyond current experimental capabilities. Advances in machine learning have also enhanced our working understanding of nucleic acid receptors via simulations for molecular docking and binding dynamics.[116, 117, 118] One challenge in engineering aptamer designs is in identifying the ligand-bound nucleic acid conformation, since the most thermodynamically stable conformation is not always in agreement with the highest affinity interaction.[**oliveira_modeling_2022**]

Molecular docking simulations have allowed for the identification of metastable structures leading to more accurate aptamer-target binding interaction predictions.[117] By understanding target binding interactions, we may rationally fine-tune nucleic acid receptor designs. The goal dynamic range for in situ sensing applications as well as the temporal resolution must be considered when engineering nucleic acid receptors for continuous biosensing. Further, oligonucleotide length, mismatched

bases, and structure should also be examined to optimize the signal transduction of nucleic acid-based sensing schemes. While in silico modeling has enhanced aptamer discovery and conformation predictions, future work is needed to experimentally characterize aptamer structures and better understand nucleic acid-target interactions. Development of nucleic acid characterization techniques will help to validate predictive machine learning models.

### 3.4.3 Sensor Stability

Sensor stability is a key characteristic for accurate continuous sensor measurements. Stability of wearable and implantable biosensors may be impacted by several factors including chemical stability of redox reporters, self-assembled monolayer (SAM) degradation, voltage-induced desorption of receptor elements, and biofouling.[119, 120, 121] Signal drift can be mitigated through thoughtful sensor design choices as well as algorithmic corrections. Developing stable nucleic acid-based sensors will be necessary for the translation of these sensors to implantable devices for long-term use.

A major design consideration for many electrochemical nucleic acid-based sensors is the choice of redox probe for enhanced electron transfer rate, signal quality, and stability. One of the most common redox reporters in the literature is MB, and for good reason, since MB demonstrates exceptional stability over time, under repeated voltametric interrogation, and under repeated nucleic acid sensor target regeneration.[121] MB also has a redox peak around -0.26V, which is well below the redox potential for common conductive substrates, ensuring high SNR. However, the negative potential window of MB is a disadvantage for negatively charged nucleic acid-based sensors, due to voltage-induced repulsion and desorption. Stability experiments demonstrate that the more negative bias potential exposure the nucleic acid-based sensor experiences (e.g., low SWV frequency, high measurement frequency), the more the signal decays.[119] This suggests that redox reporters with a positive redox potential, such as a Fc derivative, merit further investigation for long term sensor stability.

Electrochemical nucleic acid-based sensors are often functionalized relying on solution-based processing to generate SAMs on the surface of electrode substrates, which ensures the uniformity of the DNA layer. The volume of the solution used for forming SAMs does not significantly impact the process. By utilizing uniform lengths of DNA, the thickness of the nucleic acid layer can be precisely controlled,

allowing for a consistent detection layer thickness and the formation of fine-sized sensor patterns.[122, 123] In contrast, drop casting techniques, widely used in electrochemical sensing, often suffer from issues such as the coffee ring effect, which can alter the distribution of enzymes drop-cast onto an electrode. Unlike the manual drop casting of enzyme films, the solution modification process for creating SAMs yields higher reproducibility, thereby reducing variability in sensor performance. This enhanced reproducibility is crucial for the reliable detection of chemical biomarkers, making SAMs a superior alternative for precise and consistent sensor fabrication.[124]

Passivation by alkylthiolate chains supports the alignment of the nucleic acid monolayer and prevents nonspecific redox reactions at the gold surface. These monolayers must withstand repetitive voltage perturbations as well as prolonged biofluid interactions. Ongoing work to improve upon the standard of mercaptohexanol has prioritized gold binding interactions and enhanced lateral van der Waals interactions between monolayer molecules.[125] Increasing the alkylthiolate length by two methylene groups demonstrated improved week-long stability at 37 °C.[125] Longer monolayer alkylthiolate chains may improve stability but at the cost of reduced electron transfer kinetics.[41] Crosslinking monolayers also increases the strength of the interactions between monolayer molecules to limit desorption susceptibility.[126] SAM stability may additionally be enhanced using multidentate anchoring groups to increase attachment points to the electrode surface.[126] The oxidation of thiol-based monolayers to disulfide dimers contributes to monolayer instability. Performing electrochemical scans in a negative potential range, while bad for the nucleic acid receptor, may actually suppress oxidation of alkylthiolate monolayers.[125] N-Heterocyclic carbenes have recently been explored as an alternative to thiol-based monolayers with strong affinity to gold, robust monolayer stability, and efficient bioconjugation chemistry. However, N-heterocyclic carbene monolayers were found to desorb at voltages less than -0.1V and above 0.25V, thus limiting the potential scanning range for redox reporters.[127] Continued work is needed to explore new alternative passivation layers that promote long-term sensor stability in biofluids.

Beyond sensor design, signal drift can also be corrected for algorithmically, current methods including dual frequency measurements and ratiometric self-calibration. Aptamer-based sensors exhibit SWV frequency-dependent behavior. If the aptamer exhibits a concentration-independent signal response at a nonresponsive frequency,

ratiometric corrections may be used to self-calibrate sensors, reducing interelectrode variability and correcting for drift.[43, 128] For aptamers that exhibit a signal-on and a signal-off domain, the kinetic differential measurement (KDM) may be used to enhance the SNR and correct for signal drift assuming these two measurements exhibit matching background responses.[42, 98] The KDM signal is obtained by taking the difference between the signal-on and signal-off SWV peak current measurements divided by their average. These algorithmic corrections require careful optimization of the SWV frequency, which varies between aptamers with structure and electron transfer kinetics.

Alternatively, internal controls may be incorporated into the sensor design for ratiometric self-calibration. Interrogating the response of a target-sensitive nucleic acid sequence and a non-binding oligonucleotide strand in either a dual-electrode or single-electrode system may inform the nucleic acid sensor's degradation over time. A ratiometric electrochemical aptasensor was designed to self-calibrate based on the combined signal from a Fc-labeled aptamer and a Fc-labeled DNA hybridized to the same template strand.[129] This technique demonstrated a more stable response under varying temperature and pH conditions than conventional EABs. Dual-aptamer measurements have been studied to improve stability by screening for and selecting aptamers with similar drifts.[130] Differential signal responses for self-calibration can also be achieved with adjustment of the redox reporter position or use of a secondary intercalated redox reporter.[130, 131]

While these "self-calibration" techniques offer methods to correct for signal drift, they are a temporary fix to the stability problem of nucleic acid sensors. Current drift correction techniques lack generalizability across nucleic acid sensors with significant optimization required between sensors of different targets. Additionally, these techniques often require two SWV scans for a single measurement, thus reducing the time resolution and potentially accelerating sensor degradation. Future work is needed to further enhance the stability of nucleic acid-based sensors through rational design of redox reporters and stable electrode functionalization. We next discuss how stability is one of many issues exacerbated by operation in biofluids. The importance of in vivo long-term stability requires that implanted sensors overcome biocompatibility challenges.

### 3.4.4 Operation in Complex Biofluids

Sensor operation in complex biofluids introduces challenges of high protein and cellular content, and variable media conditions (pH, ionic strength, temperature, interferents, etc.). Surface fouling is a major concern for any bioelectronic interface. When biomolecules in the sampled biofluid adsorb on the electrode surface, electron mobility is disrupted, impacting the signal transduction of the sensor. Fouling-induced desorption of sensor elements has been found to be a primary source of signal degradation of nucleic acid-based sensors in biological fluids.[120, 125, 132] Antifouling design considerations to enhance sensor stability in biofluids are described, including the use of porous membranes, hydrogel encapsulation, polymer coatings, SAMs, and nanoporous conductive substrates. Considering that body fluid compositions may vary intra- and inter-individually, we introduce methods to improve the sensor's performance across variable conditions, such as temperature, pH, and ionic strength.

During initial exposure of the sensor to biofluids, foulants occupy defects in the monolayer of the nucleic acid-based sensor often leading to a drop in signal. These foulants may then further accelerate desorption around the defect due to intermolecular interactions with the monolayer molecules, emphasizing the importance of a stable SAM.[125] Thiolated molecules present in biofluids, such as cysteine and glutathione, compete with gold-thiol bound nucleic acid bioreceptors resulting in monolayer displacement.[119] While nonspecific adsorption of proteins on the sensor surface has demonstrated long-term stability by reducing monolayer desorption, unpredictable protein unfolding interactions may interfere with nucleic acid bioreceptors and constrain movement in conformation-switching sensors.[119, 133]

In order to mitigate fouling, physical and chemical barriers may be used to protect the sensor. Applying a hydrogel membrane limits diffusion to small molecules as determined by the porosity of the hydrogel design. Polybetaine-, agarose-, and polyacrylamide-based hydrogels have been used to encapsulate aptamer sensors to prevent sensor signal degradation when deployed in biological tissue, serum, and cells.[102, 125, 134] Macroporous hydrogels embedded with aptamer-functionalized AuNPs have also been used to prevent foreign body rejection of implantable sensors.[135] Porous conductive substrates, such as nanoporous gold and gold nanocomposites, dually benefit from efficient electron transfer as well as antifouling properties.[105, 107, 136] Semipermeable polymer coatings like Nafion also provide antifouling properties and may prevent small molecule interferents from

contacting the sensor.[137, 138, 139] Zwitterionic monolayers have demonstrated reduced protein adsorption. For example, phosphatidylcholine-terminated SAMs promote an antifouling surface chemistry by mimicking the cell membrane.[140, 141] With these antifouling methods, week-long in vivo nucleic acid-based sensing is a feasible goal that may soon be realized.[125]

As the sensor stability improves past several weeks, implant device form factor must also be considered to prevent foreign body reaction and encapsulation. Limiting protein aggregation through antifouling techniques evades the attraction of immune cells to the device. Minimizing implant size and matching the Young's modulus of the surrounding soft tissue with viscoelastic, soft electronics may help address this problem. Chemical non-toxicity of the sensor's components is important to prevent localized necrosis and subsequent immune responses. Mechanical strength of the sensor and resistance to in vivo shearing and degradation is key to prevent long-term toxicity through particulate accumulation in distal organs such as the liver and kidneys. Careful consideration must be taken for the types of nanomaterials used in the sensor design.[142]

Although blood is one of the most complex biofluids from a fouling standpoint due to its biomolecular diversity, circulating blood conditions are homeostatic resulting in consistent narrow ranges of variability over time and between individuals. ISF and CSF are filtered blood derivatives for wearables, subcutaneous implants, and neural implants that also maintain essential homeostatic conditions. However, when considering alternative biofluids, such as sweat, saliva, intestinal fluid, and urine, media conditions must be monitored as they may vary significantly between samples. In the case of sweat, pH may vary widely from 5 to 9 due to sweat induction methods, sweat rate, and individual physiochemical response.[12] Sweat ion concentration also varies with sweat rate. Sweat as a highly filtered, yet variable biofluid presents opposing design challenges to blood.

To account for variable media conditions, the nucleic acid-based sensor must be robust and operable under wide-ranging biochemistries. pH may significantly impact electron transfer kinetics, so pH-insensitive redox reporters have been studied to handle variable media conditions.[143] Electrochemical nucleic acid-based sensors have improved signal transduction at decreasing ion concentrations, as is the case with sweat, due to reduced charge screening effects.[105] As mentioned previously, dual-nucleic acid measurements can help to reduce the sensor variation to environmental factors, such as pH, ion concentration, and temperature.[129, 130]

However, in most cases, variable sensor responses will need to be calibrated using a multiplexed sensing platform that monitor these media conditions simultaneously.

### 3.4.5 Biofluidic Sensor Interface

The performance of wearable and implantable sensors is heavily influenced by how they interface with dynamic and diverse compositions of biofluid matrices. The sensing platform efficiently samples and conducts the biofluid to the surface of the nucleic acid-based sensor via layered microfluidics. The in situ sensing platform may contain several sensors for calibration and multibiomarker analysis also interfacing with the sampled biofluid. Minimally invasive, flexible form factors are key elements for consideration when designing the sensing platform for wearable and implantable applications.

As mentioned previously, nucleic acid-based sensors may require multiplexed platform calibration to account for variable conditions such as temperature, pH, and ionic strength, especially when working with blood-alternative biofluids. Electrode impedance can be used to measure ionic strength. A polyaniline-based potentiometric pH sensor was used for sweat calibration in a wearable ring platform.[44] When fabricating aptamer-FET sensors, it may be convenient for associated platform sensors to also be transistor-based, so a FET pH sensor was developed for a flexible FET biosensor array for real-time cortisol sweat sensing.[46]

While implanted sensors are under constant exposure to biofluids, wearable sensors must noninvasively capture the biofluid. Janus membranes have been studied for ultralow volume biofluid sampling. The asymmetric wettability of porous Janus membranes enables unidirectional liquid transport and self-pumping for high efficiency biofluid collection.[144] Janus membranes are an attractive strategy for passive natural sweat collection without external stimuli (exercise, temperature) at low sweat rates.[145] They also aid in filtering out large insoluble impurities often present on the skin's surface. Sweat may also be stimulated using cholinergic agents delivered via iontophoresis.[44] Microfluidic inlets conformed to the skin may then effectively capture sweat from the local stimulated area. Microfluidic designs may provide important control over the biofluid sensor interface. The microfluidics for a singular sensing region in a label-free continuous sensing platform may be simple when it comes to fluid transport, but it is important that the refreshing dynamics of the sensing region are evaluated and microfluidic inlet and outlet design optimized.[146] In other platforms, CBVs may be necessary for microfluidic gating to

control the reservoir filling order.[147] This can be used to provide chronologic sampling of a biofluid without mixing of old and new samples. This technique can be used to capture multiple measurements with a sensor array on a single platform thus leveraging a single-use sensor for continuous monitoring. CBVs may also be used to control fluid flow for incubation in the sensing region. A wearable platform for female hormone analysis used microfluidic CBVs to precisely control sweat sampling during a strand displacement assay.[44]

Soft, flexible electronics are key to interfacing sensors with tissues. Wearable sensors must conform to the complex wrinkles of the skin, curvatures of the body, and withstand repeated strain and bending deformation associated with body movement. Adopting mechanical properties that mimic the elasticity of skin allows the sensor to remain in position for localized sample collection and maintain performance for continuous sensing. Flexible thin-film polymer substrates, stretchable conductive polymer composites, liquid metal-based conductors, flexible graphene electrodes, strain-releasing lead patterns, and bioadhesives are some strategies used toward a tissue conforming sensing interface.[145, 148, 149, 150, 151, 152, 153] Implantable sensors must interface well with the surrounding tissue and demonstrate strong biocompatibility to prevent encapsulation that would limit the long-term performance of the sensor.[81] Beyond flexibility, soft electronics with macroporous scaffolds are key for vascularization and tissue integration. For example, embedding AuNPs into a hydrogel improved the tissue response to two months of implantation with minimal fibrous encapsulation.[135] Minimizing the size of the sensor may also reduce the risk of a foreign body reaction. Thin, flexible conductive fibers are a promising direction for implantable sensing due to the matching mechanical properties for in vivo use.[81] For example, a graphene-elastomer composite neurotransmitter sensor called NeuroString was fabricated as long strings for brain implantation versus as a thin film for use in the larger gut cavity.[150] The current response decreases with size for sensors that rely on 1:1 redox probe labeled nucleic acid signaling strands. The amplification provided by nucleic acid-based transistors thus bolsters the use of transistor design schemes for miniaturized implantable sensors.[85, 86]

Using multiplexed sensor arrays, spatial information may also be collected at the tissue interface. EAB sensors were placed at multiple sites along a probe implanted into tumor tissue for radial measurements of chemotherapeutic drug delivery and uptake within the tumor.[101] Wearable microneedle array patches allow for high density spatial sensing across the skin surface but may not reveal varied spatial re-

sults beyond local epidermal health (melanoma, wound healing). Tissue-conforming meshes allow for 2D measurement, which may elucidate important signaling and activity information when interfaced with the brain and heart.[151, 153] Nucleic acid-based microtransistor arrays will be the optimal strategy to achieve high-density spatial resolution since transistors maintain an amplified signal upon miniaturization. Spatiotemporal data may also be collected using smart pill designs in which the ingestible capsule collects data as it naturally moves through the digestive system.[154, 155]

From biofluid sampling to sensor calibration, rational design decisions must be made to support the translation of nucleic acid-based sensors to wearable and implantable devices. While nucleic acid receptors have the potential to be selective for diverse small molecule targets, these receptors must be engineered with regeneration in mind. Continuous monitoring requires kinetically favorable receptors and sensing mechanisms capable of detecting fluctuating analyte concentrations without user intervention. Yet, the primary challenge to overcome in continuous nucleic acid-based sensor design will be long-term stability. Compatible design choices of redox reporter, passivation layer, antifouling membrane, and electrochemical interrogation methods will extend the stability and robustness of nucleic acid-based sensors for effective continuous use in complex biofluids. Given the challenges in realizing continuous long-term sensing, disposable sensor patches with sensor arrays may be a more attractive and realistic translation of nucleic acid-based sensors for wearable platforms. However, for sensor implants to be worthwhile, these design challenges will need to be overcome for implantation without the need for frequent surgical replacement.

## 3.5 Conclusion

The development of continuous implantable and wearable electrochemical sensors represents a major advancement in the field of precision medicine and personalized healthcare. For example, implantable and wearable sensors may provide key information for effective drug delivery and dosing based on individual pharmacokinetics. Implantable and wearable devices may synergistically be used to implement closed-loop therapeutic systems with in vivo data access and noninvasive modulation. In addition, continuous monitoring using implantable and wearable sensors may provide advanced diagnostic data with respect to personalized baselines and trends that would allow for early intervention. This review has showcased the potential of

nucleic acid-based sensors to provide continuous, real-time monitoring of a broad spectrum of biomarkers directly in various biofluids. By leveraging the high specificity and sensitivity of the affinity of nucleic acids toward target biomarkers, these sensors offer a promising solution to the limitations of traditional health monitoring methods, which are often intermittent, invasive, and unable to capture the dynamic nature of physiological changes.

We have delved into various nucleic acid sensing strategies, with a particular focus on nucleic acid-based recognition elements and their role in enhancing the performance of biosensors. The integration of these sensors into both implantable and wearable platforms has been discussed, demonstrating their versatility and potential for widespread application in continuous at-home health monitoring. We critically evaluated challenges such as ensuring sensor longevity, navigating the intricacies of biofluids, and achieving reagentless detection, and proposed innovative interdisciplinary solutions to address these issues. Continuous efforts to improve sensor design, along with advancements in materials science, bioengineering, and computational modeling, are imperative for overcoming current limitations and enhancing the functionality and reliability of these devices. The integration of these sensors with digital health platforms could further enable real-time data analysis, fostering a proactive approach to health management and disease prevention. As we navigate the complexities of their development and implementation, the promise of transforming personalized medicine into a tangible reality becomes increasingly attainable, heralding a new era of health monitoring and intervention.

## References

[1] Juliane R. Sempionatto et al. "Wearable chemical sensors for biomarker discovery in the omics era". *Nature Reviews Chemistry* **2022**, *6* (12), 899–915. DOI: 10.1038/s41570-022-00439-w

[2] Jayoung Kim et al. "Wearable biosensors for healthcare monitoring". *Nature Biotechnology* **2019**, *37* (4), 389–406. DOI: 10.1038/s41587-019-0045-y

[3] Mark Friedel et al. "Opportunities and challenges in the diagnostic utility of dermal interstitial fluid". *Nature Biomedical Engineering* **2023**, *7* (12), 1541–1555. DOI: 10.1038/s41551-022-00998-9

[4] Yiran Yang and Wei Gao. "Wearable and flexible electronics for continuous molecular monitoring". *Chemical Society Reviews* **2019**, *48* (6), 1465–1491. DOI: 10.1039/C7CS00730B

[5] Tyler R. Ray et al. “Bio-Integrated Wearable Systems: A Comprehensive Review”. *Chemical Reviews* **2019**, *119* (8), 5461–5533. DOI: 10.1021/acs.chemrev.8b00573

[6] H. Ceren Ates et al. “End-to-end design of wearable sensors”. *Nature Reviews Materials* **2022**, *7* (11), 887–907. DOI: 10.1038/s41578-022-00460-x

[7] Changhao Xu, Yiran Yang, and Wei Gao. “Skin-Interfaced Sensors in Digital Medicine: from Materials to Applications”. *Matter* **2020**, *2* (6), 1414–1445. DOI: 10.1016/j.matt.2020.03.020

[8] Changhao Xu, Samuel A. Solomon, and Wei Gao. “Artificial intelligence-powered electronic skin”. *Nature Machine Intelligence* **2023**, *5* (12), 1344–1355. DOI: 10.1038/s42256-023-00760-z

[9] Changhao Xu et al. “A physicochemical-sensing electronic skin for stress response monitoring”. *Nature Electronics* **2024**, *7* (2), 168–179. DOI: 10.1038/s41928-023-01116-6

[10] Chao Tan et al. “Recent Advances in In Vivo Neurochemical Monitoring”. *Micromachines* **2021**, *12* (2), 208. DOI: 10.3390/mi12020208

[11] Jason Heikenfeld et al. “Accessing analytes in biofluids for peripheral biochemical monitoring”. *Nature Biotechnology* **2019**, *37* (4), 407–419. DOI: 10.1038/s41587-019-0040-3

[12] Jihong Min et al. “Skin-Interfaced Wearable Sweat Sensors for Precision Medicine”. *Chemical Reviews* **2023**, *123* (8), 5049–5138. DOI: 10.1021/acs.chemrev.2c00823

[13] Jiaobing Tu et al. “The Era of Digital Health: A Review of Portable and Wearable Affinity Biosensors”. *Advanced Functional Materials* **2020**, *30* (29), 1906713. DOI: 10.1002/adfm.201906713

[14] Connor D. Flynn et al. “Biomolecular sensors for advanced physiological monitoring”. *Nature Reviews Bioengineering* **2023**, *1* (8), 560–575. DOI: 10.1038/s44222-023-00067-z

[15] Kevin W. Plaxco and H. Tom Soh. “Switch-based biosensors: a new approach towards real-time, in vivo molecular detection”. *Trends in Biotechnology* **2011**, *29* (1), 1–5. DOI: 10.1016/j.tibtech.2010.10.005

[16] Gokul Chandra Biswas, Md. Taufiqur Mannan Khan, and Jagotamoy Das. “Wearable nucleic acid testing platform - A perspective on rapid self-diagnosis and surveillance of infectious diseases”. *Biosensors and Bioelectronics* **2023**, *226*, 115115. DOI: 10.1016/j.bios.2023.115115

[17] Alex M. Downs and Kevin W. Plaxco. “Real-Time, In Vivo Molecular Monitoring Using Electrochemical Aptamer Based Sensors: Opportunities and Challenges”. *ACS Sensors* **2022**, *7* (10), 2823–2832. DOI: 10.1021/acssensors.2c01428

[18] Sanjay Tyagi and Fred Russell Kramer. “Molecular Beacons: Probes that Fluoresce upon Hybridization”. *Nature Biotechnology* **1996**, *14* (3), 303–308. DOI: 10.1038/nbt0396-303

[19] Andrew D. Ellington and Jack W. Szostak. “In vitro selection of RNA molecules that bind specific ligands”. *Nature* **1990**, *346* (6287), 818–822. DOI: 10.1038/346818a0

[20] Shundong Cai et al. “Investigations on the interface of nucleic acid aptamers and binding targets”. *Analyst* **2018**, *143* (22), 5317–5338. DOI: 10.1039/C8AN01467A

[21] Trevor A. Feagin, Nicolò Maganzini, and Hyongsok Tom Soh. “Strategies for Creating Structure-Switching Aptamers”. *ACS Sensors* **2018**, *3* (9), 1611–1615. DOI: 10.1021/acssensors.8b00516

[22] Kyung-Ae Yang, Renjun Pei, and Milan N. Stojanovic. “In vitro selection and amplification protocols for isolation of aptameric sensors for small molecules”. *Methods* **2016**, *106*, 58–65. DOI: 10.1016/j.ymeth.2016.04.032

[23] Razvan Nutiu and Yingfu Li. “In Vitro Selection of Structure-Switching Signaling Aptamers”. *Angewandte Chemie International Edition* **2005**, *44* (7), 1061–1065. DOI: 10.1002/anie.200461848

[24] Alexandra E. Rangel et al. “Engineering Aptamer Switches for Multifunctional Stimulus-Responsive Nanosystems”. *Advanced Materials* **2020**, *32* (50), 2003704. DOI: 10.1002/adma.202003704

[25] Elnaz Bagheri et al. “Triple-helix molecular switch-based aptasensors and DNA sensors”. *Biosensors and Bioelectronics* **2018**, *111*, 1–9. DOI: 10.1016/j.bios.2018.03.070

[26] Wei Xu et al. “Surpassing the detection limit and accuracy of the electrochemical DNA sensor through the application of CRISPR Cas systems”. *Biosensors and Bioelectronics* **2020**, *155*, 112100. DOI: 10.1016/j.bios.2020.112100

[27] Reza Hajian et al. “Detection of unamplified target genes via CRISPR–Cas9 immobilized on a graphene field-effect transistor”. *Nature Biomedical Engineering* **2019**, *3* (6), 427–437. DOI: 10.1038/s41551-019-0371-x

[28] Yifan Dai et al. “Exploring the Trans-Cleavage Activity of CRISPR-Cas12a (cpf1) for the Development of a Universal Electrochemical Biosensor”. *Angewandte Chemie International Edition* **2019**, *58* (48), 17399–17405. DOI: 10.1002/anie.201910772

[29] Akkapol Suea-Ngam, Philip D. Howes, and Andrew J. deMello. “An amplification-free ultra-sensitive electrochemical CRISPR/Cas biosensor for drug-resistant bacteria detection”. *Chemical Science* **2021**, *12* (38), 12733–12743. DOI: 10.1039/D1SC02197D

[30] Bin Yang, Jilie Kong, and Xueen Fang. "Programmable CRISPR-Cas9 microneedle patch for long-term capture and real-time monitoring of universal cell-free DNA". *Nature Communications* **2022**, *13* (1), 3999. DOI: 10.1038/s41467-022-31740-3

[31] Peter Q. Nguyen et al. "Wearable materials with embedded synthetic biology sensors for biomolecule detection". *Nature Biotechnology* **2021**, *39* (11), 1366–1374. DOI: 10.1038/s41587-021-00950-3

[32] Ian A.P. Thompson et al. "An antibody-based molecular switch for continuous small-molecule biosensing". *Science Advances* **2023**, *9* (38), eadh4978. DOI: 10.1126/sciadv.adh4978

[33] Xiaowen Yan, X. Chris Le, and Hongquan Zhang. "Antibody-Bridged Beacon for Homogeneous Detection of Small Molecules". *Analytical Chemistry* **2018**, *90* (16), 9667–9672. DOI: 10.1021/acs.analchem.8b02510

[34] Jagotamoy Das et al. "Reagentless biomolecular analysis using a molecular pendulum". *Nature Chemistry* **2021**, *13* (5), 428–434. DOI: 10.1038/s41557-021-00644-y

[35] Hanie Yousefi et al. "Detection of SARS-CoV-2 Viral Particles Using Direct, Reagent-Free Electrochemical Sensing". *Journal of the American Chemical Society* **2021**, *143* (4), 1722–1727. DOI: 10.1021/jacs.0c10810

[36] Alam Mahmud et al. "Monitoring Cardiac Biomarkers with Aptamer-Based Molecular Pendulum Sensors". *Angewandte Chemie* **2023**, *135* (20), e202213567. DOI: 10.1002/ange.202213567

[37] Manjula Rajendran and Andrew D. Ellington. "In vitro selection of molecular beacons". *Nucleic Acids Research* **2003**, *31* (19), 5700–5713. DOI: 10.1093/nar/gkg764

[38] Philippe Dauphin-Ducharme et al. "Electrochemical Aptamer-Based Sensors: A Platform Approach to High-Frequency Molecular Monitoring In Situ in the Living Body". In: *Biomedical Engineering Technologies: Volume 1*. Ed. by Miguel R. Ossandon, Houston Baker, and Avraham Rasooly. Methods in Molecular Biology. New York, NY: Springer US, 2022, pp. 479–492. ISBN: 978-1-07-161803-5. DOI: 10.1007/978-1-0716-1803-5_25. URL: https://doi.org/10.1007/978-1-0716-1803-5_25 (visited on 01/17/2022).

[39] Mirelis Santos-Cancel, Robert A. Lazenby, and Ryan J. White. "Rapid Two-Millisecond Interrogation of Electrochemical, Aptamer-Based Sensor Response Using Intermittent Pulse Amperometry". *ACS Sensors* **2018**, *3* (6), 1203–1209. DOI: 10.1021/acssensors.8b00278

[40] Netzahualcóyotl Arroyo-Currás et al. "Subsecond-Resolved Molecular Measurements in the Living Body Using Chronoamperometrically Interrogated Aptamer-Based Sensors". *ACS Sensors* **2018**, *3* (2), 360–366. DOI: 10.1021/acssensors.7b00787

[41] Philippe Dauphin-Ducharme and Kevin W. Plaxco. "Maximizing the Signal Gain of Electrochemical-DNA Sensors". *Analytical Chemistry* **2016**, *88* (23), 11654–11662. DOI: 10.1021/acs.analchem.6b03227

[42] Alex M. Downs et al. "Improved calibration of electrochemical aptamer-based sensors". *Scientific Reports* **2022**, *12* (1), 5535. DOI: 10.1038/s41598-022-09070-7

[43] Hui Li et al. "Calibration-Free Electrochemical Biosensors Supporting Accurate Molecular Measurements Directly in Undiluted Whole Blood". *Journal of the American Chemical Society* **2017**, *139* (32), 11207–11213. DOI: 10.1021/jacs.7b05412

[44] Cui Ye, Minqiang Wang, Jihong Min, Roland Yingjie Tay, Heather Lukas, Juliane R. Sempionatto, Jiahong Li, Changhao Xu, and Wei Gao. "A wearable aptamer nanobiosensor for non-invasive female hormone monitoring". *Nature Nanotechnology* **2023**, 1–8. DOI: 10.1038/s41565-023-01513-0

[45] Nako Nakatsuka et al. "Aptamer–field-effect transistors overcome Debye length limitations for small-molecule sensing". *Science* **2018**, *362* (6412), 319–324. DOI: 10.1126/science.aao6750

[46] Bo Wang et al. "Wearable aptamer-field-effect transistor sensing system for noninvasive cortisol monitoring". *Science Advances* **2022**, *8* (1), eabk0967. DOI: 10.1126/sciadv.abk0967

[47] Kevin M. Cheung et al. "Phenylalanine Monitoring via Aptamer-Field-Effect Transistor Sensors". *ACS Sensors* **2019**, *4* (12), 3308–3317. DOI: 10.1021/acssensors.9b01963

[48] Liqian Wang et al. "Rapid and ultrasensitive electromechanical detection of ions, biomolecules and SARS-CoV-2 RNA in unamplified samples". *Nature Biomedical Engineering* **2022**, *6* (3), 276–285. DOI: 10.1038/s41551-021-00833-7

[49] I. Gualandi et al. "Textile Organic Electrochemical Transistors as a Platform for Wearable Biosensors". *Scientific Reports* **2016**, *6* (1), 33637. DOI: 10.1038/srep33637

[50] Onur Parlak et al. "Molecularly selective nanoporous membrane-based wearable organic electrochemical device for noninvasive cortisol sensing". *Science Advances* **2018**, *4* (7), eaar2904. DOI: 10.1126/sciadv.aar2904

[51] Sophia L. Bidinger et al. "Pulsed transistor operation enables miniaturization of electrochemical aptamer-based sensors". *Science Advances* **2022**, *8* (46), eadd4111. DOI: 10.1126/sciadv.add4111

[52] Yuanying Liang et al. "Amplification of aptamer sensor signals by four orders of magnitude via interdigitated organic electrochemical transistors". *Biosensors and Bioelectronics* **2019**, *144*, 111668. DOI: 10.1016/j.bios.2019.111668

[53] Nileshi Saraf et al. “Highly selective aptamer based organic electrochemical biosensor with pico-level detection”. *Biosensors and Bioelectronics* **2018**, *117*, 40–46. DOI: 10.1016/j.bios.2018.05.031

[54] Minqiang Wang, Yiran Yang, and Wei Gao. “Laser-engraved graphene for flexible and wearable electronics”. *Trends in Chemistry* **2021**, *3* (11), 969–981. DOI: 10.1016/j.trechm.2021.09.001

[55] Yuanjing Lin, Mallika Bariya, and Ali Javey. “Wearable Biosensors for Body Computing”. *Advanced Functional Materials* **2021**, *31* (39), 2008087. DOI: 10.1002/adfm.202008087

[56] Daniel Sim et al. “Biomarkers and Detection Platforms for Human Health and Performance Monitoring: A Review”. *Advanced Science* **2022**, *9* (7), 2104426. DOI: 10.1002/advs.202104426

[57] Zijie Zhang et al. “Development of Nucleic-Acid-Based Electrochemical Biosensors for Clinical Applications”. *Angewandte Chemie* **2022**, *134* (50), e202212496. DOI: 10.1002/ange.202212496

[58] Hazhir Teymourian et al. “Lab under the Skin: Microneedle Based Wearable Devices”. *Advanced Healthcare Materials* **2021**, *10* (17), 2002255. DOI: 10.1002/adhm.202002255

[59] Hongyi Sun et al. “Wearable Clinic: From Microneedle-Based Sensors to Next-Generation Healthcare Platforms”. *Small* **2023**, *19* (51), 2207539. DOI: 10.1002/smll.202207539

[60] Yao Wu et al. “Microneedle Aptamer-Based Sensors for Continuous, Real-Time Therapeutic Drug Monitoring”. *Analytical Chemistry* **2022**, DOI: 10.1021/acs.analchem.2c00829

[61] Pei-Heng Lin et al. “Wearable hydrogel patch with noninvasive, electrochemical glucose sensor for natural sweat detection”. *Talanta* **2022**, *241*, 123187. DOI: 10.1016/j.talanta.2021.123187

[62] Bin Yang et al. “Long-term monitoring of ultratrace nucleic acids using tetrahedral nanostructure-based NgAgo on wearable microneedles”. *Nature Communications* **2024**, *15* (1), 1936. DOI: 10.1038/s41467-024-46215-w

[63] Bin Yang, Xueen Fang, and Jilie Kong. “Engineered Microneedles for Interstitial Fluid Cell-Free DNA Capture and Sensing Using Iontophoretic Dual-Extraction Wearable Patch”. *Advanced Functional Materials* **2020**, *30* (24), 2000591. DOI: 10.1002/adfm.202000591

[64] Mark Friedel et al. “Continuous molecular monitoring of human dermal interstitial fluid with microneedle-enabled electrochemical aptamer sensors”. *Lab on a Chip* **2023**, *23* (14), 3289–3299. DOI: 10.1039/D3LC00210A

[65] Ze Xiong et al. “A wireless and battery-free wound infection sensor based on DNA hydrogel”. *Science Advances* **2021**, *7* (47), eabj1617. DOI: 10.1126/sciadv.abj1617

[66] Yuji Gao et al. “A flexible multiplexed immunosensor for point-of-care in situ wound monitoring”. *Science Advances* **2021**, *7* (21), eabg9614. DOI: 10.1126/sciadv.abg9614

[67] Ali K. Yetisen et al. “Wearables in Medicine”. *Advanced Materials* **2018**, *30* (33), 1706910. DOI: 10.1002/adma.201706910

[68] Jiaobing Tu et al. “A wireless patch for the monitoring of C-reactive protein in sweat”. *Nature Biomedical Engineering* **2023**, *7* (10), 1293–1306. DOI: 10.1038/s41551-023-01059-5

[69] Rebeca M. Torrente-Rodríguez et al. “Investigation of Cortisol Dynamics in Human Sweat Using a Graphene-Based Wireless mHealth System”. *Matter* **2020**, *2* (4), 921–937. DOI: 10.1016/j.matt.2020.01.021

[70] Jai Eun An et al. “Wearable Cortisol Aptasensor for Simple and Rapid Real-Time Monitoring”. *ACS Sensors* **2022**, *7* (1), 99–108. DOI: 10.1021/acssensors.1c01734

[71] Canran Wang, Ehsan Shirzaei Sani, and Wei Gao. “Wearable Bioelectronics for Chronic Wound Management”. *Advanced Functional Materials* **2022**, *32* (17), 2111022. DOI: 10.1002/adfm.202111022

[72] Surachate Kalasin, Pantawan Sangnuang, and Werasak Surareungchai. “Intelligent Wearable Sensors Interconnected with Advanced Wound Dressing Bandages for Contactless Chronic Skin Monitoring: Artificial Intelligence for Predicting Tissue Regeneration”. *Analytical Chemistry* **2022**, *94* (18), 6842–6852. DOI: 10.1021/acs.analchem.2c00782

[73] Ehsan Shirzaei Sani et al. “A stretchable wireless wearable bioelectronic system for multiplexed monitoring and combination treatment of infected chronic wounds”. *Science Advances* **2023**, *9* (12), eadf7388. DOI: 10.1126/sciadv.adf7388

[74] Wei Gao et al. “Fully integrated wearable sensor arrays for multiplexed in situ perspiration analysis”. *Nature* **2016**, *529* (7587), 509–514. DOI: 10.1038/nature16521

[75] Chen Hu et al. “Recent Development of Implantable Chemical Sensors Utilizing Flexible and Biodegradable Materials for Biomedical Applications”. *ACS Nano* **2024**, *18* (5), 3969–3995. DOI: 10.1021/acsnano.3c11832

[76] Jin Zhou et al. “Implantable Electrochemical Microsensors for In Vivo Monitoring of Animal Physiological Information”. *Nano-Micro Letters* **2023**, *16* (1), 49. DOI: 10.1007/s40820-023-01274-4

[77] Jianyou Feng et al. “Implantable Fiber Biosensors Based on Carbon Nanotubes”. *Accounts of Materials Research* **2021**, *2* (3), 138–146. DOI: 10.1021/accountsmr.0c00109

[78] Željko Janićijević et al. “Design and Development of Transient Sensing Devices for Healthcare Applications”. *Advanced Science* **2024**, *11* (20), 2307232. DOI: 10.1002/advs.202307232

[79] Aman Bhatia et al. “Wireless Battery-free and Fully Implantable Organ Interfaces”. *Chemical Reviews* **2024**, *124* (5), 2205–2280. DOI: 10.1021/acs.chemrev.3c00425

[80] Florian Fallegger, Giuseppe Schiavone, and Stéphanie P. Lacour. “Conformable Hybrid Systems for Implantable Bioelectronic Interfaces”. *Advanced Materials* **2020**, *32* (15), 1903904. DOI: 10.1002/adma.201903904

[81] Jiajia Wang et al. “Long-term In Vivo Monitoring of Chemicals with Fiber Sensors”. *Advanced Fiber Materials* **2021**, *3* (1), 47–58. DOI: 10.1007/s42765-020-00061-9

[82] Shidi Wang et al. “In Vivo Electrochemical Biosensors: Recent Advances in Molecular Design, Electrode Materials, and Electrochemical Devices”. *Analytical Chemistry* **2023**, *95* (1), 388–406. DOI: 10.1021/acs.analchem.2c04541

[83] Hanfeng Hou et al. “A Generalizable and Noncovalent Strategy for Interfacing Aptamers with a Microelectrode for the Selective Sensing of Neurotransmitters In Vivo”. *Angewandte Chemie International Edition* **2020**, *59* (43), 18996–19000. DOI: 10.1002/anie.202008284

[84] Tomoki Saizaki et al. “The Development of Aptamer-Coupled Microelectrode Fiber Sensors (apta-FS) for Highly Selective Neurochemical Sensing”. *Analytical Chemistry* **2023**, *95* (17), 6791–6800. DOI: 10.1021/acs.analchem.2c05046

[85] Chuanzhen Zhao et al. “Implantable aptamer–field-effect transistor neuroprobes for in vivo neurotransmitter monitoring”. *Science Advances* **2021**, *7* (48), eabj7422. DOI: 10.1126/sciadv.abj7422

[86] Guangfu Wu et al. “Implantable Aptamer-Graphene Microtransistors for Real-Time Monitoring of Neurochemical Release in Vivo”. *Nano Letters* **2022**, *22* (9), 3668–3677. DOI: 10.1021/acs.nanolett.2c00289

[87] Yuqian Zhang, Nan Jiang, and Ali K. Yetisen. “Brain neurochemical monitoring”. *Biosensors and Bioelectronics* **2021**, *189*, 113351. DOI: 10.1016/j.bios.2021.113351

[88] Rugare G. Chingarande et al. “Real-time label-free detection of dynamic aptamer–small molecule interactions using a nanopore nucleic acid conformational sensor”. *Proceedings of the National Academy of Sciences* **2023**, *120* (24), e2108118120. DOI: 10.1073/pnas.2108118120

[89] Marlon P. Quinones and Rima Kaddurah-Daouk. "Metabolomics tools for identifying biomarkers for neuropsychiatric diseases". *Neurobiology of Disease* **2009**, *35* (2), 165–176. DOI: 10.1016/j.nbd.2009.02.019

[90] Matthew A. Hopcroft, William D. Nix, and Thomas W. Kenny. "What is the Young's Modulus of Silicon?" *Journal of Microelectromechanical Systems* **2010**, *19* (2), 229–238. DOI: 10.1109/JMEMS.2009.2039697

[91] Chuanzhen Zhao et al. "Flexible and Implantable Polyimide Aptamer-Field-Effect Transistor Biosensors". *ACS Sensors* **2022**, *7* (12), 3644–3653. DOI: 10.1021/acssensors.2c01909

[92] Manfred Westphal and Katrin Lamszus. "Circulating biomarkers for gliomas". *Nature Reviews Neurology* **2015**, *11* (10), 556–566. DOI: 10.1038/nrneurol.2015.171

[93] Katelyn N Seale and Katherine H R Tkaczuk. "Circulating Biomarkers in Breast Cancer". *Clinical Breast Cancer* **2022**, *22* (3), e319–e331. DOI: 10.1016/j.clbc.2021.09.006

[94] Philip Johnson et al. "Circulating biomarkers in the diagnosis and management of hepatocellular carcinoma". *Nature Reviews Gastroenterology & Hepatology* **2022**, *19* (10), 670–681. DOI: 10.1038/s41575-022-00620-y

[95] Mahla Poudineh et al. "Profiling circulating tumour cells and other biomarkers of invasive cancers". *Nature Biomedical Engineering* **2018**, *2* (2), 72–84. DOI: 10.1038/s41551-018-0190-5

[96] Samir M. Hanash, Christina S. Baik, and Olli Kallioniemi. "Emerging molecular biomarkers—blood-based strategies to detect and monitor cancer". *Nature Reviews Clinical Oncology* **2011**, *8* (3), 142–150. DOI: 10.1038/nrclinonc.2010.220

[97] Liyuan Wang et al. "Functionalized helical fibre bundles of carbon nanotubes as electrochemical sensors for long-term in vivo monitoring of multiple disease biomarkers". *Nature Biomedical Engineering* **2020**, *4* (2), 159–171. DOI: 10.1038/s41551-019-0462-8

[98] Brian Scott Ferguson et al. "Real-Time, Aptamer-Based Tracking of Circulating Therapeutic Agents in Living Animals". *Science Translational Medicine* **2013**, DOI: 10.1126/scitranslmed.3007095

[99] Netzahualcóyotl Arroyo-Currás et al. "Real-time measurement of small molecules directly in awake, ambulatory animals". *Proceedings of the National Academy of Sciences* **2017**, *114* (4), 645–650. DOI: 10.1073/pnas.1613458114

[100] Philippe Dauphin-Ducharme et al. "Electrochemical Aptamer-Based Sensors for Improved Therapeutic Drug Monitoring and High-Precision, Feedback-Controlled Drug Delivery". *ACS Sensors* **2019**, *4* (10), 2832–2837. DOI: 10.1021/acssensors.9b01616

[101] Ji-Won Seo et al. “Real-time monitoring of drug pharmacokinetics within tumor tissue in live animals”. *Science Advances* **2022**, *8* (1), eabk2901. DOI: 10.1126/sciadv.abk2901

[102] Shaoguang Li et al. “Implantable Hydrogel-Protective DNA Aptamer-Based Sensor Supports Accurate, Continuous Electrochemical Analysis of Drugs at Multiple Sites in Living Rats”. *ACS Nano* **2023**, *17* (18), 18525–18538. DOI: 10.1021/acsnano.3c06520

[103] Brian Roehrich et al. “Calibration-Free, Seconds-Resolved In Vivo Molecular Measurements using Fourier-Transform Impedance Spectroscopy Interrogation of Electrochemical Aptamer Sensors”. *ACS Sensors* **2023**, *8* (8), 3051–3059. DOI: 10.1021/acssensors.3c00632

[104] Jenise B. Chen et al. “Nanostructured Architectures for Biomolecular Detection inside and outside the Cell”. *Advanced Functional Materials* **2020**, *30* (37), 1907701. DOI: 10.1002/adfm.201907701

[105] Kaiyu Fu et al. “Accelerated Electron Transfer in Nanostructured Electrodes Improves the Sensitivity of Electrochemical Biosensors”. *Advanced Science* **2021**, *8* (23), 2102495. DOI: 10.1002/advs.202102495

[106] Hossein Zargartalebi et al. “Capillary-Assisted Molecular Pendulum Bioanalysis”. *Journal of the American Chemical Society* **2022**, *144* (40), 18338–18349. DOI: 10.1021/jacs.2c06192

[107] Naveen K. Singh et al. “Cortisol Detection in Undiluted Human Serum Using a Sensitive Electrochemical Structure-Switching Aptamer over an Antifouling Nanocomposite Layer”. *ACS Omega* **2021**, *6* (42), 27888–27897. DOI: 10.1021/acsomega.1c03552

[108] Carlotta Peruzzi et al. “Interfacing aptamers, nanoparticles and graphene in a hierarchical structure for highly selective detection of biomolecules in OECT devices”. *Scientific Reports* **2021**, *11* (1), 9380. DOI: 10.1038/s41598-021-88546-4

[109] Ning Gao et al. “Specific detection of biomolecules in physiological solutions using graphene transistor biosensors”. *Proceedings of the National Academy of Sciences* **2016**, *113* (51), 14633–14638. DOI: 10.1073/pnas.1625010114

[110] Erika Komiya et al. “Exploration and Application of DNA-Binding Proteins to Make a Versatile DNA–Protein Covalent-Linking Patch (D-Pclip): The Case of a Biosensing Element”. *Journal of the American Chemical Society* **2024**, DOI: 10.1021/jacs.3c12668

[111] Alessandro Porchetta et al. “Using Distal-Site Mutations and Allosteric Inhibition To Tune, Extend, and Narrow the Useful Dynamic Range of Aptamer-Based Sensors”. *Journal of the American Chemical Society* **2012**, *134* (51), 20601–20604. DOI: 10.1021/ja310585e

[112] Brandon D. Wilson et al. “Independent control of the thermodynamic and kinetic properties of aptamer switches”. *Nature Communications* **2019**, *10* (1), 5079. DOI: 10.1038/s41467-019-13137-x

[113] Ali Bashir et al. “Machine learning guided aptamer refinement and discovery”. *Nature Communications* **2021**, *12* (1), 2366. DOI: 10.1038/s41467-021-22555-9

[114] Jia Song et al. “A Sequential Multidimensional Analysis Algorithm for Aptamer Identification based on Structure Analysis and Machine Learning”. *Analytical Chemistry* **2020**, *92* (4), 3307–3314. DOI: 10.1021/acs.analchem.9b05203

[115] Zongjie Wang et al. “Apta FastZ: An Algorithm for the Rapid Identification of Aptamers with Defined Binding Affinities”. *Analytical Chemistry* **2023**, *95* (48), 17438–17443. DOI: 10.1021/acs.analchem.3c02881

[116] Rajesh Ahirwar et al. “In silico selection of an aptamer to estrogen receptor alpha using computational docking employing estrogen response elements as aptamer-alike molecules”. *Scientific Reports* **2016**, *6* (1), 21285. DOI: 10.1038/srep21285

[117] Alan Fernando Rodríguez Serrano and I-Ming Hsing. “Prediction of Aptamer–Small-Molecule Interactions Using Metastable States from Multiple Independent Molecular Dynamics Simulations”. *Journal of Chemical Information and Modeling* **2022**, *62* (19), 4799–4809. DOI: 10.1021/acs.jcim.2c00734

[118] Neda Emami and Reza Ferdousi. “AptaNet as a deep learning approach for aptamer–protein interaction prediction”. *Scientific Reports* **2021**, *11* (1), 6074. DOI: 10.1038/s41598-021-85629-0

[119] Vincent Clark, Miguel Aller Pellitero, and Netzahualcóyotl Arroyo-Currás. “Explaining the Decay of Nucleic Acid-Based Sensors under Continuous Voltammetric Interrogation”. *Analytical Chemistry* **2023**, *95* (11), 4974–4983. DOI: 10.1021/acs.analchem.2c05158

[120] Kaylyn K. Leung et al. “Elucidating the Mechanisms Underlying the Signal Drift of Electrochemical Aptamer-Based Sensors in Whole Blood”. *ACS Sensors* **2021**, *6* (9), 3340–3347. DOI: 10.1021/acssensors.1c01183

[121] Di Kang et al. “Survey of Redox-Active Moieties for Application in Multiplexed Electrochemical Biosensors”. *Analytical Chemistry* **2016**, *88* (21), 10452–10458. DOI: 10.1021/acs.analchem.6b02376

[122] B. Göhler et al. “Spin Selectivity in Electron Transmission Through Self-Assembled Monolayers of Double-Stranded DNA”. *Science* **2011**, *331* (6019), 894–897. DOI: 10.1126/science.1199339

[123] S. G. Ray et al. “Chirality-Induced Spin-Selective Properties of Self-Assembled Monolayers of DNA on Gold”. *Physical Review Letters* **2006**, *96* (3), 036101. DOI: 10.1103/PhysRevLett.96.036101

[124] A. Kaliyaraj Selva Kumar, D. Li, and R. G. Compton. "A mini-review: how reliable is the drop casting technique?" *Electrochemistry Communications* **2020**, *121*,

. [125] Zach Watkins et al. "Week-Long Operation of Electrochemical Aptamer Sensors: New Insights into Self-Assembled Monolayer Degradation Mechanisms and Solutions for Stability in Serum at Body Temperature". *ACS Sensors* **2023**, *8* (3), 1119–1131. DOI: 10.1021/acssensors.2c02403

[126] Alexander Shaver and Netzahualcóyotl Arroyo-Currás. "The challenge of long-term stability for nucleic acid-based electrochemical sensors". *Current Opinion in Electrochemistry* **2022**, *32*, 100902. DOI: 10.1016/j.coelec.2021.100902

[127] Miguel Aller Pellitero et al. "Stability of N-Heterocyclic Carbene Monolayers under Continuous Voltammetric Interrogation". *ACS Applied Materials & Interfaces* **2023**, *15* (29), 35701–35709. DOI: 10.1021/acsami.3c06148

[128] Andrea Idili et al. "Calibration-Free Measurement of Phenylalanine Levels in the Blood Using an Electrochemical Aptamer-Based Sensor Suitable for Point-of-Care Applications". *ACS Sensors* **2019**, *4* (12), 3227–3233. DOI: 10.1021/acssensors.9b01703

[129] Ting Chen et al. "Temperature and pH tolerance ratiometric aptasensor: Efficiently self-calibrating electrochemical detection of aflatoxin B1". *Talanta* **2022**, *242*, 123280. DOI: 10.1016/j.talanta.2022.123280

[130] Ya-Chen Tsai et al. "Dual-Aptamer Drift Canceling Techniques to Improve Long-Term Stability of Real-Time Structure-Switching Aptasensors". *ACS Sensors* **2023**, *8* (9), 3380–3388. DOI: 10.1021/acssensors.3c00509

[131] Man Zhu et al. "Employing an Intercalated Redox Reporter in Electrochemical Aptamer-Based Biosensors to Enable Calibration-Free Molecular Measurements in Undiluted Serum". *Analytical Chemistry* **2020**, *92* (18), 12437–12441. DOI: 10.1021/acs.analchem.0c02205

[132] Alexander Shaver et al. "Nuclease Hydrolysis Does Not Drive the Rapid Signaling Decay of DNA Aptamer-Based Electrochemical Sensors in Biological Fluids". *Langmuir* **2021**, *37* (17), 5213–5221. DOI: 10.1021/acs.langmuir.1c00166

[133] Alexander Shaver, Samuel D. Curtis, and Netzahualcóyotl Arroyo-Currás. "Alkanethiol Monolayer End Groups Affect the Long-Term Operational Stability and Signaling of Electrochemical, Aptamer-Based Sensors in Biological Fluids". *ACS Applied Materials & Interfaces* **2020**, *12* (9), 11214–11223. DOI: 10.1021/acsami.9b22385

[134] Lise J. Nielsen, Lars F. Olsen, and Veli C. Ozalp. "Aptamers Embedded in Polyacrylamide Nanoparticles: A Tool for in Vivo Metabolite Sensing". *ACS Nano* **2010**, *4* (8), 4361–4370. DOI: 10.1021/nn100635j

[135] Katharina Kaefer et al. “Implantable Sensors Based on Gold Nanoparticles for Continuous Long-Term Concentration Monitoring in the Body”. *Nano Letters* **2021**, *21* (7), 3325–3330. DOI: 10.1021/acs.nanolett.1c00887

[136] Pallavi Daggumati et al. “Biofouling-Resilient Nanoporous Gold Electrodes for DNA Sensing”. *Analytical Chemistry* **2015**, *87* (17), 8618–8622. DOI: 10.1021/acs.analchem.5b02969

[137] Elaheh Farjami et al. “RNA Aptamer-Based Electrochemical Biosensor for Selective and Label-Free Analysis of Dopamine”. *Analytical Chemistry* **2013**, *85* (1), 121–128. DOI: 10.1021/ac302134s

[138] Ziran Wang et al. “A Flexible and Regenerative Aptameric Graphene–Nafion Biosensor for Cytokine Storm Biomarker Monitoring in Undiluted Biofluids toward Wearable Applications”. *Advanced Functional Materials* **2021**, *31* (4), 2005958. DOI: 10.1002/adfm.202005958

[139] Jing-Yi Huang et al. “A high-sensitivity electrochemical aptasensor of carcinoembryonic antigen based on graphene quantum dots-ionic liquid-nafion nanomatrix and DNAzyme-assisted signal amplification strategy”. *Biosensors and Bioelectronics* **2018**, *99*, 28–33. DOI: 10.1016/j.bios.2017.07.036

[140] Hui Li et al. “A Biomimetic Phosphatidylcholine-Terminated Monolayer Greatly Improves the In Vivo Performance of Electrochemical Aptamer-Based Sensors”. *Angewandte Chemie International Edition* **2017**, *56* (26), 7492–7495. DOI: 10.1002/anie.201700748

[141] Shaoguang Li et al. “Exploring End-Group Effect of Alkanethiol Self-Assembled Monolayers on Electrochemical Aptamer-Based Sensors in Biological Fluids”. *Analytical Chemistry* **2021**, *93* (14), 5849–5855. DOI: 10.1021/acs.analchem.1c00085

[142] Jiulong Li, Chunying Chen, and Tian Xia. “Understanding Nanomaterial–Liver Interactions to Facilitate the Development of Safer Nanoapplications”. *Advanced Materials* **2022**, *34* (11), 2106456. DOI: 10.1002/adma.202106456

[143] Madoka Nagata et al. “An Amine-Reactive Phenazine Ethosulfate (arPES)—A Novel Redox Probe for Electrochemical Aptamer-Based Sensor”. *Sensors* **2022**, *22* (5), 1760. DOI: 10.3390/s22051760

[144] Xiao Hong et al. “Hybrid Janus Membrane with Dual-Asymmetry Integration of Wettability and Conductivity for Ultra-Low-Volume Sweat Sensing”. *ACS Applied Materials & Interfaces* **2022**, *14* (7), 9644–9654. DOI: 10.1021/acsami.1c16820

[145] Cong Huang et al. “A Flexible Aptameric Graphene Field-Effect Nanosensor Capable of Automatic Liquid Collection/Filtering for Cytokine Storm Biomarker Monitoring in Undiluted Sweat”. *Advanced Functional Materials* **2024**, *34* (9), 2309447. DOI: 10.1002/adfm.202309447

[146] Yiran Yang et al. “A laser-engraved wearable sensor for sensitive detection of uric acid and tyrosine in sweat”. *Nature Biotechnology* **2020**, *38* (2), 217–224. DOI: 10.1038/s41587-019-0321-x

[147] Jungil Choi et al. “Thin, Soft, Skin-Mounted Microfluidic Networks with Capillary Bursting Valves for Chrono-Sampling of Sweat”. *Advanced Healthcare Materials* **2017**, *6* (5), 1601355. DOI: 10.1002/adhm.201601355

[148] Suji Choi et al. “Highly conductive, stretchable and biocompatible Ag–Au core–sheath nanowire composite for wearable and implantable bioelectronics”. *Nature Nanotechnology* **2018**, *13* (11), 1048–1056. DOI: 10.1038/s41565-018-0226-8

[149] Zhi Jiang et al. “A 1.3-micrometre-thick elastic conductor for seamless on-skin and implantable sensors”. *Nature Electronics* **2022**, *5* (11), 784–793. DOI: 10.1038/s41928-022-00868-x

[150] Jinxing Li et al. “A tissue-like neurotransmitter sensor for the brain and gut”. *Nature* **2022**, *606* (7912), 94–101. DOI: 10.1038/s41586-022-04615-2

[151] Ying-Shi Guan et al. “Elastic electronics based on micromesh-structured rubbery semiconductor films”. *Nature Electronics* **2022**, *5* (12), 881–892. DOI: 10.1038/s41928-022-00874-z

[152] Duhwan Seong et al. “Sticky and Strain-Gradient Artificial Epineurium for Sutureless Nerve Repair in Rodents and Nonhuman Primates”. *Advanced Materials* **2024**, *36* (16), 2307810. DOI: 10.1002/adma.202307810

[153] Heewon Choi et al. “Adhesive bioelectronics for sutureless epicardial interfacing”. *Nature Electronics* **2023**, *6* (10), 779–789. DOI: 10.1038/s41928-023-01023-w

[154] Ernesto De la Paz et al. “A self-powered ingestible wireless biosensing system for real-time in situ monitoring of gastrointestinal tract metabolites”. *Nature Communications* **2022**, *13* (1), 7405. DOI: 10.1038/s41467-022-35074-y

[155] Saransh Sharma et al. “Location-aware ingestible microdevices for wireless monitoring of gastrointestinal dynamics”. *Nature Electronics* **2023**, *6* (3), 242–256. DOI: 10.1038/s41928-023-00916-0

*Chapter 4*

# CONTINUOUS SEROTONIN APTAMER SENSOR FOR GASTROINTESTINAL TRACT MONITORING

*Materials from this chapter appear in:*
Jihong Min et al. "Continuous biochemical profiling of the gastrointestinal tract using a multiparametric ingestible capsule". *Nature Electronics* **submitted July 2024**,

The gastrointestinal (GI) tract plays dual, pivotal roles: it serves as a vital conduit for nutrient absorption and waste expulsion, and acts as a complex interface linking overall health to our internal physiological processes. [1, 2] This multifaceted system, woven through various compartments, hosts the gut microbiota, which, alongside the central and enteric nervous systems, regulates a myriad of processes. [3, 4] These include the precise breakdown and selective absorption of nutrients, as well as an unexpected influence over our emotional and cognitive states. [5] Such influence can materialize directly through hormone production or indirectly by triggering brain signals through metabolites or stimulating immune cells to release cytokines. [6, 7] Dysbiosis, a perturbation of the delicate ecosystem within the GI tract, is intertwined with a diverse array of disorders. These extend beyond GI issues like irritable bowel syndrome (IBS) and inflammatory bowel disease (IBD) to central nervous system (CNS) disorders such as autism, anxiety, depression, and Parkinson's disease. [8, 9]

The biochemical profile of the GI tract governs its health and the overall-being of the host (Figure 4.1A). For example, serotonin is crucial for regulating gut motility and substantially impacts mood, appetite, and cognitive functions, with about 95% of the body's serotonin synthesized in the GI tract. [10, 11] Short-chain fatty acids (SCFAs), the end products of dietary fiber fermentation by anaerobic intestinal microbiota, play a vital role in maintaining gut health, regulating metabolism, and supporting immune function. [12, 13] The pH level in the GI tract affects digestive enzyme activity and the composition of gut microbiota, making it important for

maintaining a healthy digestive system. [14, 15] Ionic strength, which measures the concentration of ions in GI fluids, is essential for electrolyte balance and cellular function, with abnormalities potentially indicating various health issues. [16] Glucose levels provide information on nutrient absorption efficiency and metabolic health, influencing microbial activity in the gut and helping detect conditions like diabetes and malabsorption issues. [17, 18] Monitoring GI biochemicals is essential not only for understanding metabolic health and functionality of the GI tract but also for preventing and managing diseases. [19, 20]

Recent advancements in wireless sensing technology open the door to the development of ingestible capsules for GI tract monitoring. [21, 22, 23, 24, 25] Commercial ingestible technologies, such as capsule endoscopes and pH/pressure sensing capsules, primarily detect optical and physical alterations in the GI tract caused by underlying disorders. [1, 21] While these devices aid in diagnosing disease symptoms, they frequently fail to reveal early signs or ascertain the underlying cause of the disease. Moreover, although emerging ingestible capsules show promising potential to monitor vital signs, [26, 27] gas molecules, [28] radiotherapy, [29] as well as inflammation, [30, 31] significant limitations persist in biomolecular profiling in the GI tract. [32] An ingestible capsule platform capable of continuously and selectively monitoring a broad spectrum of chemical signals in GI fluids could provide a more complete understanding of GI health, facilitating earlier diagnosis and intervention. Despite the high demand for such a platform, its development has been hindered by substantial challenges, including selective in situ sensing, high variability in the GI environment, and the integration of low-power miniaturized systems.

In response to these challenges, and to adeptly navigate the intricacies of GI tract biochemistry, we introduce PillTrek, a fully integrated smart capsule platform that encapsulates a multimodal electrochemical sensor array and a low power wireless electronic system for real-time, continuous, and multiplexed monitoring of the GI tract (Figure 4.1B). With a compact form under 1 $cm^3$ in volume, PillTrek is capable of monitoring a wide range of molecular biomarkers in complex gut fluids. It employs highly selective bioreceptors, including aptamers, enzymes, and ion-selective membranes, to ensure precise target recognition. PillTrek can perform a variety of signal transduction measurements, such as potentiometry, amperometry, voltammetry, and impedimetry, allowing it to interface with diverse electrochemical sensors and detect various parameters of interest in the gut (Figure 4.1C–E). Compared to previously reported ingestible electronic capsules, PillTrek

offers the most powerful and versatile electrochemical sensing capabilities within a highly miniaturized form factor (Supplementary Table B.1).

An array of GI biomarker sensors including aptamer-based voltammetric serotonin sensors, enzymatic amperometric glucose sensors, ion-selective potentiometric pH sensors, and impedimetric ionic strength sensors, were developed and validated for the analysis of GI biofluids, such as intestinal fluids and fecal fluids. To achieve high-accuracy in situ sensing in the complex GI environment, various real-time calibration mechanisms were integrated, including an adaptive ratiometric dual-frequency measurement scheme for aptamer-based sensors, as well as pH, ionic

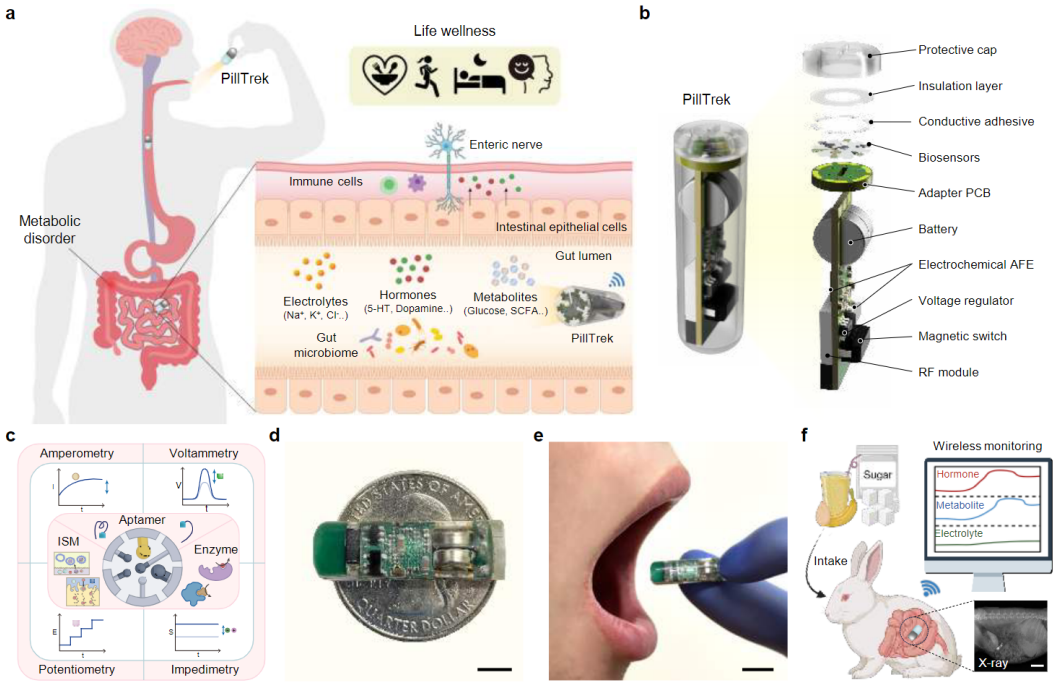


Figure 4.1: PillTrek, an ingestible electrochemical platform for continuous, multiplexed gastrointestinal fluid analysis

(A) Illustration of the PillTrek navigating through the GI tract, flourishing with biochemical markers. 5-HT, serotonin; SCFA, short-chain fatty acid. (B) Schematic of the fully assembled and exploded views of PillTrek, showing components including batteries, electronics, biosensors, and protection. PCB, printed circuit board; AFE, analog front-end; RF, radio frequency. (C) Diagram demonstrating the various recognition elements compatible with PillTrek, such as ion-selective membranes (ISMs), aptamers, and enzymes. The device supports diverse electrochemical techniques, including potentiometry, amperometry, voltammetry, and impedimetry, for detecting a wide range of biochemical markers. (D,E) Photos showcasing the miniature form factor (<1 $cm^3$) of the PillTrek, displayed on a coin (D) and held by a model (E). Scale bars, 0.5 cm and 1 cm, respectively. (F) Schematic illustrating the miniaturized PillTrek monitoring diet-induced biomarker level changes in the intestines of a rabbit model. Scale bar, 3.5 cm.

strength, and temperature compensation for the voltammetric and amperometric sensing.

The fully integrated PillTrek was evaluated in vitro in the intestines of a rat model and in vivo in a rabbit model for the multiplexed analysis of GI biomarkers in response to nutrient-enriched diets (Figure 4.1F). PillTrek has the potential to provide a nuanced biochemical portrait of the GI tract, revealing the intricate and often obscured chemical activities related to gut health, and thereby facilitating the development of personalized monitoring and targeted therapies for safeguarding GI health.

## 4.1 Design of PillTrek for Continuous in Vivo Biochemical Analysis

PillTrek consists of a rectangular main printed circuit board (PCB) (6.5 mm $\times$ 23 mm) for signal processing and wireless communication, and a circular adapter PCB (6.5 mm in diameter) that is mounted perpendicularly to the main PCB to directly interface the sensor array (Figure 4.1B, and Supplementary Figs. B.1 and B.2). The main PCB features a cavity to hold two silver oxide batteries (3.1 V, 16 mAh) that can be remotely disconnected from the circuit via a magnetic reed switch. This design allows the PCBs, once encapsulated in PDMS through injection molding, to be stored next to a magnet for extended periods without draining the battery. During operation, the electronic system can maintain a Bluetooth Low Energy (BLE) connection and perform complex electrochemical analysis sequences continuously for over 22 hours.

Meanwhile, the sensor array is mass-produced sequentially through laser patterning to form vias for contacting the adapter PCB and through inkjet printing to accurately pattern gold, carbon, and silver electrodes (Supplementary Figure B.1). After sensor modification, the sensor array is patterned and conductively affixed to the encapsulated electronic system. Additionally, the array is then protected by a 3D-printed chamber, creating a fully packaged ingestible system with a diameter of 7 mm and a length of 25 mm. This size is comparable to common pills and substantially smaller than most commercial electronic capsule systems (Figure 4.1G,H and Supplementary Figure B.2).

### 4.1.1 Materials and Methods

#### Materials and Reagents

Silver nitrate, iron chloride (III), and hydrogen tetrachloroaurate (III) hydrate were purchased from Alfa Aesar. Mercaptohexanol (MCH), sodium thiosulfate pentahydrate, sodium thiosulfate pentahydrate, PVB resin BUTVAR B-98, tris(hydroxymethyl)aminomethane hydrochloride (Tris-HCl), tris-(2-carboxyethyl)-phosphine hydrochloride (TCEP), ethylenediaminetetraacetic acid (EDTA), Nafion 117, L-lactic acid, hydrochloric acid, and toluene were purchased from Sigma Aldrich. Potassium ferricyanide (III), and potassium ferrocyanide (IV) was purchased from Acros Organics. Potassium chloride, N, N-dimethylformamide, D-glucose anhydrous, and serotonin hydrochloride were purchased from Thermo Fisher Scientific. Sodium chloride, dimethylformamide (DMF), calcium chloride dihydrate, 10× phosphate-buffered saline (PBS), magnesium chloride, and acetic acid were purchased from Fisher Scientific. The ELISA kit for serotonin analysis was purchased from DLD Diagnostika GmbH. Polyethylene terephthalate (PET) films (75 μm thick) were purchased from McMaster-Carr. The serotonin aptamer 5'-Thiol-$C_6$Linker-CGACTGG TAGGCAGATAGGGGAAGCTGATTCGATGCGTGGGTCG-MB-3' was ordered from Integrated DNA Technologies. Carbon ink (5 wt%) and silver ink (25 wt%) were purchased from NovaCentrix. Gold ink (10 wt%) was purchased from C-INK Co. Ltd. PDMS (SYLGARD 184) was purchased from Dow Corning. Serum was purchased from ATCC. Plain Au electrodes (as the control) were fabricated on a PET substrate by photolithography and electron-beam evaporation (30 nm Cr/100 nm Au).

#### Assembly of the Ingestible Capsule Device

A 2-part aluminum mold for the ingestible capsule device, consisting of a cylindrical cavity for device encapsulation and lid for device alignment, was fabricated by milling an aluminum block as designed by Fusion 360. Meanwhile, the main PCB was milled to form a cavity that fits two silver oxide batteries, and nickel tabs were soldered on the inner walls of the PCB cavities for holding and forming an electrical contact with the batteries. A slight extrusion in the main PCB was used as a plug to align and fit into the slot of the adapter PCB, prior to soldering the connection pads (Supplementary Figure B.1). After assembling the PCBs and batteries, the electronic system was fixed on the aluminum mold lid and then submerged into the

PDMS filled aluminum cavity mold. A magnet was attached to the mold during PDMS curing to prevent battery discharge through a PCB mounted magnetic reed switch. After PDMS encapsulation, the sensor array prepared as described in the section below was conductively glued onto the adapter PCB using silver paint, prior to fixing a protective cap fabricated by a resin 3D printer (ELEGOO Mars 3).

**Preparation and Characterization of the Multimodal Sensor Array**

A 50 W $CO_2$ laser cutter (Universal Laser System) was used to pattern vias on a PET substrate, creating electrical contacts between the sensor array and adapter PCB prior to inkjet-printing the electrode arrays. The substrates were then cleaned via $O_2$ plasma surface treatment (Plasma Etch PE-25, 10-20 $cm^3$ $min^{-1}$ $O_2$, 100 W, 150-200 mTorr) to remove debris and enhance surface hydrophilicity. An inkjet printer (DMP-2850, Fujifilm) was employed to print gold, carbon, and silver electrodes, as well as SU-8 for electrode insulation. The reference and working electrodes were further modified via electrochemical deposition (CHI 660E) and drop-casting methods. Both the electrochemical workstation and an ingestible device were applied in the sensor characterization procedures.

**Serotonin sensor:** Aptamers were prepared by dissolving them to a concentration of 100 µM in 1× Tris-EDTA buffer, and then frozen in individual aliquots at -20 °C. The AuNPs electrode was electrochemically cleaned using cyclic voltammetry (CV) in 0.5 M NaOH, executing 100 cycles from -1 to -1.6 V at a scan rate of 1 V $s^{-1}$, and subsequently rinsed with deionized water. Concurrently, TCEP reduction was carried out to reduce disulfide bonds by mixing 5 µl of a 10 µM DNA aliquot and 5 µl of 1 mM TCEP at room temperature in the dark for 1 h, followed by dilution with 1× PBS (pH 7.4) to 2.5 µM. The aptamer (2.5 µM, 5 µl) was immobilized onto the cleaned working electrode by incubation for 2 h at room temperature in the dark, and unbound aptamers were rinsed with 1× PBS. 5 mM MCH in 1× PBS was treated overnight to passivate the unbound electroactive surface of the Au electrodes, and finally the aptamer-modified electrodes were thoroughly rinsed with 1× PBS. For measurements in real biofluids, 0.5 % Nafion was drop-casted and incubated overnight. The Nafion-modified sensors were rinsed with 1× PBS.

**Glucose sensor:** A nanostructured Au film was electrodeposited on the carbon electrodes to increase the electrode surface area, involving multi-potential deposition

in a solution of 50 mM chloroauric acid and 0.1 M HCl, undergoing 1500 cycles (-0.9 V for 0.02 s and 0.9 V for 0.02 s). The Prussian blue (PB) layer was deposited onto the nanostructured Au electrodes in a fresh solution containing 2.5 mM $FeCl_3$, 2.5 mM $K_3[Fe(CN)_6]$, 100 mM KCl, and 100 mM HCl by 20 CV cycles (-0.2 V to 0.6 V versus Ag/AgCl) at a scan rate of 50 mV $s^{-1}$. The NiHCF layer was then deposited in a fresh solution containing 0.5 mM $NiCl_2$, 0.5 mM $K_3Fe(CN)_6$, 100 mM KCl and 100 mM HCl by 25 CV cycles (0 to 0.8 V vs. Ag/AgCl) at a scan rate of 100 mV $s^{-1}$. For an enzyme solution, 1% chitosan was dissolved in a 2% acetic acid by magnetic stirring for 1 h, followed by mixing with 2 mg/ml multi wall carbon nanotubes (MWCNTs) through ultrasonication. A glucose oxidase (GOx) (10 mg $ml^{-1}$ in 1× PBS) was mixed with chitosan/MWCNTs solution with a volume ratio of 2:1. Next, 1 µl of enzyme cocktail was drop-casted onto the NiHCF/PB/carbon electrode and dried. Finally, 2 µl polyurethane (PU) solution containing 15 mg $ml^{-1}$ of PU in THF and N,N'-dimethylformamide (volume ratio 98:2) was drop-casted and dried overnight at 4 °C.

**pH sensor:** The carbon electrode was initially cleaned using 0.5 M HCl by 10 CV cycles (-0.1 V to 0.9 V) at a scan rate of 0.1 V $s^{-1}$. A polyaniline (PANI) film was deposited in a 0.1 M aniline dissolved in 1 M HCl by applying 12 CV cycles (-0.2 to 1 V) at a scan rate of 0.1 V $s^{-1}$. The same deposition procedure was repeated and dried overnight at 4 °C.

**Reference electrode:** A silver layer was deposited onto the AuNPs electrode in a solution containing 250 mM silver nitrate, 750 mM sodium thiosulfate, and 500 mM sodium bisulfite using multi-current deposition (30 s at -1 µA, 30 s at -5 µA, 30 s at -10 µA, 30 s at -50 µA, 30 s at -0.1 mA and 30 s at -0.2 mA), followed by drop-casting a 1 µl of 0.1 M $FeCl_3$ for 1 min. Then, 1 µl of PVB/NaCl solution containing 78.1 mg of PVB and 50 mg of NaCl in 1 ml of methanol was drop-casted onto the Ag/AgCl electrode and air dried overnight at 4 °C.

**Preparation of Simulated Intestinal Fluid (SIF)**

The SIF contains 5.76 mM KCl, 1.44 mM $KH_2PO_4$, 115.4 mM NaCl, 8 mM $Na_2HPO_4$, and 0.33 mM $MgCl_2(H_2O)_6$ in deionized water. The pH was adjusted to 7.0 by adding HCl. [33]

**Electronic System Design and Characterization**

An electronic system is integrated into a highly compact 4-layer PCB, having dimensions of a mere 23 mm × 6.5 mm, crafted using Eagle CAD. The system's energy is harnessed from two series-connected silver oxide batteries (SR521SW; Energizer), delivering a combined voltage of 3.1 V with a capacity of 16 mAh. Power management within the system is diligently administered through a magnetic reed switch (MK24-B-3-OE; Standex-Meder Electronics) and a voltage regulator (ADP162; Analog Devices), ensuring consistent and stable power output. Wireless communication and control processes are managed by an adept RF module (STM32WB1MMC; STMicroelectronics), responsible for wireless data transmission, signal processing, and overseeing the electrochemical instrumentation system, which operates principally through the AD5940 (Analog Devices) and is complemented by a voltage buffer (LPV521; Texas Instruments). The electronic system is proficient in continuous measurement operations, maintaining a power consumption below 340 μW, thereby theoretically allowing for sustained operation for over 22 hours.

The power consumption of the electronic system was measured using a power profiler (PPK2; Nordic Semiconductor), and the dynamic power supply potentials during ingestible device operation were recorded using a multiplexed electrochemical workstation (PalmSens 4; PalmSens). For in vitro characterization of the ingestible device's operation during constant motion and collisions, a clear fishing line was connected to the capsule, and the motion of the capsule was controlled by rotating a 3D-printed reel (ELEGOO Mars 3; ELEGOO) using a stepper motor controlled by an Arduino UNO.

### 4.1.2 Characterization of Sensor Array for Multiplexed Monitoring of GI Biomarkers

A custom-developed miniaturized sensor array was designed for real-time, multimodal monitoring of four distinct biomarkers in GI fluids. Integrated with a versatile electronic system, this sensor array can multiplex amperometric, impedimetric, potentiometric, and voltammetric techniques to interface a wide spectrum of sensors that incorporate recognition elements such as enzymes, ion-selective membranes, and aptamers. For this study, we selected an array of gut biomarkers, including the hormone serotonin, the metabolite glucose, pH, and ionic strength (Figure 4.2A).

The sensor array is constructed on a PET substrate with mass-producible inkjet-printed electrodes, ensuring both adaptability and precision in detection processes (Figure 4.2B). The modified electrode array, mounted on the ingestible electronic system, can accurately detect a wide range of key biomarkers in GI fluids, including serotonin, glucose, pH, and ionic strength (Figure 4.2C–E).

Each sensor within the array has been meticulously optimized for robust detection in GI fluids. For the selective detection of intestinal glucose levels, glucose oxidase (GOx) was immobilized in a highly permeable and biocompatible chitosan matrix atop a Prussian blue (PB) redox mediator layer to facilitate electron transfer from GOx to the electrode. To accommodate the wide range of physiologically relevant glucose levels in the GI tract, a polyurethane (PU) diffusion-limiting layer was coated on the glucose sensor to extend its linear range (Supplementary Figure B.3). The glucose sensor exhibits a consistent linear response to glucose concentrations ranging from 0 mM to 50 mM (Figure 4.2F). The pH sensor features an electrodeposited polyaniline (PANI) layer as an ion-selective membrane and shows a consistent linear response from pH 4 to 8 (Figure 4.2G). To quantify the ionic strength of target solutions, impedance is measured between two carbon electrodes. The ionic strength sensor accurately measures salt concentrations from 0.1× to 2× simulated intestinal fluid (SIF), with 1× SIF approximating 140 mM (Figure 4.2H).

In situ detection of serotonin in the gut fluid is highly challenging due to its low concentration, the complex fluid matrix, and the presence of major interfering electroactive molecules. Traditional oxidation-charge detection approaches, based on fast-scan cyclic voltammetry or differential pulse voltammetry, offer high temporal resolution and sensitivity but fail to selectively monitor basal serotonin levels in gut fluids.[34, 35] To achieve both sensitivity and selectivity for serotonin detection, an inkjet-printed AuNP electrode with a large electroactive surface area was integrated with a serotonin aptamer tagged with the redox molecule methylene blue (MB) (Supplementary Figure B.4). When the aptamer binds to the serotonin molecule, target binding-induced conformational changes alter the distance of the MB redox reporter from the electrode surface, resulting in varied electron transfer efficiency. Nuanced and reversible detection of varying serotonin concentrations can be achieved by quantifying the MB redox signal via square wave voltammetry (SWV). Depending on the SWV frequency, the serotonin aptamer sensor could demonstrate log-linear responses between physiologically relevant serotonin levels (0 to 100 μM) and the SWV peak current height in SIF in a signal-off, non-responsive, or signal-on manner

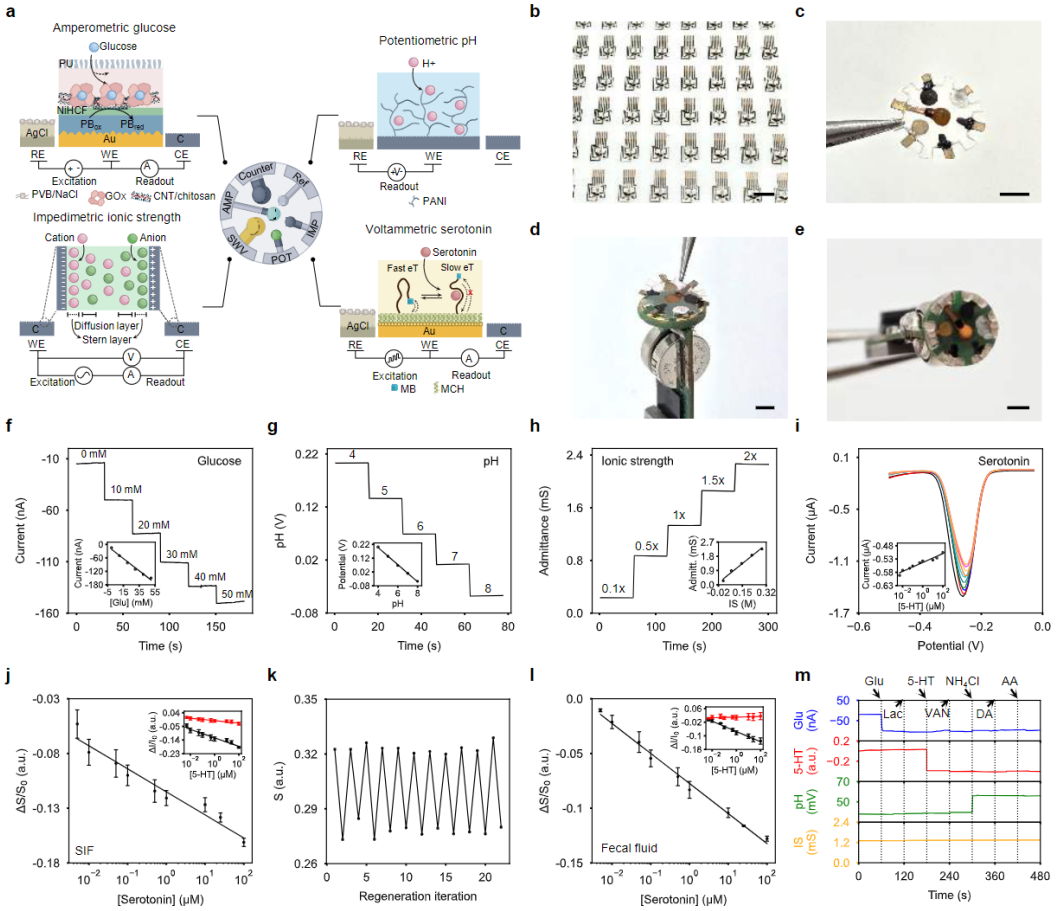


Figure 4.2: Ingestible sensor array of PillTrek for multiplexed detection of gastrointestinal biomarkers

(A) Schematic illustration of inkjet-printed electrochemical sensor array, detailing the operation mechanism for each sensor, including the amperometric enzyme-based glucose sensor, potentiometric ion-selective pH sensor, impedimetric ionic strength sensor, and voltammetric aptamer-based serotonin sensor. PU, polyurethane; CNT, carbon nanotube; RE, reference electrode; WE, working electrode; CE, counter electrode; PVB, polyvinyl butyral; NiHCF, nickel hexacyanoferrate; GOx, glucose oxidase; PANI, polyaniline; MB, methylene blue; eT, electron transfer; MCH, mercaptohexanol. (B) Photo of sensor arrays mass-produced via inkjet printing on a PET substrate. Scale bar, 1 cm. (C-E) Photos of a standalone biosensor array (C) and a biosensor array before (D) and after (E) integration into the ingestible capsule system. Scale bars, 0.2 cm. (F) Amperometric response and corresponding calibration plot (inset) of the glucose sensors in SIF. (G) Potentiometric response and corresponding calibration plot (inset) of the pH sensors in SIF. (H) Impedimetric response and corresponding calibration plot (inset) of the ionic strength sensors in SIF. (I) Square wave voltammetry (SWV) response and corresponding calibration plot (inset) of the serotonin sensors in SIF recorded under a signal-off SWV frequency of 10 Hz. (J) Calibration curve based on the relative ratiometric signal ($S=I_{10Hz}/I_{20Hz}$) of the serotonin sensor in SIF where I represents the SWV peak current height. The inset shows... *Figure caption continues in Footnote 1.*

due to the binding dynamics of the aptamer probe (Figure 4.2I,J[1] and Supplementary Figure B.5). The aptamer conditions for aptamer functionalization, such as concentration and incubation time, were optimized to achieve a high SWV peak current height, thereby enhancing sensitivity (Supplementary Figs. B.6 and B.7).

To mitigate the influence of sensor-to-sensor variations and the complex biofluid matrix to sensing accuracy of the aptamer-based serotonin sensor, a dual frequency method is employed. In this approach, the signal-off or signal-on frequency response is calibrated against the non-responsive frequency response where the sensor response is independent of analyte concentration as the bound and unbound state currents are equal.[36] To maximize sensor performance in SIF, we identified the optimal SWV parameters as follows: responsive frequency of 10 Hz, non-responsive frequency of 20 Hz, and amplitude of 45 mV (Supplementary Figs. B.8 and B.9). With optimized parameters, we were able to achieve a low detection limit of 50 nM and a log-linear sensor response over a wide range of serotonin levels in SIF using this dual-frequency method (Figure 4.2J and Supplementary Note 1). Additionally, the serotonin sensor can be automatically and readily regenerated in SIF as serotonin levels change, indicating its capability for continuous target monitoring (Figure 4.2K). Furthermore, these aptamer-based sensors demonstrated batch-to-batch reproducibility and high stability over a 15-day storage period at 4 °C (Supplementary Figure B.10). To further enhance the sensor performance in biofluids, a 0.5%-Nafion antifouling protective layer was applied (Supplementary Figure B.11).

The developed glucose, pH, and serotonin biosensors were successfully evaluated in real biofluids for target biomarker analysis. In human serum, human fecal fluid, and intestinal fluids collected from rats and rabbits, all biosensors demonstrated stable sensor response and low sensor-to-sensor variations across the physiologically relevant biomarker concentration ranges (Figure 4.2L and Supplementary Figs. B.12-B.17). It should be noted that while the serotonin sensor maintained its original signal-off responsive frequency of 10 Hz, the non-responsive frequencies varied in different sample matrices: 30, 50, 70, and 70 Hz were identified as the

[1]**Continued caption from Figure 4.2...** relative changes in peak current under 10 Hz (red) and 20 Hz (black). $S_0$, relative ratiometric signal at blank serotonin concentration; $I_0$, SWV peak current height at blank serotonin concentration. Error bars represent the s.d. of the mean from three sensors. (K) Continuous sensing and regeneration of a serotonin sensor in SIF containing 0.1 μM and 10 μM serotonin. (L) Calibration curve based on the relative ratiometric signal ($S=I_{10Hz}/I_{70Hz}$) of the serotonin sensor in human fecal fluid. Error bars represent the s.d. of the mean from three sensors. (M) Selectivity test of the sensor array in SIF upon the sequential addition of 10 mM glucose (Glu), 10 mM lactate (Lac), 20 μM serotonin (5-HT), 20 μM vancomycin (VAN), 10 mM ammonium chloride ($NH_4Cl$), 20 μM dopamine (DA), and 20 μM ascorbic acid (AA).

non-responsive frequencies for phosphate-buffered saline, serum, fecal fluid, and intestinal fluids (Supplementary Figure B.16). The accuracy of the serotonin sensors for biofluid analysis was validated using the laboratory gold-standard enzyme-linked immunosorbent assay (ELISA) with rat intestinal fluids, resulting in a linear correlation coefficient of 0.91 between the ELISA and biosensor measurements (Supplementary Figure B.18).

When integrated into the multiplexed sensor patch, all sensors display high selectivity against common interferent molecules such as glucose, lactate, dopamine, vancomycin, ammonium chloride, and ascorbic acid (Figure 4.2M). Additionally, the sensor array's dependence on factors such as solution pH, ionic strength, and temperature was thoroughly studied (Supplementary Figs. B.19-B.22). The glucose, serotonin, and ionic strength sensors showed increased responses with rising temperatures. The serotonin sensor was also found to be sensitive to changes in solution pH and ionic strength. Furthermore, temperature variations affected the electron transfer kinetics of the serotonin sensor, resulting in different non-responsive frequencies. By incorporating real-time sensor calibration based on fluid pH, ionic strength, fluid types, and temperature, accurate in situ gut fluid biomarker analysis can be achieved.

### 4.1.3 System-Level Integration of Ingestible Electronic Device

In the creation of an ingestible electronic system, paramount considerations were directed toward its size, power efficiency, and wireless transmission capabilities to facilitate accurate measurements within the GI tract. Emphasizing miniaturization, PillTrek features a compact form factor, occupying a volume just under 1 $cm^3$, ensuring high ingestibility and easy maneuverability through the GI transit pathways (Figure 4.3A). At its core, the main PCB integrates essential components such as silver oxide batteries, a magnetic reed switch, and a low dropout voltage regulator for stable power delivery to the wireless sensor interface (Figure 4.3B, Supplementary Figure B.23, and Supplementary Table B.2). To provide a stable supply voltage to the analog circuitry, the 3.1 V battery voltage is regulated to 2.8 V for powering the radio frequency (RF) module and electrochemical analog frontend. This wireless sensor interface supports a comprehensive suite of electrochemical techniques, including potentiometry, amperometry, square wave voltammetry, and impedance measurements with data wirelessly transmitted to a custom mobile phone application (Figure 4.3C).

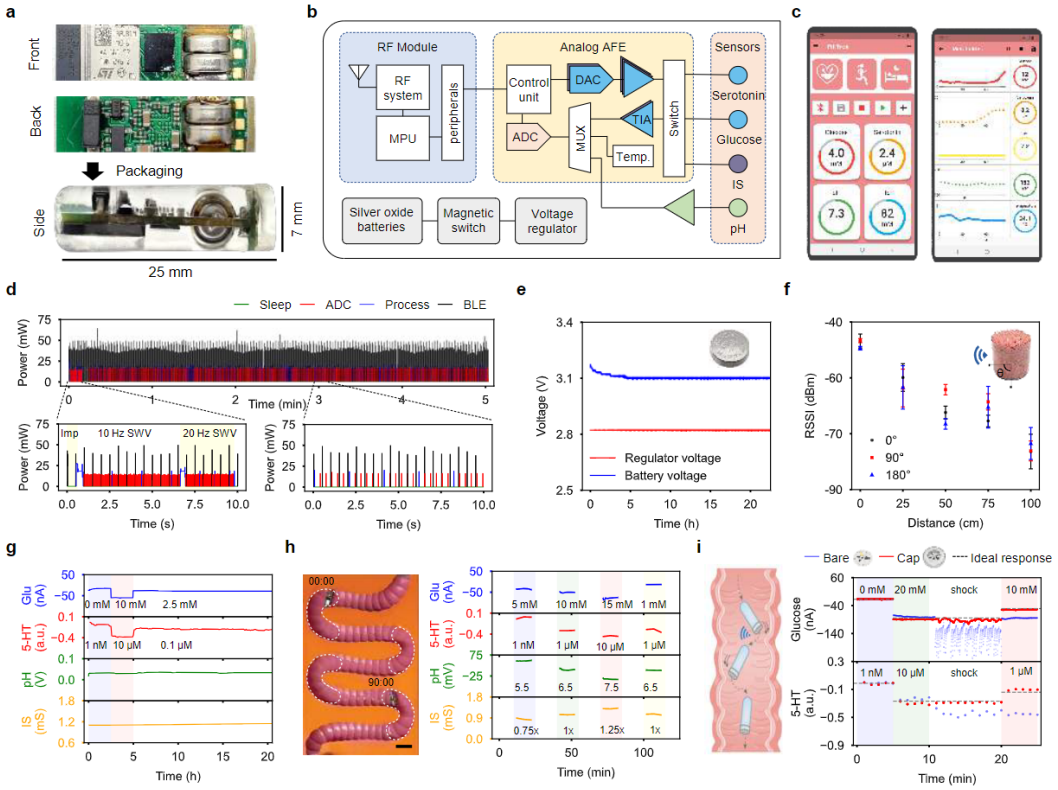


Figure 4.3: The system integration of PillTrek for prolonged wireless operation in GI tract

(A) Photos of the electronic system from the front view (top) and back view (bottom) before PDMS encapsulation, and side view of the fully packaged device. (B) System-level block diagram of PillTrek. RF, radio frequency; MPU, microprocessor unit; ADC, analog to digital converter; DAC, digital to analog converter; MUX, multiplexer; TIA, transimpedance amplifier; Temp., temperature. (C) Custom mobile application for monitoring data from PillTrek. (D) Real-time power consumption profile of PillTrek during continuous multimodal sensing operation over a 5-minute repeated cycle (top), with zoomed-in power profiles during impedance, SWV (bottom left), and multiplexed amperometric, potentiometric, and temperature measurements (bottom right). (E) Long-term battery performance and voltage regulator output potential during continuous multimodal sensing operation. (F) Received signal strength indicator (RSSI) of PillTrek when placed in a meal-filled container, measured by a smartphone from varying angles up to 1 meter away. (G) Long-term operation and multimodal sensing stability of PillTrek in SIF, showing electrochemical responses of glucose, serotonin, pH, and ionic strength sensors. (H) Dynamic biomarker tracking capability of PillTrek as it travels through a phantom intestine model over a 90-min period. Scale bar, 2.5 cm. (I) Glucose (top) and serotonin (bottom) sensor responses of PillTrek devices with and without a protective cap, demonstrating the impact of repeated contact with intestinal tissue.

Power management is a crucial facet of the design strategy, aimed at promoting operational stability and longevity. To optimize power consumption during mul-

timodal operation, a custom-developed embedded algorithm keeps the electronic system in sleep mode for most of the time, waking it briefly for transient data measurement, processing, and transmission events. The system operates on a 5-minute cycle, performing an impedimetric measurement followed by two SWV scans at responsive and non-responsive frequencies in the first 10 s, and then multiplexed potentiometric, amperometric, and temperature measurements for the remainder of the cycle (Figure 4.3D). This approach results in an average power consumption below 340 µW. Powered by two silver oxide batteries in series, the PillTrek system can maintain a stable supply voltage of 2.8 V for over 20 hours (Figure 4.3E).

Furthermore, wireless data transmission capabilities are critical for enabling real-time monitoring of GI biomarkers in vivo. To evaluate the wireless signal strength through tissue, the ingestible capsule, intended for testing in a rabbit model, was placed in the center of a cylindrical tank (12-inch diameter, 12-inch height) filled with ground pork (Figure 4.3F). The receiver signal strength intensity (RSSI) was measured at various angles relative to the capsule's orientation within the tank. Signal strengths higher than -90 dBm were recorded up to a meter away from the cylindrical tank, demonstrating the system's ability to reliably transmit data through dense biological tissue.

The long-term multiplexed sensing capability of the capsule was validated by submerging the device in an intestine-simulating tube filled with SIF, exposing it to dynamic glucose and serotonin concentrations for over 20 hours (Figure 4.3G). This further confirmed the system's ability for continuous operation, the robust integrity of its encapsulation, and the long-term stability of the electrochemical sensors. To simulate in vivo conditions with continuous motion and intermittent fluid availability, the capsule system was pulled through a phantom intestine with SIF-filled wells for 2.5 hours using a stepper motor, reel, and string (Figure 4.3H and Supplementary Figure B.24).

To mitigate the influence of the mechanical contact on sensor performance, a 3D-printed cap was added to the sensor array. Two ingestible devices, one with and one without the protective cap, underwent controlled and repetitive collisions for 10 minutes. The sensor responses following the collisions were recorded (Figure 4.3I, and Supplementary Figure B.25). The capped sensors maintained stable responses during the test, while uncapped sensors experienced altered responses with only the pH and ionic strength sensors recovering functional responses afterward.

As PillTrek is designed for internal use in the GI tract, its biocompatibility is cru-

cial for practical applications. The cell viability of cells seeded on a PillTrek was analyzed using a commercial live/dead kit. Live/dead staining images of human colorectal adenocarcinoma HT29 cells over extended culture periods demonstrated robust cell viability (Supplementary Figure B.26). This underscores the high cytocompatibility of PillTrek, supporting its potential utility for in vivo tests.

## 4.2 Validation of PillTrek for Intestinal Fluid Analysis

### 4.2.1 Animal Study Design

#### Animal Studies

Animal studies were conducted in vitro with a rat model to examine the influence of varying dietary intakes on GI biomarker levels and in vivo with a rabbit model to evaluate the performance of the fully integrated capsule device in a real intestinal environment. These study protocols were approved by the Institutional Animal Care and Use Committee (protocol nos. IA23-1800 for the rodent study and IA23-1865 for the rabbit study) at California Institute of Technology.

**In vitro rat diet studies:** Healthy female Sprague Dawley rats, weighing between 200-300 g, were fasted for 12 hours before replacing their water supply with either more water, sugar-infused water (85.5 g sugar in 250 ml water), or a custom blended smoothie (20 g sugar, 1 banana, and 50 g chia seeds in 250 ml almond milk). After 2 hours of feeding, the animals were sacrificed, and the intestines were extracted for intestinal fluid collection. The collected fluids were analyzed using the ingestible sensor array. The serotonin content of the rat intestinal fluids was further analyzed via ELISA.

**In vivo rabbit studies:** For in vivo evaluation of PillTrek, male *Oryctolagus cuniculus* rabbits, weighing between 3.6 and 4 kg, were fasted for 12 hours prior to surgery. The rabbits were induced with ketamine (35 mg $kg^{-1}$, IM) and xylazine (5 mg $kg^{-1}$, IM), and with acepromazine (0.25-1 mg $kg^{-1}$, SQ) used for fractious rabbits. Glycopyrrolate (0.1 mg $kg^{-1}$, SQ) was administered to reduce salivary secretions, and ophthalmic ointment was applied to the corneas. An intravenous catheter was placed in the ear vein for blood sample collection. The rabbits were transitioned to a gas mask with isoflurane (1-5%) for continuous anesthesia, positioned supine, and monitored with a pulse oximeter and an electrocardiogram (ECG) device. The

surgical area was shaved, disinfected with 70% ethanol, and anesthetic depth was monitored by toe pinching, heart rate, and respiratory rate.

Incisions were made along the midline at the linea alba using a blade. After opening the abdominal cavity, a 1-2 cm incision was made in the duodenum to insert the Pill-Trek and duodenostomy tube for administering PBS containing glucose or serotonin over several hours with a flow rate of 2 ml $h^{-1}$. The intestinal incision was sutured with 5-0 sterile sutures, and the abdominal incision was closed with 4-0 sterile sutures. An X-ray confirmed the capsule's location, and the rabbits remained under anesthesia during imaging and testing. Wireless data from the robotic capsules were transmitted to a laptop or smartphone. Following the procedure, the duodenostomy tube was surgically removed, and another X-ray verified the capsule's position.

### Preparation of Sampled Biofluids

**Human fecal fluid:** Human stool was collected and mixed with deionized water at a 1:2 weight-to-volume ratio. This mixture was centrifuged for 30 minutes at 12,500 revolutions per minute (rpm). The supernatant was collected and filtered using a spin column (Whatman Centrifuge Tube Filter 400 µl, polypropylene, 0.45 µm). The filtered samples were stored at -80 °C.

**Rat intestinal fluid:** Rat intestines were extracted from female Sprague Dawley rats after euthanasia and sectioned into five parts. The interior fluid was collected from each section and centrifuged for 10 minutes at 12,000 rpm to filter out impurities and leftover material. The samples were stored at -80 °C.

### Cytocompatibility Studies

The cytocompatibility of PillTrek was examined by culturing with human colorectal adenocarcinoma HT29 cells (ATCC, cultured under 37 °C and 5% $CO_2$). A commercial calcein AM/ethidium homodimer-1 live/dead kit (Invitrogen) was used to evaluate cell viability. Zeiss confocal microscope was used for cell imaging. Presto blue staining (Invitrogen) was used for quantitative analysis of cell viability and Biotek plate reader was used for optical density measurements.

### 4.2.2 In Vitro Evaluation of PillTrek Intestinal Fluid Biomarker Analysis in Response to Varying Diets

While the blood biomarker levels post-dietary intake are well studied, GI biomarker levels remain obscure due to the inaccessibility of these fluids. However, understanding biochemical profile of intestinal fluids can elucidate the complex interplay of various GI physiologies. Given the well-documented influence of diet on the human gut microbiome, [37] the multimodal ingestible sensor array was first utilized for the in vitro evaluation of GI biomarker levels in response to varying dietary intakes.

After fasting for 12 hours, three groups of rats were either further fasting, given 1 M sugar-infused water, or given a tryptophan-rich smoothie for an additional 2 hours. The intestines of the sacrificed rats were sectioned into 5 segments, and the intestinal fluids were harvested and analyzed with the PillTrek sensor platform (Figure 4.4A–H). Rats that drank sugar water had visibly bloated intestines, likely due to the osmotic effects of the high sugar concentration (Figure 4.4A and Supplementary Figure B.27).

Fasting rats had low glucose concentrations (< 3 mM) throughout the GI tract, with serotonin levels of 4.06±1.55 μM in the small intestine and 5.53±3.31 μM in the large intestine (Figure 4.4B,E,F). Rats exposed to sugar water consumed 9-10 g, resulting in high glucose levels in the small intestine (40.5±7.49 mM) and moderately elevated levels in the large intestine (10.5±6.70 mM) (Figure 4.4C,E). Interestingly, serotonin levels in the small and large intestines were lower than in fasted animals, at 3.24±1.26 μM and 4.13±1.61 μM, respectively (Figure 4.4F). This decrease may be due to high glucose concentrations downregulating tryptophan hydroxylase (TPH) expression or altering metabolic pathways and receptors, thereby reducing serotonin production and release from enterochromaffin cells (ECs). [38, 39]

The last group of rats consumed 6-8 g of a high-tryptophan smoothie containing ingredients such as bananas and chia seeds (Figure 4.4D). Glucose levels in these rats were elevated, though less than those in the sugar water group, at 19.2±9.31 mM in the small intestine and 4.12±0.78 mM in the large intestine, respectively (Figure 4.4E). Serotonin levels in the small and large intestines were substantially higher, at 8.07±3.03 μM and 11.1±2.52 μM, respectively (Figure 4.4F). This increase could be attributed to the high tryptophan content in the smoothie, promoting serotonin production by ECs through the TPH and aromatic amino acid decarboxylase (AAAD) pathway. Elevated serotonin levels in the colon, where the smoothie likely hadn't

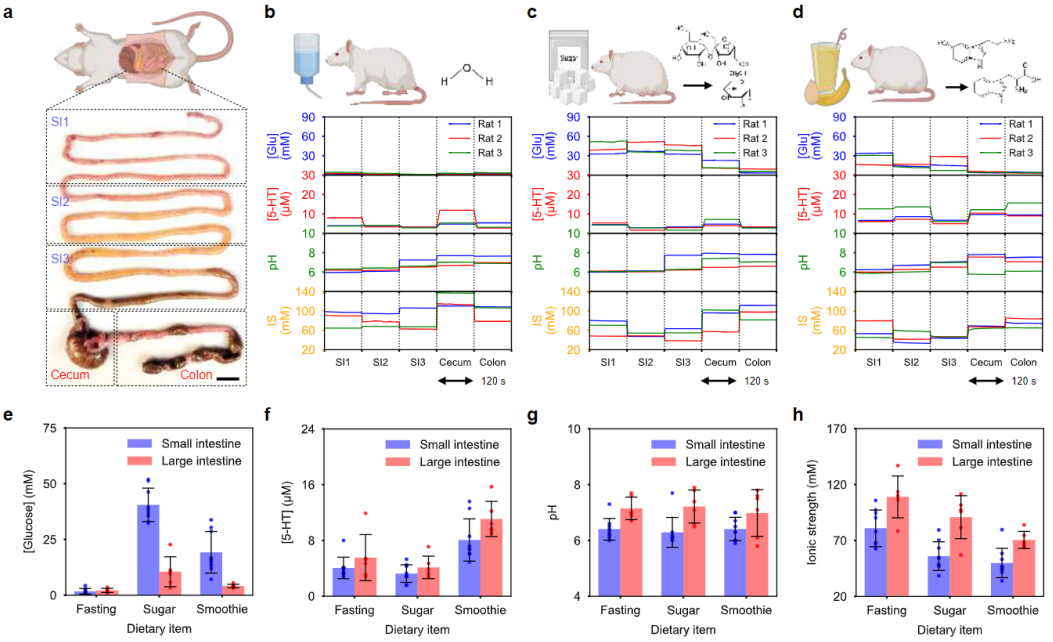


Figure 4.4: In vitro evaluation of PillTrek for assessing the dietary influences on GI biomarker levels in rats

(A) Intestines of a rat divided into 5 sections for regional analysis. SI, small intestine. Scale bar, 1 cm. (B-D) Glucose, serotonin, pH, and ionic strength levels in various intestinal sections of fasted rats (B) rats after sugar water intake (C), and rats after tryptophan-rich smoothie intake (D) measured with the biosensor array. (E-H) Bar plots representing the levels of glucose (E), serotonin (F), pH (G), and ionic strength (H) in the small (SI1, SI2 and SI3) and large (cecum and colon) intestines of rats after different dietary intakes. Error bars represent the s.d. of the mean from intestine samples (n=9 for small intestine, n=6 for large intestine).

reached within 2 hours, suggest additional factors at play. [40]

The pH of the intestinal fluids was consistent across all rats, while ionic strength was highest in fasted rats (Figs. 4.4g,h). Intra-animal trends were also noticeable: glucose levels were consistently higher in the small intestine compared to the large intestine, likely due to the rapid glucose absorption in the small intestine. Conversely, the serotonin levels were generally greater in the large intestine, where enterochromaffin cells are more abundant, and SCFAs from carbohydrate fermentation by gut microbiota stimulate serotonin release. [6] Higher pH and ionic strength levels in the large intestine can be attributed to the production of alkaline substances by gut microbiota and the reabsorption of water and electrolytes, concentrating ions in the intestinal fluid.

### 4.2.3 In Vivo Evaluation of PillTrek in Rabbits for Real-Time GI Biomarker Profiling

The miniaturized capsule is compact enough to easily navigate through the small intestine of a rabbit (diameter of duodenum: 1.71±0.11 cm). [41] To demonstrate PillTrek's capability for real-time in vivo monitoring of biomarkers, rabbits were fasted for 12 hours before the surgical insertion of the ingestible device and a duodenostomy tube into the duodenum. Serotonin and glucose levels in the GI tract were modulated through an peristaltic pump, altering biomarker levels, while the ingestible device performed multiplexed measurements and wirelessly transmitted data on intestinal glucose, serotonin, pH, ionic strength, and temperature levels (Figure 4.5A and Supplementary Figure B.28).

During the procedure, the rabbits' vital signs were continuously monitored to ensure their health, and an x-ray image confirmed the PillTrek's location within a rabbit (Figure 4.5B,C). Throughout the study in two different rabbits, the ingestible systems accurately monitored changes in biomarker concentrations. A continuous infusion of 10 µM serotonin was administered at 30 minutes, followed by an infusion of 20 mM glucose in addition to the 10 µM serotonin at 60 minutes. The sensor responses were calibrated in real-time based on temperature, pH, and ionic strength. PillTrek accurately monitored the trends in which measured serotonin and glucose levels gradually increased after 30 minutes and 60 minutes, respectively, following nutrient delivery, and remained stable over time. Consistent GI pH, temperature and

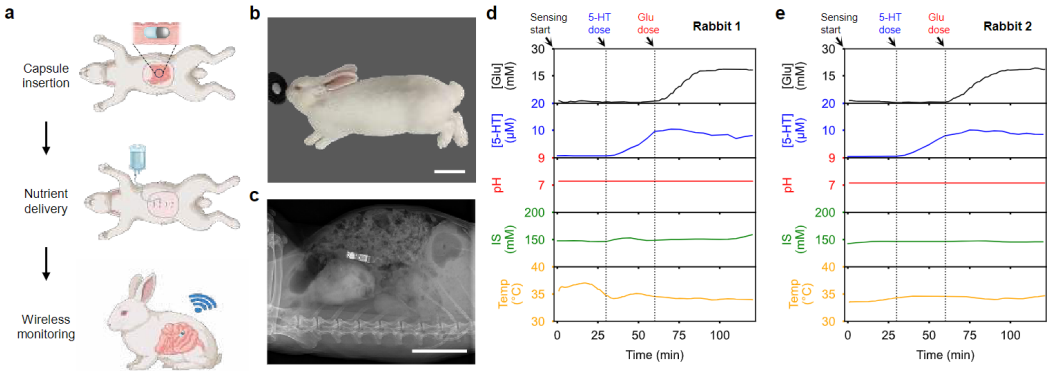


Figure 4.5: In vivo validation of PillTrek for real-time multimodal monitoring of GI biomarkers in rabbits

(A) Schematic illustrating the experimental flow for in vivo rabbit studies. (B) Photo of the sutured stomach of a rabbit during the in vivo study. Scale bar, 10 cm. (C) X-ray image showing the location of PillTrek in the rabbit intestines. Scale bar, 5 cm. (D,E) PillTrek-enabled multimodal GI biomarker profiling in Rabbit 1 (D) and in Rabbit 2 (E).

ionic strength were observed throughout the study. The results demonstrated that PillTrek could reliably perform real-time profiling of GI biomarkers, validating its potential for continuous monitoring in vivo (Figure 4.5D,E).

## 4.3 Conclusion

In this research, the compact ingestible device PillTrek has proven to be a highly valuable tool for advancing our understanding of the GI tract's chemical landscape. By enabling simultaneous, continuous, and multiplexed monitoring of key biochemical markers such as pH, glucose, serotonin, ionic strength, and temperature in complex GI environment, through meticulously designed biosensors and powerful electrochemical techniques, this device overcomes the limitations of traditional invasive methods and existing commercial capsule devices, offering detailed chemical profiles noninvasively.

Looking ahead, PillTrek holds immense potential for widespread adoption in continuous GI health monitoring. By providing real-time insights into the GI tract's biochemical environment, it enhances our ability to explore and monitor the effects of various interventions on GI health. Future directions include expanding the range of detectable biomarkers and refining the technology for human clinical applications, paving the way for personalized GI health monitoring. Additionally, future studies will investigate how different long-term dietary interventions impact GI biomarkers, potentially linking these changes to behavioral outcomes and deepening our understanding of the gut-brain axis. Ultimately, this multi-dimensional approach has the potential to link gut biochemical dynamics with observable behavioral manifestations, enhancing our understanding of GI health and contributing substantially to personalized and precision medicine in both GI and CNS health.

## References

[1] Christoph Steiger et al. "Ingestible electronics for diagnostics and therapy". *Nature Reviews Materials* **2019**, *4* (2), 83–98. DOI: 10.1038/s41578-018-0070-3

[2] Kim E. Barrett et al. *Physiology of the Gastrointestinal Tract*. Google-Books-ID: CNwLlih2C60C. Elsevier, May 10, 2006. 2098 pp. ISBN: 978-0-08-045615-7.

[3] Walburga Dieterich, Monic Schink, and Yurdagül Zopf. "Microbiota in the Gastrointestinal Tract". *Medical Sciences* **2018**, *6* (4), 116. DOI: 10.3390/medsci6040116

[4] Giselle McCallum and Carolina Tropini. "The gut microbiota and its biogeography". *Nature Reviews Microbiology* **2024**, *22* (2), 105–118. DOI: 10.1038/s41579-023-00969-0

[5] Peter Andrey Smith. "The tantalizing links between gut microbes and the brain". *Nature* **2015**, *526* (7573), 312–314. DOI: 10.1038/526312a

[6] Jessica M. Yano et al. "Indigenous Bacteria from the Gut Microbiota Regulate Host Serotonin Biosynthesis". *Cell* **2015**, *161* (2), 264–276. DOI: 10.1016/j.cell.2015.02.047

[7] Kieran Rea, Timothy G. Dinan, and John F. Cryan. "The microbiome: A key regulator of stress and neuroinflammation". *Neurobiology of Stress* **2016**, *4*, 23–33. DOI: 10.1016/j.ynstr.2016.03.001

[8] Asima Bhattacharyya et al. "Oxidative Stress: An Essential Factor in the Pathogenesis of Gastrointestinal Mucosal Diseases". *Physiological Reviews* **2014**, *94* (2), 329–354. DOI: 10.1152/physrev.00040.2012

[9] Piero Vernia et al. "Fecal Lactate and Ulcerative Colitis". *Gastroenterology* **1988**, *95* (6), 1564–1568. DOI: 10.1016/S0016-5085(88)80078-7

[10] Gary M. Mawe and Jill M. Hoffman. "Serotonin signalling in the gut—functions, dysfunctions and therapeutic targets". *Nature Reviews Gastroenterology & Hepatology* **2013**, *10* (8), 473–486. DOI: 10.1038/nrgastro.2013.105

[11] Michael D. Gershon and Jan Tack. "The Serotonin Signaling System: From Basic Understanding To Drug Development for Functional GI Disorders". *Gastroenterology* **2007**, *132* (1), 397–414. DOI: 10.1053/j.gastro.2006.11.002

[12] Camille Martin-Gallausiaux et al. "SCFA: mechanisms and functional importance in the gut". *Proceedings of the Nutrition Society* **2021**, *80* (1), 37–49. DOI: 10.1017/S0029665120006916

[13] Boushra Dalile et al. "The role of short-chain fatty acids in microbiota–gut–brain communication". *Nature Reviews Gastroenterology & Hepatology* **2019**, *16* (8), 461–478. DOI: 10.1038/s41575-019-0157-3

[14] J Fallingborg. "Intraluminal pH of the human gastrointestinal tract". *Danish medical bulletin* **1999**, *46* (3), 183–196

. [15] Press et al. "Gastrointestinal pH profiles in patients with inflammatory bowel disease". *Alimentary Pharmacology & Therapeutics* **1998**, *12* (7), 673–678. DOI: 10.1046/j.1365-2036.1998.00358.x

[16] Eugene B. Chang and Po Sing Leung. “Intestinal Water and Electrolyte Transport”. In: *The Gastrointestinal System: Gastrointestinal, Nutritional and Hepatobiliary Physiology*. Ed. by Po Sing Leung. Dordrecht: Springer Netherlands, 2014, pp. 107–134. ISBN: 978-94-017-8771-0. DOI: 10.1007/978-94-017-8771-0_5. URL: https://doi.org/10.1007/978-94-017-8771-0_5 (visited on 07/30/2024).

[17] D. Maggs, I. MacDonald, and M. A. Nauck. “Glucose homeostasis and the gastrointestinal tract: insights into the treatment of diabetes”. *Diabetes, Obesity and Metabolism* **2008**, *10* (1), 18–33. DOI: 10.1111/j.1463-1326.2007.00737.x

[18] Audren Fournel et al. “Glucosensing in the gastrointestinal tract: Impact on glucose metabolism”. *American Journal of Physiology-Gastrointestinal and Liver Physiology* **2016**, *310* (9), G645–G658. DOI: 10.1152/ajpgi.00015.2016

[19] L. Caetano M. Antunes, Julian E. Davies, and B. Brett Finlay. “Chemical signaling in the gastrointestinal tract”. *F1000 Biology Reports* **2011**, *3*, 4. DOI: 10.3410/B3-4

[20] Dari Shalon et al. “Profiling the human intestinal environment under physiological conditions”. *Nature* **2023**, *617* (7961), 581–591. DOI: 10.1038/s41586-023-05989-7

[21] Kourosh Kalantar-zadeh et al. “Ingestible Sensors”. *ACS Sensors* **2017**, *2* (4), 468–483. DOI: 10.1021/acssensors.7b00045

[22] Qing Cao et al. “Robotic wireless capsule endoscopy: recent advances and upcoming technologies”. *Nature Communications* **2024**, *15* (1), 4597. DOI: 10.1038/s41467-024-49019-0

[23] Kewang Nan et al. “Mucosa-interfacing electronics”. *Nature Reviews Materials* **2022**, *7* (11), 908–925. DOI: 10.1038/s41578-022-00477-2

[24] Jihong Min et al. “Robotics in the Gut”. *Advanced Therapeutics* **2020**, *3* (4), 1900125. DOI: 10.1002/adtp.201900125

[25] Angsagan Abdigazy et al. “End-to-end design of ingestible electronics”. *Nature Electronics* **2024**, *7* (2), 102–118. DOI: 10.1038/s41928-024-01122-2

[26] Giovanni Traverso et al. “First-in-human trial of an ingestible vitals-monitoring pill”. *Device* **2023**, *1* (5), DOI: 10.1016/j.device.2023.100125

[27] Siheng Sean You et al. “An ingestible device for gastric electrophysiology”. *Nature Electronics* **2024**, *7* (6), 497–508. DOI: 10.1038/s41928-024-01160-w

[28] Kourosh Kalantar-Zadeh et al. “A human pilot trial of ingestible electronic capsules capable of sensing different gases in the gut”. *Nature Electronics* **2018**, *1* (1), 79–87. DOI: 10.1038/s41928-017-0004-x

[29] Bo Hou et al. “A swallowable X-ray dosimeter for the real-time monitoring of radiotherapy”. *Nature Biomedical Engineering* **2023**, *7* (10), 1242–1251. DOI: 10.1038/s41551-023-01024-2

[30] M. E. Inda-Webb et al. “Sub-1.4 cm3 capsule for detecting labile inflammatory biomarkers in situ”. *Nature* **2023**, *620* (7973), 386–392. DOI: 10.1038/s41586-023-06369-x

[31] Mark Mimee et al. “An ingestible bacterial-electronic system to monitor gastrointestinal health”. *Science* **2018**, *360* (6391), 915–918. DOI: 10.1126/science.aas9315

[32] Ernesto De la Paz et al. “A self-powered ingestible wireless biosensing system for real-time in situ monitoring of gastrointestinal tract metabolites”. *Nature Communications* **2022**, *13* (1), 7405. DOI: 10.1038/s41467-022-35074-y

[33] André Brodkorb et al. “INFOGEST static in vitro simulation of gastrointestinal food digestion”. *Nature Protocols* **2019**, *14* (4), 991–1014. DOI: 10.1038/s41596-018-0119-1

[34] B. Jill Venton and Qun Cao. “Fundamentals of fast-scan cyclic voltammetry for dopamine detection”. *Analyst* **2020**, *145* (4), 1158–1168. DOI: 10.1039/C9AN01586H

[35] Jinxing Li et al. “A tissue-like neurotransmitter sensor for the brain and gut”. *Nature* **2022**, *606* (7912), 94–101. DOI: 10.1038/s41586-022-04615-2

[36] Hui Li et al. “Calibration-Free Electrochemical Biosensors Supporting Accurate Molecular Measurements Directly in Undiluted Whole Blood”. *Journal of the American Chemical Society* **2017**, *139* (32), 11207–11213. DOI: 10.1021/jacs.7b05412

[37] Lawrence A. David et al. “Diet rapidly and reproducibly alters the human gut microbiome”. *Nature* **2014**, *505* (7484), 559–563. DOI: 10.1038/nature12820

[38] Kara Gross Margolis et al. “Pharmacological reduction of mucosal but not neuronal serotonin opposes inflammation in mouse intestine”. *Gut* **2014**, *63* (6), 928–937. DOI: 10.1136/gutjnl-2013-304901

[39] Leah Zelkas et al. “Serotonin-secreting enteroendocrine cells respond via diverse mechanisms to acute and chronic changes in glucose availability”. *Nutrition & Metabolism* **2015**, *12* (1), 55. DOI: 10.1186/s12986-015-0051-0

[40] S. M. O’Mahony et al. “Serotonin, tryptophan metabolism and the brain-gut-microbiome axis”. *Behavioural Brain Research* **2015**, *277*, 32–48. DOI: 10.1016/j.bbr.2014.07.027

[41] Sabuj Nath et al. “Topographical and biometrical anatomy of the digestive tract of White New Zealand Rabbit (Oryctolagus cuniculus)”. *Journal of Advanced Veterinary and Animal Research* **2016**, *3* (2), 145. DOI: 10.5455/javar.2016.c144

*Chapter 5*

# ELECTROCHEMICAL PERIPLASMIC BINDING PROTEIN FOR NICOTINE SENSING

Prescription drug abuse and addiction remains a significant problem in the U.S. The U.S. opioid epidemic has led to the number of opioid-related deaths doubling over the last 10 years. [1] Continuous molecular monitoring would be an important tool to personalize drug dosing in a therapeutic range (too high may be toxic; too low may be ineffective and potentially lead to drug resistance). Additionally, to treat addiction and combat overdose-related deaths, noninvasively monitoring abused drugs may help to understand individual drug pharmacokinetics to guide minimally effective and safe dosing regimens. For example, opioid users often struggle to shift from potent drugs like heroin to maintenance drugs while avoiding withdrawal symptoms.

A continuous drug monitor requires the design of a label-free, rapid sensor that captures the dynamic drug concentration in an electric signal for real-time data processing and transmission. Wearable sensors for opioid and nicotine detection have been developed relying on direct voltametric detection, [2, 3] however this method is prone to selectivity issues and a high background signal in complex media. Incorporating a bioaffinity element can improve the signal-to-noise ratio and sensor performance in biofluids. But, there is a lack of regenerable biorecognition elements beyond enzymes, which are difficult to synthetically engineer. An enzymatic nicotine sensor utilized cytochrome P450 2B6 (CYP2B6) to oxidize nicotine with a current response of 4.3 nA/μM. [4] Yet, CYP2B6 metabolizes a large variety of drugs. [5] This poor selectivity combined with a low signal response relative to physiological nicotine levels suggest other affinity sensors are needed.

Electrochemical aptamer-based (EAB) sensors have been explored for the noninvasive detection of drugs of abuse. [6, 7] EAB sensors produce a label-free electrochemical signal through binding-induced conformation changes. Some aptamers, including those against drugs including aminoglycoside antibiotics, doxorubicin, and cocaine, have demonstrated spontaneous reversibility enabling continuous monitoring of the sample environment. [8, 9, 10] Aptamer selection processes (SELEX) often screen for high-affinity binding sequences with unpredictable dissociation

constants. Current methods to tune aptamer binding affinities involve destabilizing the structure through post-SELEX modifications, but without available tools to characterize aptamer binding interactions and tertiary structures, aptamers remain a challenge to engineer as continuous electrochemical biorecognition elements.

Periplasmic binding protein (PBP) receptors present a versatile class of bioreceptors that by nature selectively bind and release their targets to mediate bacterial chemotaxis and solute uptake. [11] Over 1000 PBP crystal structures have been characterized, all of which conserve the distinct clamshell binding motion of this receptor class (Figure 5.1A). [12, 13] This generalized binding-induced conformation change can be exploited for signal transduction. Additionally, well-established protein characterization and engineering techniques such as X-ray crystallography and site-directed mutagenesis enable the directed evolution of PBP biosensors. [14]

The binding-induced conformational changes of PBP receptors have been used for fluorometric biosensing by circularly permuting green fluorescent protein (GFP) to the PBP to produce intensity-based sensing fluorescent reporters (iSnFRs) (Figure 5.1B). [15, 16] iSnFRs for a variety of addictive drugs, including nicotine and opioids, have been developed and well-characterized. [17] Optical signal transduction allows for efficient protein screening, selection, and characterization. For on-body continuous sensing, an electrochemical signal is preferred for platform miniaturization and efficient signal processing and communication (Figure 5.1C). Prior work has demonstrated the feasibility of an electrochemical PBP sensor using L-glutamine, glutamate, and maltose binding proteins. [18, 19, 20] We thus aim to adapt the iSnFR construct for electrochemical sensing as a step toward the development of a wearable continuous drug monitor.

Using structure-switching EAB sensors as a framework, we sought to design an electrochemical PBP (ePBP) sensor scheme. An ePBP sensor necessitates (i) redox probe coupling, (ii) oriented immobilization on the electrode surface, and (iii) positional optimization of these two components such that the binding-induced movement of the redox probe relative to the electrode surface is maximized. In this chapter, we discuss the various strategies explored to address these design requirements. We present the preliminary data in developing and optimizing the ePBP sensor design and provide a roadmap forward for continued ePBP development and validation.

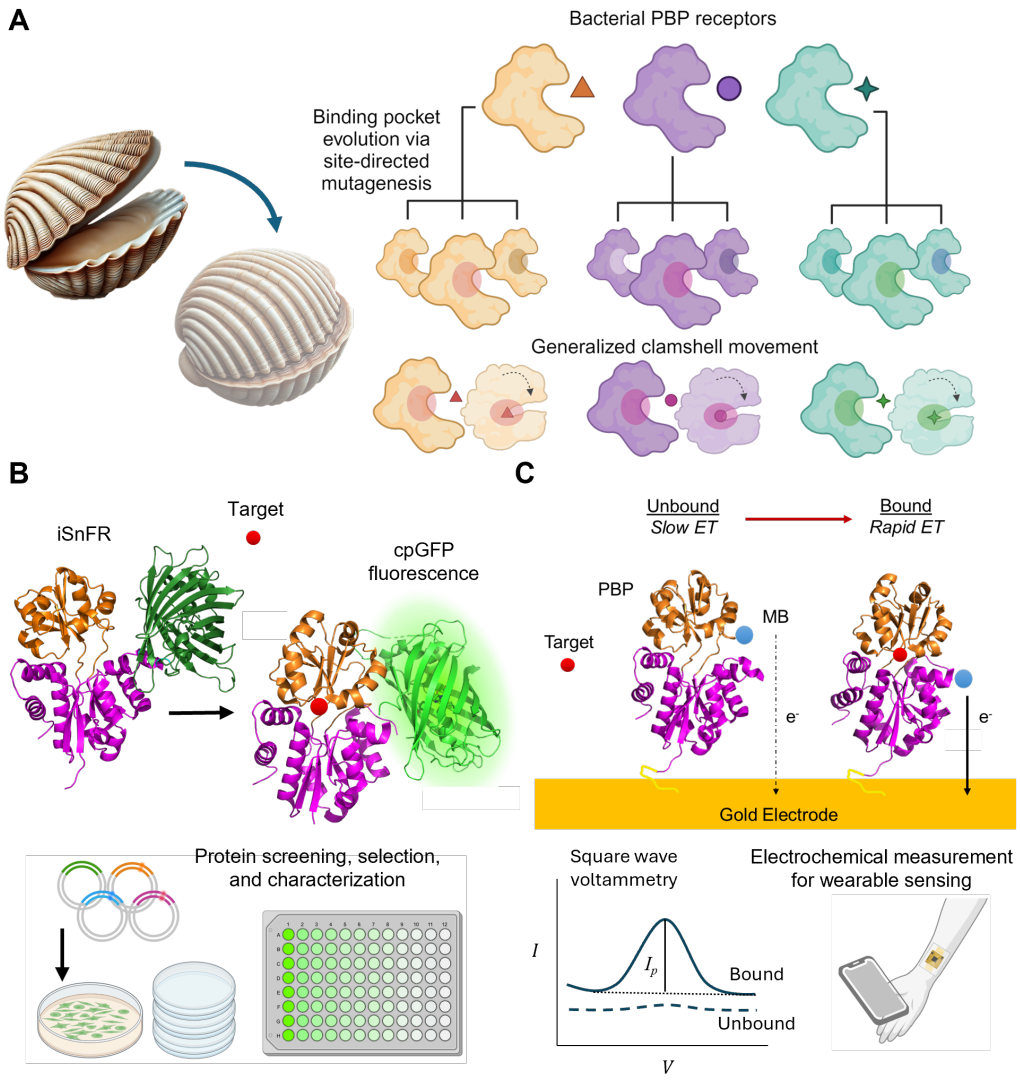


Figure 5.1: Overview of PBP biosensing using fluorescence and electrochemical signal transduction

(A) Naturally occurring bacterial PBP receptors may be expanded to many additional biochemical targets through the use of site-directed mutagenesis while maintaining their clamshell movement in common. This binding-induced conformation change may be exploited for generalized signal transduction across the class of receptors. (B) The iSnFR fluorescent biosensor uses a circularly permuted GFP (cpGFP) to produce a fluorescent signal upon binding. Fluorescent signal transduction allows for high efficiency protein screening, selection, and characterization in solution. (C) Oriented immobilization of redox probe-labeled PBPs on electrodes can be used to produce an electrochemical PBP (ePBP) sensor for continuous wearable sensing. Created with BioRender.com.

## 5.1 Materials and Methods

### Reagents

N-(3-dimethyl-aminopropyl)-N'-ethylcarbodiimide (EDC), N-hydroxysulfosuccinimide sodium salt (sulfo-NHS), 6-mercapto-1-hexanol (MCH), Atto MB2 maleimide, Atto

MB2, methylene blue, hydrochloric acid, and sodium hydroxide were purchased from Sigma Aldrich. Potassium ferricyanide (III) and potassium ferrocyanide (IV) was purchased from Acros Organics. 10× phosphate-buffered saline (PBS), sulfuric acid, potassium chloride, sodium chloride, and (-)-nicotine tartrate were purchased from Fisher Scientific. Dithiobis(C2-NTA) was purchased from Dojindo Molecular Technologies.

**Protein Purification**

iNicSnFR12 wildtype (WT) was prepared using the methods outlined in Ref. [16, 21]. NicPBP12 was isolated from iNicSnFR12 to remove the cpGFP component to evaluate the decoupled bioreceptor's performance and the effect of increased packing density on the sensor performance. Au-binding protein linker sequences were inserted at the N-terminus and the $His_6$-Tag was moved to the C-terminus by Gibson assembly for comparison of oriented protein immobilization schemes.

The crystal structure of iNicSnFR3a was analyzed in apo (PDB: 7s7v) and varenicline bound states (PDB: 7s7t) using PyMOL software.[16] The bound and unbound states were overlaid to analyze the movement of residues. Single-site point mutations were performed to insert cysteine residues at positions of significant movement (>4 Å).

**Redox Labeling**

iNicSnFR12 wildtype and mutants were labeled with Atto MB2 (MB) as a redox probe. Pan-labeling of the iNicSnFR12 was performed using EDC/NHS coupling. 250 mM EDC HCl and 500 mM sulfo-NHS was prepared in pH 5, 10 mM MES buffer. 50 mM stock Atto MB2 was prepared in DMSO. EDC-NHS solution and MB-COOH stock were combined in equal parts, mixed, and reacted for 10 min at RT. Amine-reactive MB was diluted with 20 mM tricine buffer, pH 8 to 2.5 mM MB and combined with 50 µM protein and incubated for 2 h at RT in the dark. Atto MB2 maleimide was coupled to cysteine residues on the protein. 50-100 uM protein was reacted with Atto MB2 maleimide in a ratio based on the number of cysteines present on the protein. The reaction was carried out in 1× PBS, pH 8.0, overnight at RT on a rotator in the dark. After the MB coupling reaction, the protein was purified in 1× PBS, pH 7.4 using a desalting column, followed by 3 passes through a 30 kDa MW spin column, and then was concentrated using a 0.5 mL centrifugal

spin column (Amicon Ultra). Prepared redox-labeled protein was stored in the dark at 4 °C.

### Labeling Characterization

The redox labeling efficiency was evaluated by ultraviolet–visible spectroscopy (UV-vis) (Thermo Scientific NanoDrop). Absorbance measurements were performed at 280 and 395 nm (A280, A395). Calibration curves were developed with the MB dye, $f_\lambda([MB])$, and the protein, $g_\lambda([Protein])$, individually, for each absorbance and applied to the following equations.

$$[Protein] = g_{395}^{-1}(A395)$$

$$[MB] = f_{280}^{-1}\left(A280 - g_{280}([Protein])\right)$$

To characterize which residues on the protein were modified from the redox probe labeling reaction, labeled protein samples were digested and analyzed by UPLC-MS in the Proteome Exploration Laboratory at California Institute of Technology. Protein sample was digested using chymotrypsin, desalted, and analyzed using Eclipse mass spectrometer coupled to Vanquish Neo. Peptides were separated on an Aurora UHPLC Column (25 cm × 75 µm, 1.7 µm C18, AUR3-25075C18-TS, Ion Opticks) with a flow rate of 0.35 µL/min for a total duration of 0.5 hour and ionized at 1.8 kV in the positive ion mode. Data was analyzed using FragPipe (V22.0) to identify the mass shifts for ATTO-MB2 in chymotrypsin-digested iNicSnFR12 WT protein. An unannotated mass shift of 337.1248 Da was found at high amounts likely corresponding to the ATTO-MB2 modification. MS raw data files were searched against the protein sequence using the Proteome Discoverer 3.0 software based on the Sequest HT algorithm. Oxidation / +15.995 Da (M) and ATTO-MB2-3H / +337.1248 Da (K) were set as dynamic modifications; carbamidomethylation / +57.021 Da (C) was set as a fixed modification. The precursor mass tolerance was set to 10 ppm, and fragment mass tolerance was set to 0.6 Da. The maximum false peptide discovery rate was specified as 0.01 using the Target decoy PSM validator Node.

A Tecan Spark M10 96-well fluorescence plate reader (Tecan, Männedorf, Switzerland) was used to measure baseline and drug-induced fluorescence ($F_0$ and $\Delta F$, respectively). 100 nM iNicSnFR12 WT and 3× PBS, pH 7.0 was used in these dose-response relation experiments. cpGFP fluorescence was tested with excitation

at 485 nm and emission at 535 nm. The effective concentration at 50% (EC50) of the maximum response was evaluated.

### Electrode Modification

2 mm diameter Au disk working electrodes (AuE), Ag/AgCl reference electrodes, and platinum wire counter electrodes were purchased from CH Instruments (CHI). All electrochemical sensor characterizations were performed using a CHI 1040C potentiostat.

AuEs were polished and then cleaned electrochemically in 0.5M NaOH for 300 cyclic voltammetry (CV) scans from -1 V to -1.6 V at a scan rate of 1 V $s^{-1}$. AuEs were electrochemically roughened in 0.5 M $H_2SO_4$ using 10,000 pulse cycles alternating between 0 V and 2 V with a 20 ms pulse duration. The electroactive surface area was characterized in 0.05 M $H_2SO_4$ using CV, scanning from 0 V to 1.8 V at a scan rate of 0.1 V $s^{-1}$.

### Protein Immobilization

**Ni/NTA:** Roughened AuEs were immersed in 50 µM $C_2$-NTA prepared in ethanol and incubated overnight at RT. AuEs were rinsed with deionized (DI) water and immersed in 40 mM $NiCl_2$ and incubated for 2 h at RT. AuEs were rinsed with DI water and modified by drop-casting 10 µL of 10 µM $His_6$-tagged protein in 10% glycerol, 1× PBS, pH 7.4, incubated for 1 h at RT in the dark. Electrodes were rinsed and stored in 1× PBS, pH 7.4 at 4 °C until use.

**Au-Binding Peptide Sequence:** Several Au-binding peptide sequences from the literature were tested. The Au-binding sequences were inserted at the N-terminus with a 5× glycine linker before the biosensor domain. The "L" sequence is defined as follows N-term-LKAHLPPSRLPS-GGGGG. [22, 23] The "M" sequence is defined as follows N-term-MHGKTQATSGTIQ-GGGGG. [24, 23] The "AuBP1-2" sequence is defined as follows N-term-WAGAKALVLRRE-GGGGG. [25] Roughened AuEs were modified via drop-casting 1 µM protein in 10% glycerol, 1× PBS, pH 7.4, incubated for 1 h at RT. 5 mM MCH in 1× PBS, pH 7.4 was used to passivate the electrode surface by drop-casting and incubating for 1 h at 4 °C.

### Surface Plasmon Resonance Immobilization Characterization

Surface plasmon resonance (SPR) was used to evaluate the binding affinity of Au-binding peptide sequence linkers. Experiments were conducted using a Sierra SPR-32 Pro (Bruker) high throughput SPR instrument with Orbitor RS2 in the Protein Expression Center at California Institute of Technology. Planar bare Au sensor chips were purchased from XanTec bioanalytics GmbH (Lot.-No.:SPSM Au 0322 P43). The following protocol was applied across the microfluidic chip: 2× degas step; 6× protein application of serial dilution series increasing protein concentration (6.75 nM, 12.5 nM, 25 nM, 50 nM, 100 nM, and 200 nM) with a 30 μL $min^{-1}$ flow rate, 180 s association phase, and 180 s wash phase, with no regeneration between applications; 1× 100 mM NaOH with a 30 μL $min^{-1}$ flow rate, 300 s on phase, and 300 s wash phase; 2× needle wash; 3× regeneration step using 10% bleach with a 30 μL $min^{-1}$ flow rate, 60 s association phase, and 60 s wash phase; 2× needle wash.

### Electrochemical Sensor Characterization

Differential pulse voltammetry (DPV) scans were used to validate electrode modification steps using 2.0 mM $K_4Fe(CN)_6/K_3Fe(CN)_6$ in 0.1 M KCl scanning from -0.2 V to 0.6 V with a pulse width of 0.2 s, increment of 4 mV, and amplitude of 50 mV. CV scans from 0 V to -0.5 V at a scan rate of 0.1 V $s^{-1}$ were performed in 1× PBS, pH 7.4 and 0.25× PBS, pH 7.0. Square wave voltammetry (SWV) was used to measure the reduction of MB by scanning from 0 V to -0.5 V with an increment of 4 mV, amplitude of 50 mV, and variable optimized frequency. SWV measurements were performed by immersing the modified electrodes in 0.25× PBS, pH 7.0 with increasing nicotine concentrations. The peak SWV current response was measured in Python using linear baseline subtraction.

## 5.2 Redox Moiety Labeling of ePBP

Two approaches have previously been used to label an electrochemical PBP with redox moieties. [18, 20] Firstly, the protein may be labeled nonspecifically by reacting amine side chains on native lysine residues distributed throughout the protein. Second, the protein may be labeled at a site-specific location through the insertion of a cysteine residue at a reaction site that exhibits significant movement relative to the anchored position on the electrode. Given that the PBP construct does not have any cysteine residues (two are present in GFP domain of iSnFR),

cysteines are an optimal residue to insert using site-directed mutagenesis and label with thiol-maleimide chemistry. We evaluated the potential of both redox labeling strategies in parallel in developing our nicotine ePBP sensor (Figure 5.2).

The pan-labeling technique may maximize absolute signal by increasing the number of coupled redox probes that may capture movement. Takamatsu et al. [18] modified a Ni/NTA/$His_6$ immobilized L-glutamine-binding protein with amine-reactive phenazine ethosulfate for the nonspecific modification of solvent-exposed lysine groups. For a signal-on sensor with a labeled binding reaction, such as a sandwich immunosensor, nonspecific labeling of surface-exposed residues is optimal to maximize the signal-on current response associated with a binding event. [26] However, for a reagentless sensor where the redox moiety is always present at the electrode surface, more redox probes may lead to a higher background signal. Sensors exploiting a binding-induced conformation change rely on redox probes to move directionally away or toward the working electrode. During the complex binding interaction between a protein and its ligand, some positions on the protein may move in opposite directions such that nonspecific pan-labeling results in a diminished signal change. Ideally, activated bioreceptors across the sensor surface would move in concert to produce an additive signal response.

iNicSnFR12 and NicPBP12 contain about 50 and 30 lysine residues, respectively. Chymotripsin digestion and UPLC-MS characterization of lysine-labeled iNicSnFR12 reaction revealed the positions of 24 sites that are labeled with MB within a sample (Figure 5.2A,B). We improved upon the PBP redox probe labeling methods of prior art by performing coupling in solution rather than on the electrode to enhance the labeling efficiency, to remove excess unbound MB, and to characterize the labeled protein. The differential absorption spectra of GFP and MB allowed for the labeling ratio of MB to protein to be determined with measurements at 280 nm and 395 nm wavelengths (Figure 5.2C, Supplementary Figure C.1). Using EDC/NHS coupling in a 50:1 ratio of MB to protein, we found that 1.2 lysines were labeled with MB on average.

Site-specific labeling may enhance the signal-to-noise ratio by ensuring that all redox probes move in coordination assuming an oriented protein monolayer. Candidate insertion sites were identified by overlaying crystal structures of iNicSnFR3a in the apo and varenicline bound states and measuring the change in position (Figure 5.2D). Five residues were identified on the top lobe of the PBP with estimated movement in the range of 4.5-7.2 Å. iNicSnFR3a was oriented using the N-terminus as an anchor,

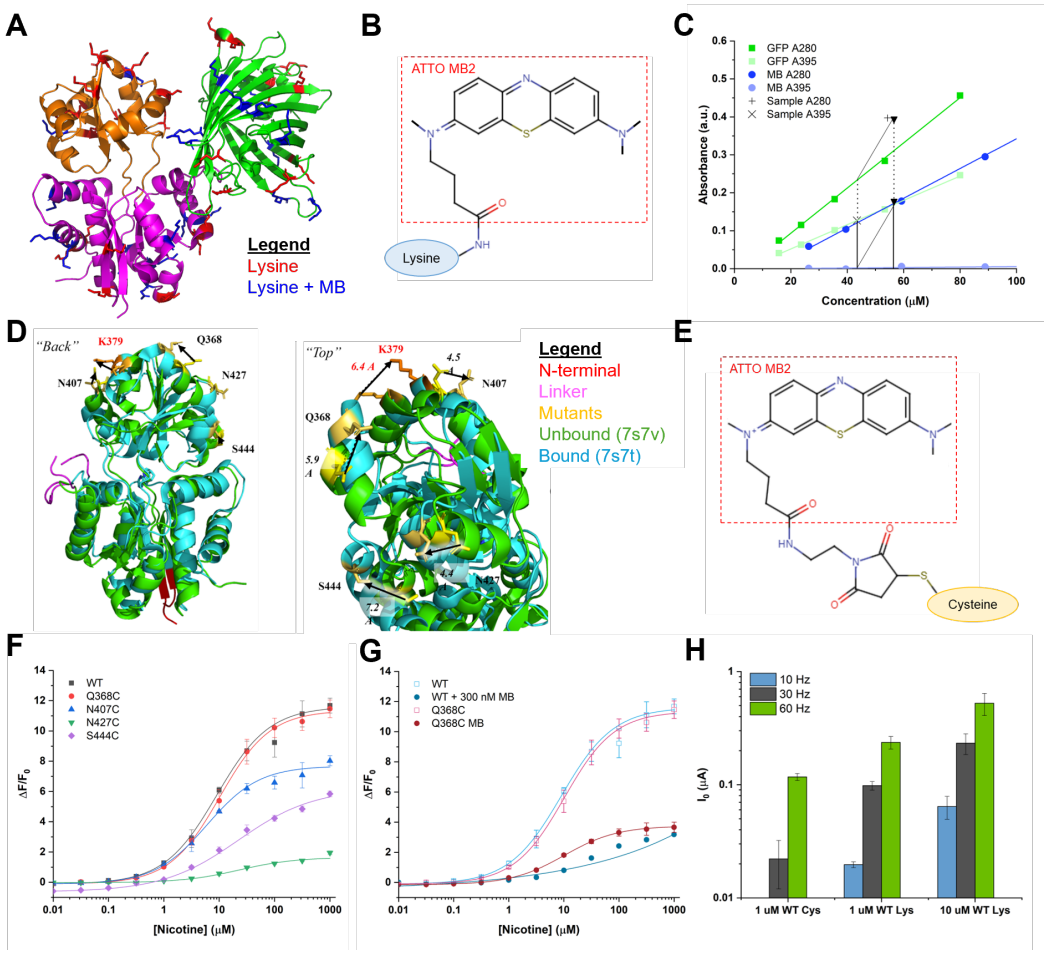


Figure 5.2: Redox moiety labeling of iNicSnFR12

(A) iNicSnFR12 contains 51 lysines with 24 labeled positions (blue) during nonspecific pan-labeling with MB. (B) Chemical drawing of MB conjugation to the lysine amine side chain. (C) Calibration plots for GFP concentration and MB concentration. The concentration of protein is determined by the absorbance at 395 nm, and then mapped to the 280 nm absorbance, which is subtracted from the sample absorbance at 280 nm to determine the MB contribution. (D) Overlay of the apo and bound states with movement vectors of candidate positions for site-specific labeling. (E) Chemical drawing of MB conjugation to the cysteine thiol side chain. (F) Dose-response relations for iNicSnFR12 cysteine mutants. (G) Dose-response relation for iNicSnFR12 WT in the presence of 300 nM free MB and Q368C mutant labeled with MB. (H) Comparison of the background SWV current response at different frequencies using iNicSnFR12 WT labeled at either cysteine or lysine residues. The protein was immobilized at 1 or 10 μM on Ni/NTA/Au electrodes and tested in 0.25× PBS, pH 7.0. Error bars represent the s.d. of the mean (n=2,3,3).

so promising candidates would require a significant movement perpendicular to the anchored electrode plane. Among the five residue candidates, Q368 appeared to have the largest perpendicular vector component. Five mutants of iNicSnFR12 were developed through the site-directed insertion of a cysteine residue, including

Q368C, N407C, N427C, S444C, and a quad mutation to couple MB (Figure 5.2E). The cysteine mutants were evaluated relative to iNicSnFR12 WT to ensure that nicotine binding performance was conserved (Figure 5.2F, Supplementary Figure C.2). Q368C nicotine binding and GFP activation is not significantly impacted by the cysteine insertion. N407C and S444C exhibit a change in the normalized fluorescence indicative of impacted GFP activation, but the EC50 remains consistent within the range of 5-11 μM.

Cysteine residues of iNicSnFR12 and Q368C were labeled with MB with a labeling ratio of 1.7 and 1.8 MB to protein, respectively. These results demonstrate that the pair of cpGFP cysteine residues are being modified (Supplementary Figure C.3). Dose response curves of the unlabeled and labeled biosensor were compared (Figure 5.2G, Supplementary Figure C.4). It was found that the MB labeled response was consistently lower but that EC50 values were maintained. A control of iNicSnFR12 WT mixed with 300 nM free methylene blue demonstrated that MB seems to impact the fluorescence output rather than receptor function. The contribution of cpGFP cysteines to the MB signal was evaluated by substituting C223 residue with threonine (C223T) (Supplementary Figure C.5). Removal of C223 reduces the SWV current response in comparison to MB-labeled WT. cpGFP cysteines are located closer to the electrode surface assuming N-terminus anchoring than Q368C, so a MB redox probe at these locations would provide a larger signal contribution. A decrease in signal for the C223T Q368C mutant indicates that the surface-exposed Q368C mutant is more likely labeled relative to the internal C245 residue.

Comparing the magnitude of the SWV current response we see that MB coupling to lysine residues results in a larger signal than the cysteine modification (Figure 5.2H). Despite iNicSnFR12 WT having a higher labeling ratio in the cysteine reaction over the lysine reaction, the lysine labeling positions the MB on average closer to the electrode surface to produce a larger signal. This agrees with UPLC-MS analysis that demonstrated that of the 24 labeled lysine positions, 11 were in the bottom lobe (N-terminus labeling makes 12), 11 were in the cpGFP, and 2 were in the top lobe. Broad lysine residue screening may identify key positions for site-specific cysteine insertions. Combining these two techniques for redox moiety labeling may improve the performance of the electrochemical signal transduction in an ePBP sensor.

## 5.3 Oriented Immobilization of ePBP on Gold

Key to the coordinated movement of a binding-induced conformation change is the oriented immobilization of the bioreceptor. ePBP designs in the literature have relied on $His_6$-Tag coordination with nickel [20, 18] and gold-thiol binding through site-inserted cysteine residues. [19] Ni/NTA is a well-established surface for protein capture that makes use of the already present $His_6$-Tag used for protein purification. Yet, in comparison to absorption on Au, Ni/NTA reduces the electron tunneling leading to a lower current response by MB-labeled iNicSnFR12 WT (Supplementary Figure C.6). Additionally, having a variety of linker options will be ideal to optimize the modification pair for immobilization and redox labeling.

Au-binding peptide (AuBP) sequences were explored as an alternative to Ni/NTA immobilization. AuBP have been used previously to enhance the direct electron transfer of the redox enzyme carbon monoxide dehydrogenase through oriented immobilization. [22] A selection of three promising AuBP from the literature were incorporated at the N-terminus and were tested in the iNicSnFR12 Q368C mutant. Initial electrochemical testing appeared promising, but led to batch-to-batch inconsistencies and potential washing effects (Supplementary Figure C.7). We evaluated the iNicSnFR12 AuBP binding affinity using surface plasmon resonance (SPR) (Figure 5.3). Negative controls revealed that iNicSnFR12 WT aggregates on the gold surface. This result is likely not due to the Au-thiol binding at GFP cysteine residues since the C223T mutant displays similar resonance despite substitution of the surface-exposed cysteine residue. Among the AuBP, AuM had the highest binding affinity to gold, and repeating the AuBP sequence in duplicate enhanced the binding affinity for each sequence.

Oriented gold binding must compete with amorphous gold binding, and it appears that the AuBP sequences do not provide the binding affinity necessary for robust immobilization. Moving forward, a Ni/NTA self-assembled monolayer (SAM) remains a promising method for oriented protein immobilization. AuBP sequence sensor results indicated that passivation of the electrode surface using MCH is important to reduce background signal. MCH passivation should be tried post-Ni/NTA SAM modification in future design iterations in an effort to reduce the background signal and improve the MB peak resolution.

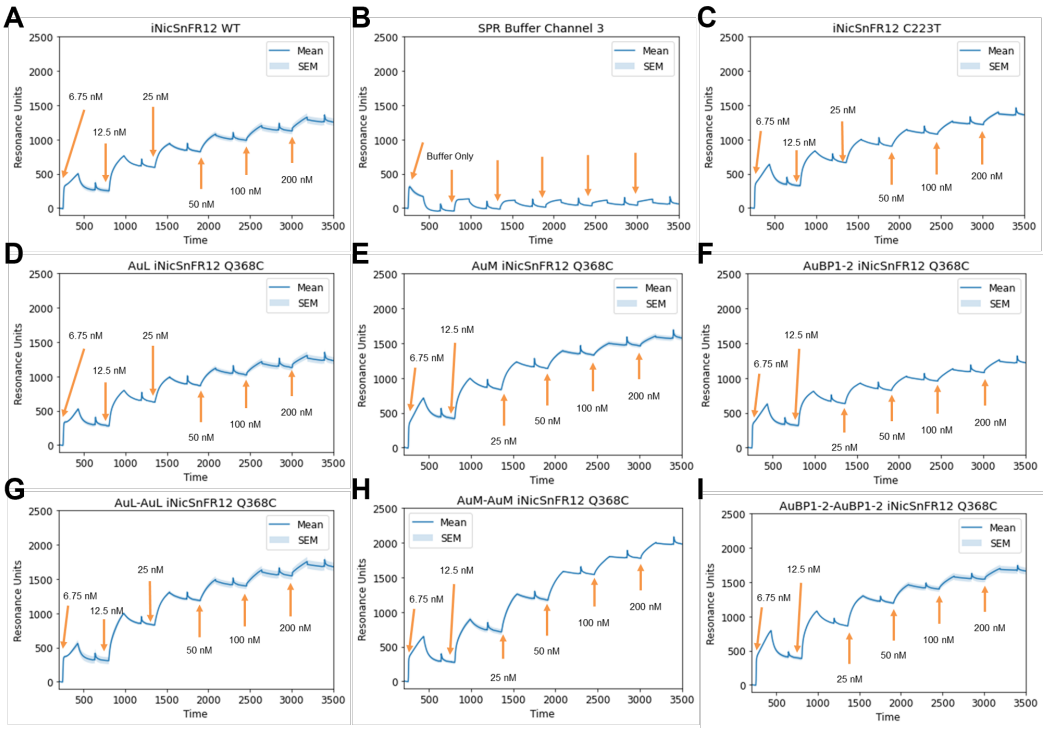


Figure 5.3: SPR evaluation of iNicSnFR12 immobilization using Au-binding peptide sequences

SPR association and dissociation cycles to gold of (A) iNicSnFR12 WT, (B) buffer control, (C) iNicSnFR12 C223T, (D) AuL iNicSnFR12 Q368C, (E) AuM iNicSnFR12 Q368C, (F) AuBP1-2 iNicSnFR12 Q368C, and (G-I) repeated Au-binding sequences of L, M, and AuBP1-2.

## 5.4 Electrochemical Characterization of ePBP Nicotine Sensor

Preliminary results of an electrochemical iNicSnFR12 immobilized using $His_6$-Tag/Ni/NTA affinity binding and probed with MB-coupled lysine residues demonstrate the potential for this sensor scheme to be used for the micromolar detection of nicotine (Figure 5.4A). This ePBP scheme produces clear SWV current peaks associated with the reduction of MB around -0.22V (Figure 5.4B). The peak current response for SWV at 10 Hz is associated with a linear signal-off response (Figure 5.4C). The sensor demonstrates good stability over repeated measurements and a clear difference is observed between the signal-off nicotine response and signal-off artifacts due to signal drift (Figure 5.4D,E). For use as a continuous sensor, the ePBP must be regenerable to handle dynamic analyte concentrations. The ePBP sensor demonstrated good regeneration over 3 cycles of alternating between 0 and 10 µM nicotine solutions (Figure 5.4F).

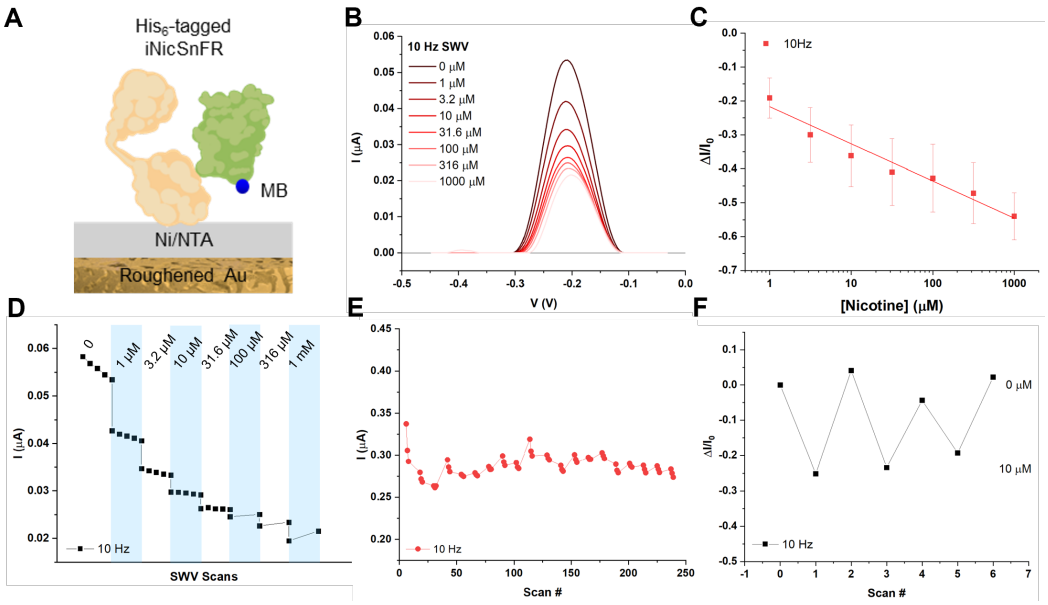


Figure 5.4: Electrochemical characterization of iNicSnFR12 with MB-labeled lysine residues on Ni/NTA/Au electrodes

(A) Sensor scheme. (B) 10 Hz SWV traces for the ePBP sensor immersed in increasing nicotine concentrations in 0.25× PBS, pH 7.0. (C) Calibration plot of the normalized SWV peak current as a function of [Nicotine] using 3 min incubation periods. Error bars represent the s.d. of the mean (n = 4). (D) Sequential concentration testing indicates that the sensor becomes more stable over repeated scans. (E) Sensor stability in 0.25× PBS, pH 7.0 buffer during repeated SWV scanning. Initial scans excluded due to time-dependent variable recovered signal. Repeated 10 Hz measurements were made with a 10 s intermediate quiet time. (E) Sensor regeneration as it alternates between buffer and 10 µM nicotine with a 3 min incubation period.

Further sensor characterization is necessary for confidence in the ePBP sensor scheme. The selectivity of the ePBP sensor against endogenous small molecules must be evaluated along with the performance in biofluids. Additionally, future experiments are needed to determine the sensor time resolution. The sensor should be tested in a flow cell with high SWV sampling frequencies as the nicotine concentration is stepped up and down.

The nanoampere current response of this sensor scheme is an area for improvement and continued optimization. AuEs were electrochemically roughened to enhance the electroactive surface area and enhance electron transfer (Supplementary Figure C.8). [27] Other nanostructured electrodes may be explored to improve electron mobility and signal transduction. Additionally, the signal may be increased by enhancing the efficiency of the EDC/NHS AttoMB2 labeling reaction to maximize the amount of redox probes per protein. Removal of the GFP for this sensor scheme

needs to be tested to understand how packing density increases with NicPBP12.

## 5.5 Conclusion and Future Work

PBPs represent a class of bioreceptors that bind target ligands with high specificity and efficient binding kinetics naturally designed for chemical sensing by bacteria. The hinge-like bending between the two lobes results in a large mechanical movement upon binding. Our initial results demonstrate that this movement can be transduced into an electrochemical signal through the coupling of redox probes to the protein cleft and oriented monolayer assembly on an electrode surface.

Further sensor design iteration and optimization is needed to improve the performance of the sensor. Different redox moieties should be surveyed since they vary in electron transfer rate, stability, and pH-sensitivity. [28, 29] Aside from methylene blue, the performance of ferrocene, Ru(II), and phenazine derivatives should be evaluated. Pairwise positional optimization of redox probe and anchor are needed. Using the crystal structure of iNicSnFR12, residue movement relative to the electrode plane may be simulated with different anchor positions to identify the best candidate anchor and redox coupled residue pair based on movement and Debye lengths from the electrode. Additionally, protein immobilization with multiple anchors should be evaluated as it may both enhance the stability of the protein orientation and the stability of the monolayer under sample flow rates. [22]

ePBP sensors have high potential to be a generalizable sensing approach through the directed evolution of PBP receptor classes to desired small molecule and peptide targets. To validate the generalizability of this sensor scheme, future work will test the electrochemical translation of other OpuBC mutants for which iSnFR cpGFP fluorescence can be used as a control for protein characterization. This work may enable a pipeline of continuous drug monitors based on iDrugSnFR screening. [21] We will then confirm if this sensor scheme can be extended to other classes of PBPs beginning with those previously reported in the literature, including maltose binding protein and glutamine binding protein. Additionally, glucose binding protein may be explored as a non-enzymatic CGM. Assuming generalizability, screening methods will need to be optimized for ePBP pipeline efficiency. Incorporating a working cpGFP domain for screening each PBP, only to remove it for electrochemical modification will be tedious. Future work will be needed to develop a method of large batch electrochemical screening of PBP constructs ideally in cell lysate.

In summary, ePBP sensors are worthwhile exploring for the development of continu-

ous reagentless non-enzymatic electrochemical sensors. Our initial work progresses the development of an ePBP-based continuous nicotine monitor with the potential for expansion to opioids, antidepressants, and other psychoactive drugs. Continuous drug monitors may be applied in future wearable devices for sweat analysis, thus requiring additional considerations for ePBP sensor design. The development of such wearable drug monitoring devices has high potential to curb addiction through personalized and safe dosing regimens and prevent overdose deaths with platform drug toxicity and vital sign monitoring.

## References


[1] FB Ahmad et al. *Provisional Drug Overdose Data*. National Center for Health Statistics. July 8, 2024. URL: https://www.cdc.gov/nchs/nvss/vsrr/drug-overdose-data.htm (visited on 08/03/2024).

[2] Rupesh K. Mishra et al. "Continuous Opioid Monitoring along with Nerve Agents on a Wearable Microneedle Sensor Array". *Journal of the American Chemical Society* **2020**, *142* (13), 5991–5995. DOI: 10.1021/jacs.0c01883

[3] Eda Mehmeti et al. "Electrochemical determination of nicotine in smokers' sweat". *Microchemical Journal* **2020**, *158*, 105155. DOI: 10.1016/j.microc.2020.105155

[4] Li-Chia Tai et al. "Nicotine Monitoring with a Wearable Sweat Band". *ACS Sensors* **2020**, *5* (6), 1831–1837. DOI: 10.1021/acssensors.0c00791

[5] William D. Hedrich, Hazem E. Hassan, and Hongbing Wang. "Insights into CYP2B6-mediated drug–drug interactions". *Acta Pharmaceutica Sinica. B* **2016**, *6* (5), 413–425. DOI: 10.1016/j.apsb.2016.07.016

[6] Xiaoyu Zhang et al. "Integrated Aptasensor Array for Sweat Drug Analysis". *Analytical Chemistry* **2022**, *94* (22), 7936–7943. DOI: 10.1021/acs.analchem.2c00736

[7] Obtin Alkhamis et al. "High-Affinity Aptamers for In Vitro and In Vivo Cocaine Sensing". *Journal of the American Chemical Society* **2024**, *146* (5), 3230–3240. DOI: 10.1021/jacs.3c11350

[8] Netzahualcóyotl Arroyo-Currás et al. "Real-time measurement of small molecules directly in awake, ambulatory animals". *Proceedings of the National Academy of Sciences* **2017**, *114* (4), 645–650. DOI: 10.1073/pnas.1613458114

[9] Ji-Won Seo et al. "Real-time monitoring of drug pharmacokinetics within tumor tissue in live animals". *Science Advances* **2022**, *8* (1), eabk2901. DOI: 10.1126/sciadv.abk2901

[10] Philippe Dauphin-Ducharme et al. "Electrochemical Aptamer-Based Sensors for Improved Therapeutic Drug Monitoring and High-Precision, Feedback-Controlled Drug Delivery". *ACS Sensors* **2019**, *4* (10), 2832–2837. DOI: 10.1021/acssensors.9b01616

[11] Mary A Dwyer and Homme W Hellinga. "Periplasmic binding proteins: a versatile superfamily for protein engineering". *Current Opinion in Structural Biology* **2004**, *14* (4), 495–504. DOI: 10.1016/j.sbi.2004.07.004

[12] Giel H. Scheepers, Jelger A. Lycklama a Nijeholt, and Bert Poolman. "An updated structural classification of substrate-binding proteins". *FEBS Letters* **2016**, *590* (23), 4393–4401. DOI: 10.1002/1873-3468.12445

[13] Shantanu Shukla, Dean A. Myles, and Matthew J. Cuneo. "Mapping periplasmic binding protein oligosaccharide recognition with neutron crystallography". *Scientific Reports* **2022**, *12* (1), 17647. DOI: 10.1038/s41598-022-20542-8

[14] Katie A. Edwards. "Periplasmic-binding protein-based biosensors and bioanalytical assay platforms: Advances, considerations, and strategies for optimal utility". *Talanta Open* **2021**, *3*, 100038. DOI: 10.1016/j.talo.2021.100038

[15] Amol V. Shivange et al. "Determining the pharmacokinetics of nicotinic drugs in the endoplasmic reticulum using biosensors". *Journal of General Physiology* **2019**, *151* (6), 738–757. DOI: 10.1085/jgp.201812201

[16] Aaron L Nichols et al. "Fluorescence activation mechanism and imaging of drug permeation with new sensors for smoking-cessation ligands". *eLife* **2022**, *11*, e74648. DOI: 10.7554/eLife.74648

[17] Anand K. Muthusamy et al. "Three Mutations Convert the Selectivity of a Protein Sensor from Nicotinic Agonists to S-Methadone for Use in Cells, Organelles, and Biofluids". *Journal of the American Chemical Society* **2022**, DOI: 10.1021/jacs.2c02323

[18] Shouhei Takamatsu et al. "Continuous electrochemical monitoring of L-glutamine using redox-probe-modified L-glutamine-binding protein based on intermittent pulse amperometry". *Sensors and Actuators B: Chemical* **2021**, *346*, 130554. DOI: 10.1016/j.snb.2021.130554

[19] Elnaz Zeynaloo et al. "Design of a mediator-free, non-enzymatic electrochemical biosensor for glutamate detection". *Nanomedicine: Nanotechnology, Biology and Medicine* **2021**, *31*, 102305. DOI: 10.1016/j.nano.2020.102305

[20] David E. Benson et al. "Design of Bioelectronic Interfaces by Exploiting Hinge-Bending Motions in Proteins". *Science* **2001**, *293* (5535), 1641–1644. DOI: 10.1126/science.1062461

[21] Zoe Beatty et al. “Fluorescence Screens for Identifying Central Nervous System–Acting Drug–Biosensor Pairs for Subcellular and Supracellular Pharmacokinetics”. *BIO-PROTOCOL* **2022**, *12* (22), DOI: 10.21769/BioProtoc.4551

[22] Stacy Simai Reginald et al. “Control of carbon monoxide dehydrogenase orientation by site-specific immobilization enables direct electrical contact between enzyme cofactor and solid surface”. *Communications Biology* **2022**, *5* (1), 390. DOI: 10.1038/s42003-022-03335-7

[23] Hyeryeong Lee et al. “Peptide sequence-driven direct electron transfer properties and binding behaviors of gold-binding peptide-fused glucose dehydrogenase on electrode”. *iScience* **2021**, *24* (11), 103373. DOI: 10.1016/j.isci.2021.103373

[24] Stanley Brown. “Metal-recognition by repeating polypeptides”. *Nature Biotechnology* **1997**, *15* (3), 269–272. DOI: 10.1038/nbt0397-269

[25] Zak E. Hughes et al. “Tuning Materials-Binding Peptide Sequences toward Gold- and Silver-Binding Selectivity with Bayesian Optimization”. *ACS Nano* **2021**, *15* (11), 18260–18269. DOI: 10.1021/acsnano.1c07298

[26] Jiaobing Tu et al. “A wireless patch for the monitoring of C-reactive protein in sweat”. *Nature Biomedical Engineering* **2023**, *7* (10), 1293–1306. DOI: 10.1038/s41551-023-01059-5

[27] Kaiyu Fu et al. “Accelerated Electron Transfer in Nanostructured Electrodes Improves the Sensitivity of Electrochemical Biosensors”. *Advanced Science* **2021**, *8* (23), 2102495. DOI: 10.1002/advs.202102495

[28] Di Kang et al. “Survey of Redox-Active Moieties for Application in Multiplexed Electrochemical Biosensors”. *Analytical Chemistry* **2016**, *88* (21), 10452–10458. DOI: 10.1021/acs.analchem.6b02376

[29] Madoka Nagata et al. “An Amine-Reactive Phenazine Ethosulfate (arPES)—A Novel Redox Probe for Electrochemical Aptamer-Based Sensor”. *Sensors* **2022**, *22* (5), 1760. DOI: 10.3390/s22051760

*Chapter 6*

# APPLICATION IN WEARABLE SWEAT ANALYSIS

*Materials from this chapter appear in:*
Jihong Min et al. "Skin-interfaced wearable sweat sensors for precision medicine". *Chemical Reviews* **2023**, *123* (8), 5049–5138. DOI: 10.1021/acs.chemrev.2c00823

Wearable sensors hold the promise of providing noninvasive and continuous insight into the biochemical landscape of our body.[1, 2, 3, 4, 5, 6, 7] From their simple origin as pedometers, wearable sensors have evolved tremendously into the more complex field of health monitoring. Fueled by increasing urbanization, improved lifestyle, and increasing awareness toward health and safety, the wearable sensor industry has witnessed an exponential growth in the demand for technologies that offer continuous health monitoring in the past decade.[8] Current state-of-the-art commercial wearable devices primarily focus on monitoring biophysical signals (temperature, heart rate) that indicate the physical manifestations of an underlying health state or condition which constrain the application of these devices within well-being services. Owing to the complexity and multidimensional nature of various diseases, deeper, multiplexed information acquired at the molecular level is needed before wearable sensors can be adopted for disease monitoring. From smart watches to e-skins, innovations in wearable sweat sensors promise to address this technological gap by expanding the biometrics accessible noninvasively through the skin.

Sweat contains a wealth of biochemical information that can be noninvasively and readily accessed on-demand or even continuously.[3, 9, 10, 11] Compared with the complexities and discomforts associated in the sampling of other biofluids like blood, interstitial fluid, tear, saliva, and urine, sweat sampling can be conveniently and unobtrusively achieved by placing a sensor patch on accessible locations of the skin. Molecular biomarkers unveiled by wearable sweat sensors through continuous and noninvasive monitoring can provide a more detailed understanding

of the biochemical processes that govern our health, enabling precision medicine through personalized monitoring of an individual's fitness and health conditions, as well as disease diagnosis and prognosis. Furthermore, the large amounts of biochemical profiles collected by sweat sensors from patients and healthy populations during the daily activities can be processed through predictive algorithms to realize personalized therapeutics and preventative care. At the same time, large data sets collected at the population-level can improve real-time epidemiological surveillance and enhance the precision of public health responses.

Advances in sensor technologies, materials science, and electronics lead to the advent of the first fully integrated multiplexed wearable sweat sensor in 2016.[12] Since then, numerous wearable sweat sensing systems have been developed, typically consisting of a flexible sweat sensor array for conformal contact, a flexible printed circuit board (FPCB) with rigid electronic components for signal processing and wireless communication, and a power source such as a lithium-ion battery to power the electronics. However, for the widespread commercial adoption of wearable sweat sensors, several challenges need to be addressed.

Rigid or thick elements in sweat-sensing systems often impede the device from achieving a stable, conformal, and breathable interface with the skin, potentially leading to motion-induced artifacts, discomfort, and skin irritations. Furthermore, effective sweat sampling often requires airtight contact with the skin which can be achieved by straps on wristwatches and headbands, or by novel deformable adhesives. Breakthroughs in elastic wearable materials could gradually replace rigid and bulky parts of wearable sweat sensing systems with lightweight and deformable counterparts to seamlessly interface the skin, evolving from semirigid wristband sensors to e-textile sensors or e-skin sensors.

Next, the continuity and reliability of sweat sensor data are fundamental for achieving continuous health monitoring. Effective sweat sampling is the first step toward achieving continuous and accurate biomarker analysis. Early sweat sampling methods for analyzing biomarkers in sweat were often confounded by discrepancies due to skin contamination, sweat evaporation, sweat stimulation methods, and sweat rate effects. In addition, sweat stimulation was primarily achieved physically through exercise or thermal stress, leading to large variations in sweat rate and limiting sweat collection to very specific scenarios. Chemical sweat stimulation methods, as well as efficient sweat collection materials and microfluidic designs, can minimize fouling of sweat samples and extend the use of sweat sensors to sedentary and

everyday scenarios. Ultimately, highly precise, specific, and stable sweat sensors for detecting a wide range of biomarkers need to be developed or improved upon. These sensors should also be supported by calibration sensors that simultaneously analyze variables that can potentially influence sensor readings or sweat content, such as skin temperature, sweat electrolyte balance, and sweat rate. Lastly, the vast amount of continuous data collected by sweat sensors can be aggregated through big-data and cloud computing techniques to better comprehend the meaning of the biomarker levels in terms of personal health status.

This chapter provides an overview of wearable sweat analysis with a discussion on sensor considerations for application in sweat. We review the physiology of sweat to understand molecular partitioning to this biofluid and use this information to consider localized sweat induction methods using iontophoresis for on-demand sampling and measurement. We conducted a high-performance liquid chromatography (HPLC) analysis of the sweat profile to validate the physiological mechanisms of sweat generation and evaluate the presence of cholinergic agonists in the final secreted sweat. Using this information, we evaluated the readiness of a nicotine sensor for sweat analysis to inform the future wearable platform design. Finally, we discuss how wearable sweat sensors may be translated out of the lab by outlining their path to commercialization.

## 6.1 Physiology of Sweat

Sweat is produced from glands located deep within the skin, the body's largest organ by surface area. The skin has a stratified structure including the stratum corneum, epidermis, dermis, and hypodermis. The dermis is the major component of the skin containing blood vessels, nerve endings, and the base of sweat glands, sebaceous glands, and hair follicles (Figure 6.1A). The average eccrine sweat gland density is 200/cm$^2$, but this varies between individuals and across the body with the highest density among the palms and soles (~400/cm$^2$).[13, 14] The total number of eccrine sweat glands is on the order of 1.6-5 million.[13]

Sweat plays a very important role in maintaining the body's core temperature, providing a means of thermoregulation. Should body core temperatures rise above 40 °C without modulation, there is a risk of protein denaturation, cell death, and subsequent organ failure.[13] Beyond thermal regulation, sweat also participates in skin homeostasis. Moisturizing factors in sweat, such as lactate and urea, maintain the plasticity and barrier integrity of the stratum corneum. Secretion of antimicrobial

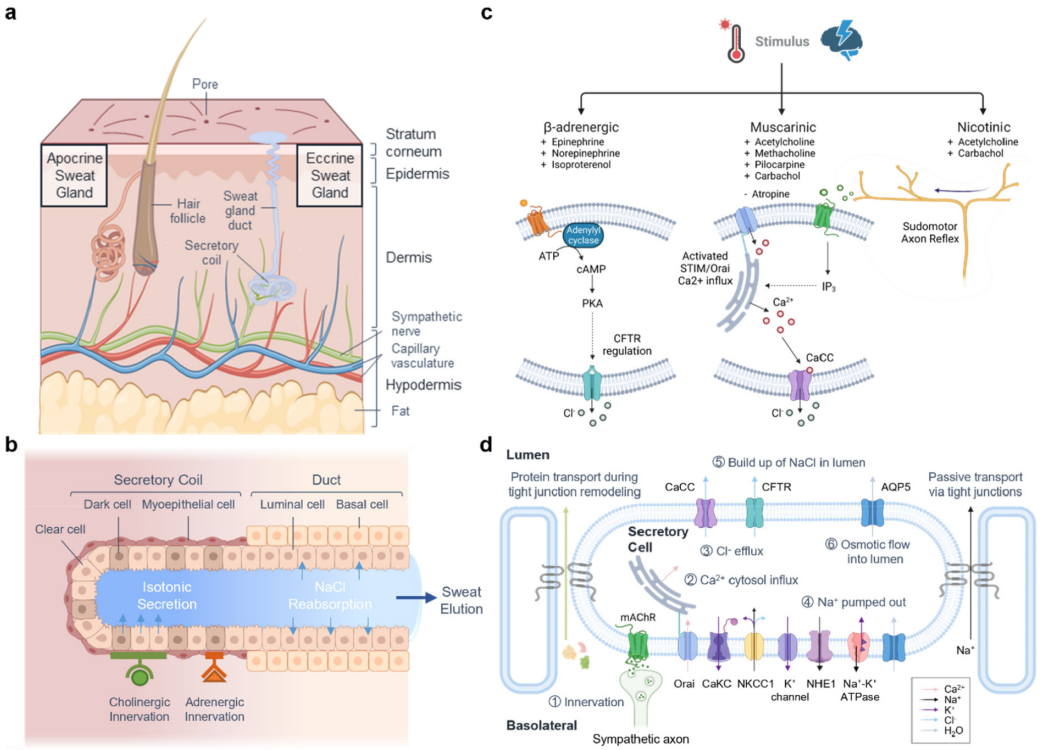


Figure 6.1: Physiology of sweat glands and eccrine sweat secretion

(A) Structure of the skin, including apocrine and eccrine sweat glands. (B) The eccrine sweat gland can be broken down into two primary components: the secretory coil and the sweat duct where isotonic secretion and reabsorption occur, respectively, to produce a hypotonic aqueous fluid. (C) Sweat is stimulated primarily through $\beta$-adrenergic and muscarinic innervation. $\beta$-adrenergic and muscarinic signaling pathways use cAMP and $Ca^{2+}$ as second messengers, respectively, to activate chloride channels. Activation of nicotinic receptors may amplify the sweating response beyond the localized region via the sudomotor axon reflex. (D) Several membrane channels are involved in the secretion of electrolytes and the subsequent osmotic flow into the lumen. Created with BioRender.com.

compounds such as dermcidin, lactoferrin, lysozymes, and immunoglobulin E (IgE) antibodies contributes to the skin's first line of defense against infection.[15] The loss of sweat glands after severe damage as in the case of burn victims presents new challenges in regenerative wound healing and demands further research into sweat gland physiology.

Eccrine sweat glands secrete a highly filtered, aqueous fluid composed of electrolytes, metabolites, and additional molecules. Apocrine sweat glands secrete a viscous fluid containing lipids, proteins, steroids, and ions, by exocytosis in the apocrine gland coil.[16] Volatile organic compounds from apocrine secretions act as pheromones.[13] Apocrine and eccrine sweat glands are differentially stimulated.

| Biomarkers | | | Sweat concentration (mM) | Blood concentration (mM) | Molecular weight (Da) |
|---|---|---|---|---|---|
| Electrolytes | Sodium | | 10–100 | 135–150 | 23 |
| | Chloride | | 10–100 | 97–107 | 35 |
| | Potassium | | 1–20 | 3.5–5 | 39 |
| | Ammonium | | 0.5–8 | 0.01–0.4 | 18 |
| Metabolites | Lactate | | 5–60 | 0.5–25 | 90 |
| | Glucose | | 0.01–0.3 | 3.3–17.3 | 180 |
| | Urea | | 2–40 | 1.8–7.1 | 60 |
| | Uric acid | | 0.02–0.1 | 0.1–0.5 | 168 |
| | Creatinine | | 0.01–0.03 | 0.065–0.12 | 113 |
| Minerals | Calcium | | 0.2–2 | 2.2–2.7 | 30 |
| | Magnesium | | 0.02–0.4 | 0.7–0.95 | 24 |
| | Iron | | 0.0001–0.03 | 0.006–0.027 | 56 |
| | Zinc | | 0.0001–0.02 | 0.01–0.017 | 65 |
| Nutrients | Amino acids | Tyrosine | 0.2–0.4 | 0.055–0.3 | 181 |
| | | Tryptophan | 0.055–0.08 | 0.02–0.091 | 204 |
| | | BCAAs[a] | 0.2–1 | 0.2–1.2 | 117–131 |
| | Vitamin C | | $0.01–50 \times 10^{-3}$ | $2.8–200 \times 10^{-3}$ | 176 |
| Hormones | Cortisol | | $0.1–20 \times 10^{-3}$ | $0.07–690 \times 10^{-3}$ | 362 |
| | Testosterone | | $0.8–1.6 \times 10^{-6}$ | $0.5–35 \times 10^{-6}$ | 288 |
| | Dehydroepiandrosterone | | $6.9–455 \times 10^{-6}$ | $0.35–11.91 \times 10^{-3}$ | 288 |
| | Neuropeptide Y | | $1.9–6.8 \times 10^{-10}$ | $1.4–6.1 \times 10^{-10}$ | 4272 |
| Proteins | C-reactive protein | | $4.2–250 \times 10^{-9}$ | $7–29 \times 10^{-6}$ | 120,000 |
| | Cytokines | Interleukin 6 | $3.7–6.9 \times 10^{-10}$ | $2.4–5.6 \times 10^{-10}$ | 21,000 |
| | | Interleukin 8 | $1.8–7.2 \times 10^{-10}$ | $1.5–6.5 \times 10^{-10}$ | 8452 |
| Substances | Ethanol | | 2.5–22.5 | 2–22.5 | 46 |
| | Acetaminophen | | $<50 \times 10^{-3}$ | $66–132 \times 10^{-3}$ | 151 |
| | Levodopa | | $<2.5 \times 10^{-3}$ | $<5 \times 10^{-3}$ | 197 |

[a]BCAAs: branched-chain amino acids.

Table 6.1: Composition of sweat.

The apocrine sweat gland responds strongly to emotional stimuli and sympathomimetic drugs via adrenergic innervation, but does not respond to cholinergic or thermal stimulation like the eccrine sweat gland.[15, 17] The apoeccrine sweat gland shares properties of both eccrine and apocrine glands; it may develop during puberty in the axillae region from existing eccrine sweat glands. The gland retains an eccrine-like sweat duct but has an apocrine-like secretory tubule. Apoeccrine sweat ultimately resembles aqueous eccrine sweat and arises from an intermediate type of stimulation.[18] This review focuses on eccrine sweat as eccrine sweat glands are the most abundant and active source of sweat.

In this section, we present the physiology of eccrine sweat from stimulated innervation to sweat secretion. We describe sweat gland development and structure. Additionally, we discuss molecule partitioning into sweat and give an overview of accessible biomarkers in sweat.

### 6.1.1 Structure and Mechanisms

The eccrine sweat tubule is a conduit for sweat and electrolyte exchange 4-8 mm in length. At the base, the secretory coil is 500-700 μm in size with a lumen inner diameter of 30-40 μm and a coil outer diameter of 60-120 μm.13 The secretory coil is interwoven with capillaries for vascular exchange and sudomotor nerve fibers for autonomic modulation.[14, 19] The secretory tubule straightens into the dermal duct with an inner diameter of 10-20 μm and outer diameter of 50-80 μm composed of two to three layers of epithelial cells.[13] The sweat duct is straight from the dermis to the epidermis, and then transitions to a helical structure in the epidermis that terminates in the stratum corneum. The number of turns of the helical duct varies from 4 to 6 and varies proportionally to the stratum corneum thickness, yet the pitch angle remains constant across sweat glands.[20] The helical structure makes the sweat duct act as a helical antenna resulting in resonance behavior. Sweat duct dimensions, density, distribution, and the dielectric properties of the stratum corneum all determine the resonant frequency and subsequent skin-THz wave interactions. The duct length varies from 150 to 600 μm and varies proportionally to the stratum corneum thickness.[20] The sweat duct widens into the acrosyringium, a pore on the outer surface. The acrosyringium is composed of epithelial cells with no clear distinction or border to the epidermis. The lumen has a diameter of 20-60 μm and may also contain cornified cells.[13]

Humans are born with almost all their sweat glands, with gland development occurring mostly during the first two trimesters. This is one explanation for higher observed duct densities in children than adults.[20] The sweat gland develops from a group of multipotent $K14^{+}$ progenitors, descendants of epidermal stem cells. It grows downward as a straight duct, stratifying in the lower half to proliferative $K14^{low}/K18^{+}$ suprabasal progenitors. The $K14^{low}/K18^{+}$ suprabasal progenitors develop into luminal cells, while the remaining $K14^{+}$ progenitors give way to myoepithelial cells.[21] Although sweat glands have limited turnover and proliferation capabilities, there is some promise of regeneration. Stem cells associated with secretory luminal and myoepithelial cells were found to promote epidermis and sweat gland regeneration when amplified and seeded in the wound bed.[22] Additionally, the use of three-dimensional (3D) bioprinting matrices has been studied for sweat gland morphogenesis with tissue-level self-organization.[23]

The secretory coil and duct define the two major steps of sweat generation: isotonic secretion and salt reabsorption (Figure 6.1B). Ductal cells facilitate transcellular

reabsorption with mitochondria-rich basal cells contributing to uptake. The secretory coil is made up of basal myoepithelial cells and luminal clear and dark cells, named for their appearance in eosin, toluidine blue, and methylene blue stains.[13] Myoepithelial cells strengthen the structure of the secretory coil and create a microenvironment for gland stem cell differentiation.[24] Clear cells contain many mitochondria suggesting that they facilitate most of the active sweat secretion and osmotic flow.[13] Dark cells are granular, containing many vesicles. Dark cells are more involved in the secretion of proteins, including periodic acid-Schiff (PAS)-positive diastase-resistant glycoproteins, dermicidin, and sialomucin.[24] The interdependent relationship between clear and dark cells requires further investigation.

Sweat secretion is stimulated by adrenergic and cholinergic innervation (Figure 6.1C). The sudomotor response involves several adenosine triphosphate (ATP)-dependent steps, and is suppressed by ouabain and metabolic inhibitors.[14] When the secretory cell is stimulated, a signaling cascade occurs involving $Ca^{2+}$ or cyclic adenosine monophosphate (cAMP) as second messengers to trigger the efflux of $Cl^-$ into the lumen of the secretory coil. $Na^+$ is pumped out at the basolateral membrane and diffuses down its electrochemical gradient into the lumen. The buildup of electrolytes in the lumen renders it hypertonic with respect to the cytosol; this osmotic gradient drives the primary sweat solution out of the cell and into the secretory lumen (Figure 6.1D). Advective mass transport drives fluid up the eccrine sweat duct. Along the sweat duct, luminal cells reabsorb ions to produce a hypotonic sweat solution. We describe this process in further detail below.

### 6.1.2 Sweat Stimulation

Thermoregulatory sweating is an autonomic response to signals from thermoreceptors in the preoptic-anterior hypothalamus area. Upon an increase in core temperature, thermoreceptors send through efferent pathways to postganglionic sympathetic neurons in the dermis.[14] Cholinergic nerve fibers around the secretory coil release acetylcholine, thus activating muscarinic receptors on the membrane of the eccrine secretory cell. Activation of muscarinic G-protein-coupled receptors (GPCRs) increases intracellular inositol trisphosphate ($IP_3$). $IP_3$ binds to receptors on the endoplasmic reticulum (ER) membrane to release $Ca^{2+}$ into the cytosol.[25] Stromal interaction molecule protein, stromal interaction molecule 1 (STIM1), monitors the ER $Ca^{2+}$ levels, and when $Ca^{2+}$ stores are depleted STIM1 induces store-operated $Ca^{2+}$ entry by binding to and activating Orai, a $Ca^{2+}$ channel on the plasma mem-

brane.[25] This influx of $Ca^{2+}$ mediates the exchange of electrolytes resulting in sweat secretion.

Sweating is also adrenergically stimulated under the "fight or flight" response. The physical reaction to stress, anxiety, fear, and pain occurs mostly in the palms, soles, and axillary region and may have the selective advantage of increasing palmoplantar friction for fleeing.[13] "Emotional" sweating is controlled by the limbic system, and efferent signals are sent to adrenergic nerve fibers in the sweat secretory coil. Release of epinephrine and norepinephrine in signaling stimulates $\alpha$- and $\beta$-adrenoreceptors in sweat secretory cells. A synthetic sympathomimetic drug, isoproterenol, selectively stimulates $\beta$-adrenoreceptors and has been used to further differentiate the two pathways. $\beta$-Adrenergic stimulation is the dominant pathway in emotional sweating. The magnitude of stimulated sweat secretion (measured by secretory rate) is 4:2:1 for cholinergic, $\beta$-adrenergic, and $\alpha$-adrenergic pathways, respectively.[26] $\alpha$-Adrenergic stimulation results in $Ca^{2+}$ influx similar to cholinergic pathways. $\beta$-Adrenergic GPCRs activate adenylyl cyclase and increase the intracellular concentration of cAMP. cAMP activates protein kinase A (PKA), which in turn mediates $Cl^-$ secretion by opening the cystic fibrosis transmembrane conductance regulator (CFTR).[27, 28] In the case of cystic fibrosis, CFTR is defective or absent, resulting in blocked CFTR $Cl^-$ secretion during $\beta$-adrenergic stimulation and inhibited $Cl^-$ reabsorption. A "ratiometric" sweat rate test comparing adrenergic and cholinergic sweat rates may be used to assess CFTR functional activity.[29]

Sweat may be generated at the periphery of a stimulated region via the sudomotor axon reflex (Figure 6.1C). Nicotinic agonists interact with receptors on postganglionic sudomotor terminals at the base of the sweat gland, causing antidromic axonal conduction toward a branch point followed by orthograde conduction down the branching fibers. Acetylcholine is then released at the nerve terminals and binds to muscarinic receptors on the eccrine sweat gland, resulting in sweat secretion similar to the direct iontophoretic response.[14, 30] The spatial extension of this sweating could be millimeters beyond the periphery of the stimulation region.[31] The sudomotor axon reflex may be used to assess autonomic nervous system disorders, such as diabetic neuropathy.[14, 32] The sudomotor axon reflex may also be used to separate drug-induced sweat stimulation and sweat sampling regions to prevent cross-contamination.[30] The sudomotor axon response has a longer latency than the direct cholinergic response by about 5 s, which accounts for axonal conduction and neuroglandular transmission. The sudomotor axon response and direct

response produce similar sweat volumes in the presence of nicotinic agonists. In contrast to the direct stimulated sweat response, which continues over an hour after cessation of the stimulus, the sudomotor axon response returns to baseline 3-5 min after stimulus cessation.[33]

The sweat rate is modulated in part by nonuniform, localized activation. Under mental stress, sweat production of adjacent sweat glands varied strongly.[34] The cumulative sweating response controlled by the sympathetic nerve is discretized into active and inactive sweat glands.[34] The sweat rate in healthy individuals ranges from 0.2 to 1 $\mu L/cm^2/min$.[35, 36] At an average sweat gland density of $200/cm^2$, this equals 1-5 nL/gland/min. The sweat rate is affected by local skin temperature.[13] Sweat stimulated pharmacologically may also further increase the sweat rate to approximately 10 nL/gland/min.[37] Sweat rate decay and cessation occur in part due to the subcutaneous elimination of the sweat stimulant (e.g., acetylcholinesterase).[14, 38] Interindividual variations in sweat rate are likely due to differences in the function and responsiveness of the sweat gland.[39] Many factors may influence the sweat response including gender, physical fitness, menstrual cycle, and circadian rhythm.[13] Intraindividual regional variations in observed sweat rate may be associated with variations in sweat gland density and distribution.[20, 39] For example, the forehead has a high density of sweat glands and has the highest tested sweat rate region during both active and passive thermal sweating.[39, 40]

### 6.1.3 Sweat Secretion and Electrolyte Reabsorption

Upon stimulation, $Ca^{2+}$ and cAMP act as intracellular messengers for sweat secretion. $Ca^{2+}$ activates transmembrane $K^+$ and $Cl^-$ channels. TMEM16A and bestrophin 2 are $Ca^{2+}$-activated chloride channels (CaCCs) located on the apical membrane of secretory gland cells. Bestrophin 2 is expressed only in dark cells, yet it is necessary for sweat generation.[41] CFTR is the active $Cl^-$ channel in cAMP-mediated $\beta$-adrenergic sweat secretion. PKA-independent CFTR activation via calmodulin-mediated $Ca^{2+}$ signaling results in cross-talk between cAMP and $Ca^{2+}$ signaling for CFTR regulation.[42] It is possible CFTR may be involved in both sweat secretion pathways.

As $Cl^-$ diffuses into the lumen at the apical membrane, $Cl^-$ enters the cell via basolateral Na-K-Cl cotransporter 1 (NKCC1), a $Na^+$-$K^+$-$2Cl^-$ electroneutral cotransporter. Excess accumulated Na+ is then actively pumped out via $Na^+/H^+$ exchanger 1 (NHE1) and $Na^+$-$K^+$ ATPase.[25] $Na^+$ is passively transported paracellularly down

the electrochemical gradient established in the lumen. A buildup of electrolytes in the lumen of the secretory coil results in an osmotic gradient driving transcellular fluid flow via aquaporin 5 (AQP5) and paracellular flow from the interstitial fluid (ISF).[19, 24] As a result, the aqueous fluid in the secretory coil becomes isotonic with respect to ISF, blood, and cytosol.

Continued sweat secretion drives flow up the sweat duct, where reabsorption of electrolytes results in a hypotonic final sweat secretion. CFTR is necessary for $Cl^-$ reabsorption. Unlike in the secretory coil, CFTR in the sweat duct is constitutively active. CFTR activity is complexly regulated by intracellular cAMP, ATP, and $K^+$ levels. CFTR conduction of $Cl^-$ is transcellular, but CFTR is present at a greater surface density on the apical membrane.[27] In contrast to the secretory coil, $Na^+$ transport in the duct is transcellular rather than paracellular. $Na^+$ is reabsorbed passively by the epithelial sodium channel (ENaC) at the apical membrane and actively pumped at the basolateral membrane by $Na^+/K^+$ ATPase.[13] ENaC and CFTR interact with each other in complex ways.[27, 43] $Na^+$ reabsorption is reduced by increases in luminal $Ca^{2+}$.[44] ENaC is regulated by $Ca^{2+}$ in other reabsorption cells,[45] suggesting that inhibition of ENaC by increases in $Ca^{2+}$ reduces the membrane permeability and passive $Na^+$ flux at the apical luminal cell membrane. As sweat rate increases, $Na^+$ reabsorption increases; however, the $Na^+$ secretion rate increases relatively more, resulting in higher salt concentrations at higher sweat rates.[46]

Bicarbonate ($HCO_3^-$) is involved in both sweat secretion and reabsorption, yet the mechanisms remain unclear. $HCO_3^-$ exchange is mediated by both CFTR and Bestrophin 2 channels.[24, 27] Various carbonic anhydrase isoforms also regulate $HCO_3^-$ by reversibly converting $CO_2$ to $HCO_3^-$. Carbonic anhydrase II (CA2) operates intracellularly in secretory coil clear cells and ductal cells.[13, 25] Carbonic anhydrase XII (CA12) is a transmembrane protein also broadly expressed in the sweat gland. Defective CA12 results in excessive Na secretion in sweat.[24] $HCO_3^-$ plays an important role in regulating the acid-base chemistry of sweat secretion both intracellularly and extracellularly. Cytosolic pH affects ion channel activity. For example, ENaC becomes inhibited at acidic cytosolic pH in ductal cells.[24] pH-sensitive phosphatases occur in the intercellular canaliculi of secretory cells. $HCO_3^-$ may also be secreted in coordination with acidic proteins, such as sialomucin, to neutralize the pH in the lumen.[24] Final sweat pH can range from roughly 5 to 7 and is positively correlated with sweat rate. Sweat pH in the secretory coil has a neutral

pH, like ISF; but pH decreases as it moves through the sweat duct. This suggests that ductal $HCO_3^-$ reabsorption at low sweat rates contributes to the acidification of sweat.[47] Fluctuations in sweat pH represent a challenge in sweat sensing, both because pH may affect partitioning of detected molecules and also because pH may directly affect biosensor performance.

Acclimatization to thermal (and physical) stimuli markedly affects sweat generation. Physically fit individuals have higher glandular functions and sweat rates per gland after methacholine stimulation.[48] Over a multiweek exercise series, acclimatization due to increased fitness resulted in a reduced lactic acid concentration in sweat.[49] Additionally, thermal acclimatization increases the $Na^+$ reabsorption capacity of the human eccrine sweat gland.[35]

### 6.1.4 Biomarkers in Sweat

Sweat is an information-rich biofluid containing many molecules that can serve as biomarkers. Sweat is composed of various electrolytes, metabolites, hormones, proteins, and peptides (Table 6.1). Sweat samples may be analyzed using metrics such as biomarker concentrations, biomarker flux, sweat rate, sweat pH, and ionic strength to provide important information as they correlate to health. In some cases, biomarker flux may represent a better metric of analysis since it accounts for the dynamic water flux, which may affect concentration measurements. Biomarker flux may be calculated using the product of sweat rate and biomarker concentration.[50] Recent reports have shown promising correlations between the levels of a number of sweat and blood analytes,[19] indicating the great potential of using sweat as an alternative source for personalized healthcare. Since sweat is readily available for noninvasive sampling, sweat is an attractive biofluid for point-of-care (POC), at-home, and continuous diagnostics. Moreover, new biomarker discovery for precision medicine can be greatly facilitated by the continuous, large sets of data collected through noninvasive sweat analysis in daily activities.[51]

#### Analyte Transport and Partitioning

Prior to electrolyte reabsorption in the sweat duct, initial sweat secretion is isotonic and resembles filtered ISF. Passive sweat secretion may result in reduced concentrations 10- to 1000-fold lower than in ISF and blood plasma. However, blood-to-sweat correlations vary based on the analyte and its subsequent partitioning. Analyte

partitioning occurs primarily via transcellular and paracellular transport. Small, uncharged analytes readily enter sweat transcellularly via diffusion through the plasma membrane of capillary endothelial cells.[19] Large, hydrophilic molecules enter sweat paracellularly via diffusion and advective transport through the intercellular canaliculi between adjacent cells.

Transcellular transport of small, lipophilic molecules results in strong blood-sweat correlations as these molecules freely diffuse across the selectively permeable cell membrane. This is likely the dominant transport mechanism for several classes of analytes, including steroid hormones (i.e., cortisol[52]), ethanol,[53] and many therapeutic and abused drugs (e.g., nicotine, fentanyl). Partitioning is limited by the least permeable state. This results in plasma correlations that hold only for the unbound fractions of the analyte as is the case with cortisol.[19] For instance, ionization may impede the molecule from transcellular transport. The pH of sweat may become an important consideration for weak acids and weak bases due to the possibility of ion trapping. In the case of ammonia ($NH_3$), which has a $pK_a$ of 9.3, $NH_3$ diffuses readily into the secretory lumen but under acidic sweat conditions (as in the case of exercise), $NH_3$ protonates to become ammonium ($NH_4^+$). In the protonated form, transcellular exchange is impeded and $NH_4^+$ accumulates in the lumen of the sweat gland. This phenomenon results in amplified sweat concentrations.[52] Since primary sweat pH is 7.2 to 7.3 in the secretory coil,[47] this phenomenon is likely to mostly impact reabsorption in the sweat duct. While ion trapping is a common topic of research in subcellular pharmacokinetics, the role of ion trapping in sweat partitioning warrants further consideration.

The intercellular canaliculi forms a >10 nm gap for paracellular molecular transport, but tight junctions adjoining secretory cells act as a roadblock.[19] Tight junctions are formed by over 40 different proteins, with the claudin family of transmembrane proteins defining the structure and selective permeability of the tight junction.[19] Paracellular sweat partitioning is likely to occur during tight-junction remodeling allowing for ISF molecules in the canaliculi to make their way into the lumen. Tight junctions may be modulated using calcium chelators. For example, citrate addition leads to a >10× increased flux of glucose to sweat from ISF.[50] Although paracellular sweat partitioning may result in significant dilution from blood plasma protein levels, this nonspecific channel for proteins from the ISF may still result in correlated blood plasma ratios for trend analysis.

The observed lag time between blood and sweat measurements is on the order of

ones to tens of minutes. The secretory coil is highly vascularized, minimizing the lag in circulating blood changes.[19] In the simplified case of transcellular transport, the rate of diffusion determines the time to enter the lumen of the sweat duct. Once in the lumen, advective transport by osmotic fluid flow (i.e., sweat rate) determines the time from analyte secretion to analyte elution. When the correlation of blood alcohol and sweat alcohol content was measured continuously, the lag time for signal onset ranged 2.3-11.4 min and 19.32-34.44 min for the overall curve.[53] The relative contributions of sweat flow rates and analyte partitioning mechanisms on the sensor response remains obscure. For sweat generation or refreshing to be the rate-limiting step, the sweat collection designs should be further optimized. Further work is required to better define the variation in lag of different analyte partitioning. However, real-time sensing is contextual; the measurement of an analyte whose concentration changes slowly relative to the lag in transport and sensing is effectively a real-time measurement.

**Sweat Composition Analysis**

Sweat has been surveyed broadly using liquid chromatography (LC) or gas chromatography (GC), mass spectrometry (MS), and nuclear magnetic resonance (NMR) techniques. NMR requires minimal sample preparation but achieves a lower sensitivity. MS is often preceded by chromatographic techniques to enhance detection quality.[16] A high coverage LC-MS technique based on chemical isotope labeling was used to identify over 2707 unique metabolites across 54 sweat samples.[54] Subsequently, 83 metabolites were identified with high confidence. With such a diverse data set, LC-MS may be used to characterize the sweat submetabolome and draw statistically significant observations based on gender and activity duration.[54] LC-MS and GC-MS represent the gold standard of trace concentration sweat biomarker identification and quantification. The disadvantage of these techniques is that they require expensive equipment along with complex protocols that require thorough validation for use in metabolite identification and quantification.

Regional variations in sweat composition have been studied using a variety of assays, recently including NMR and multiplexed immunoassays.[55, 56] In general, there are minimal variations in sweat composition when sampling from different body locations. No significant difference was observed for sweat cytokine composition at different arm locations, and metabolic profiles are generally conserved across the body.[55, 56] Sweat from the upper chest, upper back, arms, and forehead exhibited

similar NMR spectra.[55] Sweat from the lower back, axillary, and inguinal regions contained a higher fat content, but this may be due to sweat mixing with sebum since these areas also contain a high density of sebaceous glands. Forehead sweat exhibited high levels of lactate, pyruvate, glycerol, and serine relative to the arm sweat. Serine content was also high on the hands and feet.[55] Since serine is active in skin regeneration, this is indicative that these regions may undergo more epithelial turnover. The hands appear to have a lower content of natural moisturizing factors, such as glycerol and urea.[55, 57] For electrolytes, regional sodium chloride concentrations are well-correlated with whole-body sweat concentrations, with the exception of forehead sweat possibly due to the effects of a significantly higher sweat rate. The forearm, thigh, and calf were all highly correlated and are potential single-site sweat collection areas. $HCO_3^-$ concentration was high at the forearm despite the average sweat rate. K+ and lactate concentrations were higher at the extremities (foot, hand, and forearm).[40]

**Electrolytes.** $Na^+$ and $Cl^-$, the most copious electrolytes found in sweat, are partitioned into sweat via active mechanisms that are tied to the osmotic secretion of water. Therefore, $Na^+$ and $Cl^-$ serve as potent biomarkers of electrolyte balance and hydration status for cystic fibrosis diagnostics and fitness monitoring applications. According to the $Na^+$-$K^+$-$2Cl^-$ cotransport model as outlined previously, a series of cascading effects instigated by the stimulation of cholinergic nerve endings surrounding the sweat gland induce the influx of NaCl into the secretory coil lumen, which then causes the osmotic influx of water.[47, 58, 59] In this primary sweat, $Na^+$ levels are isotonic and $Cl^-$ levels are slightly hypertonic to plasma. However, as this fluid gets pumped through the duct, $Na^+$ and $Cl^-$ ions are reabsorbed through ENaC and CFTR to prevent rapid electrolyte loss. Despite wide ranging concentrations, resulting sweat $Na^+$ and $Cl^-$ levels are often hypotonic to plasma levels. Additionally, as reabsorption of these ions occurs at steady rates, increased sweat rates correlate with increased $Na^+$ and $Cl^-$ levels in final sweat.

$K^+$ is another electrolyte secreted via the $Na^+$-$K^+$-$2Cl^-$ cotransport model that is relevant to the function of nerve and muscle cells.[47] While understanding of the exact partitioning mechanism of $K^+$ requires further investigation, studies have shown that $K^+$ levels of primary sweat in the secretory coil are isotonic to plasma levels but increase to hypertonic levels in final sweat exiting the duct.[60, 61] Furthermore, $K^+$ concentrations seem to not have a strong correlation with sweat

rate.[40, 62]

$NH_4^+$, an electrolyte found in sweat with metabolic origins, is of interest for tracking liver and kidney function, as well as exercise intensity.[63] As described previously, $NH_3$ is a small and uncharged polar molecule with a $pK_a$ of 9.3 (weakly basic), allowing for passive diffusion into the sweat gland lumen where weakly acidic conditions result in increased protonation to ammonium. Due to its charge, the ammonium ion gets entrapped in the lumen of the sweat gland, yielding sweat ammonium levels to be 20-50 times higher than plasma ammonium levels. Furthermore, sweat ammonium levels have been reported to decrease with increased sweat pH and sweat rates.[52]

**Metabolites.** Blood glucose monitoring is critical for managing diabetes, and sweat glucose has the potential to serve as a noninvasive surrogate. Some studies have shown positive correlations between sweat and blood glucose levels, and while the exact partitioning mechanism is still being studied, the primary source of sweat glucose is likely to be from blood through paracellular transport.[50, 64, 65] The rather large size and polarity of glucose likely limit its passage through the tight junctions of the sweat gland, resulting in sweat glucose levels being ~100 times lower than blood glucose levels.

Lactate is a metabolite found in sweat that has been extensively studied as a potential biomarker for muscle exertion and fatigue. While the transport mechanism of lactate from plasma to sweat is obscure and the correlation between lactate levels in sweat and plasma is weak, sweat lactate is also produced from sweat gland metabolism and can still be reflective of whole-body exertion. Sweat lactate levels are typically higher than blood lactate levels and decrease with increased sweat rates, potentially due to dilution.

Along with ammonia, urea, uric acid, and creatinine are nitrogenous compounds produced from protein metabolism that indicate renal function. As a small polar molecule that can passively diffuse through the sweat gland through paracellular transport, sweat urea has been speculated to primarily originate from the blood.[47, 66] However, reported sweat urea concentrations are often significantly higher than blood urea concentrations (up to 50 times), potentially indicative of additional sources of urea in sweat. A popular hypothesis is that there is a finite pool of urea in the epidermis that gets depleted during profuse sweating, supported by studies showing that sweat urea levels trend toward blood urea levels with increased

sweating.[67] Additionally, studies indicate the potential for active mechanisms of urea excretion through sweat as an alternative method for excreting excess metabolic wastes.[68, 69, 70] Uric acid and creatinine are slightly larger molecules that are found in sweat at micromolar levels and around 5 times lower than in blood.[71, 72, 73, 74, 75] While the partitioning mechanism of these metabolites has not been studied in detail, a positive correlation between sweat and serum uric acid levels has been reported.[74]

**Minerals.** Trace minerals such as $Ca^{2+}$, $Mg^{2+}$, $Fe^{2+}$, and $Zn^{2+}$ are often found in sweat at concentrations similar to or slightly lower than blood concentrations.[76, 77, 78, 79] Due to their small size and hydrophilicity, these trace minerals have the potential to be secreted through sweat via paracellular mechanisms in their free and ionized states. However, approximately 30-45% of plasma $Mg^{2+}$, 50% of plasma $Ca^{2+}$, 70% of plasma $Zn^{2+}$, and above 95% of plasma $Fe^{2+}$ are bound to proteins or complexed with anions, likely impeding passive diffusion into the sweat glands.[80, 81]

**Nutrients.** Water-soluble vitamins such as ascorbic acid and thiamine, which are large and polar molecules, have been reported in sweat at concentrations significantly lower than in blood.[82, 83] On the other hand, amino acids, which are the building blocks of protein in our bodies, are often found in sweat at concentrations similar to or sometimes even higher than in blood.[57, 84, 85, 86] The levels of amino acids in sweat are likely attributed to partitioning from plasma, as well as production of natural moisturizing factors (NMF) and hydrolysis of the epidermal protein filaggrin in the stratum corneum.[87] As such, studies have shown that sweat amino acid concentrations decline with increased sweat rates.[88] Positive correlations between sweat and serum levels, as well as increases in sweat concentrations after supplement intake, have been reported for nutrients such as ascorbic acid and branch-chain amino acids (BCAAs).[82, 86]

**Hormones.** Hormones are chemicals that carry signals throughout our bodies for regulating physiological processes and behavior. Cortisol is a primary glucocorticoid hormone produced by the adrenal glands to regulate the body's stress response. As a large lipid-soluble molecule that can diffuse through lipid bilayer membranes via intracellular passive transport, unbound cortisol is found in various body flu-

ids.[89] However, over 90% of endogenous cortisol in blood is bound to carrier proteins that hinder intracellular passive transport.[90, 91, 92] While significantly lower in concentration than serum cortisol levels, cortisol levels in sweat and saliva have been reported to correlate with unbound cortisol in serum.[92, 93]

Neuropeptide Y (NPY) is one of the most abundant peptides in the central nervous system and acts as a hormone that has close ties with stress, appetite, and depression.[94] When the levels of various cytokines and neuropeptides were compared between women with and without major depressive disorder (MDD), elevated sweat NPY levels were observed in patient subjects.[95] In addition, a good correlation was found between NPY levels in sweat and blood.[95]

**Proteins.** Proteins are macromolecules (>5 kDa) constructed by numerous amino acids. In sweat, proteins with protective functions for maintaining the epidermal barrier integrity (dermicidin, apolipoprotein D, clusterin, prolactin-includible protein, and serum albumin) make up 91% of the secreted proteins.[96, 97, 98] Trace-level proteins such as c-reactive protein (CRP) and cytokines are of particular interest as they modulate the body's inflammation and immune response. While CRP levels in sweat have been reported to be significantly lower than in blood, many cytokines have been reported to be in sweat at concentrations similar to or higher than in blood.[95, 99, 100] While the exact partitioning mechanism of cytokines into sweat is uncertain, promising correlations between sweat and blood cytokine levels have been widely reported.[95, 99] Considering their large size, it is likely that most of the cytokines found in sweat are produced locally by the eccrine gland. However, their production is often due to a systemic response throughout the body, and therefore sweat cytokine levels can still be reflective of systemic levels.

**Substances.** Exogenous substances including toxins and drugs are often metabolized by enzymes and excreted via urine and sweat. When alcohol is ingested, 90% of the ethanol is broken down sequentially into acetaldehyde, acetate, and acetyl coenzyme A (CoA); a portion of the remaining ethanol is excreted through sweat. As ethanol is both soluble in water and lipids, it can passively diffuse through most membranes in the body, leading to strong correlations between sweat and blood ethanol levels.

### 6.1.5 Sweat Physiology Outlook

There is much yet to learn about sweat gland physiology. Human sweat duct density and distribution have been investigated using ductal pore counting, colorimetry, and plastic impression techniques.[20] The advent of optical coherence tomography has allowed for noninvasive morphological visualization.[20, 34] 3D sweat gland tissue models are being developed to better understand sweat physiology for pathology and tissue regeneration.[15] These models will contextualize sweat measurements and correlated analyte concentrations by revealing interdependent pathways. Improved sweat gland models may help in developing algorithms for calibration.

The development of continuous, compact, on-body collection-to-analysis sweat sensing platforms will further improve the quality and quantity of data for sweat characterization. Real-time multiplexed sweat measurements will also contribute to our understanding of the physiological sweat response. Tissue-level sweat pH regulation remains a hurdle for pH-dependent sensing platforms. Understanding the acid-base controls in the sweat gland may aid in designing on-body stimulation and collection platforms at predictable sweat pH. Elucidating the factors that contribute to dynamic sweat concentrations and analyte partitioning is necessary to relate noninvasive sweat measurements to system-level changes both in time and concentration. Increasing our understanding of the physiology of the sweat gland and surrounding skin tissue may also better explain variations in localized sweat measurements from systemic trends. Data from biological models and wearable sweat sensors will complement each other for growth in both fields.

## 6.2 Iontophoresis Sweat Induction

Sweat can be induced in various manners, such as thermal stimulation, exercise, natural secretion, and iontophoresis. For thermal stimulation, subjects are placed in a heated environment (e.g., sauna bathing) to induce thermal sweat at a skin temperature of 40-41 °C, with a full-body sweat production of 0.6-1 kg/h.[101, 102, 103] Exercise-induced sweat is prevalent in many studies; however, the sweat rate could fluctuate with respect to variations in exercise type and intensity. Some common exercises include treadmill running and stationary biking, where the exercise intensity could be controlled and recorded. As thermal and exercise induction could impose constraints on subjects' physical conditions and testing environment, there is an increasing trend in using naturally occurring sweat for downstream sensing.[**moon_noninvasive_2021**, 104, 105, 106, 107, 108] The naturally secreted

sweat, also called “background sweat”, occurs during regular routines and entails relatively low sweat rates around 10 times lower than that of exercise sweat.[106] In contrast to these methods, iontophoresis sweat induction may produce significant sweat volumes in a localized area for on-demand sweat sampling and analysis.

Iontophoresis is a procedure where a small current delivers a cholinergic drug loaded in hydrogel into the skin. Two pieces of hydrogels are attached to the skin; the anode hydrogel contains a cholinergic agent while the cathode hydrogel contains electrolytes to facilitate current flow (Figure 6.2). As the cholinergic agent stimulates the muscarinic 3 (M3) receptors on sweat glands, a direct sweat response is elicited. Depending on nicotinic receptor specificity, the iontophoretic drug may induce peripheral sudomotor axon reflex sweating.[30]

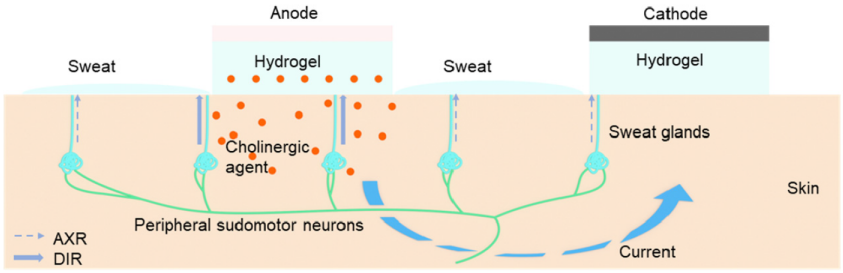


Figure 6.2: Scheme of iontophoresis-based sweat induction

AXR: Axon-reflex mediated sweating. DIR: direct stimulated sweating.

### 6.2.1 Sweating Response by Different Cholinergic Agents

Different cholinergic agonists could be used to induce sweating, and the sweating response varies in duration and area, which is determined by the receptor activity and susceptibility to acetylcholinesterase (AChE) hydrolysis. Acetylcholine and methacholine are hydrolyzed by AChE and thus have a shorter sweating duration. On the other hand, the nicotinic activity of the cholinergic agents affects the indirect axon-reflex sweating and thus the area of the sweat response. For example, the $\beta$-methyl group of bethanechol limited the nicotinic activity and thus the sweating response is highly localized and occurs directly underneath the placement of the iontophoresis gel. Detailed studies and summaries of the receptor activities and sweating response can be found in previous literature.[33, 37, 109, 110]

### 6.2.2 Wearable Platforms for Sweat Iontophoresis

Over the past decade, various iontophoresis devices have been developed for wearable sweat induction. The commercially available Macroduct system is Food and Drug Administration (FDA)-approved for iontophoresis-based sweat induction for cystic fibrosis diagnosis and uses pilocarpine as the cholinergic agonist. After initial current ramping, a constant current is administered through the pilocarpine gel discs strapped onto the arm. The device automatically ramps down the current and shuts down after 5 min. Although the device provides customizable options with the straps for stimulation at different locations on extremities and across different age groups (babies to adults), the system remains bulky and unsuitable for regular wear. Similar systems could be achieved for initial prototype testing with an iontophoresis device and custom lab-made hydrogels loaded with selected cholinergic agonists.[37] To improve wearability, a flexible wristband containing iontophoresis electrodes and housing an FPCB was developed (Figure 6.3A).[111] The sweating response to iontophoresis gels loaded with different cholinergic agonists (acetylcholine, methacholine, and pilocarpine) was characterized in terms of response latency, sweating duration, peak sweat rate, time to peak and time at peak rate (Figure 6.3B). Moreover, periodic iontophoresis of different acetylcholine loads was performed and higher sweat rate with longer sweat duration was observed for the 10% acetylcholine gel compared to the 1% acetylcholine gel (Figure 6.3C). In addition to the gel-based wearable systems,[112, 113, 114, 115, 116, 117] a pilocarpine-loaded microneedle patch was recently developed for sweat testing.[118] With an array of 100 microneedles at a length of 600 μm, the iontophoresis patch is much smaller and thinner than a regular commercial iontophoresis gel (Figure 6.3D). In an equine model, the microneedle patch produces a much higher sweating volume per unit area and unit dose compared to the pilocarpine hydrogel (Figure 6.3E,F). While the previous studies focused on local sweating, the first use of carbachol for sweat extraction was integrated into a band-aid-shaped system with an external iontophoresis device (Figure 6.3G).[53, 119, 120] With the custom-made carbachol gels compared with pilocarpine gels, the group also studied the sweating duration at high sweat rates (Figure 6.3H) and at low sweat rates (Figure 6.3I) over a long time frame (over 10 hours). More recently, a flexible laser-engraved iontophoresis patch with a much smaller form factor was developed with small carbachol gels cast onto laser-engraved graphene electrodes, and on-demand sweat induction was achieved by integrated FPCB (Figure 6.3J).[86] The sweat rates at the stimulated area and the surrounding skin areas were characterized after a 5 min iontophoresis with pilo-

carpine and carbachol (Figure 6.3K,L). In addition to novel form factors, variation in the current profile for enhanced sweat volume was studied and a sinusoidal pulsed current profile was suggested for use in patients with sweat problems.[121]

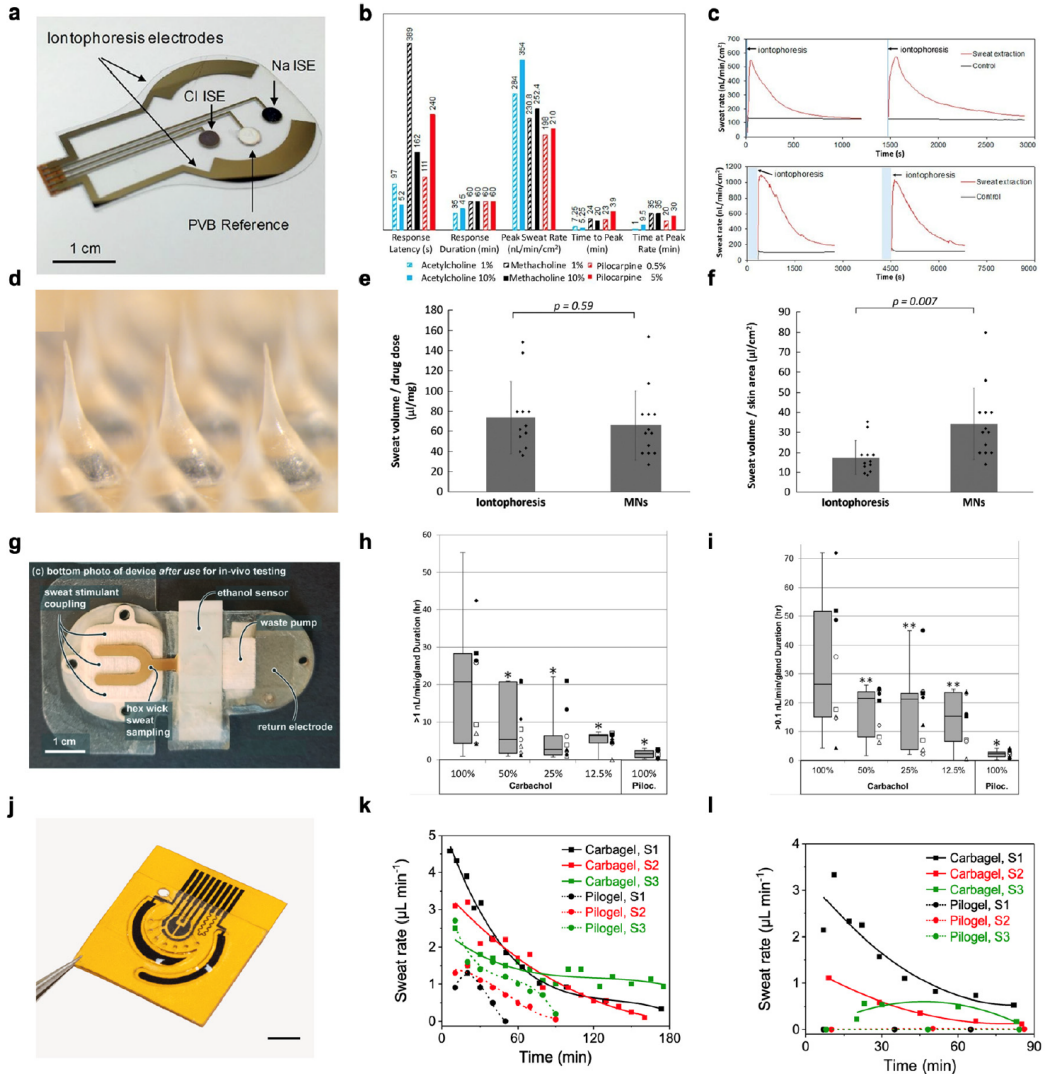


Figure 6.3: Iontophoresis-based sweat induction

(A-C) An iontophoresis patch (A) and sweating responses to different cholinergic agents (B,C). [111] (D-F), A microneedle-based iontophoresis device (D) and in vivo sweat responses of the device (E,F). [118] (G) A carbachol-based iontophoresis sensing device. [53] (H,I), High sweat rate (H) and low sweat rate (I) duration of carbachol and pilocarpine iontophoresis stimulation, respectively. [37] (J), A flexible laser-engraved iontophoresis sensing patch. Scale bar, 5 mm. [86] (K,L), Localized sweat rates measured from the stimulated (K) and surrounding (L) skin areas after a 5 min iontophoresis with pilocarpine and carbachol. [86]

### 6.2.3 Sweat Composition by Different Induction Methods

The composition of sweat may vary across sweat induction methods. First, the pH of sweat tends to be higher in iontophoresis-induced sweat compared to thermogenic sweat.[122] High sweat rates and low ductal $HCO_3^-$ reabsorption may contribute to this higher pH. $Ca^{2+}$ and $Mg^{2+}$ levels were observed to be higher in sweat obtained from the sauna than in sweat obtained from exercise.[123] Recent metabolomic studies also revealed variations in lipid profiles[124] and metabolites[105] among iontophoresis-induced, exercise-induced, and natural sweat, including notable variations in L-alanine, pyruvate, L-aspartate, BCAAs, asparagine, lysine, and fumarate concentrations.[105] The stability of metabolites in sweat also plays a critical role in the quantitation process; sweat metabolite stability was shown to last for 90 min at simulated body temperature.[125] For natural sweat at a much slower sweat rate, it is suggested that quantitation results may be compromised due to metabolic quenching of enzymatic reactions and metabolite stability, an issue especially relevant for untargeted metabolomics analysis.[126] For targeted metabolomics analysis, such as drug tests, controlled stability studies should be done to achieve repeatable quantitation within the applicable detection range.[127] Moreover, tissue-dependent factors (e.g., keratin amount and thickness of stratum corneum) affect the iontophoresis response between individuals and at different body locations, potentially also impacting the sweat composition.[126]

## 6.3 HPLC Analysis of Iontophoresis Sweat Profile

Sweat is an excellent biofluid for small molecule sensing since it is a noninvasive, accessible biofluid that is highly filtered of large fouling proteins. The reported nicotine content in sweat is three orders of magnitude higher than that reported in blood, ranging from 12-62 nM for smokers.[128] Nicotine content in sweat has previously been reported in the range of 3-7 μM and 16-24 μM for light smokers (<10 cigarettes/day) and heavy smokers (>25 cigarettes/day), respectively.[129, 130, 131] This is likely due to acid trapping in the sweat duct, an effect observed similarly in gastric juice, saliva, as well as intracellularly in acid vesicles.[132, 133]

For accurate analytical measurements, it is important that biosensors are selective for their target molecule. Yet for nicotine sensing, there is a concern that the sweat stimulation pathway via the sudomotor axon reflex is governed by nicotinic receptors as described previously. Acetylcholine and carbachol both bind to nicotinic receptors to activate this sweat response. Additionally, the iNicSnFR bioreceptor used in this

work was evolved from the *Bacillus subtilis* choline-binding protein OpuBC.[134] We thus hypothesized that iNicSnFR would bind cholinergic agonists important to the sweat gland physiology.

In this section, we perform ultra-performance liquid chromatography-mass spectrometry (UPLC-MS) to evaluate the composition of sweat for key interferents relevant to nicotine sensing. We aimed to determine the relative concentration of cholinergic agonists in sweat versus nicotine such that the nonspecific signal response of iNicSnFR could be further evaluated.

### 6.3.1 Materials and Methods

#### Reagents

Acetylcholine chloride, choline bitartrate salt, and pilocarpine nitrate salt were purchased from Sigma-Aldrich. Carbachol was purchased from Alfa Aesar. Agarose, potassium chloride, (-)-nicotine tartrate, and liquid chromatography–mass spectrometry (LC–MS)-grade acetonitrile was purchased from Fisher Scientific. 1.0 mg $mL^{-1}$ (-)-cotinine in methanol (C-016), 0.1 mg $mL^{-1}$ (±)-cotinine-$D_3$ in methanol (C-017), and 0.1 mg $mL^{-1}$ (±)-nicotine-$D_4$ in acetonitrile (N-048) reference standards were purchased from Cerilliant.

#### Liquid Chromatography-Mass Spectrometry

Acetylcholine (ACh), choline (Chol), nicotine (Nic), cotinine (Cot), carbachol, and pilocarpine levels were measured in sweat using ultra-performance liquid chromatography-mass spectrometry (UPLC-MS). Analysis was performed using an Acquity UPLC system coupled to a Xevo ToF mass spectrometer (Waters Corporation, Milford, MA, USA), located in the Water and Environment Laboratory at California Institute of Technology. Chromatographic separations of ACh, Chol, Nic, Cot, carbachol, and pilocarpine were achieved using an Acquity BEH HILIC column (2.1 × 100 mm, particle size 1.7 µm) using the same method outlined by [135]. The column temperature was held constant at 27 °C. The mass spectrometer was operated in positive electrospray ionization mode. MassLynx software (v. 4.1) was used for data acquisition and analysis. LC-MS chromatograms of ACh, Chol, Nic, Cot, carbachol, and pilocarpine were acquired by selection for $[M+H]^+$ with retention times of 2.94 min, 3.02 min, 3.025 min, 1.995 min, 3.01 min, and 2.69 min,

respectively, with a retention time window of 0.3 min, and m/z of 146.12, 104.11, 163.12, 177.11, 147.11, and 209.13, respectively, with a mass window of ±0.02 Da. Cotinine-$D_3$ (Cot-$D_3$) (m/z: 180.12; retention time: 2.05 min) and nicotine-$D_4$ (Nic-$D_4$) (m/z: 167.15; retention time: 3.07 min) were used as internal standards. For quality control, a standard was repeatedly tested 15 times initially and once every 10 samples.

### Sample Preparation

Stock standards were prepared in methanol. Mixed calibration standards were prepared with 0.1-10 µM ACh, 1.0-30 µM Chol, 0.1-10 µM Nic, 0.1-10 µM Cot, 10-50 µM carbachol, 10-50 µM pilocarpine. Internal standards of 1 µM Cot-$D_3$ and 1 µM Nic-$D_4$ were added to each sample. Aqueous samples were diluted 8× with acetonitrile.

### Biofluid Sample Collection

**Iontophoresis Sweat.** Cholinergic drugs were added to agarose (3% w/w) hydrogels for iontophoresis drug delivery. 1% carbachol or 0.5% pilocarpine were added for the anode hydrogel and KCl (1% w/w) was added for the cathode hydrogel. Agarose is heated and dissolved in deionized water and concentrated drug or KCl dissolved in deionized water is added to agarose upon mixing and continued heating at ~80 °C. Agarose should be warm to the touch prior to drug addition to prevent chemical degradation.

Iontophoresis was implemented using a Model 3700 Macroduct Sweat Collection System for sweat induction. The stimulated skin area on the anterior forearm was cleaned with an alcohol swab prior to iontophoresis and sweat collection. Transdermal drug delivery occurs via iontophoresis for 5 min at a constant current of 1.5 mA. The participants were asked to wear a Macroduct collector over a 1 hour period for sweat collection.

**Exercise Sweat.** Exercise sweat was collected directly from the skin during treadmill running. The sweat was filtered and centrifuged prior to testing to remove dead skin cells and particulate that were present on the skin surface. Sweat samples were stored at -20 °C prior to testing.

**Serum Collection.** Fresh blood samples were collected once prior to smoking and twice after smoking, using a lancet finger-prick approach. Blood was clotted at room temperature for 15 min, and serum was separated by centrifuging at 1,500 *g* for 10 min and instantly stored at -20 °C prior to testing.

### Nicotine Intake Study

Carbachol-stimulated sweat was collected during a participant's regular smoking session. The participant was a light, daily smoker (5-7 cigarettes/day), male, 30-40-year age range. Sweat was collected for 15 minutes prior to the smoking session. The participant was asked to smoke ad libitum with their nicotine source of choice. Marlboro Green menthol cigarettes were used with a nicotine content of 0.6 mg per stick. The participant smoked one cigarette over a 5-minute period. The participant then returned for sweat collection. Sweat was collected for 40 minutes post-smoking session. For time series analysis, $t = 0$ refers to the last puff of the smoking session.

## 6.3.2 Results and Discussion

Using hydrophilic interaction LC-MS we were able to isolate acetylcholine, choline, nicotine, cotinine, carbachol, and pilocarpine peaks to quantify their presence within a single sample. This technique was then used to analyze various sweat and serum samples. These results provide key information regarding the relative concentrations of relevant sweat interferents and outline design requirements for a nicotine sweat sensor.

As a measurement tool, LC-MS allowed for nanomolar-level analysis consuming minimal sample volume. Internal standards, such as Cot-$D_3$ and Nic-$D_4$, provided important stability controls throughout the experiment (Figure C.11). Quality controls such as repeating the same standard every 10 measurements as done here could be used in future analysis to correct for drift throughout the course of the experiment. This method may be used in future experiments for time course data with sampling frequencies of every 3 min assuming a sweat rate of 1 µl $min^{-1}$ (3 µl of sweat was consumed for 2 × dilution factor).

LC-MS was performed as a ground truth for sweat nicotine quantification (Figure 6.4). We compared the nicotine content in sweat samples of a smoker immediately after smoking with endogenous levels in the sweat of a non-smoker. Non-smoker sweat contained a mean endogenous nicotine concentration of 8.0 ± 13.5 nM (n

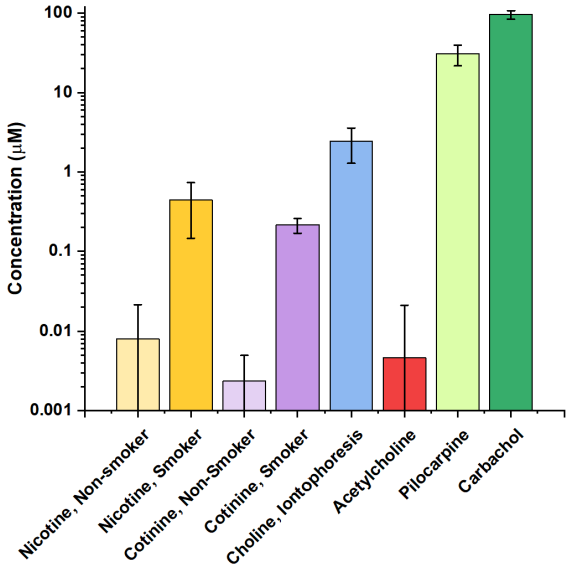


Figure 6.4: Analytes in iontophoresis-stimulated sweat determined by LC-MS

Average concentrations of sweat analytes that represent potential interferents for iNicSnFR. Nicotine and cotinine results were analyzed in non-smoker and smoker participants. Nicotine analysis is performed based on measurements post-smoking session. Choline and acetylcholine results are shown for iontophoresis-stimulated sweat by either pilocarpine or carbachol. Error bars represent s.d. for n = 20, 11, 20, 23, 42, 43, 11, 9 for each analyte in order.

= 20), whereas smoker sweat contained a mean nicotine concentration of 439.5 ± 293.3 nM (n = 11). The nicotine metabolite cotinine was endogenous at a mean concentration of 2.3 ± 2.6 nM (n = 20) and elevated in smoker sweat to 214.1 ± 45.1 nM (n = 23) on average. Serum nicotine and cotinine levels were also evaluated in smoking participants with means of 67.7 ± 13.1 nM (n = 3) and 254.6 ± 64.2 nM (n = 6), respectively.

Cholinergic agonists acetylcholine, pilocarpine, and carbachol were also evaluated. The mean sweat acetylcholine level was 4.6 ± 16.6 nM (n = 43). Its metabolite choline was present at 2.43 ± 1.14 μM (n = 42) for iontophoresis stimulated sweat and elevated at 21.95 μM (n = 1) for exercise stimulated sweat. In comparison, serum choline levels were found to be 33.92 ± 3.38 μM (n = 6) (Figure 6.5). Choline levels are higher in exercise sweat since acetylcholine is the primary agonist for natural sweat secretion. For pilocarpine and carbachol iontophoresis, these cholinergic agonists were found to be present in the stimulated sweat at average levels of 30.64 ± 8.94 μM (n = 11) and 95.86 ± 11.70 μM (n = 9), respectively. Pilocarpine levels decreased by 41.18% over the course of 30 min of sweating stabilizing around 25

µM after the first 10 min. Carbachol levels decreased by 21.86% over the course of an hour of sweating, stabilizing around 85 µM after the first 30 min.

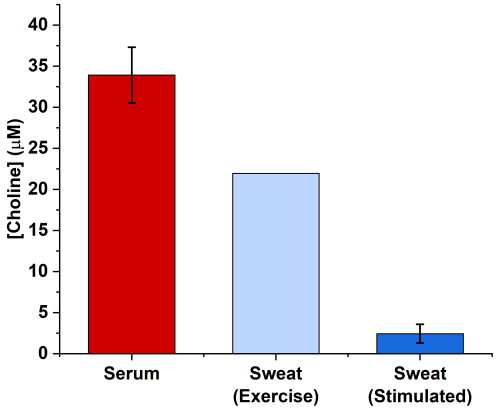


Figure 6.5: Choline concentrations in serum and sweat induced by exercise or iontophoresis

We also compared nicotine and cotinine time course data during a smoking session (Figure 6.6). Sweat cotinine levels remain mostly constant throughout the experiment, but nicotine levels increase. Pilocarpine stimulated sweat sees a jump in nicotine levels about 15 min after smoking. For carbachol stimulated sweat, nicotine levels increase prior to smoking. The cause of this is uncertain. The difference in baseline nicotine levels between the two sweat stimulations is likely due to time differences since last smoking session and other external factors, since the cotinine levels remain consistent across the two sweat types. Additional work is needed to determine how the sweat rate, which varies between stimulants and individuals, may impact nicotine partitioning.

While there is a significant difference between smoker and non-smoker sweat nicotine levels, the sweat nicotine levels are lower than anticipated based on prior art. One distinction is that the sweat analyzed in this work was generated using iontophoresis stimulation rather than exercise stimulation as performed in the literature. It is possible that the values reported in the literature that were measured with CYP2B6-based and voltametric-based sensors are measuring sweat interferents. [130, 136] The selectivity of these sensors against choline should be evaluated given it is significantly more present in exercise sweat than in iontophoresis sweat. Amr et al. [130] also measured nicotine content using gas chromatography. These discrepancies may be in part due to the volunteers in this study smoking considerably more frequently

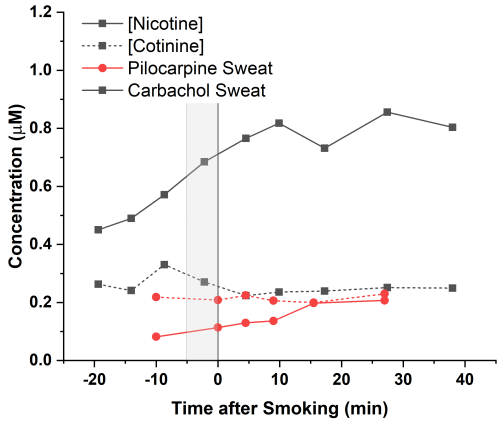


Figure 6.6: Time course of sweat nicotine and cotinine concentrations before and after smoking

Sweat was either stimulated by pilocarpine (red) or carbachol (black) iontophoresis. One cigarette was consumed during the smoking session defined by the gray shaded area. Cotinine concentrations (dashed line) remain relatively constant, whereas nicotine concentrations (solid line) increase after smoking.

and with heavier doses than the smoker participant we sampled from. Adjusting for this increased nicotine intake using smoking pharmacokinetic simulations accounts for an order of magnitude change in blood (Figure C.12).[134] The additional 4 × lower variation may be the result of different sweat collection mechanisms. It is also possible that due to acid trapping effects, nicotine does not partition with a linear blood-sweat correlation.

In summary, these results indicate that a sweat nicotine sensor should have a detection limit of 100 nM for use in light, daily smokers. Additionally, the sweat nicotine levels are much lower than the level of cholinergic agonists in sweat. It is important to evaluate the sensor's selectivity against these agonists as this may inform the type of sweat used. These results also demonstrate the need for further research to optimize iontophoresis sweat induction methods based on the pharmacokinetics of carbachol and pilocarpine.

## 6.4 iNicSnFR Readiness for Nicotine Sweat Sensing

In this section, we evaluate iNicSnFR's performance as a bioreceptor under sweat conditions of low ionic strength and in the presence of cholinergic agonists.

### 6.4.1 Materials and Methods

A Tecan Spark M10 96-well fluorescence plate reader (Tecan, Männedorf, Switzerland) was used to measure baseline and drug-induced fluorescence ($F_0$ and $\Delta F$, respectively). 100 nM iNicSnFR12 wildtype was used in these dose-response relation experiments. cpGFP fluorescence was tested with excitation at 485 nm and emission at 535 nm. The effective concentration at 50% (EC50) of the maximum response was evaluated.

Dose-response curves were generated at varying ionic strengths while buffering capacity and pH was held constant. Since NaCl is the dominant salt modulating sweat IS, NaCl was added to 0.2× PBS (corresponding to 30 mM IS), pH 7.0 buffered solution to adjust the IS. Serially diluted nicotine concentrations were prepared from a pH-adjusted nicotine stock, with added salts accounted for during pH adjustment. IS levels from 30-150 mM were tested.

Dose-response relations were tested for pilocarpine and carbachol in 3× PBS, pH 7.0. Nicotine dose-response relation was also tested in a 1:1 mix of exercise sweat and 3× PBS, pH 7.0

### 6.4.2 Results and Discussion

Sweat electrolyte concentration is variable due to a variety of factors including hydration level and sweat rate. Sweat IS typically ranges from 20-100 mM.[137] It is known that IS has significant effects on the signal response of electrochemical sensors that rely on redox probe localization through binding-induced conformation changes due to charge screening effects on the Debye length.[138] However, it is unknown whether IS will impact the binding dynamics of the bioreceptor itself.

We evaluated iNicSnFR12's fluorescent behavior at low IS. There was a clear difference in the fluorescent behavior between IS <60 mM and >75 mM, with the signal gain increased at low electrolyte concentrations (Figure 6.7). The EC50 also decreased with IS. It is unclear from this experiment if IS impacts the target-binding or the fluorescent signal transduction. IS has been found previously to impact the absorption spectra of the GFP variants with decreases in fluorescence attributed due to charge screening effects on the chromophore and the surrounding protein environment.[139, 140] These results indicate that iNicSnFR12 performance is enhanced at the low IS conditions of sweat, but that IS calibration would be needed to interpret fluorescence measurements under variable sweat IS conditions.

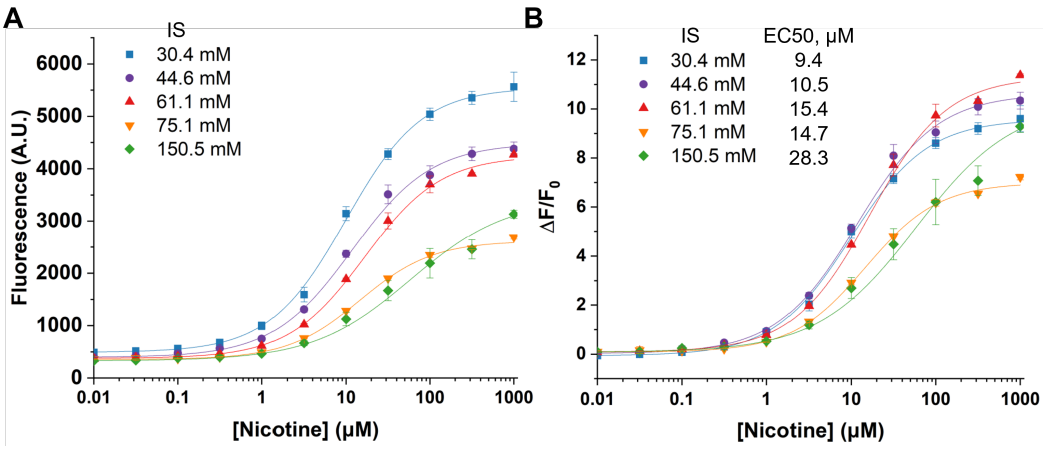


Figure 6.7: Nicotine dose-response relations of iNicSnFR12 at varying ionic strengths

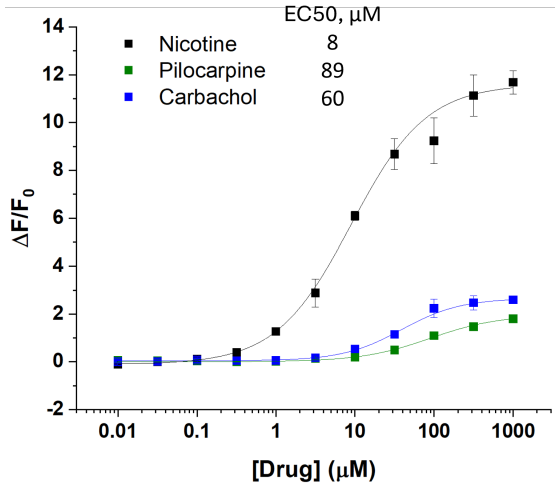


Figure 6.8: Dose-response relation of iNicSnFR12 to cholinergic drugs, pilocarpine and carbachol, in 3× PBS, pH 7.0

The selectivity of iNicSnFR12 against iontophoresis cholinergic agonists was evaluated (Figure 6.8, Supplementary Figure C.13). iNicSnFR12 showed low activation by pilocarpine and carbachol with a significantly reduced maximum $\Delta F/F_0$. iNicSnFR12 exhibited a stronger binding affinity for carbachol over pilocarpine. This is expected since carbachol, like acetylcholine, activates nicotinic sudomotor nerve receptors at the base of the sweat gland triggering peripheral sweating via the sudomotor axon reflex. Through this mechanism, carbachol generates greater sweat rates than pilocarpine. LC-MS analysis show that carbachol and pilocarpine iontophoresis may produce agonist concentrations in sweat of approximately 95 μM and 30 μM, respectively, which translate to $\Delta F/F_0$ artifacts of 1.988 and 0.508 and

background raw fluorescence, a.u., of 1854 and 755, respectively. Despite these interferents being present in sweat at orders of magnitude larger than nicotine, their low fluorescence response allows for some fluctuation in the sweat stimulant concentration without significantly impacting the fluorescent response. With a consistent iontophoresis method, the background activation can be adjusted for in the nicotine concentration back-calculations.

We tested the performance of iNicSnFR12 in 0.5× exercise sweat (Figure 6.9, Supplementary Figure C.14). The EC50 of iNicSnFR12 was comparable to its performance in 3× PBS, yet the background fluorescence was very high. Exercise sweat choline is a likely contributor to this background signal with a ~ 20 μM concentration due to the metabolism of acetylcholine, which activates sweat gland signaling pathways. However, this would only account for at most 10% of the observed $F_0$. Further investigation is needed to understand the cpGFP activation in sweat and if this phenomenon is variable across population.

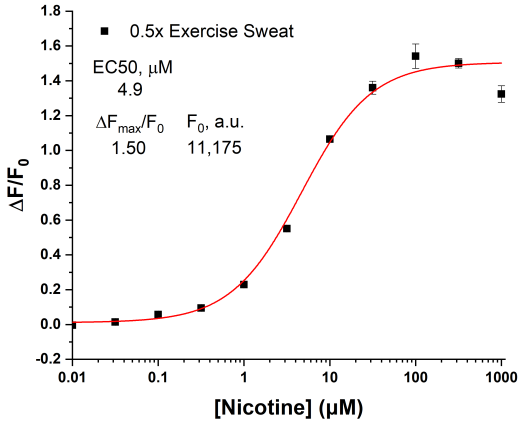


Figure 6.9: Nicotine dose-response relation of iNicSnFR12 in 0.5× exercise sweat

1:1 mix of exercise sweat and nicotine solution in 3× PBS, pH 7.0.

While the variable of pH was not evaluated here, we anticipate pH to primarily impact the signal transducer element. GFP-based fluorescent biosensors exhibit decreased fluorescence at acidic pHs. [141] Additionally, for future ePBP variants, methylene blue among other redox moieties are pH-sensitive. [142]

Overall, these results show promise for the translation of iNicSnFR12 to a wearable sweat sensing platform. An iNicSnFR12 sweat sensing platform would require the incorporation of calibration sensors including a pH sensor and impedance sensor for ionic strength. Additionally, a sweat stimulant should be chosen based on the

monitoring context. Pilocarpine only produces sweat in the stimulated skin area, requiring pilocarpine contamination, and the sweating effects typically only last for about 1 h. However, pilocarpine sweat typically has a neutral pH and iNicSnFR12 has a lower binding affinity to it. In contrast, carbachol generates high sweat rates with sweating effects lasting >24 h in some. But, carbachol sweat is typically basic and it activates iNicSnFR12 more. Since carbachol activates localized sweating, it is possible that contamination could be reduced by collecting sweat in a different area than was stimulated. [30, 86, 143] It is possible that the peripheral sweat collection may still contain choline as a biproduct of the sudomotor axon reflex stimulation. With cholinergic agonist interference being unavoidable for sweat stimulation, priority should be placed on design constraints of on-body monitoring duration and pH, which may render fluorescent and electrochemical transducers inoperable, when determining which iontophoretic drug to use.

## 6.5 Path to Commercialization for Wearable Sweat Sensors

There is tremendous translational value in the technologies described in this review. Translational value is determined by the ability to blend market and design factors in a way that meets a clinical need.[144] Wearable sweat sensors can address the need for noninvasive biomarker data collection. Applications of wearable sweat sensors include but are not limited to fitness and recovery, mental health, personalized healthcare, and telemedicine. High translational value establishes a path to commercialization. In this section, the medical device product life cycle is detailed along with industry and regulatory challenges. The emerging sweat sensing market is summarized, and future growth trends are discussed.

### 6.5.1 Product Life Cycle

The medical device product life cycle (Figure 6.10) begins with conception, design, and prototype development. During this phase, it is important to file intellectual property and licensing.[145] Upon prototype development, design specifications are tested and verified. Considerations should be made for scaling feasibility via low-cost mass manufacturing techniques. Next, regulatory compliance strategy must be considered to bring the product to market in a timely manner. Preclinical investigation validates the product performance, identifies failure modes, and refines risk mitigation strategies. Product compliance with FDA regulations is evaluated based on robust clinical trials, the extent of which varies based on device classifica-

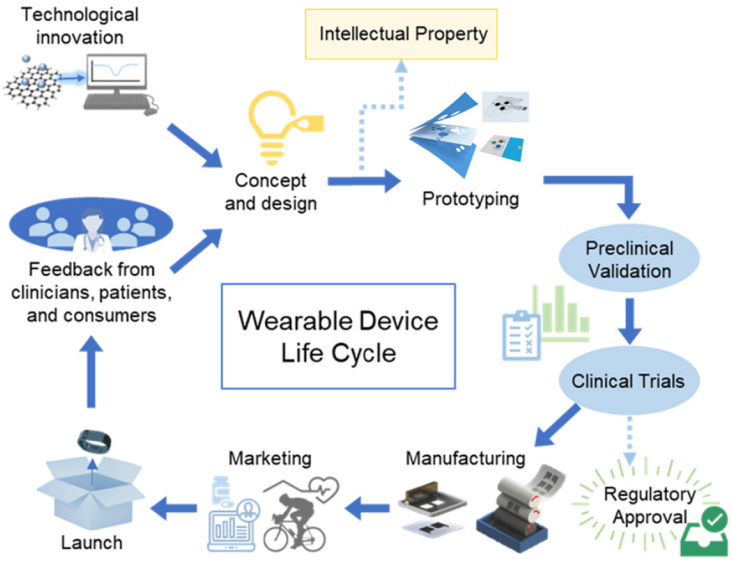


Figure 6.10: Wearable device product life cycle

tion. After FDA approval and product launch, postmarket risk is mitigated through adverse event reporting, surveillance, and patient focused registry. Product enhancements are also made based on market feedback from stakeholders and regulatory approval. Finally at the end of product life, it is important to communicate with stakeholders the timeline for the end of manufacturing, end of support, and end of availability.[145]

The medical device product life cycle may also be characterized by the device deployment duration, how long or often the device is in use by the patient.[145] Single-use, frequent use, and continuous use durations are determined by contextual design factors of the wearable device. How quickly and how often biomarker levels change may determine the required time resolution of measurements. While a single-point daily or weekly measurement may be sufficient to monitor or screen for certain abnormalities, one may need to integrate continuous sampling to perform trend analysis and pattern recognition. For continuous use, the wearable deployment duration is determined by the limitations of the device itself (e.g., sweat generation, sensor degradation) or the monitoring context (e.g., period of exercise, treatment course). Device duration may inform the scale of deployment.

To make the devices accessible, the design should be scalable at low-cost using high-throughput manufacturing methods. Screen printing, inkjet printing, roll-to-roll (R2R) manufacturing, and laser engraving are all methods that achieve high efficiency patterning and good conductivity for the flexible electronics found in

wearable sweat sensing platforms. Screen printing is one of the most established low-cost mass-manufacturing methods. Screen-printed electrodes are commercially available in a variety of conductive materials and patterns with highly reliable offerings from companies such as DropSens by Metrohm. Screen printing uses a stencil to deposit functional inks onto a flexible substrate, while simultaneously removing excess ink (Figure 6.11A).[146] Screen printed film thickness is wide ranging (0.02-100 μm).[147] Many considerations go into formulating a conductive ink, including the nanomaterial properties, homogeneity, viscosity, and substrate compatibility. Laser-induced graphene on PI film may be harvested and made into an ink with ideal electrochemical and mechanical properties for flexible electronics.[148] Conductive (e.g., PEDOT:PSS) and elastomeric (e.g., polyester-polyurethane) binding agents can enhance the performance of conductive inks.[148] Surfactants and polymers prevent particle aggregation and are important additives to conductive inks, which require stable dispersion for low resistivity.[149] High viscosity inks are required for screen printing, leading to challenges in creating fine pattern features and often resulting in resolutions on the order of tens of microns in commercial use.[150]

In inkjet printing, designs are digitally controlled and fabricated by droplet addition according to its design dot matrix (Figure 6.11B).[151] On-demand ink ejection generates droplets through piezoelectric, thermal, electrohydrodynamic, and other pulsatile methods.[149] Inkjet-printed films can vary in thickness based on additive droplet control and rheological properties of the ink. Ink viscosity and surface tension are important parameters for good printing quality and jettability. Bioinks have added challenges of biomolecular stability during printing and nonspecific adsorption to the ink tank resulting in protein loss (solved with BSA additive).[149] Inkjet printing is highly efficient with minimal materials wasted, reducing the cost per print. With high customizability and precise spatial control, inkjet printing is ideal for printing complex patterns using multiple inks, as in the case of e-skins.[151] Biosensors can be fabricated by serial printing the electrodes and connections, encapsulation, functionalization, and entrapment.

R2R manufacturing is a technique that allows for sequential modifications, including pattern transfer, etching, gravure printing, heating, UV curing, and others.[152, 154] R2R gravure printing uses an engraved cylinder that stamps a substrate feed and continually refreshes with ink as it rotates. The bending and rotations of the feed during R2R limit this process to flexible substrates.[147] In comparison to

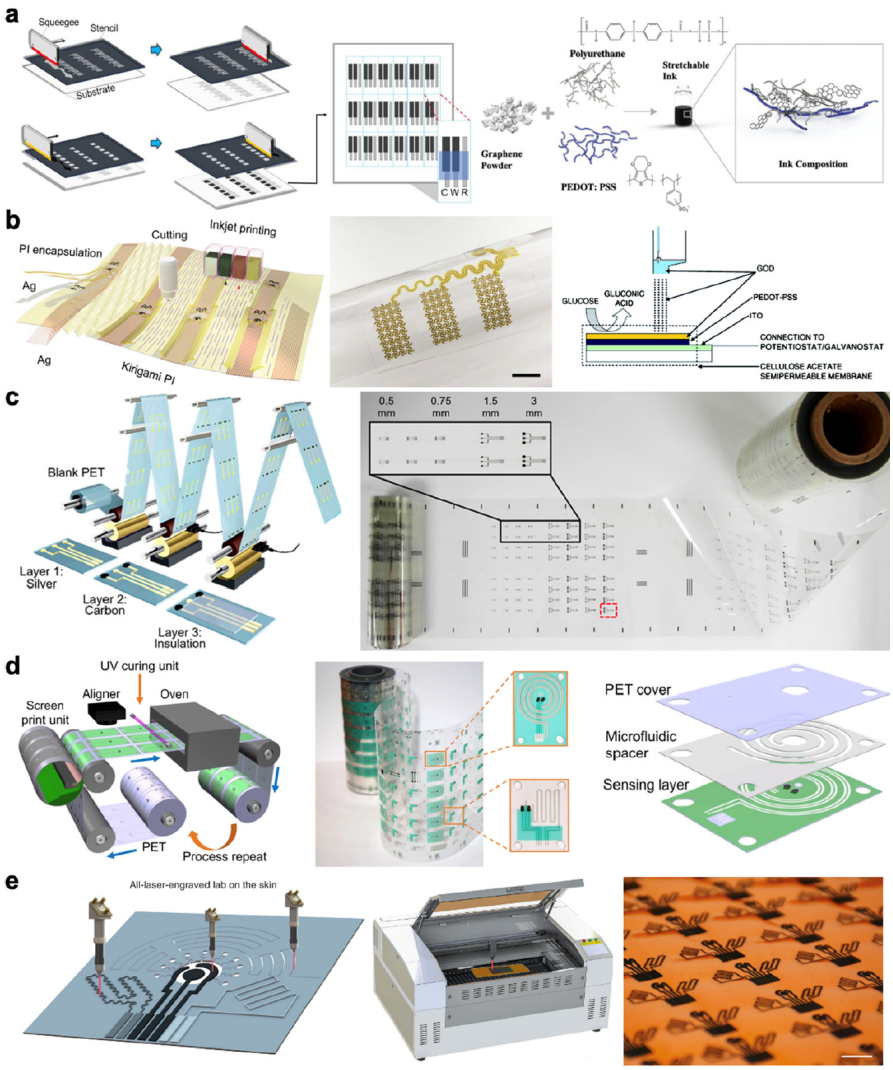


Figure 6.11: Mass manufacturing techniques for low-cost wearable electronics and microfluidic patches

(A) Screen-printed electrode fabrication and flexible graphene ink formulation. [146, 148] (B) Inkjet printing of electrodes and bioink enzyme functionalization. Scale bar, 1 cm. [151] (C) Roll-to-roll electrode fabrication. [152] (D) Roll-to-roll lab-on-a-chip fabrication. [153] (E) Laser-engraved lab on the skin. Scale bar, 1 cm. [74]

screen printing, R2R gravure printing mechanics can operate at faster speeds with high resolution and consistency, but ink deposition is relatively thin, around 10 µm, increasing the resistivity.[147, 150] Using a bilayer working electrode scheme, thin R2R gravure printed carbon electrodes may be supported by a silver ink layer (Figure 6.11C).[152] This morphology enables high-throughput R2R manufacturing of flexible electronics while maintaining mechanical and electrochemical robustness. R2R manufacturing may be used for microfluidic fabrication and full device assem-

bly (Figure 6.11D). R2R rotary electrode screen printing was combined with R2R laser cutting of microfluidics (bilayer microfluidic adhesive spacer and flexible PET cover) to assemble a wearable sweat sensor layer-by-layer.[153] A camera module was used to monitor the alignment of the printed layers during R2R rotary assembly. The R2R system produced 60 devices per minute on a 100 m web length.

Laser engraving is a bottom-up method for graphene electrode fabrication using a $CO_2$ laser cutter to directly carbonize polymeric substrates (e.g., PI) (Figure 6.11e).[74, 155] Laser-engraved graphene (LEG) is low-cost and high-throughput. LEG composition, porosity, impedance, and morphology may all be tuned using laser parameters.[155] Complex patterns can be easily made digitally with resolution limited only by the focus and power of the laser. Due to a lack of binding elastomers, the poor mechanical stability of LEG may result in disconnections and an open circuit, a problem exacerbated by repeated bending of flexible substrates.[155] The laser cutter may also be used to fabricate multilayered microfluidics rapidly by laser cutting channels, inlets, outlets, and sensing regions.[74] Lastly, individual devices may be cut from mass-printed sheets using camera-assisted laser cutting.[153]

FDA oversight is present at every step of the medical device product life cycle. However, noninvasive medical devices have fewer barriers to market entry. The foundation of FDA medical device regulations are based on the reasonable assurance of safety and efficacy (21 CFR 860.7(d,e)).[145] As noninvasive wearable devices, sweat sensing platforms exhibit the most risk when they include iontophoretic sweat induction and when they are used for a serious medical diagnosis. For reference, the Macroduct sweat iontophoresis system is registered as a Class II device. However, should the device be of demonstrated substantial equivalence to another legally U.S. marketed device, then the device is exempt of the 510(k) premarket notification and may be made immediately commercially available. The FDA approval process may also be bypassed under the condition that no medical claims are made for the device and the device is noninvasive with no biological interactions.

### 6.5.2 Emerging Market Landscape

To avoid the FDA regulatory process, many early-stage sweat sensors are starting out in the consumer health and wellness space (Table 6.2). Sweat is induced during activity, so sweat stimulation is not needed in the wearable patch design. Rather than providing medical information, the data is regarded as a performance metric. Together these allow noninvasive wearable sweat sensors to be readily commer-

| Company/Product | | Market Segment | Metrics | Transduction | FDA Clearance |
|---|---|---|---|---|---|
| Epicore Biosystems | Gx Sweat Patch | Fitness (hydration) | Sweat rate, $Cl^-$ | Colorimetric | – |
| | Connected Hydration | Safety (hydration) | Sweat rate, electrolyte content, temperature, motion | Electrochemical | – |
| | My Skin Track pH | Skincare | pH | Colorimetric | – |
| | Discovery Patch | Diagnostics | None | n/a | Yes |
| Nix Biosensors | | Fitness (hydration) | Sweat rate, electrolyte content | Electrochemical | – |
| FlowBio | | | Sweat rate, electrolyte content | Electrochemical | – |
| hDrop | | | Sweat rate, temperature | Electrochemical | – |
| SM24 | | Fitness, diagnostics | Lactic acid, glucose, sweat rate | Electrochemical | – |
| Onalabs | | Fitness, diagnostics | Lactic acid, glucose | Electrochemical | – |
| Graphwear | | Diagnostics | Glucose | Electrochemical | – |
| Xsensio | | | pH, $Na^+$, $K^+$, $Ca^{2+}$, cortisol | Electrochemical | – |

Table 6.2: Wearable sweat sensor market landscape.

cialized. The Gx sweat patch by Epicore Biosystems in partnership with PepsiCo and Gatorade is the first widespread commercially available wearable sweat patch. The flexible microfluidic adhesive patch captures sweat throughout exercise and collects sweat rate and electrolyte content data using a colorimetric output.[156] The corresponding app allows for real-time analysis using ML-enabled image processing.[157] The device has been validated for hydration monitoring across 312 athletes and in a variety of use conditions.[158, 157]

Competitors to Epicore for hydration monitoring include Nix Biosensors, FlowBio, and hDrop.[159, 160] In contrast to the Gx sweat patch, these devices utilize integrated electrical components. Nix calculates sweat rate, electrolyte loss rate, and sweat composition in the sweat collection channel and transmits this data wirelessly. The electronic pod is reusable and connects to a single use sweat patch.[161] hDrop is an armband that continuously monitors hydration through skin impedance sensing.[162] Lactic acid is an important indicator of exercise intensity and muscle fatigue during training. Onalabs is developing a sweat lactate sensor for athletes prior to venturing into the clinical space (they plan to incorporate additional biochemical sensors, including glucose detection).[163] SM24 is also working toward a wearable sweat-based sensor for real-time glucose, lactate, and hydration monitoring.[164]

Epicore as a company has focused heavily on the development of flexible microfluidic sweat collection systems, referred to as "epifluidics". This establishes a template for mass customization, a marketing and manufacturing technique that allows for flexible, custom product features with low unit cost at mass production.[165] Custom biochemical sweat assays may be simple to deploy relative to changing the microfluidic structure. A colorimetric pH assay was used to assess skin health and personalized skincare needs in the My Skin Track pH platform designed with L'Oréal.[166] Customizable sweat assays are the basis for the Epicore Discovery Patch, which collects sweat, and extracts it into a cryovial for future analysis.[156]

The Discovery Patch has been used to assess cytokines in sweat.[56] The Discovery Patch is registered as a 510(k) exempt Class I FDA device.

Expanding into clinical diagnostics requires regulatory approval. The Discovery Patch serves as a springboard to on-body diagnostic assays. Epicore has clinical studies in progress for applications including stroke rehabilitation, cystic fibrosis screening, prediabetes screening, and kidney disease screening.[165] In addition to Epicore, GraphWear is performing clinical studies in preparation for FDA review of their noninvasive continuous glucose monitor. If their trials further demonstrate similar performance to other continuous glucose monitors, they may be eligible for 510(k) clearance.[167] Swiss company Xsensio hopes to develop the first commercial Lab-on-Skin sensing platform for real-time biochemical sensing. Their approach utilizes miniaturized functionalized field-effect transistors for multiplexed biomarker detection, including $Na^+$, $K^+$, $Ca^{2+}$, pH, and cortisol.[168, 169, 170, 171]

Form and comfort are important criteria for product adoption. The Nix sweat patch uses kinesiology tape for flexible adhesion and comfort, which is a material commonly used by their targeted athletic demographic.[161] Epicore Biosystems has focused heavily on the development of a flexible microfluidic sweat collection system, which is the foundation of their devices. Form defines function for Epicore's infant cystic fibrosis sweat sticker; the soft, flexible collection platform allows for low volume sweat collection and reduces leakage rates.[172] Current FDA-cleared standard sweat collection devices fail approximately 10-20% due to insufficient sweat collection, which the Epicore microfluidic patch resolves. Additionally, fun graphics on the sweat sticker were attractive to children and improved their perceived experience.[173]

Similar trends are seen in the wearable heart rate monitoring space. Early adoption in the fitness tracking space allowed for continued market testing to improve sensing and diagnostic accuracy. Some smartwatches now have FDA-cleared applications like the AppleWatch and Apple's corresponding ECG app for classifying signs of AFib and irregular rhythms.[174] With the rise in popularity of smartwatches and CGM patches, the U.S. market is primed to adopt wearable sweat sensing platforms.

Consumer adoption and physician adoption will likely vary, yet physician adoption is required to see transformative change and impact of sweat sensing technology in healthcare. Physician adoption first requires accurate data collection and FDA approval. Next, integrated data analytics and efficient summaries are required. High volume biometrics may be overwhelming and be ignored. It is important to

communicate and work closely with physicians to understand what would be most informative for them. User interface and compatibility with current electronic medical systems are additional design considerations that may impact clinical adoption. Lastly, developing a clinician-trusted brand dedicated to quality and medical-grade products is important.

Another market for wearable devices is research and clinical trials. Medidata Sensor Cloud (formerly MC10) and VivoSense provide services to collect, integrate, and analyze data from wearables in clinical trials. Medidata Sensor Cloud utilizes proprietary wearable patches (e.g., BioStamp nPoint) to collect medical-grade quality biometrics remotely.[175] Incorporating noninvasive wearable sweat sensors into clinical trials may provide important biochemical data. Wearable drug monitoring systems may determine pharmaceutical levels to maximize the efficacy of treatment while minimizing harmful side effects. Integrating vital sign sensors and contextual physiological biosensors may help better screen for important side effects.

Although few sweat sensors have been commercialized to date, many are in the pipeline. As of 2022, Epicore Biosystems has over 100 patents issued or pending.[176] The wearable device market was valued at $19.45 billion in 2020 with expected growth to $47.84 billion by 2026.[177] The rise of remote patient monitoring and telemedicine is a driver for market growth, along with the shift in healthcare from reactive to proactive intervention.[178] Medical grade wearables and predictive diagnostics will aid physicians and patients in better addressing health concerns. The FDA is actively responding with more fast-track approval paths for low-risk wearable devices that collect medical grade data while still maintaining high quality standards. The "Over-the-Counter Hearing Aid Act" of 2017 allows hearing aids to be sold direct to consumers without a prescription.[178] This paves the way for low-risk wearable devices to be made accessible upon deployment. The rollout of sweat sensors will diversify the wearable device market and the type of data available for continuous monitoring.

## References

[1] Yiran Yang and Wei Gao. "Wearable and flexible electronics for continuous molecular monitoring". *Chemical Society Reviews* **2019**, *48* (6), 1465–1491. DOI: 10.1039/C7CS00730B

[2] Changhao Xu, Yiran Yang, and Wei Gao. "Skin-Interfaced Sensors in Digital Medicine: from Materials to Applications". *Matter* **2020**, *2* (6), 1414–1445. DOI: 10.1016/j.matt.2020.03.020

[3] Jayoung Kim et al. "Wearable biosensors for healthcare monitoring". *Nature Biotechnology* **2019**, *37* (4), 389–406. DOI: 10.1038/s41587-019-0045-y

[4] H. Ceren Ates et al. "End-to-end design of wearable sensors". *Nature Reviews Materials* **2022**, *7* (11), 887–907. DOI: 10.1038/s41578-022-00460-x

[5] Shuai Xu et al. "Translational gaps and opportunities for medical wearables in digital health". *Science Translational Medicine* **2022**, *14* (666), eabn6036. DOI: 10.1126/scitranslmed.abn6036

[6] Sihong Wang et al. "Skin-Inspired Electronics: An Emerging Paradigm". *Accounts of Chemical Research* **2018**, *51* (5), 1033–1045. DOI: 10.1021/acs.accounts.8b00015

[7] Tyler R. Ray et al. "Bio-Integrated Wearable Systems: A Comprehensive Review". *Chemical Reviews* **2019**, *119* (8), 5461–5533. DOI: 10.1021/acs.chemrev.8b00573

[8] Aleksandr Ometov et al. "A Survey on Wearable Technology: History, State-of-the-Art and Current Challenges". *Computer Networks* **2021**, *193*, 108074. DOI: 10.1016/j.comnet.2021.108074

[9] Mallika Bariya, Hnin Yin Yin Nyein, and Ali Javey. "Wearable sweat sensors". *Nature Electronics* **2018**, *1* (3), 160–171. DOI: 10.1038/s41928-018-0043-y

[10] Jihong Min et al. "Wearable electrochemical biosensors in North America". *Biosensors and Bioelectronics* **2021**, *172*, 112750. DOI: 10.1016/j.bios.2020.112750

[11] You Yu et al. "Flexible Electrochemical Bioelectronics: The Rise of In Situ Bioanalysis". *Advanced Materials* **2020**, *32* (15), 1902083. DOI: 10.1002/adma.201902083

[12] Wei Gao et al. "Fully integrated wearable sensor arrays for multiplexed in situ perspiration analysis". *Nature* **2016**, *529* (7587), 509–514. DOI: 10.1038/nature16521

[13] K. Wilke et al. "A short history of sweat gland biology". *International Journal of Cosmetic Science* **2007**, *29* (3), 169–179. DOI: 10.1111/j.1467-2494.2007.00387.x

[14] Phillip A Low. "Evaluation of sudomotor function". *Clinical Neurophysiology* **2004**, *115* (7), 1506–1513. DOI: 10.1016/j.clinph.2004.01.023

[15] Patricia Klaka et al. “A novel organotypic 3D sweat gland model with physiological functionality”. *PLOS ONE* **2017**, *12* (8), e0182752. DOI: 10.1371/journal.pone.0182752

[16] Decibel P. Elpa et al. “Skin Metabolomics”. *Trends in Endocrinology & Metabolism* **2021**, *32* (2), 66–75. DOI: 10.1016/j.tem.2020.11.009

[17] Walter B. Shelley and Harry J. Hurley. “The Physiology of the Human Axillary Apocrine Sweat Gland12”. *Journal of Investigative Dermatology* **1953**, *20* (4), 285–297. DOI: 10.1038/jid.1953.35

[18] K. Sato, R. Leidal, and F. Sato. “Morphology and development of an apoeccrine sweat gland in human axillae”. *American Journal of Physiology-Regulatory, Integrative and Comparative Physiology* **1987**, *252* (1), R166–R180. DOI: 10.1152/ajpregu.1987.252.1.R166

[19] Jason Heikenfeld et al. “Accessing analytes in biofluids for peripheral biochemical monitoring”. *Nature Biotechnology* **2019**, *37* (4), 407–419. DOI: 10.1038/s41587-019-0040-3

[20] Saroj R. Tripathi et al. “Morphology of human sweat ducts observed by optical coherence tomography and their frequency of resonance in the terahertz frequency region”. *Scientific Reports* **2015**, *5* (1), 9071. DOI: 10.1038/srep09071

[21] Catherine P. Lu et al. “Identification of Stem Cell Populations in Sweat Glands and Ducts Reveals Roles in Homeostasis and Wound Repair”. *Cell* **2012**, *150* (1), 136–150. DOI: 10.1016/j.cell.2012.04.045

[22] Jinmei Diao et al. “Sweat gland organoids contribute to cutaneous wound healing and sweat gland regeneration”. *Cell Death & Disease* **2019**, *10* (3), 1–13. DOI: 10.1038/s41419-019-1485-5

[23] Nanbo Liu et al. “3D bioprinting matrices with controlled pore structure and release function guide in vitro self-organization of sweat gland”. *Scientific Reports* **2016**, *6* (1), 34410. DOI: 10.1038/srep34410

[24] Chang-Yi Cui and David Schlessinger. “Eccrine sweat gland development and sweat secretion”. *Experimental Dermatology* **2015**, *24* (9), 644–650. DOI: 10.1111/exd.12773

[25] Douglas L. Bovell. “The evolution of eccrine sweat gland research towards developing a model for human sweat gland function”. *Experimental Dermatology* **2018**, *27* (5), 544–550. DOI: 10.1111/exd.13556

[26] K. Sato and F. Sato. “Role of calcium in cholinergic and adrenergic mechanisms of eccrine sweat secretion”. *American Journal of Physiology-Cell Physiology* **1981**, *241* (3), C113–C120. DOI: 10.1152/ajpcell.1981.241.3.C113

[27] Paul M. Quinton. “Cystic Fibrosis: Lessons from the Sweat Gland”. *Physiology* **2007**, *22* (3), 212–225. DOI: 10.1152/physiol.00041.2006

[28] Csaba Mihályi et al. “Simple binding of protein kinase A prior to phosphorylation allows CFTR anion channels to be opened by nucleotides”. *Proceedings of the National Academy of Sciences* **2020**, *117* (35), 21740–21746. DOI: 10.1073/pnas.2007910117

[29] Danieli Barino Salinas et al. “Image-based -adrenergic sweat rate assay captures minimal cystic fibrosis transmembrane conductance regulator function”. *Pediatric Research* **2020**, *87* (1), 137–145. DOI: 10.1038/s41390-019-0503-8

[30] Zachary Sonner et al. “Integrated sudomotor axon reflex sweat stimulation for continuous sweat analyte analysis with individuals at rest”. *Lab on a Chip* **2017**, *17* (15), 2550–2560. DOI: 10.1039/C7LC00364A

[31] Bernhard Riedl et al. “Spatial extension of sudomotor axon reflex sweating in human skin”. *Journal of the Autonomic Nervous System* **1998**, *69* (2), 83–88. DOI: 10.1016/S0165-1838(98)00016-2

[32] Mikihiro Kihara, Tonette L. Opfer-Gehrking, and Phillip A. Low. “Comparison of directly stimulated with axon-reflex–mediated sudomotor responses in human subjects and in patients with diabetes”. *Muscle & Nerve* **1993**, *16* (6), 655–660. DOI: 10.1002/mus.880160612

[33] Phillip A. Low, Tonette L. Opfer-Gehrking, and Mikihiro Kihara. “In vivo studies on receptor pharmacology of the human eccrine sweat gland”. *Clinical Autonomic Research* **1992**, *2* (1), 29–34. DOI: 10.1007/BF01824208

[34] Masato Ohmi et al. “Dynamic analysis for mental sweating of a group of eccrine sweat glands on a human fingertip by optical coherence tomography”. *Skin Research and Technology* **2012**, *18* (3), 378–383. DOI: 10.1111/j.1600-0846.2011.00580.x

[35] Michael J. Buono, Kimberly D. Ball, and Fred W. Kolkhorst. “Sodium ion concentration vs. sweat rate relationship in humans”. *Journal of Applied Physiology* **2007**, *103* (3), 990–994. DOI: 10.1152/japplphysiol.00015.2007

[36] Tomoaki Ohashi et al. “Fluidic Patch Device to Sample Sweat for Accurate Measurement of Sweat Rate and Chemical Composition: A Proof-of-Concept Study”. *Analytical Chemistry* **2020**, *92* (23), 15534–15541. DOI: 10.1021/acs.analchem.0c03466

[37] Phillip Simmers et al. “Prolonged and localized sweat stimulation by iontophoretic delivery of the slowly-metabolized cholinergic agent carbachol”. *Journal of Dermatological Science* **2018**, *89* (1), 40–51. DOI: 10.1016/j.jdermsci.2017.10.013

[38] Manabu Shibasaki and Craig G. Crandall. “Effect of local acetylcholinesterase inhibition on sweat rate in humans”. *Journal of Applied Physiology* **2001**, *90* (3), 757–762. DOI: 10.1152/jappl.2001.90.3.757

[39] Kenzo Sato and Richard L. Dobson. “Regional and Individual Variations in the Function of the Human Eccrine Sweat Gland”. *Journal of Investigative Dermatology* **1970**, *54* (6), 443–449. DOI: 10.1111/1523-1747.ep12259272

[40] Mark J. Patterson*, Stuart D. R. Galloway, and Myra A. Nimmo. “Variations in regional sweat composition in normal human males”. *Experimental Physiology* **2000**, *85* (6), 869–875. DOI: 10.1017/S0958067000020583

[41] Chang-Yi Cui et al. “Forkhead transcription factor FoxA1 regulates sweat secretion through Bestrophin 2 anion channel and Na-K-Cl cotransporter 1”. *Proceedings of the National Academy of Sciences* **2012**, *109* (4), 1199–1203. DOI: 10.1073/pnas.1117213109

[42] Zoltan Bozoky et al. “Synergy of cAMP and calcium signaling pathways in CFTR regulation”. *Proceedings of the National Academy of Sciences* **2017**, *114* (11), E2086–E2095. DOI: 10.1073/pnas.1613546114

[43] Bakhrom K. Berdiev, Yawar J. Qadri, and Dale J. Benos. “Assessment of the CFTR and ENaC association”. *Molecular bioSystems* **2009**, *5* (2), 123–127. DOI: 10.1039/b810471a

[44] C. A. Prompt and P. M. Quinton. “Functions of calcium in sweat secretion”. *Nature* **1978**, *272* (5649), 171–172. DOI: 10.1038/272171a0

[45] Tiffany L. Thai et al. “The Polarized Effect of Intracellular Calcium on the Renal Epithelial Sodium Channel Occurs as a Result of Subcellular Calcium Signaling Domains Maintained by Mitochondria”. *The Journal of Biological Chemistry* **2015**, *290* (48), 28805–28811. DOI: 10.1074/jbc.M115.668293

[46] Michael J. Buono et al. “Na+ secretion rate increases proportionally more than the Na+ reabsorption rate with increases in sweat rate”. *Journal of Applied Physiology* **2008**, *105* (4), 1044–1048. DOI: 10.1152/japplphysiol.90503.2008

[47] K. Sato et al. “Biology of sweat glands and their disorders. I. Normal sweat gland function”. *Journal of the American Academy of Dermatology* **1989**, *20* (4), 537–563. DOI: 10.1016/S0190-9622(89)70063-3

[48] Kenzo Sato. “Update on pharmacology of the eccrine sweat gland”. *Trends in Pharmacological Sciences* **1984**, *5*, 391–393. DOI: 10.1016/0165-6147(84)90479-6

[49] J. S. Weiner and Ruth Van Heyningen. “Lactic Acid and Sweat Gland Function”. *Nature* **1949**, *164* (4165), 351–352. DOI: 10.1038/164351b0

[50] Andrew Jajack et al. “Enhancing glucose flux into sweat by increasing paracellular permeability of the sweat gland”. *PLOS ONE* **2018**, *13* (7), e0200009. DOI: 10.1371/journal.pone.0200009

[51] Juliane R. Sempionatto et al. “Wearable chemical sensors for biomarker discovery in the omics era”. *Nature Reviews Chemistry* **2022**, *6* (12), 899–915. DOI: 10.1038/s41570-022-00439-w

[52] Z. Sonner et al. “The microfluidics of the eccrine sweat gland, including biomarker partitioning, transport, and biosensing implications”. *Biomicrofluidics* **2015**, *9* (3), 031301. DOI: 10.1063/1.4921039

[53] A. Hauke et al. “Complete validation of a continuous and blood-correlated sweat biosensing device with integrated sweat stimulation”. *Lab on a Chip* **2018**, *18* (24), 3750–3759. DOI: 10.1039/C8LC01082J

[54] Kevin Hooton, Wei Han, and Liang Li. “Comprehensive and Quantitative Profiling of the Human Sweat Submetabolome Using High-Performance Chemical Isotope Labeling LC–MS”. *Analytical Chemistry* **2016**, *88* (14), 7378–7386. DOI: 10.1021/acs.analchem.6b01930

[55] Viktor P. Kutyshenko et al. “Analyzing and Mapping Sweat Metabolomics by High-Resolution NMR Spectroscopy”. *PLOS ONE* **2011**, *6* (12), e28824. DOI: 10.1371/journal.pone.0028824

[56] Alexander J. Aranyosi et al. “Rapid Capture and Extraction of Sweat for Regional Rate and Cytokine Composition Analysis Using a Wearable Soft Microfluidic System”. *Journal of Investigative Dermatology* **2021**, *141* (2), 433–437.e3. DOI: 10.1016/j.jid.2020.05.107

[57] B. Hadorn et al. “Free Amino-acids in Human Sweat from Different Parts of the Body”. *Nature* **1967**, *215* (5099), 416–417. DOI: 10.1038/215416a0

[58] Kenzo Sato, Minora Ohtsuyama, and Ghyath Samman. “Eccrine sweat gland disorders”. *Journal of the American Academy of Dermatology* **1991**, *24* (6), 1010–1014. DOI: 10.1016/S0190-9622(08)80117-X

[59] Richard L. Dobson. “The Human Eccrine Sweat Gland: Structural and Functional Interrelationships”. *Archives of Environmental Health: An International Journal* **1965**, *11* (4), 423–429. DOI: 10.1080/00039896.1965.10664242

[60] K Sato. “Sweat induction from an isolated eccrine sweat gland”. *American Journal of Physiology-Legacy Content* **1973**, *225* (5), 1147–1152. DOI: 10.1152/ajplegacy.1973.225.5.1147

[61] Michael J. Buono, Michael Stone, and Daniel T. Cannon. “Leaching from the stratum corneum does not explain the previously reported elevated potassium ion concentration in sweat”. *Journal of Basic and Clinical Physiology and Pharmacology* **2016**, *27* (2), 171–173. DOI: 10.1515/jbcpp-2015-0097

[62] Irving L. Schwartz and Jørn Hess Thaysen. “EXCRETION OF SODIUM AND POTASSIUM IN HUMAN SWEAT”. *The Journal of Clinical Investigation* **1956**, *35* (1), 114–120. DOI: 10.1172/JCI103245

[63] Maria M. Adeva et al. “Ammonium metabolism in humans”. *Metabolism - Clinical and Experimental* **2012**, *61* (11), 1495–1511. DOI: 10.1016/j.metabol.2012.07.007

[64] James Moyer et al. “Correlation Between Sweat Glucose and Blood Glucose in Subjects with Diabetes”. *Diabetes Technology & Therapeutics* **2012**, *14* (5), 398–402. DOI: 10.1089/dia.2011.0262

[65] Hiroyuki Murota et al. “Sweat in the pathogenesis of atopic dermatitis”. *Allergology International* **2018**, *67* (4), 455–459. DOI: 10.1016/j.alit.2018.06.003

[66] G. K. Komives, S. Robinson, and J. T. Roberts. “Urea transfer across the sweat glands”. *Journal of Applied Physiology* **1966**, *21* (6), 1681–1684. DOI: 10.1152/jappl.1966.21.6.1681

[67] R. S. Gordon et al. “Genesis of the sweat:plasma urea concentration gradient”. *The Journal of Investigative Dermatology* **1976**, *66* (4), 218–221. DOI: 10.1111/1523-1747.ep12482142

[68] Chan Hyun Na et al. “Integrated Transcriptomic and Proteomic Analysis of Human Eccrine Sweat Glands Identifies Missing and Novel Proteins *[S]”. *Molecular & Cellular Proteomics* **2019**, *18* (7), 1382–1395. DOI: 10.1074/mcp.RA118.001101

[69] Raymond W. Keller et al. “Urea transporters and sweat response to uremia”. *Physiological Reports* **2016**, *4* (11), e12825. DOI: 10.14814/phy2.12825

[70] Liyi Xie et al. “The Expression of AQP5 and UTs in the Sweat Glands of Uremic Patients”. *BioMed Research International* **2017**, *2017* (1), 8629783. DOI: 10.1155/2017/8629783

[71] D Czarnowski and J Górski. “[Excretion of nitrogen compounds in sweat during a sauna]”. *Polski tygodnik lekarski (Warsaw, Poland* **1991**, *46* (8), 186–187

. [72] Chien-Tsai Huang et al. “Uric acid and urea in human sweat”. *Chinese Journal of Physiology* **2002**, *45* (3), 109–116

. [73] Yassar Y. Al-Tamer, Eman A. Hadi, and Imad eldin I. Al-Badrani. “Sweat urea, uric acid and creatinine concentrations in uraemic patients”. *Urological Research* **1997**, *25* (5), 337–340. DOI: 10.1007/BF01294662

[74] Yiran Yang et al. “A laser-engraved wearable sensor for sensitive detection of uric acid and tyrosine in sweat”. *Nature Biotechnology* **2020**, *38* (2), 217–224. DOI: 10.1038/s41587-019-0321-x

[75] Earl S. Ford et al. “Serum Concentrations of Uric Acid and the Metabolic Syndrome Among US Children and Adolescents”. *Circulation* **2007**, *115* (19), 2526–2532. DOI: 10.1161/CIRCULATIONAHA.106.657627

[76] Lindsay B. Baker et al. “Exercise-Induced Trace Mineral Element Concentration in Regional Versus Whole-Body Wash-Down Sweat”. **2011**, DOI: 10.1123/ijsnem.21.3.233

[77] Scott J. Montain, Samuel N. Cheuvront, and Henry C. Lukaski. “Sweat Mineral-Element Responses during 7 h of Exercise-Heat Stress”. **2007**, DOI: 10.1123/ijsnem.17.6.574

[78] Troy D. Chinevere et al. “Effect of Heat Acclimation on Sweat Minerals”. *Medicine & Science in Sports & Exercise* **2008**, *40* (5), 886. DOI: 10.1249/MSS.0b013e3181641c04

[79] Matthew R. Ely et al. “Surface contamination artificially elevates initial sweat mineral concentrations”. *Journal of Applied Physiology* **2011**, *110* (6), 1534–1540. DOI: 10.1152/japplphysiol.01437.2010

[80] K Gibiński et al. “Calcium transit to thermal sweat”. *Acta biologica et medica Germanica* **1974**, *32* (2), 199–204

. [81] Wilhelm Jahnen-Dechent and Markus Ketteler. “Magnesium basics”. *Clinical Kidney Journal* **2012**, *5*, i3–i14. DOI: 10.1093/ndtplus/sfr163

[82] Jiangqi Zhao et al. “A Wearable Nutrition Tracker”. *Advanced Materials* **2021**, *33* (1), 2006444. DOI: 10.1002/adma.202006444

[83] JB Shields et al. “The excretion of ascorbic acid and dehydroascorbic acid in sweat and urine under different environmental conditions.” **1945**,

. [84] Stanley W Hier, Theodore Cornbleet, and O Bekgeim. “The amino acids of human sweat.” **1946**,

. [85] Christopher J. Harvey, Ryan F. LeBouf, and Aleksandr B. Stefaniak. “Formulation and stability of a novel artificial human sweat under conditions of storage and use”. *Toxicology in Vitro* **2010**, *24* (6), 1790–1796. DOI: 10.1016/j.tiv.2010.06.016

[86] Minqiang Wang et al. “A wearable electrochemical biosensor for the monitoring of metabolites and nutrients”. *Nature Biomedical Engineering* **2022**, *6* (11), 1225–1235. DOI: 10.1038/s41551-022-00916-z

[87] Harker Mark and Clive R. Harding. “Amino acid composition, including key derivatives of eccrine sweat: potential biomarkers of certain atopic skin conditions”. *International Journal of Cosmetic Science* **2013**, *35* (2), 163–168. DOI: 10.1111/ics.12019

[88] R. Hugh Dunstan et al. “Sweat Facilitated Amino Acid Losses in Male Athletes during Exercise at 32-34°C”. *PLOS ONE* **2016**, *11* (12), e0167844. DOI: 10.1371/journal.pone.0167844

[89] Clemens Kirschbaum and Dirk H. Hellhammer. “Salivary Cortisol in Psychobiological Research: An Overview”. *Neuropsychobiology* **2008**, *22* (3), 150–169. DOI: 10.1159/000118611

[90] Bo Wang et al. “Wearable aptamer-field-effect transistor sensing system for noninvasive cortisol monitoring”. *Science Advances* **2022**, *8* (1), eabk0967. DOI: 10.1126/sciadv.abk0967

[91] Paul Pearlmutter et al. “Sweat and saliva cortisol response to stress and nutrition factors”. *Scientific Reports* **2020**, *10* (1), 19050. DOI: 10.1038/s41598-020-75871-3

[92] Rebeca M. Torrente-Rodríguez et al. “Investigation of Cortisol Dynamics in Human Sweat Using a Graphene-Based Wireless mHealth System”. *Matter* **2020**, *2* (4), 921–937. DOI: 10.1016/j.matt.2020.01.021

[93] Umeda Teruhisa et al. “Use of saliva for monitoring unbound free cortisol levels in serum”. *Clinica Chimica Acta* **1981**, *110* (2), 245–253. DOI: 10.1016/0009-8981(81)90353-3

[94] Florian Reichmann and Peter Holzer. “Neuropeptide Y: A stressful review”. *Neuropeptides* **2016**, *55*, 99–109. DOI: 10.1016/j.npep.2015.09.008

[95] Giovanni Cizza et al. “Elevated Neuroimmune Biomarkers in Sweat Patches and Plasma of Premenopausal Women with Major Depressive Disorder in Remission: The POWER Study”. *Biological Psychiatry* **2008**, *64* (10), 907–911. DOI: 10.1016/j.biopsych.2008.05.035

[96] É. Csősz et al. “Highly abundant defense proteins in human sweat as revealed by targeted proteomics and label-free quantification mass spectrometry”. *Journal of the European Academy of Dermatology and Venereology* **2015**, *29* (10), 2024–2031. DOI: 10.1111/jdv.13221

[97] Benjamin A. Katchman et al. “Eccrine Sweat as a Biofluid for Profiling Immune Biomarkers”. *PROTEOMICS – Clinical Applications* **2018**, *12* (6), 1800010. DOI: 10.1002/prca.201800010

[98] Yijing Yu et al. “Proteomic and peptidomic analysis of human sweat with emphasis on proteolysis”. *Journal of Proteomics* **2017**, *155*, 40–48. DOI: 10.1016/j.jprot.2017.01.005

[99] Andrea Marques-Deak et al. “Measurement of cytokines in sweat patches and plasma in healthy women: Validation in a controlled study”. *Journal of Immunological Methods* **2006**, *315* (1), 99–109. DOI: 10.1016/j.jim.2006.07.011

[100] Anne P Jones et al. “Normal human sweat contains interleukin-8”. *Journal of Leukocyte Biology* **1995**, *57* (3), 434–437. DOI: 10.1002/jlb.57.3.434

[101] J Leppäluoto. “Human thermoregulation in sauna”. *Annals of clinical research* **1988**, *20* (4), 240–243

. [102] Michael Zech et al. “Sauna, sweat and science II – do we sweat what we drink?” *Isotopes in Environmental and Health Studies* **2019**, *55* (4), 394–403. DOI: 10.1080/10256016.2019.1635125

[103] Yi-Lang Chen, Wen-Hui Kuan, and Chao-Lin Liu. "Comparative Study of the Composition of Sweat from Eccrine and Apocrine Sweat Glands during Exercise and in Heat". *International Journal of Environmental Research and Public Health* **2020**, *17* (10), 3377. DOI: 10.3390/ijerph17103377

[104] Shuyu Lin et al. "Natural Perspiration Sampling and in Situ Electrochemical Analysis with Hydrogel Micropatches for User-Identifiable and Wireless Chemo/Biosensing". *ACS Sensors* **2020**, *5* (1), 93–102. DOI: 10.1021/acssensors.9b01727

[105] S. L. Souza, G. Graça, and A. Oliva. "Characterization of sweat induced with pilocarpine, physical exercise, and collected passively by metabolomic analysis". *Skin Research and Technology* **2018**, *24* (2), 187–195. DOI: 10.1111/srt.12412

[106] Mallika Bariya et al. "Glove-based sensors for multimodal monitoring of natural sweat". *Science Advances* **2020**, *6* (35), eabb8308. DOI: 10.1126/sciadv.abb8308

[107] Pei-Heng Lin et al. "Wearable hydrogel patch with noninvasive, electrochemical glucose sensor for natural sweat detection". *Talanta* **2022**, *241*, 123187. DOI: 10.1016/j.talanta.2021.123187

[108] Juliane R. Sempionatto, Jong-Min Moon, and Joseph Wang. "Touch-Based Fingertip Blood-Free Reliable Glucose Monitoring: Personalized Data Processing for Predicting Blood Glucose Concentrations". *ACS Sensors* **2021**, *6* (5), 1875–1883. DOI: 10.1021/acssensors.1c00139

[109] P. A. Low et al. "Quantitative sudomotor axon reflex test in normal and neuropathic subjects". *Annals of Neurology* **1983**, *14* (5), 573–580. DOI: 10.1002/ana.410140513

[110] Chantana Aromdee et al. "Serum Pilocarpine Esterase Activity and Response to Oral Pilocarpine". *Biochemical and Molecular Medicine* **1996**, *59* (1), 57–61. DOI: 10.1006/bmme.1996.0065

[111] Sam Emaminejad et al. "Autonomous sweat extraction and analysis applied to cystic fibrosis and glucose monitoring using a fully integrated wearable platform". *Proceedings of the National Academy of Sciences* **2017**, *114* (18), 4625–4630. DOI: 10.1073/pnas.1701740114

[112] Jayoung Kim et al. "Noninvasive Alcohol Monitoring Using a Wearable Tattoo-Based Iontophoretic-Biosensing System". *ACS Sensors* **2016**, *1* (8), 1011–1019. DOI: 10.1021/acssensors.6b00356

[113] Haisong Lin et al. "Autonomous wearable sweat rate monitoring based on digitized microbubble detection". *Lab on a Chip* **2022**, *22* (22), 4267–4275. DOI: 10.1039/D2LC00670G

[114] Jiangqi Zhao et al. “A Fully Integrated and Self-Powered Smartwatch for Continuous Sweat Glucose Monitoring”. *ACS Sensors* **2019**, *4* (7), 1925–1933. DOI: 10.1021/acssensors.9b00891

[115] Juliane R. Sempionatto et al. “An epidermal patch for the simultaneous monitoring of haemodynamic and metabolic biomarkers”. *Nature Biomedical Engineering* **2021**, *5* (7), 737–748. DOI: 10.1038/s41551-021-00685-1

[116] Brince Paul et al. “Printed Iontophoretic-Integrated Wearable Microfluidic Sweat-Sensing Patch for On-Demand Point-Of-Care Sweat Analysis”. *Advanced Materials Technologies* **2021**, *6* (4), 2000910. DOI: 10.1002/admt.202000910

[117] Jayoung Kim et al. “Simultaneous Monitoring of Sweat and Interstitial Fluid Using a Single Wearable Biosensor Platform”. *Advanced Science* **2018**, *5* (10), 1800880. DOI: 10.1002/advs.201800880

[118] Song Li et al. “Administration of pilocarpine by microneedle patch as a novel method for cystic fibrosis sweat testing”. *Bioengineering & Translational Medicine* **2021**, *6* (3), e10222. DOI: 10.1002/btm2.10222

[119] Michael C. Brothers et al. “Achievements and Challenges for Real-Time Sensing of Analytes in Sweat within Wearable Platforms”. *Accounts of Chemical Research* **2019**, *52* (2), 297–306. DOI: 10.1021/acs.accounts.8b00555

[120] P. Simmers et al. “Membrane isolation of repeated-use sweat stimulants for mitigating both direct dermal contact and sweat dilution”. *Biomicrofluidics* **2018**, *12* (3), 034101. DOI: 10.1063/1.5023396

[121] Carla Cristina Souza Gomez et al. “Evaluation of continuous constant current and continuous pulsed current in sweat induction for cystic fibrosis diagnosis”. *BMC Pulmonary Medicine* **2018**, *18* (1), 153. DOI: 10.1186/s12890-018-0696-3

[122] Franz Herrmann and Leona Mandol. “Studies of pH of sweat produced by different forms of stimulation”. *Journal of Investigative Dermatology* **1955**, *24* (3), 225–246

. [123] T. Verde et al. “Sweat composition in exercise and in heat”. *Journal of Applied Physiology* **1982**, *53* (6), 1540–1545. DOI: 10.1152/jappl.1982.53.6.1540

[124] Karan Agrawal et al. “Effects of stimulation technique, anatomical region, and time on human sweat lipid mediator profiles”. *Prostaglandins & Other Lipid Mediators* **2018**, *134*, 84–92. DOI: 10.1016/j.prostaglandins.2017.09.007

[125] Sean W. Harshman et al. “Metabolomic stability of exercise-induced sweat”. *Journal of Chromatography B* **2019**, *1126-1127*, 121763. DOI: 10.1016/j.jchromb.2019.121763

[126] Joy N Hussain, Nitin Mantri, and Marc M Cohen. "Working Up a Good Sweat – The Challenges of Standardising Sweat Collection for Metabolomics Analysis". *The Clinical Biochemist Reviews* **2017**, *38* (1), 13–34

. [127] N. De Giovanni and N. Fucci. "The Current Status of Sweat Testing For Drugs of Abuse: A Review". *Current Medicinal Chemistry* **2013**, *20* (4), 545–561. DOI: 10.2174/092986713804910139

[128] Quest Diagnostics. *Nicotine and Cotinine, Serum/Plasma Test Details*. URL: https://testdirectory.questdiagnostics.com/test/test-detail/90642/nicotine-and-cotinine-serumplasma?cc=MASTER (visited on 07/27/2024).

[129] Li-Chia Tai et al. "Nicotine Monitoring with a Wearable Sweat Band". *ACS Sensors* **2020**, *5* (6), 1831–1837. DOI: 10.1021/acssensors.0c00791

[130] Abd El-Galil E. Amr et al. "Paper-Based Potentiometric Sensors for Nicotine Determination in Smokers' Sweat". *ACS Omega* **2021**, *6* (17), 11340–11347. DOI: 10.1021/acsomega.1c00301

[131] Eda Mehmeti et al. "Electrochemical determination of nicotine in smokers' sweat". *Microchemical Journal* **2020**, *158*, 105155. DOI: 10.1016/j.microc.2020.105155

[132] G. Lindell, E. Lunell, and H. Graffner. "Transdermally administered nicotine accumulates in gastric juice". *European Journal of Clinical Pharmacology* **1996**, *51* (3), 315–318. DOI: 10.1007/s002280050204

[133] Li Jia et al. "Nicotine trapping causes the persistent desensitization of 42 nicotinic receptors expressed in oocytes". *Journal of Neurochemistry* **2003**, *84* (4), 753–766. DOI: 10.1046/j.1471-4159.2003.01578.x

[134] Amol V. Shivange et al. "Determining the pharmacokinetics of nicotinic drugs in the endoplasmic reticulum using biosensors". *Journal of General Physiology* **2019**, *151* (6), 738–757. DOI: 10.1085/jgp.201812201

[135] Khoa Nguyen et al. "The Impact of Sex on Changes in Plasma Corticosterone and Cotinine Levels Induced by Nicotine in C57BL/6J Mice". *Brain Sciences* **2020**, *10* (10), 705. DOI: 10.3390/brainsci10100705

[136] Sui-Lin Mo et al. "Substrate specificity, regulation, and polymorphism of human cytochrome P450 2B6". *Current Drug Metabolism* **2009**, *10* (7), 730–753. DOI: 10.2174/138920009789895534

[137] Jihong Min, Jiaobing Tu, Changhao Xu, Heather Lukas, Soyoung Shin, Yiran Yang, Samuel A. Solomon, Daniel Mukasa, and Wei Gao. "Skin-interfaced wearable sweat sensors for precision medicine". *Chemical Reviews* **2023**, *123* (8), 5049–5138. DOI: 10.1021/acs.chemrev.2c00823

[138] Kaiyu Fu et al. "Accelerated Electron Transfer in Nanostructured Electrodes Improves the Sensitivity of Electrochemical Biosensors". *Advanced Science* **2021**, *8* (23), 2102495. DOI: 10.1002/advs.202102495

[139] Olesya V. Stepanenko et al. “Sensitivity of Superfolder GFP to Ionic Agents”. *PLOS ONE* **2014**, *9* (10), e110750. DOI: 10.1371/journal.pone.0110750

[140] William W. Ward et al. “Spectral Perturbations of the Aequorea Green-Fluorescent Protein”. *Photochemistry and Photobiology* **1982**, *35* (6), 803–808. DOI: 10.1111/j.1751-1097.1982.tb02651.x

[141] Anand K. Muthusamy et al. “Three Mutations Convert the Selectivity of a Protein Sensor from Nicotinic Agonists to S-Methadone for Use in Cells, Organelles, and Biofluids”. *Journal of the American Chemical Society* **2022**, DOI: 10.1021/jacs.2c02323

[142] Madoka Nagata et al. “An Amine-Reactive Phenazine Ethosulfate (arPES)—A Novel Redox Probe for Electrochemical Aptamer-Based Sensor”. *Sensors* **2022**, *22* (5), 1760. DOI: 10.3390/s22051760

[143] Cui Ye et al. “A wearable aptamer nanobiosensor for non-invasive female hormone monitoring”. *Nature Nanotechnology* **2023**, 1–8. DOI: 10.1038/s41565-023-01513-0

[144] Dhruv R. Seshadri et al. “Clinical translation of biomedical sensors for sports medicine”. *Journal of Medical Engineering & Technology* **2019**, *43* (1), 66–81. DOI: 10.1080/03091902.2019.1612474

[145] B. A. Fiedler and Y. David. “Chapter 1 - Reframing Product Life Cycle for Medical Devices”. In: *Managing Medical Devices Within a Regulatory Framework*. Ed. by Beth Ann Fiedler. Elsevier, Jan. 1, 2017, pp. 3–16. ISBN: 978-0-12-804179-6. DOI: 10.1016/B978-0-12-804179-6.00001-0. URL: https://www.sciencedirect.com/science/article/pii/B9780128041796000010 (visited on 08/31/2022).

[146] Nathália Florência Barros Azeredo et al. “Screen-Printed Technologies Combined with Flow Analysis Techniques: Moving from Benchtop to Everywhere”. *Analytical Chemistry* **2022**, *94* (1), 250–268. DOI: 10.1021/acs.analchem.1c02637

[147] Anne Blayo and Bernard Pineaux. “Printing processes and their potential for RFID printing”. In: *Proceedings of the 2005 joint conference on Smart objects and ambient intelligence: innovative context-aware services: usages and technologies*. sOc-EUSAI ’05. New York, NY, USA: Association for Computing Machinery, Oct. 12, 2005, pp. 27–30. ISBN: 978-1-59593-304-1. DOI: 10.1145/1107548.1107559. URL: https://doi.org/10.1145/1107548.1107559 (visited on 11/07/2022).

[148] Farshad Tehrani et al. “Laser-Induced Graphene Composites for Printed, Stretchable, and Wearable Electronics”. *Advanced Materials Technologies* **2019**, *4* (8), 1900162. DOI: 10.1002/admt.201900162

[149] Jia Li, Fabrice Rossignol, and Joanne Macdonald. "Inkjet printing for biosensor fabrication: combining chemistry and technology for advanced manufacturing". *Lab on a Chip* **2015**, *15* (12), 2538–2558. DOI: 10.1039/C5LC00235D

[150] Gerd Grau et al. "Gravure-printed electronics: recent progress in tooling development, understanding of printing physics, and realization of printed devices". *Flexible and Printed Electronics* **2016**, *1* (2), 023002. DOI: 10.1088/2058-8585/1/2/023002

[151] You Yu et al. "All-printed soft human-machine interface for robotic physicochemical sensing". *Science Robotics* **2022**, *7* (67), eabn0495. DOI: 10.1126/scirobotics.abn0495

[152] Mallika Bariya et al. "Roll-to-Roll Gravure Printed Electrochemical Sensors for Wearable and Medical Devices". *ACS Nano* **2018**, *12* (7), 6978–6987. DOI: 10.1021/acsnano.8b02505

[153] Hnin Yin Yin Nyein et al. "Regional and correlative sweat analysis using high-throughput microfluidic sensing patches toward decoding sweat". *Science Advances* **2019**, *5* (8), eaaw9906. DOI: 10.1126/sciadv.aaw9906

[154] Sukang Bae et al. "Roll-to-roll production of 30-inch graphene films for transparent electrodes". *Nature Nanotechnology* **2010**, *5* (8), 574–578. DOI: 10.1038/nnano.2010.132

[155] Minqiang Wang, Yiran Yang, and Wei Gao. "Laser-engraved graphene for flexible and wearable electronics". *Trends in Chemistry* **2021**, *3* (11), 969–981. DOI: 10.1016/j.trechm.2021.09.001

[156] *Epicore Biosystems*. Epicore Biosystems. URL: https://www.epicorebiosystems.com/ (visited on 08/09/2022).

[157] Lindsay B. Baker et al. "Skin-Interfaced Microfluidic System with Machine Learning-Enabled Image Processing of Sweat Biomarkers in Remote Settings". *Advanced Materials Technologies* **2022**, *7* (11), 2200249. DOI: 10.1002/admt.202200249

[158] Lindsay B. Baker et al. "Skin-interfaced microfluidic system with personalized sweating rate and sweat chloride analytics for sports science applications". *Science Advances* **2020**, *6* (50), eabe3929. DOI: 10.1126/sciadv.abe3929

[159] Iman M. Gidado et al. "Review of Advances in the Measurement of Skin Hydration Based on Sensing of Optical and Electrical Tissue Properties". *Sensors* **2022**, *22* (19), 7151. DOI: 10.3390/s22197151

[160] *FLOWBIO*. URL: https://www.flowbio.com/ (visited on 11/01/2022).

[161] *Product*. Nix Biosensors. URL: https://nixbiosensors.com/pages/product (visited on 08/09/2022).

[162] *hDrop Hydration Wearable Monitor - Dehydration Sensor*. URL: https://hdroptech.com/ (visited on 08/08/2022).

[163] *Inicio*. Onalabs. URL: https://www.onalabs.com/en/ (visited on 11/01/2022).

[164] *Sweati is a wearable patch that tracks glucose by analyzing your sweat*. SM24. URL: https://www.sm24.ai/blogs/news/sweati-is-a-wearable-patch-that-tracks-glucose-by-analyzing-your-sweat (visited on 11/02/2022).

[165] *Patch Analyzes Sweat to Monitor, Diagnose Health Issues*. Healthcare Packaging. Jan. 2019. URL: https://www.healthcarepackaging.com/machinery-materials/adherence-delivery/article/13295801/patch-analyzes-sweat-to-monitor-diagnose-health-issues (visited on 08/09/2022).

[166] *My Skin Track Ph by La Roche-Posay won the CES 2019 Innovation Award*. URL: https://www.loreal.com/en/news/science-and-technology/research-innovation/my-skin-track-ph-by-la-roche-posay-won-the-ces-2019-innovation-award/ (visited on 08/09/2022).

[167] GraphWear Technologies Inc. *GraphWear*. URL: https://www.graphwear.co (visited on 10/31/2022).

[168] Erick Garcia-Cordero et al. "Three-Dimensional Integrated Ultra-Low-Volume Passive Microfluidics with Ion-Sensitive Field-Effect Transistors for Multiparameter Wearable Sweat Analyzers". *ACS Nano* **2018**, *12* (12), 12646–12656. DOI: 10.1021/acsnano.8b07413

[169] *Lab-on-Skin™ Technology – Xsensio | Lab-on-Skin™ Sensing Platform*. URL: https://xsensio.com/lab-on-skin-technology/ (visited on 11/01/2022).

[170] Junrui Zhang et al. "Sweat Biomarker Sensor Incorporating Picowatt, Three-Dimensional Extended Metal Gate Ion Sensitive Field Effect Transistors". *ACS Sensors* **2019**, *4* (8), 2039–2047. DOI: 10.1021/acssensors.9b00597

[171] Shokoofeh Sheibani et al. "Extended gate field-effect-transistor for sensing cortisol stress hormone". *Communications Materials* **2021**, *2* (1), 1–10. DOI: 10.1038/s43246-020-00114-x

[172] Tyler R. Ray et al. "Soft, skin-interfaced sweat stickers for cystic fibrosis diagnosis and management". *Science Translational Medicine* **2021**, *13* (587), eabd8109. DOI: 10.1126/scitranslmed.abd8109

[173] *Cystic Fibrosis Updates in Care: Part II — The "Sweat Sticker" and Clinician Q&A*. Pulmonology Advisor. May 21, 2021. URL: https://www.pulmonologyadvisor.com/home/topics/obstructive-lung-disease/cystic-fibrosis-updates-in-care-part-ii-the-sweat-sticker-and-clinician-qa/ (visited on 08/09/2022).

[174] Nick Paul Taylor. *Apple Watch monitoring features for AFib, Parkinson's cleared by FDA*. MedTech Dive. URL: https://www.medtechdive.com/news/apple-watch-afib-parkinsons-fda-clearance/625424/ (visited on 11/08/2022).

[175] *Medidata Sensor Cloud | Wearables in Clinical Trials*. Medidata Solutions. URL: https://www.medidata.com/en/clinical-trial-products/patient-centric-clinical-trials/wearable-sensors/ (visited on 11/08/2022).

[176] Chris Anderson. *Epicore Adds Sweat Sensor Tech with Eccrine Systems Buyout*. Inside Precision Medicine. May 4, 2022. URL: https://www.insideprecisionmedicine.com/topics/translational-research/biomarkers-topic/epicore-adds-sweat-sensor-tech-with-eccrine-systems-buyout/ (visited on 08/09/2022).

[177] Mordor Intelligence. *Wearable Devices Market Size, Share | 2022 - 27 | Industry Growth*. URL: https://www.mordorintelligence.com/industry-reports/global-wearable-medical-device-market-industry (visited on 10/30/2022).

[178] CB Insights. *From Wearables To Telemedicine To Direct-To-Consumer Prescriptions, Here's How Healthcare Is Becoming Consumer-Centric*. CB Insights. Jan. 24, 2018. URL: https://app.cbinsights.com/research/consumer-healthcare-relationship-expert-intelligence/ (visited on 11/07/2022).

*Chapter 7*

# CONCLUSION

The broader aim of this thesis work was to explore non-enzymatic affinity biosensors for the expansion of available personal health data. With COVID-19, we developed a multiplexed electrochemical immunosensor that could quickly provide key information regarding a person's infection status. Using accessible saliva samples, this test could be performed at-home and in conjunction with telemedicine care. Turning our attention to continuous data streams, we explored nucleic acid-based affinity sensors. An aptamer-based serotonin sensor allowed for continuous and reagentless electrochemical sensing. Incorporating a serotonin sensor in an ingestible capsule unlocked localized biochemical information in the gastrointestinal tract without the need for invasive surgical procedures. Finally, we worked on the development of an electrochemical PBP sensor, outlining techniques to develop continuous molecular monitors with the goal of generalizability across a swath of small molecule and peptide targets. Using PBPs, we developed a preliminary electrochemical continuous nicotine sensor for wearable sweat analysis to provide individualized pharmacokinetic data that could curb addiction.

Each of these bioreceptor classes have unique qualities that position them as suitable components for electrochemical sensing applications. Antibodies provide high-affinity binding for target recognition at low concentrations. Aptamers as synthetic nucleic acid sequences represent another diverse class of high-affinity binding bioreceptors. Yet, the binding-induced conformation change of aptamers is a property that may be exploited for reagentless signal transduction as well. Applying the sensor architecture of aptamers to receptor-derived proteins introduces a new, diverse class of electrochemical bioreceptors, the PBP superfamily.

To design future continuous biosensors, we must develop a better understanding of the kinetics of reversible biorecognition elements. There is a tradeoff between high-affinity sensing to achieve high sensitivity and rapid kinetics to allow for reversibility and real-time measurements. The next step in bioaffinity sensor engineering is modeling the binding kinetics of these bioaffinity receptors. This will provide key information to tune affinity based on the physiological sensing demands.

Continued work in this field is imperative for the development of future wearable

and implantable biosensors. This research contributes to the body of work aimed at developing a new generalizable class of continuous biosensors that could lead to expansive biosensing. Translation of such sensors will provide the data necessary for effective machine learning and timely health insights, which will usher in a new era of personalized medicine and predictive diagnostics.

*Appendix A*

# APPENDIX FOR SARS-COV-2 RAPIDPLEX

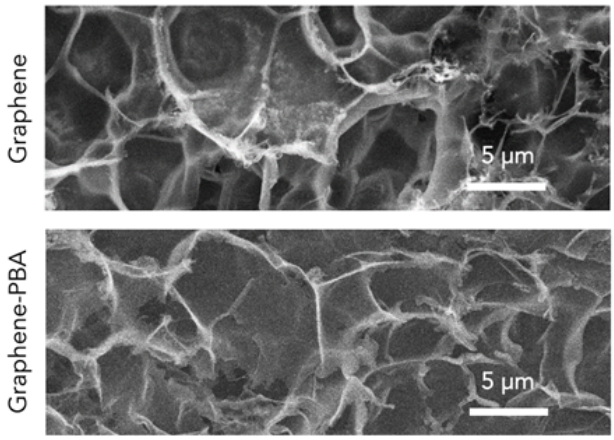


Figure A.1: SEM images of the bare graphene electrode before and after modification with PBA.

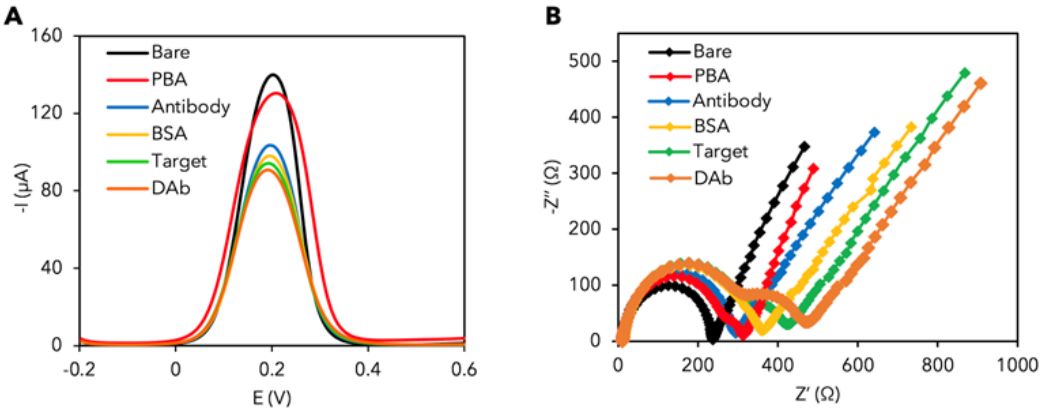


Figure A.2: Electrochemical characterization of the sandwich assay-based graphene sensor modifications

Differential pulse voltammetry (DPV) (A) and Nyquist plots (B) of a graphene electrode in 0.01 M phosphate-buffered saline (PBS, pH 7.4) containing 2.0 mM of $K_4Fe(CN)_6/K_3Fe(CN)_6$ (1:1) after each modification step (CRP assay as a representative example): bare graphene (Bare), functionalization with PBA (PBA), immobilization of antibody (Antibody), blocking with BSA (BSA), recognition of CRP (Target), and incubation with enzyme-tagged anti-CRP antibody (DAb).

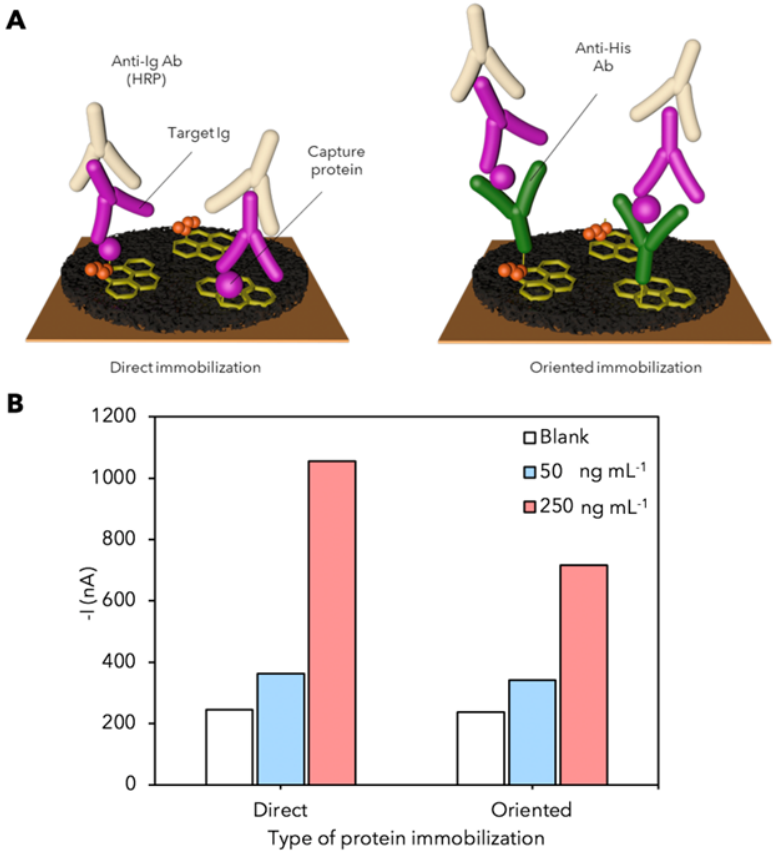


Figure A.3: Characterization of the direct and oriented protein immobilization

Schemes illustrating direct and oriented immobilization of SARS-CoV-2 antigenic protein for detection of specific IgG or IgM isotypes (A), and comparison of sensor performance for S1-IgG detection using both types of immobilizations (B).

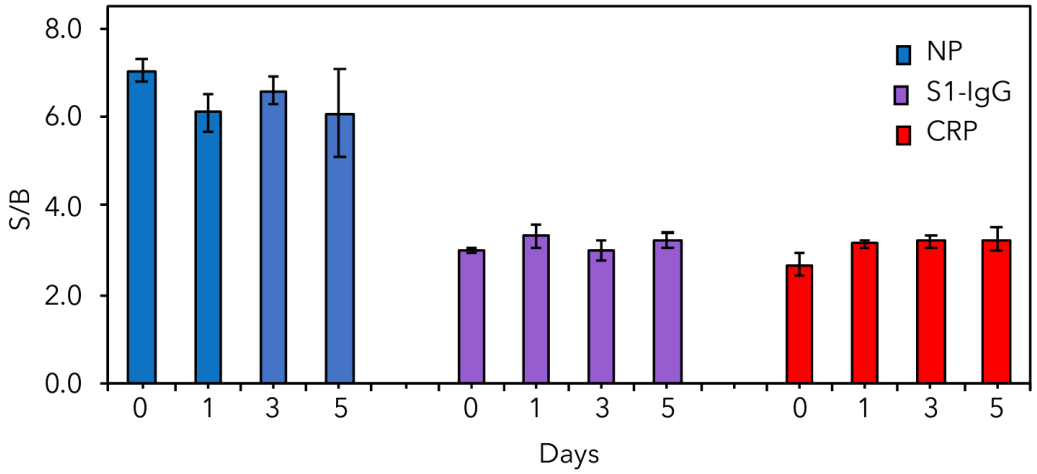


Figure A.4: Stability evaluation of the LGE electrochemical biosensors

Variation of signal (S)-to-Blank (B) ratios over days of storage (at 4 °C in 1× PBS buffered solution) for NP, S1-IgG, and CRP sensors in the presence of 500 pg $mL^{-1}$ NP, 250 ng $mL^{-1}$ S1-IgG, and 20 ng $mL^{-1}$ CRP, respectively. Data are represented as mean ± SD (n = 3).

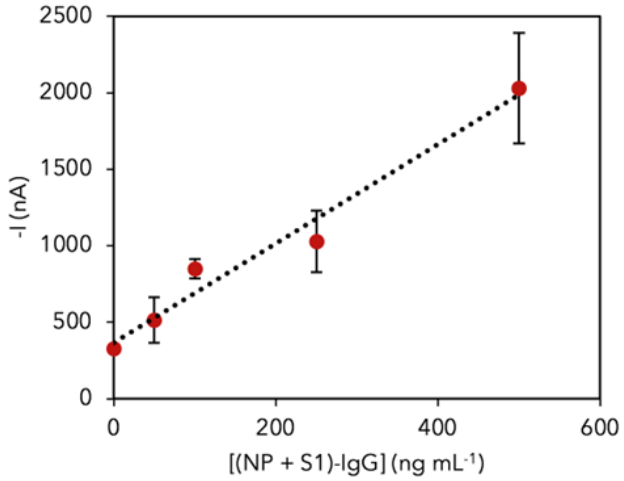


Figure A.5: (NP + S1)-IgG calibration curve

Calibration curve constructed for (NP + S1)-IgG detection in phosphate-buffered saline (PBS, pH 7.4) supplemented with 1.0% BSA. Data are presented as mean ± SD (n = 3).

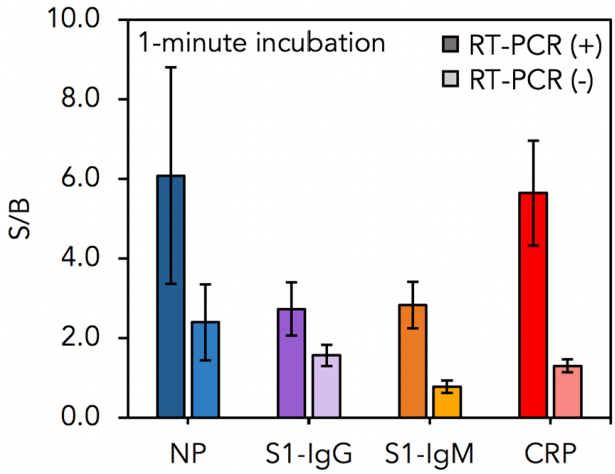


Figure A.6: 1-Minute incubation with 100× diluted serum samples

The signal (S)-to-blank (B) ratio of the LEG sensors obtained after 1-minute incubation with a 100× diluted serum sample from a COVID-19 positive patient (dark color) vs. a 100× diluted serum sample from a COVID-19 negative patient (light color). Data are represented as mean ± SD (n = 4).

| Sample Type | Sample ID | PCR Results | IgM/IgG Serology Results | Symptom Severity |
|---|---|---|---|---|
| Serum | PSer428 | + | (+)/(+) | Moderate |
| | PSer499 | + | (+)/(+) | Mild |
| | PSer565 | + | (+)/(+) | Moderate |
| | PSer458 | + | (+)/(+) | Mild |
| | PSer560 | + | (+)/(+) | Hospitalized |
| | PSer454 | + | (-)/(+) | Asymptomatic |
| | PSer619 | + | (-)/(+) | Asymptomatic |
| | PSer494 | + | (-)/(+) | Mild |
| | PSer379 | + | (-)/(+) | Mild |
| | PSer400 | + | (-)/(+) | Mild |
| | NSer4 | - | (-)/(-) | n/a |
| | NSer5 | - | (-)/(-) | n/a |
| | NSer6 | - | (-)/(-) | n/a |
| | NSer7 | - | (-)/(-) | n/a |
| | NSer8 | - | (-)/(-) | n/a |
| | NSer9 | - | (-)/(-) | n/a |
| | NSer10 | - | (-)/(-) | n/a |
| Saliva | PSal530 | + | (-)/(+) | Mild |
| | PSal664 | + | (-)/(+) | Asymptomatic |
| | PSal675 | + | (-)/(+) | Asymptomatic |
| | PSal658 | + | (-)/(+) | Asymptomatic |
| | PSal604 | + | (+)/(+) | Asymptomatic |
| | NSal3 | - | (-)/(-) | n/a |
| | NSal4 | - | (-)/(-) | n/a |
| | NSal5 | - | (-)/(-) | n/a |

Table A.1: Patient sample summary information.

*Appendix B*

# APPENDIX FOR PILLTREK

## Supplementary Note 1 | Ratiometric signal measurement of aptamer-based serotonin sensor

The square wave voltammetry (SWV) parameters were optimized to induce more accurate and sensitive measurement of the redox signal changes near the electrode surface. Initially, the amplitude, which refers to the height of the square wave pulses, was controlled to determine optimal conditions for specific fluid matrices. Sensors tested under a 50 mV amplitude in simulated intestinal fluid (SIF, pH 7.0) exhibited double peaks for serotonin concentrations over 0.5 μM, deviating from the expected log-linear trend (Supplementary Figure B.8). However, the sensors tested under a lower amplitude, such as 45 mV, displayed single peaks for serotonin concentration up to 100 μM, aligning more closely with a log-linear trend. Lower amplitudes, such as 35 mV and 40 mV, were also applied, but the peak current changes with 10 μM serotonin were smaller than those observed at 45 mV amplitude (Supplementary Figure B.9). Sensors in PBS (pH 7.4) showed similar behaviors. Consequently, the amplitude was set to 45 mV for SIF and PBS. However, more complex biofluids induced degraded double peaks at this amplitude. By scanning various amplitudes, 20 mV was identified as the optimal condition for real biofluids, such as fecal fluid, serum, rat intestinal fluid, and rabbit intestinal fluid.

Next, the sensors were interrogated with various frequencies to determine the signal-off and non-responsive conditions, referring to the rate at which the square wave oscillates. The non-responsive frequency arises from the interplay between electron transfer kinetics of the bound and unbound states of the aptamer. [1, 2] When the currents produced by the bound and unbound states are equal, the output current remains constant regardless of the target concentration. Sensors were tested across frequencies ranging from 10 to 70 Hz with serotonin concentrations ranging from 0.01 to 10 μM in various fluids, including SIF, human fecal fluid, serum, rat intestinal fluid, and rabbit intestinal fluid (Supplementary Figure B.15). The intersection point on the plot of relative peak current change versus frequency indicates the non-responsive frequency with no peak current change. The non-responsive frequency varies with fluid types and tends to increase in more complex fluids: 20, 30, 50, 70,

and 70 Hz were identified as the non-responsive frequencies for SIF, PBS, serum, fecal fluid, and intestinal fluids. A frequency of 10 Hz was used as the signal-off frequency for all fluids, while fluid specific frequencies identified through frequency scan were used as non-responsive frequency in each respective fluid.

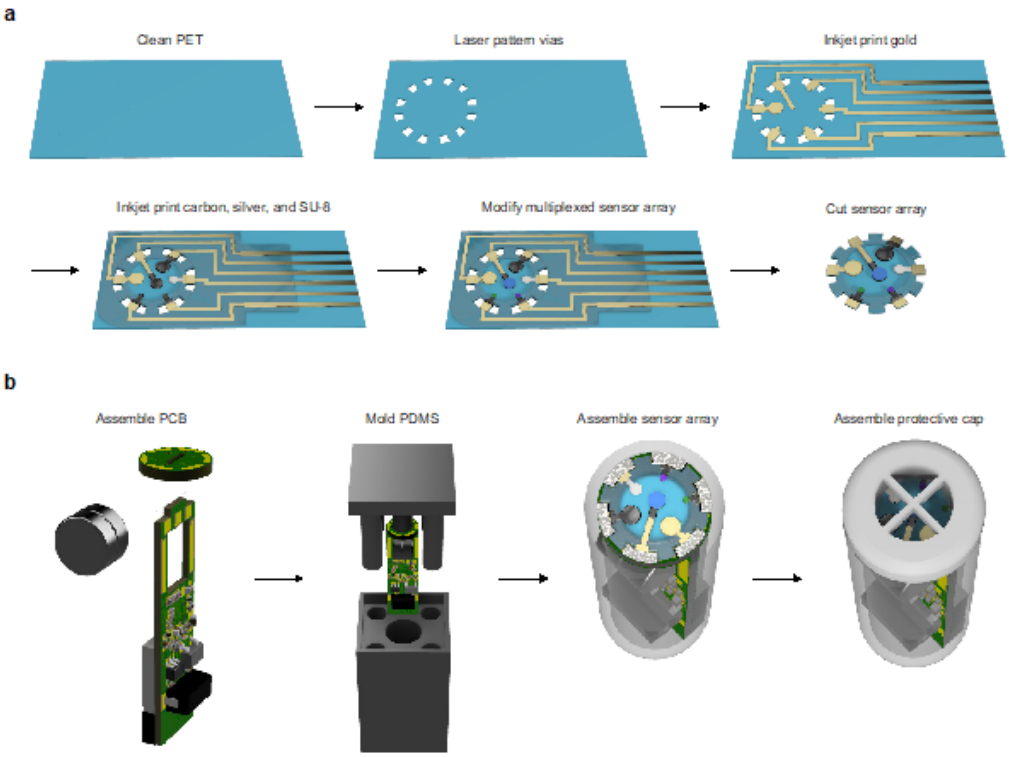


Figure B.1: Schematic illustration of the fabrication procedure for PillTrek

Procedures for preparing the multiplexed sensor (A) and fabricating the fully integrated capsule (B).

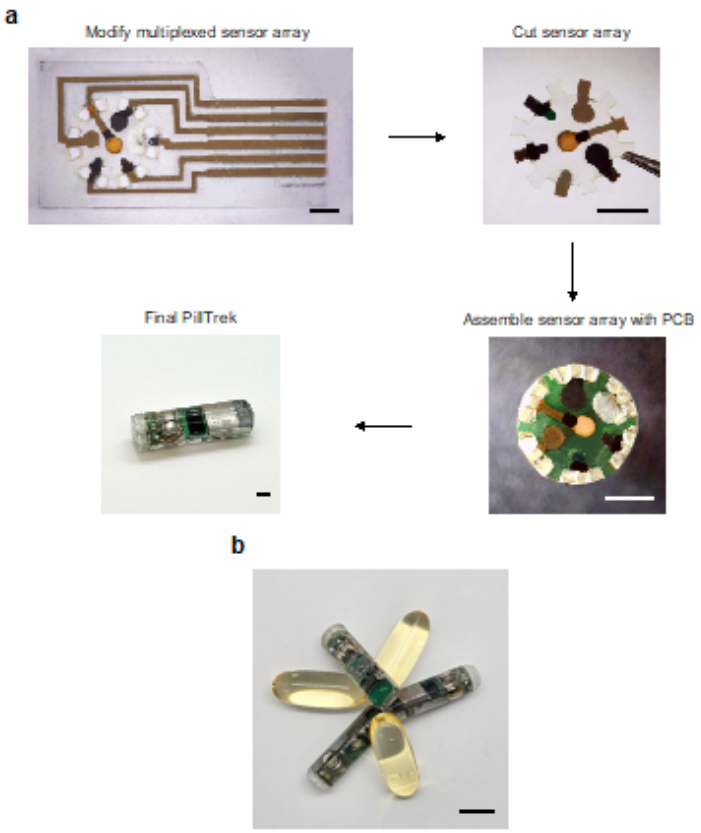


Figure B.2: Photographs of PillTrek fabrication

(A) Photos illustrating step-by-step fabrication procedures from multiplex sensor modification to the final PillTrek assembly. Scale bars, 3 mm. (B) PillTrek shown alongside commercial supplementary pills for size comparison. Scale bar, 2 cm.

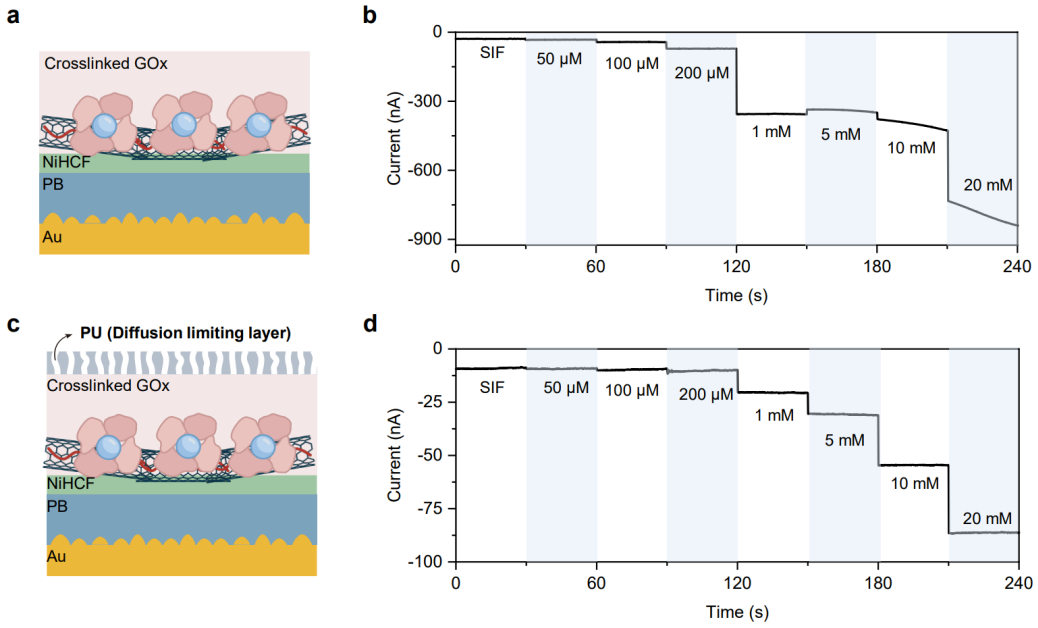


Figure B.3: Evaluation of the diffusion limiting layer for glucose sensing

(A,B) Schematic of the glucose sensor based on Au/PB-NiHCF (A) and its corresponding amperometric response ranging from 0 to 20 mM (B). (C,D) Schematic of the glucose sensor modified with a polyurethane (PU) diffusion limiting layer (C) and its corresponding amperometric response to 0-20 mM glucose (D).

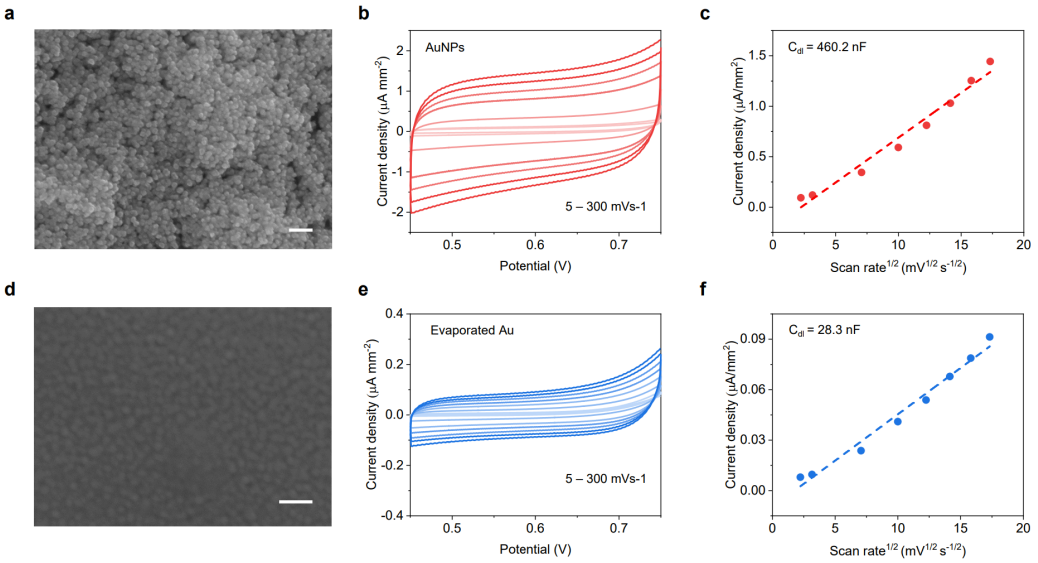


Figure B.4: Characterization of inkjet-printed AuNPs electrode and evaporated Au electrode for aptamer-based serotonin sensor

(A-C) SEM images (A), CV characterization under different scan rates (5, 10, 50, 100, 150, 200, 250, 300 mV $s^{-1}$) in SIF (B), and the corresponding calibration plots of oxidation current density height at 0.6 V vs. scan rates (C) for inkjet-printed AuNPs electrode. $C_{dl}$, electrochemical double layer capacitance. (D-F), SEM images (D), CV characterization under different scan rates (5, 10, 50, 100, 150, 200, 250, 300 mV $s^{-1}$) in SIF (E), and the corresponding calibration plots of oxidation current density height at 0.6 V vs. scan rates (F) for evaporated Au electrode. Scale bars, 200 nm.

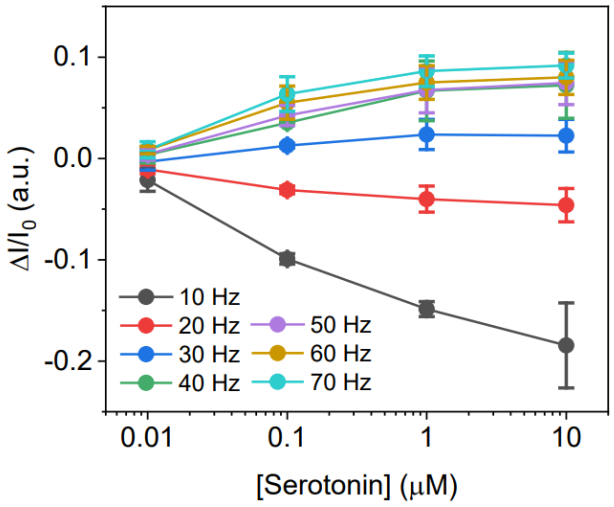


Figure B.5: The response of the serotonin sensors upon SWV frequencies in SIF

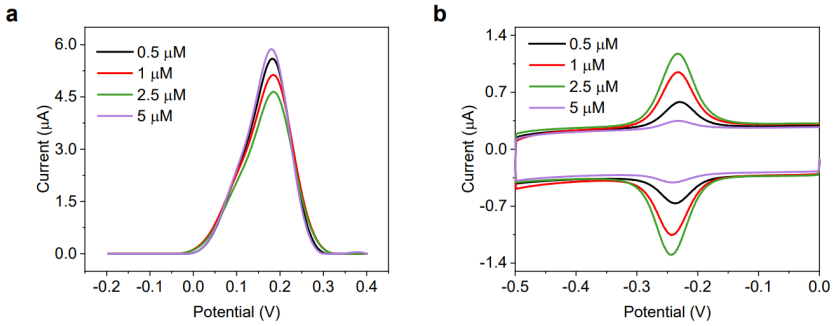


Figure B.6: Optimization of aptamer concentration for sensor functionalization

(A) DPV voltammograms of the serotonin sensor functionalized with varying concentrations of serotonin aptamer, incubated at room temperature for 4 hours, and tested in 5 mM hexacyanoferrate in 0.1 M KCl. (B) CV voltammograms of serotonin sensors functionalized with varying concentrations of serotonin aptamer, followed by overnight passivation at 4 °C with 5 mM mercaptohexanol (MCH), and tested in 1× PBS (pH 7.0).

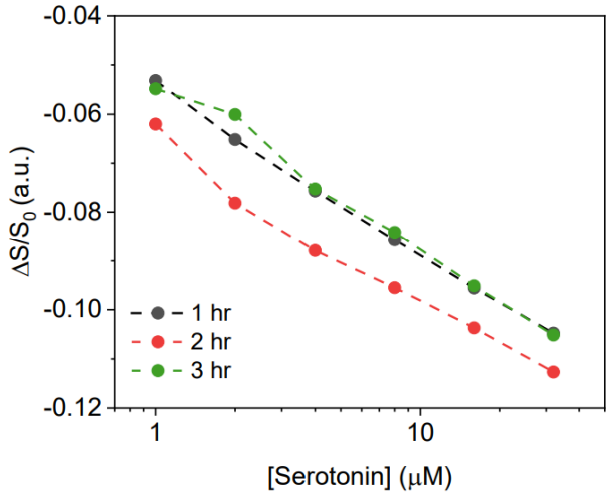


Figure B.7: Optimization of serotonin aptamer incubation time

Calibration plot based on the relative ratiometric signal of serotonin sensors functionalized with 2.5 µM aptamer, with varied incubation times at room temperature.

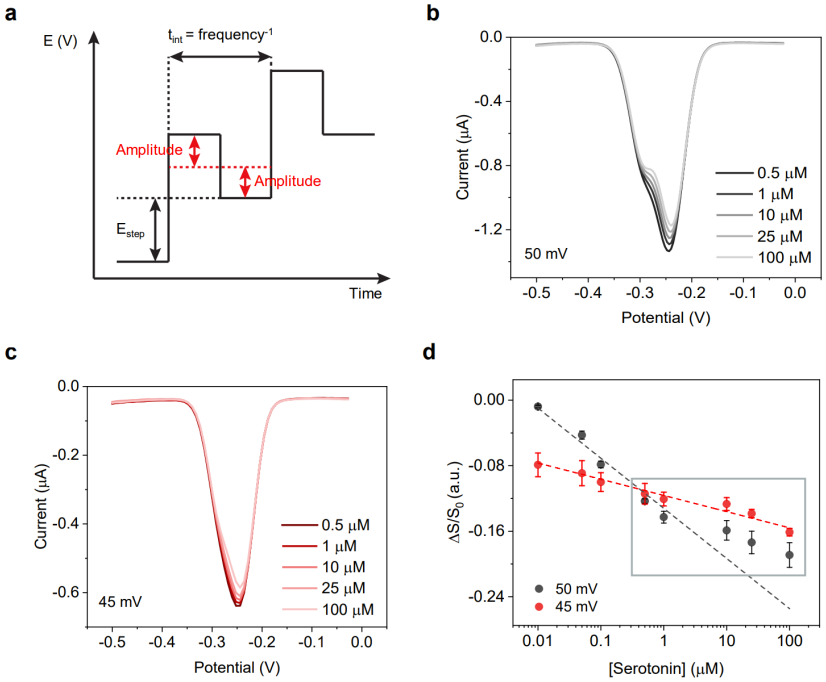


Figure B.8: Optimization of SWV amplitude for the serotonin sensor in SIF (A-C), SWV voltammograms under 50 mV amplitude (A), 45 mV amplitude (B), and the corresponding calibration plots based on the relative ratiometric signal (C) for 0-100 μM serotonin. Error bars represent the s.d. of the mean from three sensors.

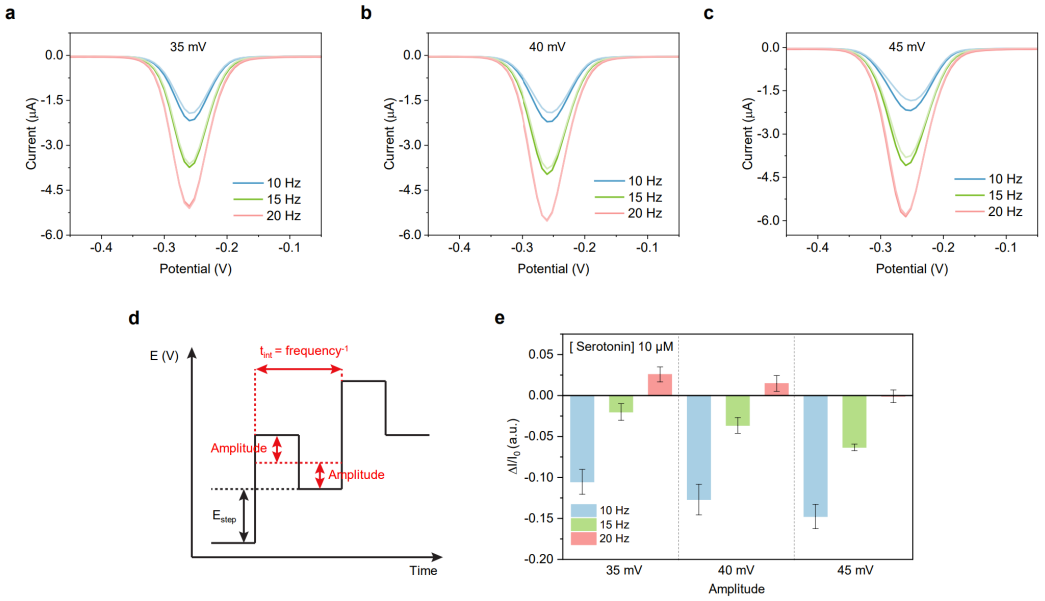


Figure B.9: Optimization of SWV amplitude and frequency for the serotonin sensor in SIF

(A-C), SWV voltammograms at 35 mV amplitude (A), 40 mV amplitude (B), and 45 mV amplitude (C) under 10 Hz, 15 Hz, and 20 Hz frequencies with and without 10 μM serotonin. (D) Relative changes in SWV voltammogram peak currents with 10 μM serotonin. Error bars represent the s.d. of the mean from three sensors.

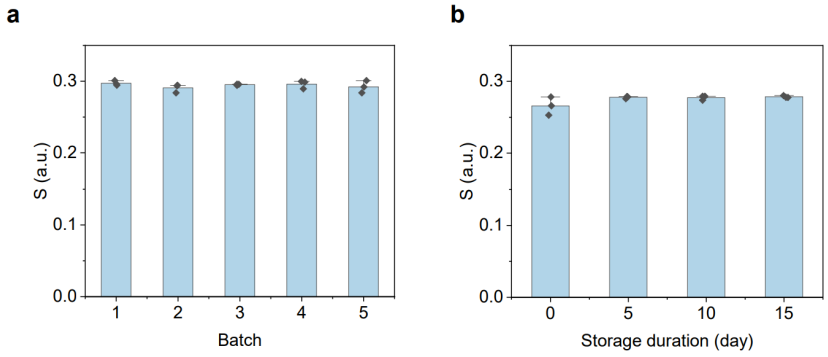


Figure B.10: Repeatability and storage stability of the aptamer serotonin sensor

(A) Batch-to-batch variations based on the normalized response ($S = I_{10Hz}/I_{20Hz}$) of serotonin sensors from five different batches, tested with 1 μM serotonin in SIF. (B) Storage stability of the serotonin sensors for detecting 1 μM serotonin in SIF over a 15-day storage period under cold conditions (4 °C). Error bars represent the s.d. of the mean from three sensors.

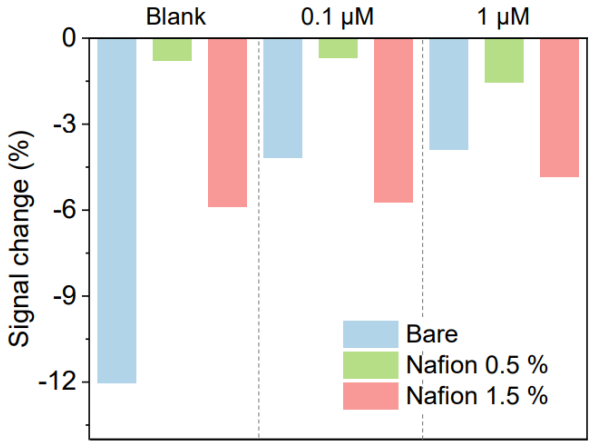


Figure B.11: Evaluation of the Nafion antifouling coating on the serotonin sensor performance in rat intestinal fluids

The ratiometric signal changes of the serotonin sensors between t = 10 min and t = 0 min in raw fluid, fluid spiked with 0.1 µM, and fluid spiked with 1 µM serotonin.

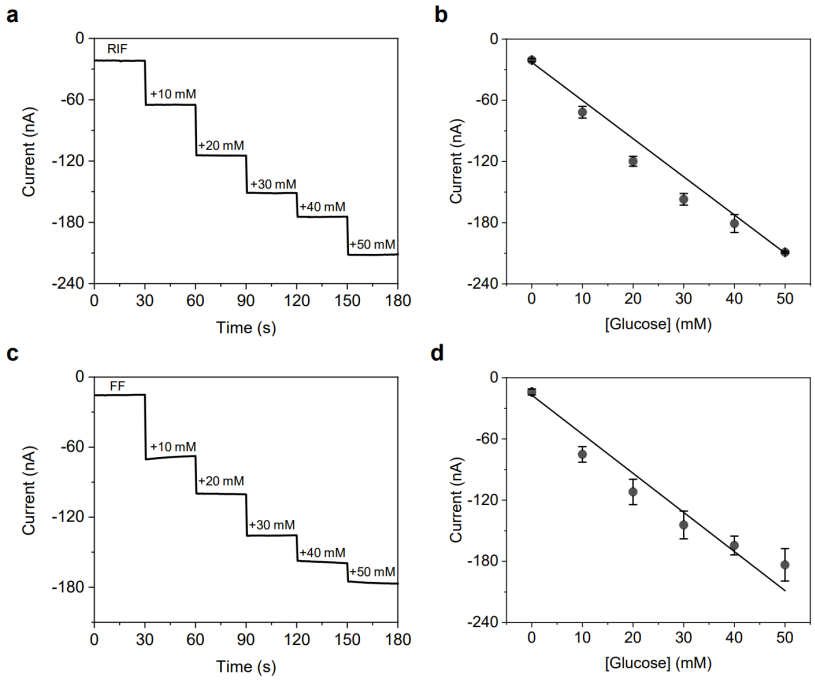


Figure B.12: Glucose sensor performances in rabbit intestinal fluid and human fecal fluid

(A,B) Amperometric response (A) and its corresponding calibration plot (B) for detecting 0-50 mM glucose in rabbit intestinal fluid. (C,D) Amperometric response (C) and its corresponding calibration plot (D) for detecting 0-50 mM glucose in human fecal fluid. Error bars represent the s.d. of the mean from three sensors. RIF, real intestinal fluid; FF, fecal fluid.

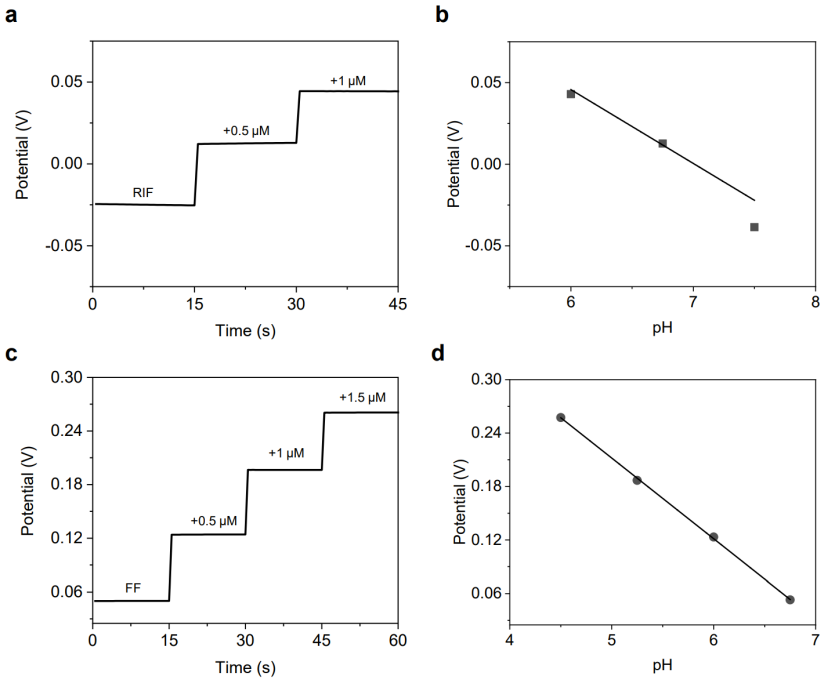


Figure B.13: pH sensor performances in rabbit intestinal fluid and human fecal fluid

(A,B) Potentiometric response (A) and its corresponding calibration plot (B) for pH sensing in rabbit intestinal fluid, with sequential addition of HCl to adjust the fluid pH. (C,D) Amperometric response (C) and its corresponding calibration plot (D) with sequential addition of HCl in human fecal fluid. Error bars represent the s.d. of the mean from three sensors.

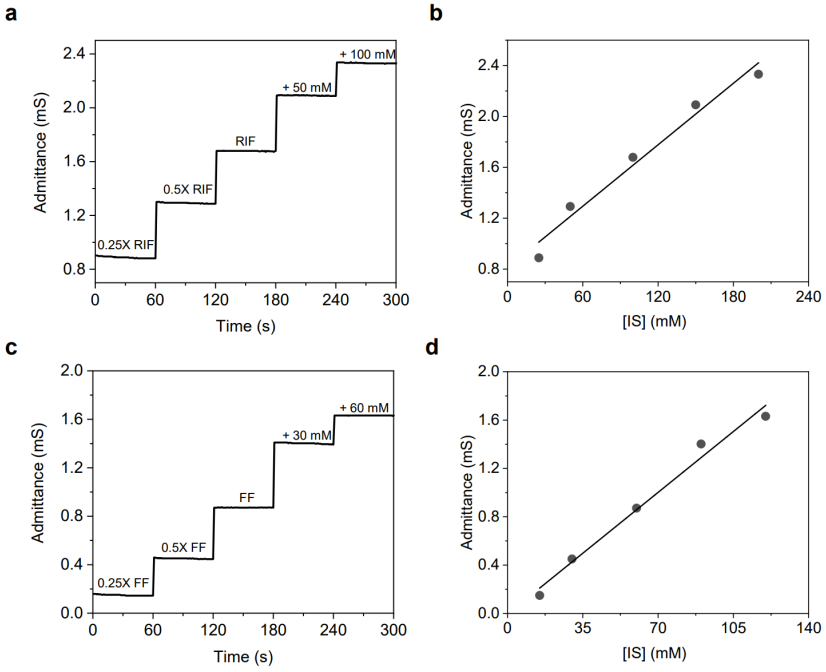


Figure B.14: Ionic strength sensor performances in rabbit intestinal fluid and human fecal fluid

(A,B) Impedance response (A) and its corresponding calibration plot (B) for ionic strength sensing in rabbit intestinal fluid to adjust the fluid ionic strength. (C,D) Impedance response (C) and its corresponding calibration plot (D) with sequential dilution of the human fecal fluid followed by the addition of NaCl to adjust the fluid ionic strength.

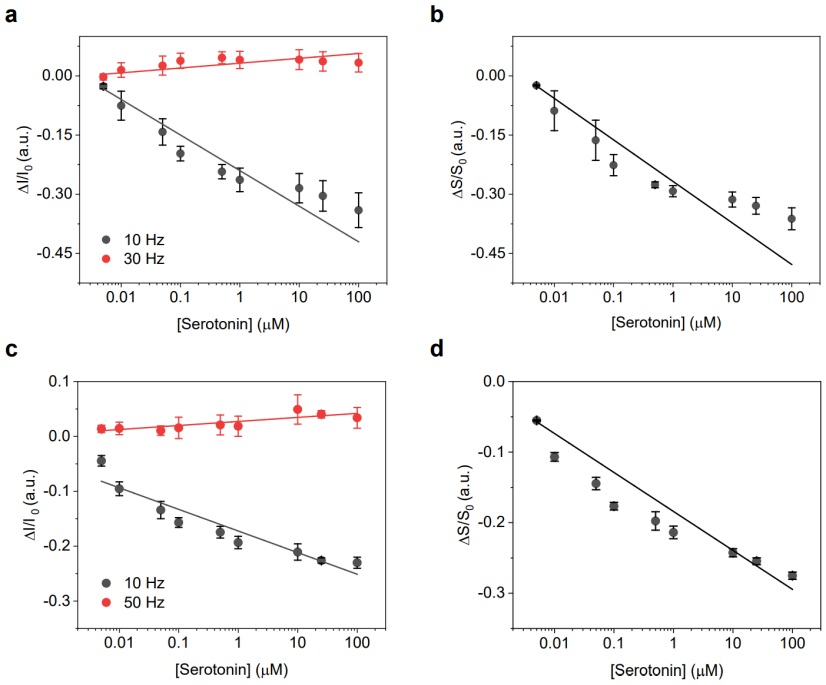


Figure B.15: Aptamer serotonin sensor performance in PBS and serum

(A,B) Relative changes in SWV peak current under 10 Hz and 30 Hz (A), and the corresponding calibration plot based on the relative ratiometric signal (B) under 0-100 μM serotonin in 1× PBS (pH 7.4). Error bars represent the s.d. of the mean from three sensors. (C,D) Relative changes in SWV peak current under 10 Hz and 50 Hz (C), and the corresponding calibration plot based on relative ratiometric signal (D) with 0-100 μM serotonin. Error bars represent the s.d. of the mean from three sensors.

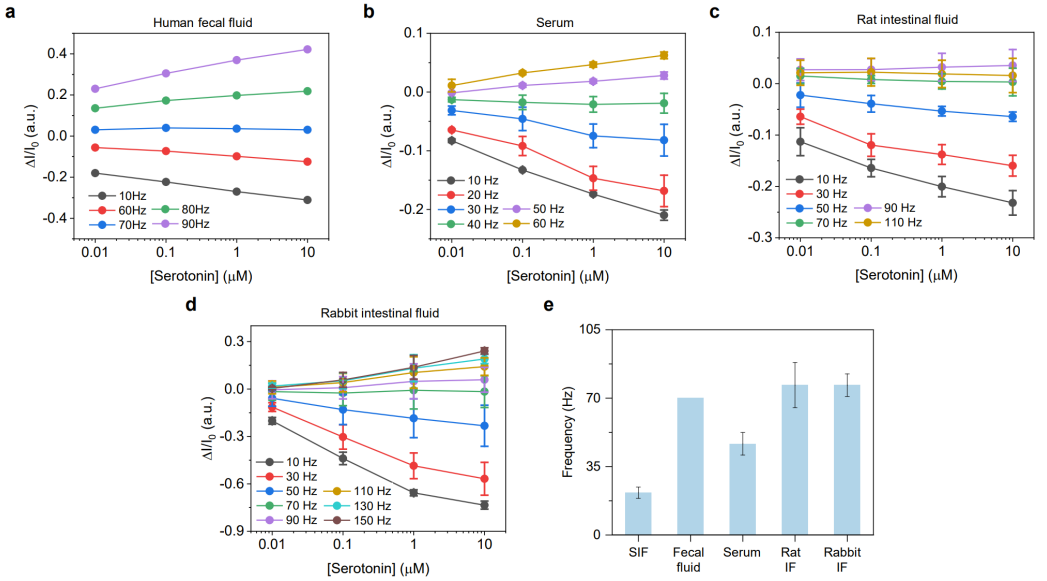


Figure B.16: Non-responsive frequencies of the serotonin sensor in various biofluids

(A-D) Relative changes in SWV peak current as a function of SWV frequencies with 0.01-10 μM of serotonin in human fecal fluid (A), serum (B), rat intestinal fluid (IF) (C), and rabbit IF (D). (E) Summary of the non-responsive frequency of the serotonin sensor in each fluid. Error bars represent the s.d. of the mean from three sensors.

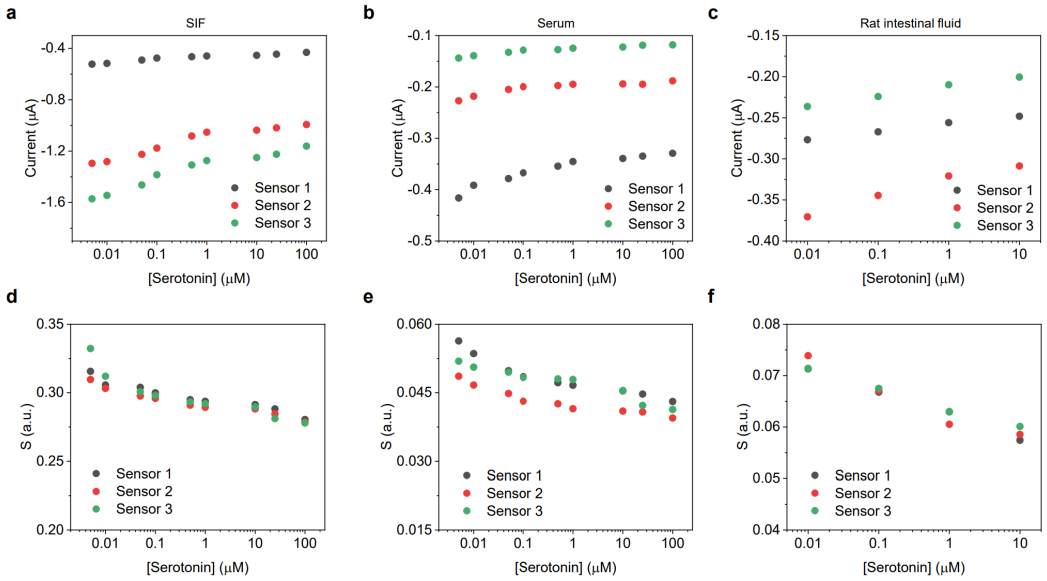


Figure B.17: Correction of sensor-to-sensor variations of the serotonin sensor through dual-frequency measurements

(A-C) SWV voltammogram peak currents of three sensors measured at 10 Hz in SIF (A), serum (B), and rat IF (C) with increasing serotonin levels. (D-F, Ratiometric signals of three sensors in SIF (D), serum (E), and rat IF (F). S was obtained using peak current under 10 Hz and the non-responsive frequency specific to each fluid.

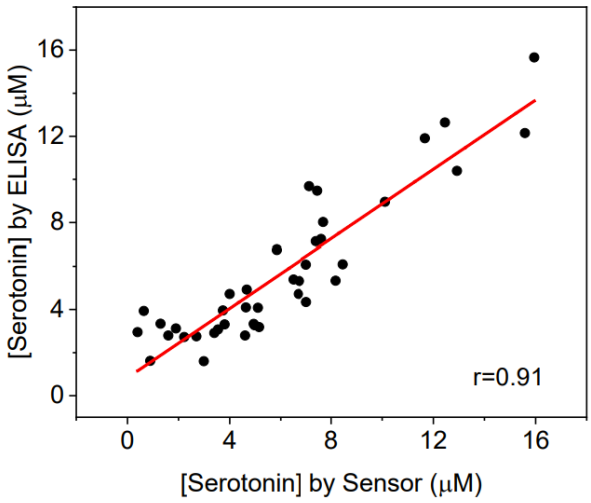


Figure B.18: Validation of the aptamer serotonin sensor for intestinal fluid analysis using ELISA

The red line represents the linear-fit trendline. The Pearson correlation coefficient (r) was acquired through linear regression (n=40).

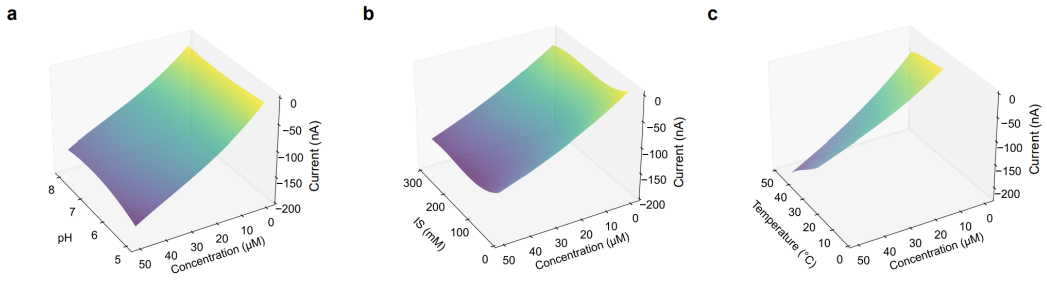


Figure B.19: Dependence of the glucose sensor response on pH, ionic strength, and temperature

(A-C), 3D color maps showing the dependence of the glucose sensor response on varying pH (A), ionic strength (B), and temperature (C).

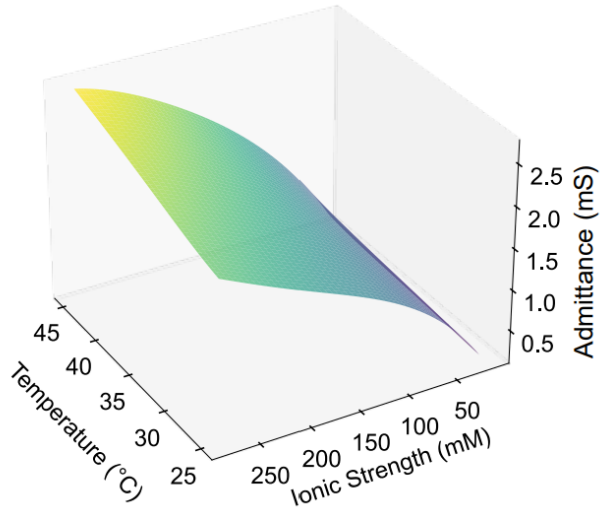


Figure B.20: Dependency of the ionic strength sensor response on temperature

3D color map showing the dependence of the ionic strength sensor response on varying temperature levels.

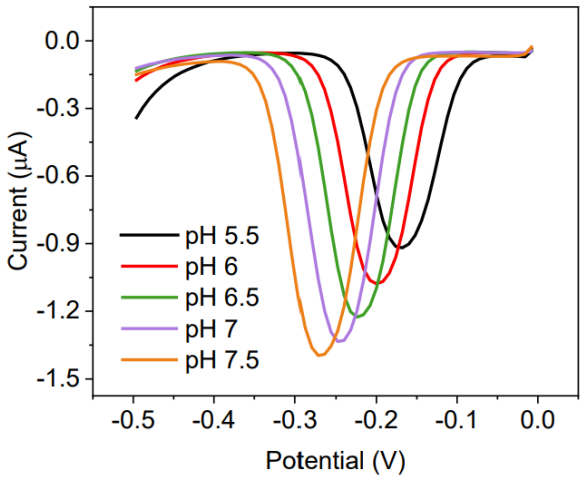


Figure B.21: Influence of solution pH on SWV peak potential and current of the serotonin sensor in SIF

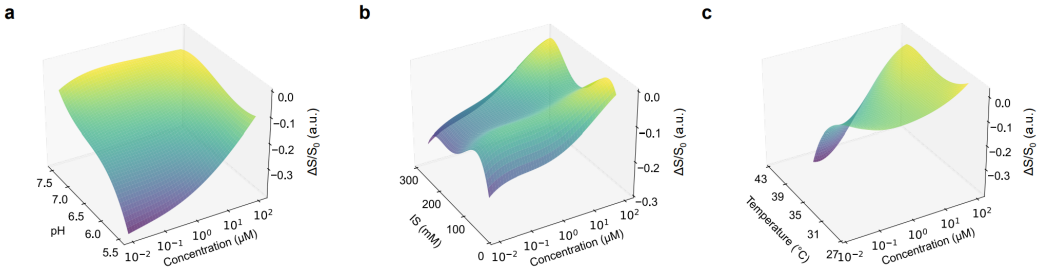


Figure B.22: Dependence of the serotonin sensor response on pH, ionic strength, and temperature

(A-C), 3D color maps showing the dependence of the serotonin sensor response on pH (A), ionic strength (B), and temperature (C).

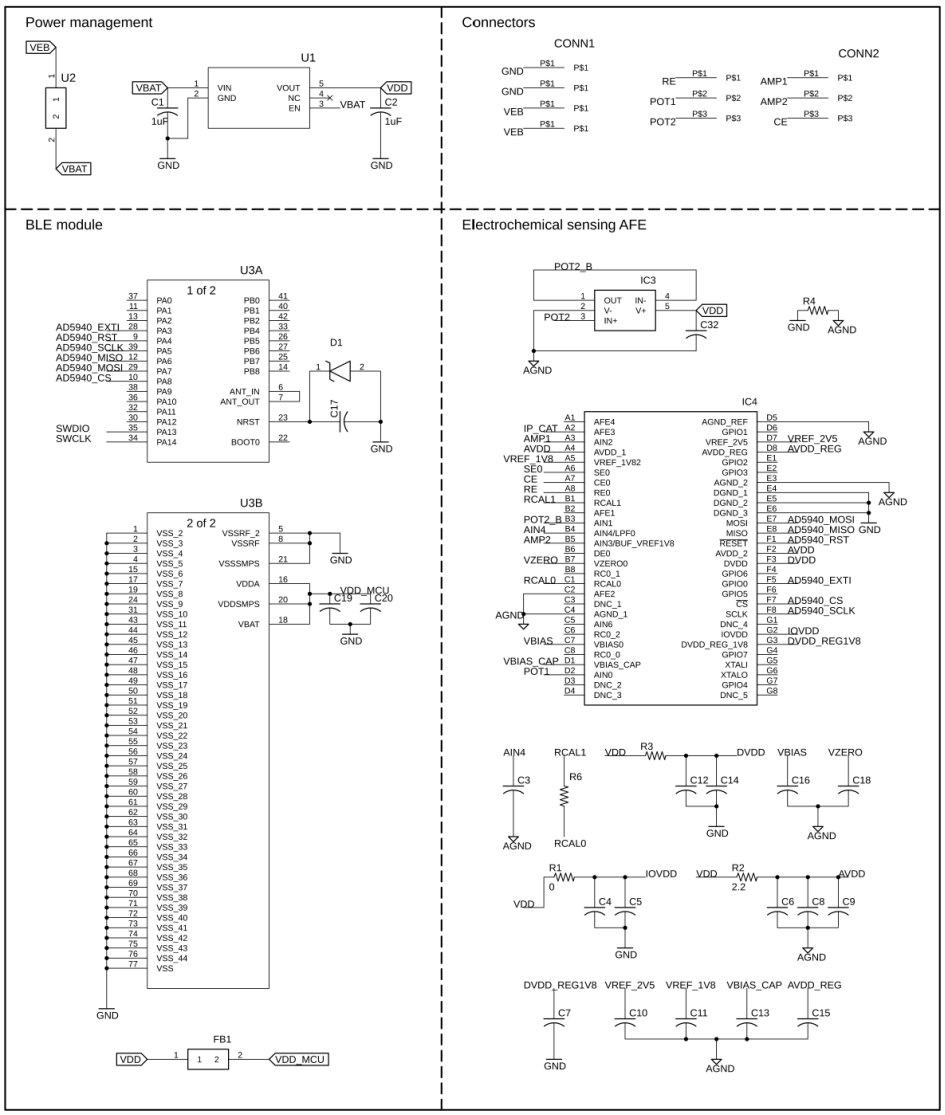


Figure B.23: Electronic circuit schematic of the ingestible electronic system

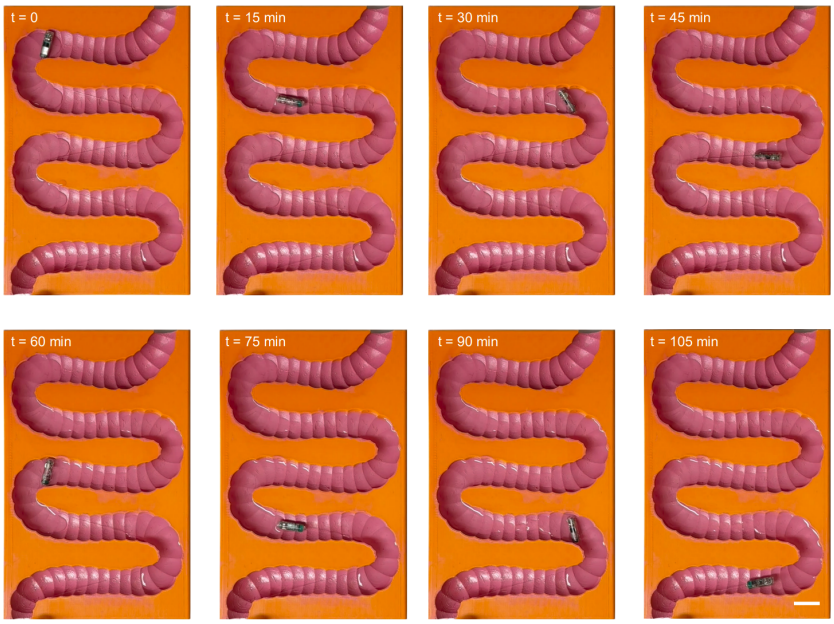


Figure B.24: Time-lapse images of the electronic capsule movements through a phantom intestine

Scale bar, 2.5 cm.

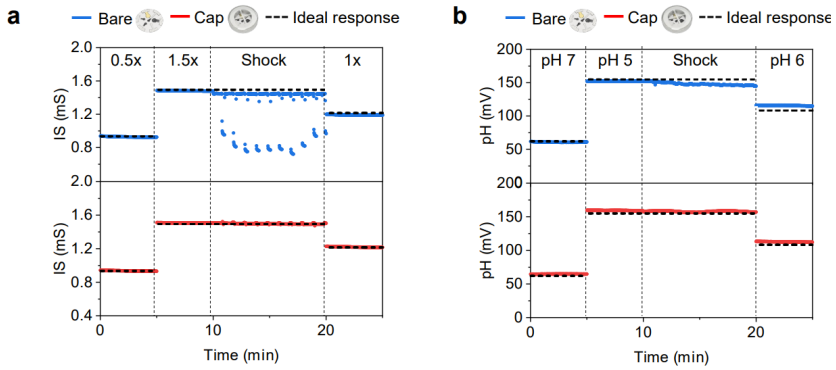


Figure B.25: Protective cap effects with pH and ionic strength sensors

(A,B) ionic strength (A) and pH (B) sensor responses of PillTrek devices with and without a protective cap, demonstrating the impact of repeated contact with intestinal tissue.

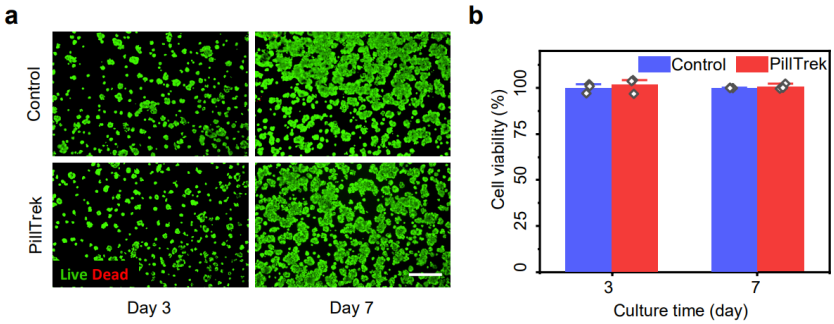


Figure B.26: Cytocompatibility of PillTrek

(A) Representative live (green)/dead (red) images of human colorectal adenocarcinoma HT29 cells after 3-day and 7-day culture with a PillTrek sensor array. Scale bar, 100 µm. (B) Quantitative analysis of cell viability over a 7-day period of culture with a PillTrek sensor array. Error bars represent the s.d. of the mean from three measurements.

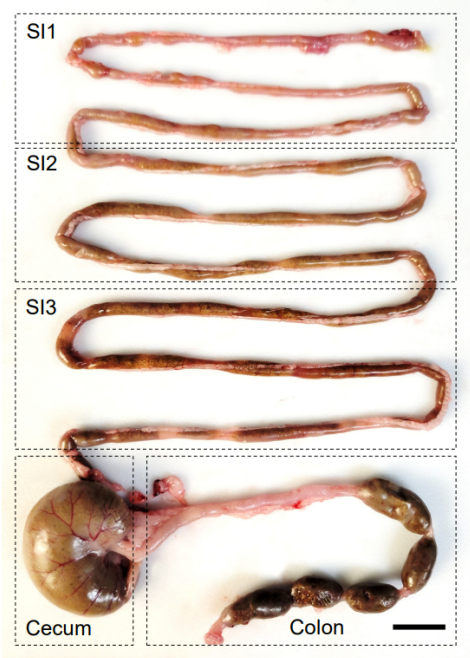


Figure B.27: Photograph of fasted rat intestine

Scale bar, 1 cm.

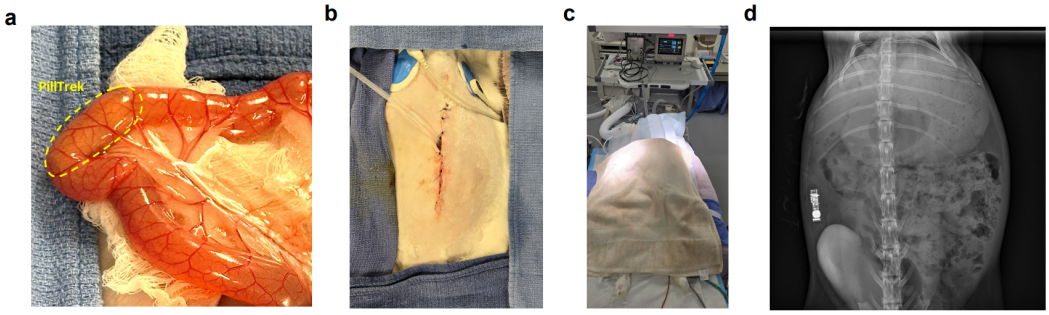


Figure B.28: Photographs of in vivo evaluation of PillTrek in rabbits

(A) Inserted PillTrek in the small intestine. Scale bar, 2 cm. (B) Sutured valley after capsule insertion. Scale bar, 2 cm. (C) Rabbits under heart rate, respiration, and temperature monitoring during PillTrek wireless monitoring. Scale bar, 10 cm. (D) X-ray image exhibiting the location of PillTrek, Scale bar, 2 cm.

| Sensing technique | Target | Size (mm) L × D | Animal study | Reference |
|---|---|---|---|---|
| Potentiometric | pH | 29 × 8.5 | N/A | [3] |
| Biofuel cell | Glucose | 26 × 9 | Pig | [4] |
| Luminescence | Heme | | Pig | [5] |
| Resistive | $O_2$, $H_2$, $CO_2$ | 26 × 9.8 | Human | [6] |
| Luminescence | NO, hydrogen peroxide ($H_2O_2$), tetrathionate and thiosulfate | 8.5 × 14.25 | Pig | [7] |
| Voltammetric | Not specific | 28 × 12 | N/A | [8] |
| Potentiometric | pH | 22.1 × 9 | N/A | [9] |
| Potentiometric | pH | | N/A | [10] |
| Amperometric | $H_2S$ | 34 × 14 | N/A | [11] |
| Potentiometric, Amperometric, Voltammetric, Impedimetric | pH, glucose, serotonin, ionic strength | 25 × 7 | Rabbit | This work |

Table B.1: Comparison between ingestible biochemical sensors and PillTrek.

Ref. [3], Ref. [4], Ref. [5], Ref. [6], Ref. [7], Ref. [8], Ref. [9], Ref. [10], Ref. [11]

| Discrete Components | Description | Value | Package |
|---|---|---|---|
| C1, C2, C18 | Capacitor | 1 µF | 0201 |
| C3, C5, C8, C9, C14, C16, C17, C20, C32 | Capacitor | 0.1 µF | 0201 |
| C4, C6, C12 | Capacitor | 10 µF | 0402 |
| C7, C10, C13, C15 | Capacitor | 0.47 µF | 0201 |
| C11,C19 | Capacitor | 4.7 µF | 0201 |
| R1, R4 | Resistor | 0 Ω | 0201 |
| R2, R3 | Resistor | 2.2 Ω | 0201 |
| R6 | Resistor | 470 Ω | 0201 |
| FB1 | Ferrite bead | 330 Ω | 0201 |
| D1 | TVS Diode | ESDALC6V1-1U2 | 0201 |
| U1 | Voltage regulator | ADP162 | TSOT-5 |
| U2 | Magnetic reed switch | MK24-B-3-OE | 2405 |
| U3 | BLE module | STM32WB1MMC | 77-LGA |
| IC3 | Operational amplifier | LPV521 | SC-70-5 |
| IC4 | Electrochemical AFE | AD5940 | 56WLCSP |

Table B.2: List of off-the-shelf electronic components used in PillTrek.

## References


[1] Hui Li et al. “Calibration-Free Electrochemical Biosensors Supporting Accurate Molecular Measurements Directly in Undiluted Whole Blood”. *Journal of the American Chemical Society* **2017**, *139* (32), 11207–11213. DOI: 10.1021/jacs.7b05412

[2] Philippe Dauphin-Ducharme et al. “Electrochemical Aptamer-Based Sensors for Improved Therapeutic Drug Monitoring and High-Precision, Feedback-Controlled Drug Delivery”. *ACS Sensors* **2019**, *4* (10), 2832–2837. DOI: 10.1021/acssensors.9b01616

[3] Cihan Asci et al. “Ingestible pH Sensing Capsule with Thread-Based Electrochemical Sensors”. In: *2022 IEEE Sensors*. 2022 IEEE Sensors. Dallas, TX, USA: IEEE, Oct. 30, 2022, pp. 1–4. ISBN: 978-1-66548-464-0. DOI: 10.1109/SENSORS52175.2022.9967347. URL: https://ieeexplore.ieee.org/document/9967347/ (visited on 07/30/2024).

[4] Ernesto De la Paz et al. “A self-powered ingestible wireless biosensing system for real-time in situ monitoring of gastrointestinal tract metabolites”. *Nature Communications* **2022**, *13* (1), 7405. DOI: 10.1038/s41467-022-35074-y

[5] Mark Mimee et al. “An ingestible bacterial-electronic system to monitor gastrointestinal health”. *Science* **2018**, *360* (6391), 915–918. DOI: 10.1126/science.aas9315

[6] Kourosh Kalantar-Zadeh et al. “A human pilot trial of ingestible electronic capsules capable of sensing different gases in the gut”. *Nature Electronics* **2018**, *1* (1), 79–87. DOI: 10.1038/s41928-017-0004-x

[7] M. E. Inda-Webb et al. “Sub-1.4 cm3 capsule for detecting labile inflammatory biomarkers in situ”. *Nature* **2023**, *620* (7973), 386–392. DOI: 10.1038/s41586-023-06369-x

[8] Cihan Asci et al. “Ingestible pH sensing device for gastrointestinal health monitoring based on thread-based electrochemical sensors”. *Microchimica Acta* **2023**, *190* (10), 385. DOI: 10.1007/s00604-023-05946-1

[9] C. Mc Caffrey, K. Twomey, and V. I. Ogurtsov. “Development of a wireless swallowable capsule with potentiostatic electrochemical sensor for gastrointestinal track investigation”. *Sensors and Actuators B: Chemical* **2015**, *218*, 8–15. DOI: 10.1016/j.snb.2015.04.063

[10] Chen Cheng et al. “A wireless, ingestible pH sensing capsule system based on iridium oxide for monitoring gastrointestinal health”. *Sensors and Actuators B: Chemical* **2021**, *349*, 130781. DOI: 10.1016/j.snb.2021.130781

[11] Justin M. Stine et al. “Miniaturized Capsule System Toward Real-Time Electrochemical Detection of H2S in the Gastrointestinal Tract (Adv. Healthcare Mater. 5/2024)”. *Advanced Healthcare Materials* **2024**, *13* (5), 2470029. DOI: 10.1002/adhm.202470029

*Appendix C*

# APPENDIX FOR EPBP NICOTINE SENSOR

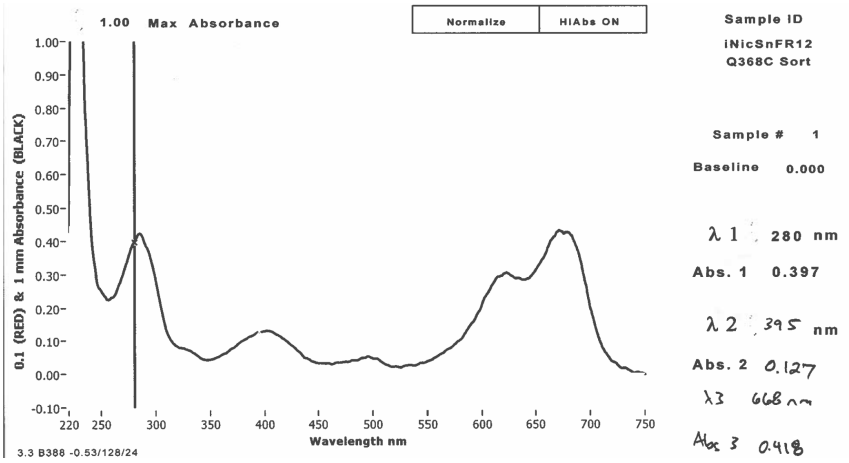


Figure C.1: Absorbance spectra of MB-labeled iNicSnFR12 Q368C mutant

Methylene blue has peak absorbance contributions at $\lambda_1$ = 280 nm and $\lambda_3$ = 668 nm. The protein with cpGFP has peak absorbance contributions at $\lambda_1$ = 280 nm and $\lambda_2$ = 395 nm.

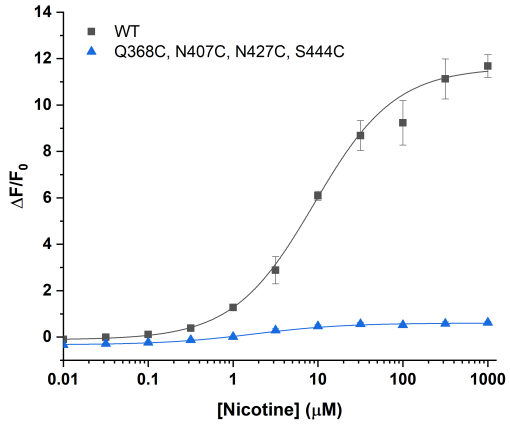


Figure C.2: Dose-response relation for iNicSnFR12 WT and quad cysteine insertion

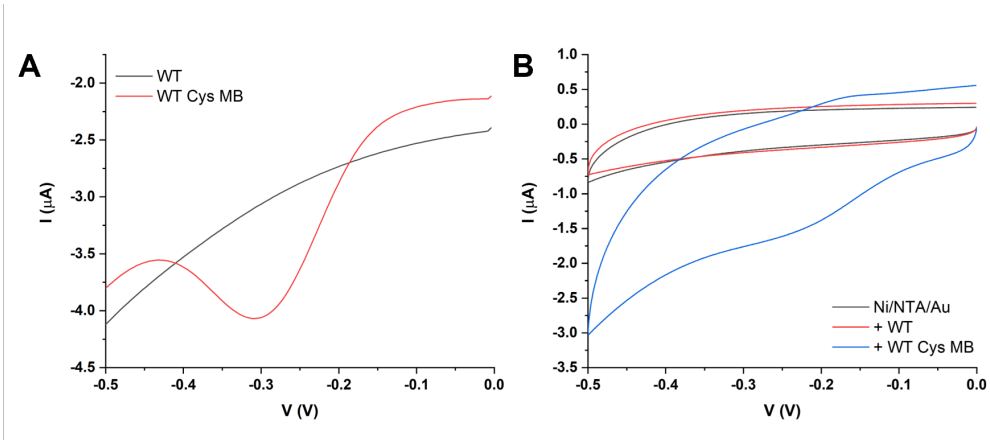


Figure C.3: Electrochemical characterization of iNicSnFR12 WT MB-labeled cysteine residues

(A) SWV trace of iNicSnFR12 WT unlabeled and MB labeled cysteines immobilized on a Ni/NTA/Au electrode in 0.25× PBS, pH 7.0. (B) CV characterization of Ni/NTA/Au modified with iNicSnFR12 WT unlabeled and MB labeled cysteines in 1× PBS, pH 7.0.

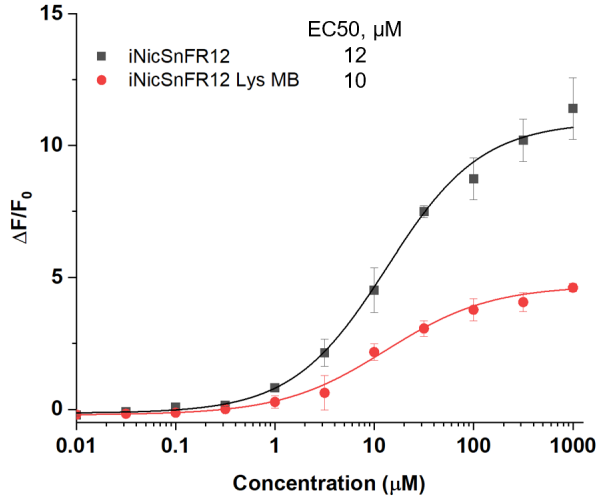


Figure C.4: Dose-response relation for iNicSnFR12 WT with MB-labeled lysines

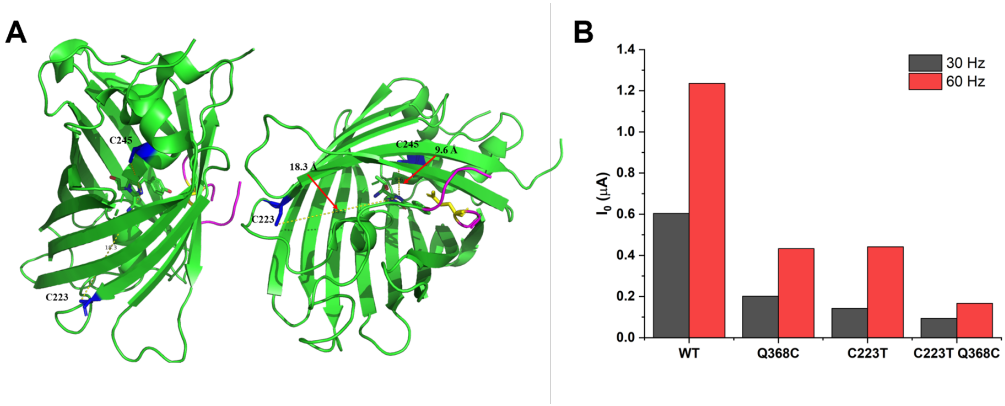


Figure C.5: Characterization of C223T GFP cysteine substitution

(A) Cysteine residues (blue) in cpGFP with distances to the center of the chromophore. C223 is a surface exposed cysteine, whereas C245 is buried within the chromophore. (B) SWV MB peak current response for iNicSnFR12 WT, Q368C, C223T, and C223T Q368C in 0.25× PBS, pH 7.0.

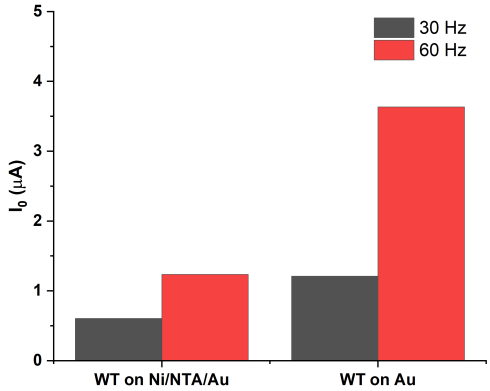


Figure C.6: Baseline current response of iNicSnFR12 WT Cys MB on Au with and without Ni/NTA modification

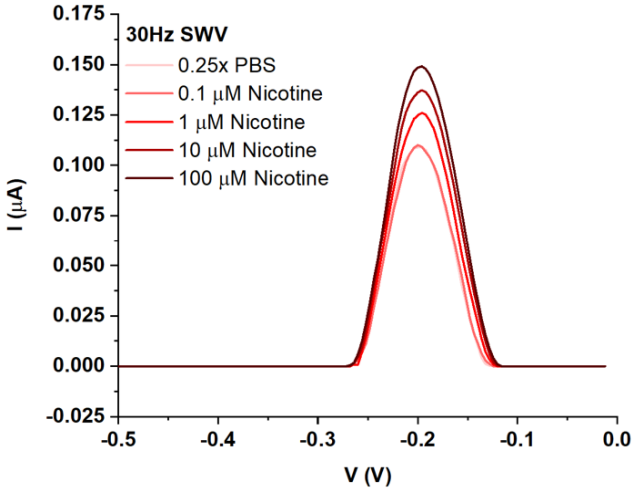


Figure C.7: SWV response of iNicSnFR12 Q368C-MB with AuL binding sequence

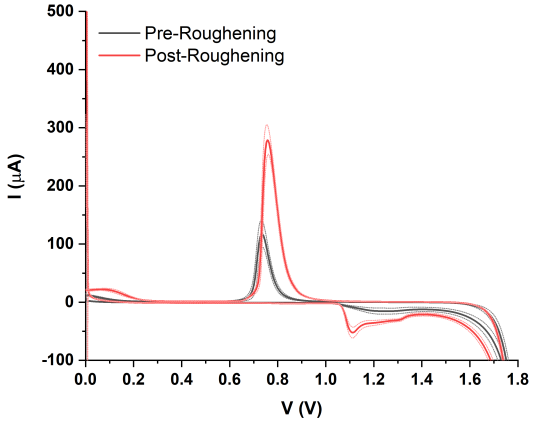


Figure C.8: Electroactive surface area increases with electrochemical roughening

10,000 cycles of electrochemical roughening of gold disk electrodes results in a 3× increase of the electroactive surface area as determined by the gold oxide reduction peak area. Dashed lines represent s.d. of mean (n = 8).

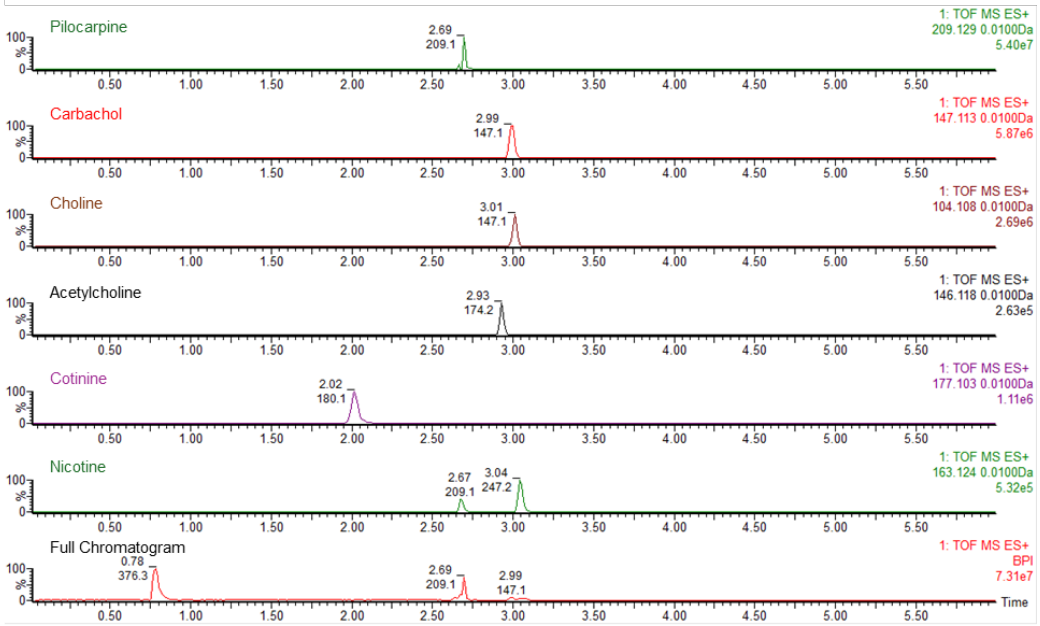


Figure C.9: Chromatogram of cholinergic interferents

Chromatogram of LC-MS standards: 0.5 µM acetylcholine, 5 µM choline, 20 µM carbachol, 20 µM pilocarpine, 0.5 µM nicotine, 0.5 µM cotinine.

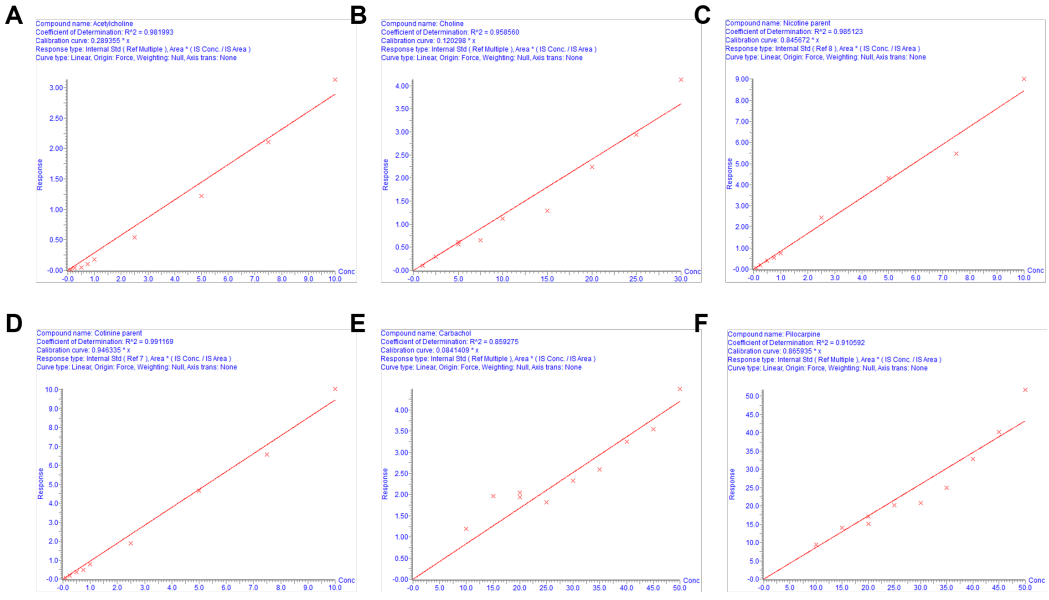


Figure C.10: LC-MS calibration

Calibration plots for (A) aceytlcholine, (B) choline, (C) nicotine, (D) cotinine, (E) carbachol, and (F) pilocarpine standards.

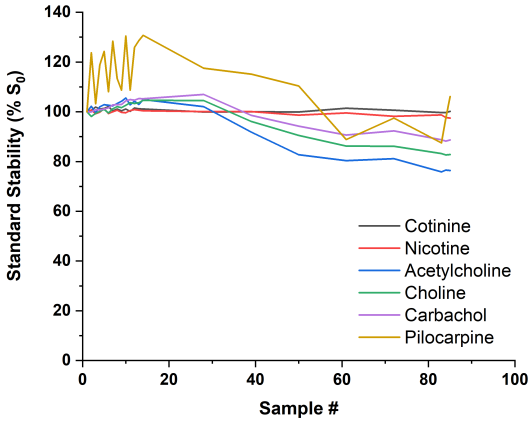


Figure C.11: Quality control of LC-MS standards

Nicotine and cotinine are the most stable analytes throughout testing due to the presence of their paired internal standards, nicotine-$D_4$ and cotinine-$D_3$, respectively.

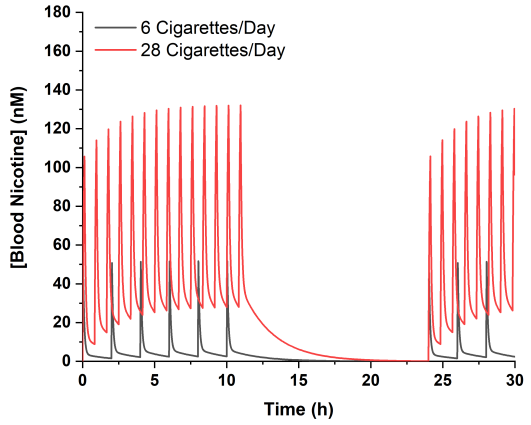


Figure C.12: Pharmacokinetic simulation of blood nicotine levels in light and heavy smokers

A light smoker (black) is modeled who smokes light cigarettes (0.6 mg nicotine), 1 cigarette per smoking session every 2 h, and smokes 6 cigarettes daily. A heavy smoker (red) is modeled who smokes standard cigarettes (1.0 mg nicotine), 2 cigarettes per smoking session every 50 min, and smokes 28 cigarettes daily. Distribution and elimination parameters (kel = 0.08 $hr^{-1}$, kf = 0.12 $hr^{-1}$, kr = 0.02 $hr^{-1}$, Vd = 200 L) and drug receptor parameters (Activation = 1000 nM, Chaperoning = 36 nM) were held constant. Generated using http://inside-out.caltech.edu:9988/webapps/home/session.html?app=NicotineApp. [6]

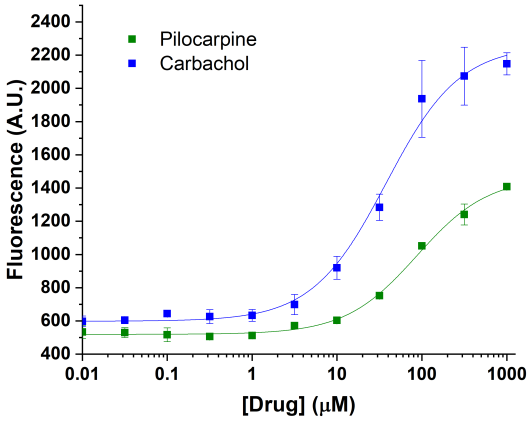


Figure C.13: Dose-response relation of iNicSnFR12 to cholinergic drugs, pilocarpine and carbachol, in 3× PBS, pH 7.0, raw fluorescence

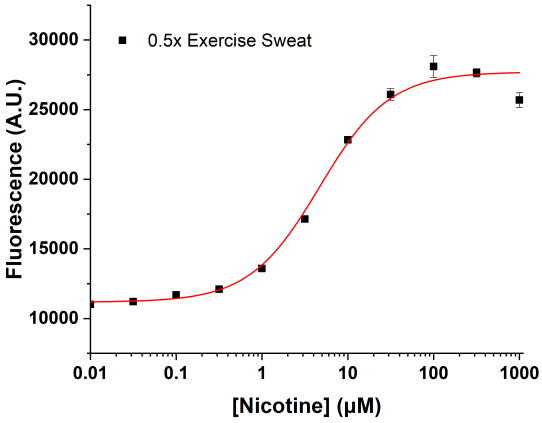


Figure C.14: Nicotine dose-response relation of iNicSnFR12 in 0.5× exercise sweat, raw fluorescence

1:1 mix of exercise sweat and nicotine solution in 3× PBS, pH 7.0.

# INDEX